

Organic Molecules on Wide-Gap Insulating Surfaces from First-Principles

**Vom der Fakultät für Mathematik und Physik
der Gottfried Wilhelm Leibniz Universität Hannover
zur Erlangung des Grades
Doktor der Naturwissenschaften
Dr. rer. nat.
genehmigte Dissertation**

von

M.Sc. Wei Chen
geboren am 11 August 1980
in Shanghai, China

Hannover
January 2011

Referent: Prof. Dr. Herbert Pfnür
Korreferent: Prof. Dr. Thomas Bredow
Tag der Promotion: 29.04.2011

Abstract

An intriguing application in the electrostatic separation process of the salt minerals in the industry is that different compounds can be distinguished by certain molecules when operated in an inhomogeneous electrical field. This effect is understood by the charge transfer model, in which the occupied and unoccupied states introduced by the molecular adsorbates play a central role. A precise control of the efficiency of the separation process requires not only the accurate knowledge of the organic molecules and the host insulator, but also the microscopic picture of the molecule-insulator interaction.

Although the properties of the conditioner molecules (such as *benzoic acid* and its phenolic derivatives) and the *rock salt* are well-known, the detailed mechanism of the interaction between the organic molecules and the insulating surface is yet absent. The interaction at the interface becomes more complicated when various defects are present at the surface. These defects are subject to have enormous impact on the adsorption configuration and the electronic structure of the adsorbate system.

This thesis investigates the adsorption of benzoic acid and its various phenolic derivatives on wide-gap insulators (e.g. NaCl and KCl surfaces) from first-principles, in an effort to demystify the contact charging effect between certain minerals mixed with organic molecules. While Kohn-Sham density functional theory (KS-DFT) becomes a *de facto* standard for the prediction of ground-state properties, it is far from being perfect because the standard semilocal density functional approximations suffer from several limitations, such as the notorious *gap problem* and the neglect of the prevalent long-range *van der Waals* interaction in the weakly bonded systems. Moreover, the problem of electronic excitations are beyond the scope of KS-DFT. In this work, a variety of *ab initio* methods are adopted at the respective level of theory, from KS-DFT (with hybrid functionals and dispersion force corrections) to Hedin’s *GW* approximation and ultimately the Bethe-Salpeter equation (BSE) to include the excitonic effect in electronic excitations.

The results reveal a complex interplay between the short-range and long-range interactions upon the adsorption of organic molecules on wide-gap insulator surfaces. The frontier molecular orbitals of the adsorbates exhibit shifts and broadenings as a result of rehybridizations. The adsorbate is stabilized by the short-range ionic interaction and the long-range *van der Waals* contribution, whereas the adsorption configuration is largely dominated by the covalent interaction. Charge transfer between the molecule and the surface is negligible on ideal surfaces. In the presence of surface color centers, the binding energy is substantially enhanced due to the charge transfer of the unpaired electron from the surface vacancy to the adsorbate. By engineering the polarity of the surface steps, it is demonstrated that the fundamental gap of the adsorbate system can be effectively reduced. Moreover, the dynamic polarization effect within the surface has been found to be responsible for the renormalization of the molecular quasiparticle levels at the molecule-insulator interfaces. The lowest excitation energies of the gas-phase molecules and the adsorbate systems are further determined by the two-particle BSE calculations.

The important roles of the nonlocal correlations, surface defects and excitonic effect are presented in the context of the molecule-insulator interfaces.

Zusammenfassung

Eine verblüffende Anwendung im elektrostatischen Trennungsprozess von Salzmineralien in der Industrie stellt die Möglichkeit dar, dass unterschiedliche Anteile des Salzes in einem inhomogenen elektrischen Feld durch Zufügen bestimmten Moleküle getrennt werden können. Dieser Effekt lässt sich mit Hilfe des Modells des Ladungstransfers verstehen, in dem die durch die absorbierten Moleküle hervorgerufenen, besetzten und unbesetzten Zustände eine zentrale Rolle spielen. Eine exakte Kontrolle der Effizienz beim Trennungsprozesses bedarf nicht nur der genauen Kenntnis der organischen Moleküle und des Wirtsisolators, sondern auch ein mikroskopisches Verständnis der Molekül-Isolator Wechselwirkung.

Obwohl die Eigenschaften der Konditioniermoleküle (wie *Benzoessäure* und seine phenolischen Derivate) und von Steinsalz bekannt sind, sind detaillierte Mechanismen der Wechselwirkung zwischen organischen Molekülen und der isolierenden Oberfläche nach wie vor unbekannt. Die Wechselwirkung an der Grenzfläche wird abermals komplizierter, sobald verschiedenartige Defekte auf der Oberfläche vorhanden sind. Defekte spielen dabei eine enorme Bedeutung für die Adsorptionsanordnung und die elektronischen Eigenschaften des Adsorbatsystems.

In dieser Arbeit werden die Grundprinzipien bei der Adsorption von *Benzoessäure* und seiner verschiedenartigen phenolischen Derivate auf Isolatoren mit großer Bandlücke (z.B. NaCl und KCl Oberflächen) untersucht, um den Kontaktaufladungseffekt zwischen mit Molekülen versetzten Mineralsalzen zu entschlüsseln. Obwohl die Kohn-Sham Dichtefunktionaltheorie (KS-DFT) zur Standardmethode bei der Vorhersage von Eigenschaften des Grundzustands geworden ist, ist sie weit davon entfernt, perfekt zu sein, da die Näherungen bei der üblichen semilokalen Dichtefunktionaltheorie diversen Einschränkungen unterliegen. Dazu zählt das offenkundige *Energielückenproblem* und die Mißachtung der vorherrschenden langreichweitigen *van der Waals* Wechselwirkung in schwach gebundenen Systemen. Zudem liegt das Problem der elektronischen Anregungen jenseits des Gültigkeitsbereichs der KS-DFT. In dieser Arbeit wurden deshalb diverse ab initio Methoden verwendet, ausgehend von KS-DFT (mit Hybridfunktionalen und Korrekturen der Dispersionskräfte) über Hedin's *GW* Näherung bis hin zur *Bethe-Salpeter Gleichung* (BSE), um excitonische Effekte in elektronischen Anregungen mit einzubeziehen.

Die Ergebnisse machen ein komplexes Zusammenspiel zwischen der kurz- und langreichweitigen Wechselwirkung bei der Adsorption organischer Moleküle auf Oberflächen von Isolatoren mit großer Bandlücke deutlich. Die an der Bindung beteiligten Molekülorbitale der Adsorbate weisen Verschiebungen und Verbreiterungen als Ergebnis der Umhybridisierung auf. Das Adsorbat wird durch die kurzreichweitige ionische Wechselwirkung und die langreichweitigen *van der Waals* Beiträge stabilisiert, wohingegen die Adsorptionsanordnung von der kovalenten Wechselwirkung dominiert wird. Ein Ladungstransfer zwischen dem Molekül und der Oberfläche ist auf idealen Oberflächen vernachlässigbar. In Gegenwart von Oberflächenfarbzentren wird im Wesentlichen die

Bindungsenergie durch den Ladungstransfer von ungepaarten Elektronen aus den Leerstellen der Oberflächen in das Adsorbat erhöht. Es zeigt sich, dass durch geschickte Anpassung der Polarität an den Stufenkanten die fundamentale Bandlücke des Adsorbatsystems effektiv verkleinert werden kann. Darüber hinaus stellte sich heraus, dass der dynamische Polarisierungseffekt verantwortlich ist für die Verschiebung der Energiezustände der am Molekül lokalisierten Quasiteilchenniveaus der Molekül-Isolator Grenzfläche. Die niedrigsten Anregungsenergien der Moleküle in der Gasphase und des Adsorbatsystems wurden durch Zweiteilchen-BSE-Berechnungen genauer bestimmt. Die wichtige Rolle von nichtlokalen Korrelationen, Oberflächendefekten und exzitonischen Effekten werden im Zusammenhang mit der Molekül-Isolator- Grenzfläche vorgestellt.

Keywords:

Adsorption, Conjugated organic molecule, Wide-gap insulator, Electronic excitation

Schlagworte:

Adsorption, Konjugierter Moleküle, Isolator, Elektronische Anregung

Contents

List of Tables	II
List of Figures	III
1 Introduction	1
I Theoretical Framework	5
2 Hartree-Fock Theory	6
2.1 Many-electron Wavefunction	6
2.2 Hartree Equation	7
2.3 Hartree-Fock Method	9
3 Density functional Theory	11
3.1 Early approximations	11
3.2 Hohenberg-Kohn Theorems	12
3.3 Kohn-Sham Formalism	13
3.4 Exchange-correlation Functionals	13
3.4.1 Local Density Approximation	14
3.4.2 Generalized Gradient Approximation	15
3.4.3 Hybrid Functional	17
3.5 van der Waals Interactions in Density Functional Theory	18
4 Implementations of Density Functional Theory	20
4.1 Basis Sets	20
4.1.1 Atomic-like orbitals	20
4.1.2 Plane-wave Basis Set	22
4.2 Pseudopotentials	23
4.2.1 Norm-conserving Pseudopotentials	23
4.2.2 Ultrasoft Pseudopotentials	25
4.2.3 Projector Augmented Wave Method	26
5 Many-body Perturbation Theory	28
5.1 Green's Function Theory	28
5.2 Hedin's GW Approximation	30
5.3 Two-particle Bethe-Salpeter Equation	35

II Gas-phase Molecules and Bulk Insulators	38
6 Benzoic Acid and Its Phenolic Derivatives	39
6.1 Ground-state Geometries	39
6.2 Electronic Structures	39
6.3 Molecular Excitonic Effect	44
7 NaCl and KCl	46
7.1 Structural Parameters	46
7.2 Band Structure	47
7.2.1 KS-DFT Electronic Structure	47
7.2.2 Quasiparticle Band Gap	48
7.3 Excitonic Effect	49
III Organic Molecules on Wide-gap Insulator Surfaces	51
8 Hydroxybenzoic Acids on Ideal NaCl(100)	52
8.1 Properties of NaCl(100) Surface	52
8.2 Adsorption of Benzoic Acid and Its Phenolic Derivatives on NaCl(100) . .	54
8.2.1 Adsorption Configurations	54
8.2.2 Electronic and Binding Properties	58
9 The Effect of van der Waals Interaction	62
9.1 Roles of vdW Forces in the Adsorption Energy	62
9.2 The Effect on the Adsorption Geometry and Electronic Structure	65
10 Generic Aspects of Adsorption on Alkali Halide (100) Surfaces	69
10.1 Adsorption Geometries	69
10.2 Effective Kohn-Sham Gap and Molecular Orbital Alignment	75
10.3 Insights From Kohn-Sham DFT	76
11 Polarization Induced Renormalization of Molecular Energy Levels	78
11.1 Classical Image Charge Theory	78
11.2 Renormalization of Electronic Levels at NaCl(100)	79
12 Excitonic Effect at Molecule-Insulator Interface	82
13 Roles of Surface Defects	85
13.1 Adsorption at Surface Color Centers	85
13.1.1 Surface Color Center at NaCl(100)	86
13.1.2 Adsorption at Surface Color Center	87
13.2 Effect of Non-Polar Stepped Surface	90
13.2.1 Bare [001]-oriented Step	90
13.2.2 Adsorption at the [001] Step	92

13.3 Roles of Polar Steps	93
13.3.1 Bare [011] Step	93
13.3.2 Adsorption at the [011] Step	96
14 Summary and Perspectives	103
14.1 Discussion	103
14.2 Outlook	105
A Tamm-Dancoff Approximation to the Absorption of Molecules	108
B Gluconic Acid on Kieserite (100) Surface	109
B.1 Bulk Properties	109
B.2 Adsorption Geometry	110
B.3 Anomalous Molecular Orbital Variation	113
C Color Centers in NaCl	116
C.1 Electronic Structure of Chlorine Vacancies	118
C.2 Thermodynamic Transition Energies and Finite-Size Corrections	120
C.2.1 Finite-Size Corrections	121
C.2.2 Chlorine Vacancy Thermodynamic Transition Energies	126
C.3 Optical Properties of the Color Center	128
C.4 Discussion	131
D Passivation of the Polar Step by Water	135
E Localized Basis Sets	137
Bibliography	141
Acknowledgment	158
Publications	159
Index	160

List of Tables

6.1	Intramolecular bond lengths of BA, SA and <i>p</i> -SA	40
6.2	Frontier molecular orbital energies of BA, SA and <i>p</i> -SA	40
7.1	Equilibrium parameters and band gap of NaCl	47
8.1	Displacements of surface atoms in NaCl(100)	53
8.2	Adsorption energies of hydroxybenzoic acids on NaCl(100).	55
8.3	Intramolecular bond length changes upon adsorption on NaCl(100)	57
9.1	vdW corrected adsorption energies of SA/NaCl(100)	63
10.1	Adsorption energies on KCl and NaCl(100) surfaces	71
10.2	Relaxed geometric parameters on KCl and NaCl(100)	72
11.1	Calculated energy gaps of BA and SA on NaCl(100)	80
13.1	Adsorption energies at the F_s center	88
13.2	Changes of intramolecular bond lengths at the F_s center	88
13.3	Geometric relaxation at the [001] step edge	91
13.4	Geometric relaxation at the [011] step	94
13.5	Adsorption energies at the Na-NaCl [011] step	98
13.6	Adsorption energies at the K-KCl [011] step site including vdW	99
B.1	Adsorption energies of a GA molecule on a $\text{MgSO}_4\cdot\text{H}_2\text{O}(100)$ surface	111
B.2	Energy gaps of the GA molecule upon adsorption	113
C.1	Calculated parameters of NaCl by various functionals	117
C.2	Displacements of the nearest-neighbor Na atoms around the color center	119
C.3	Energy levels of the a_{1g} state	120
C.4	Formation energies of Cl vacancies in various charge states	126
C.5	Vertical absorption and emission energies	130

List of Figures

1.1	Charge transfer model	3
5.1	Feynman diagram of the Dyson equation	32
5.2	Feynman diagram for the self-energy in the <i>GW</i> method	33
6.1	Structures of BA, SA and <i>p</i> -SA	39
6.2	Molecular orbital energies and electron densities of BA, SA and <i>p</i> -SA	42
6.3	Absorption spectra for BA and SA	43
6.4	Excitonic wavefunction of the lowest singlet of SA	44
7.1	Band structure and density of states of bulk NaCl	48
7.2	Absorption spectra of bulk NaCl	49
8.1	Surface energy of NaCl(100) surface	52
8.2	Band structure and density of states of NaCl(100)	54
8.3	Adsorption configurations of hydroxybenzoic acids on NaCl(100)	56
8.4	Charge density difference map for SA adsorbed on NaCl(100)	57
8.5	Band structures of BA, SA and <i>p</i> -SA adsorbed on NaCl(100)	59
8.6	Project density of states of SA upon adsorption on NaCl(100)	60
9.1	Interaction energies vs. separation for SA/NaCl(100)	64
9.2	vdW induced charge density difference in SA/NaCl(100)	66
9.3	Local density of states of the SA on NaCl(100) with vdW included	67
10.1	Adsorption configurations of BA, SA and <i>p</i> -SA on KCl(100)	70
10.2	PDOS of SA adsorbed on KCl and NaCl(100)	70
10.3	Energy diagrams of the molecular frontier orbitals	73
10.4	Band digram of BA, SA and <i>p</i> -SA on KCl and NaCl(100)	75
11.1	Evolution of the $\pi - \pi^*$ energy gap upon adsorption	79
12.1	Absorption spectra of the BA and SA adsorbed on NaCl(100)	83
13.1	Electron spin density of an F_s center at NaCl(100)	86
13.2	Adsorption geometries of BA, SA and <i>p</i> -SA at the F_s center	87
13.3	Electron spin density for SA adsorbed at NaCl(100) F_s center	89
13.4	Projected density of states upon adsorption at the F_s center	89
13.5	Slab model of [001] step on NaCl(100)	90

13.6	Adsorption configuration of SA at the [001] step edge	92
13.7	Relaxed geometries for the [011] step on NaCl(100)	93
13.8	Band structure of the relaxed NaCl [011] stepped surface	95
13.9	Adsorption geometry of SA at the Cl-NaCl [011] step	96
13.10	Band structure of SA at the Cl-NaCl [011] step	96
13.11	Adsorption geometries at the Na-NaCl [011] step surface	97
13.12	Adsorption configurations of SA and BA at the KCl [011] step	98
13.13	Band structure of SA adsorbed at the K-KCl [011] step	100
13.14	PDOS of SA adsorbed at the [011] step of NaCl and KCl	100
13.15	Band digram of BA, SA, and <i>p</i> -SA at the cation side of [011] step	101
A.1	TDA in the absorption spectra of the molecules	108
B.1	Electronic structure of $\text{MgSO}_4 \cdot \text{H}_2\text{O}$	110
B.2	Representative configurations of GA on $\text{MgSO}_4 \cdot \text{H}_2\text{O}(100)$	111
B.3	Density of states projected onto the GA molecule	114
B.4	Evolution of the HOMO-LUMO and the HOMO level	115
C.1	Electron density of the a_{1g} state	119
C.2	Correction schemes for the formation energies	123
C.3	Band structure of the -1 charged Cl vacancy	124
C.4	Calculated formation energies of the Cl vacancy	127
C.5	Thermodynamic transition levels	128
C.6	Configuration coordinate diagram	129
D.1	Water molecule at the NaCl [011] step edge	135
D.2	Band structure of the NaCl [011] step with the water adsorbates	136

Acronyms

BA	Benzoic acid
BFGS	Broyden-Fletcher-Goldfarb-Shanno
BSE	Bethe-Salpeter equation
BSSE	Basis-set superposition error
CBM	Conduction band minimum
DOS	Density of states
DFT	Density functional theory
EELS	Electron energy loss spectroscopy
GGA	Generalized gradient approximation
HF	Hartree-Fock
HOMO	Highest occupied molecular orbital
IBZ	Irreducible Brillouin zone
IPES	Inversed photoemission spectroscopy
KS-DFT	Kohn-Sham density functional theory
LAPW	Linearized augmented plane-wave
LCAO	Linear combination of atomic orbitals
LDA	Local density approximation
LDOS	Local density of states
LEED	Low-energy electron diffraction
LUMO	Lowest unoccupied molecular orbital
MBPT	Many-body perturbation theory
MP	Monkhorst-Pack
NCPP	Norm-conserving pseudopotential
PAW	Projector augmented wave
PDOS	Projected density of states
PES	Photoemission spectroscopy
<i>p</i>-SA	<i>para</i> -Salicylic acid
QP	Quasiparticle
RPA	Random phase approximation
SA	Salicylic acid
SCF	Self-consistent field
STM	Scanning tunneling microscopy
TDA	Tamm-Dancoff approximation
UPS	Ultraviolet photoemission spectroscopy
USPP	Ultrasoft pseudopotential
VBM	Valence band maximum
vdW	van der Waals
XC	Exchange-correlation

1 Introduction

We are living in a world surrounded by surfaces. There are various surfaces, either metallic or insulating, with which we are interacting every now and then in our daily life. Reactions on surfaces are so prevalent that we can easily list a few examples, such as rust and corrosion on some metal surfaces due to oxidations. In an effort to understand the physical and chemical phenomena occurring at the surface and the interface of two phases, a new field of research, *i.e.* the *surface science* is born. Heterogeneous catalysis is one of the first concept and application in the field of surface chemistry which is pioneered by Paul Sabatier and Fritz Haber [1]. A tremendous progress has been achieved since then in the understanding of microscopic characteristics of surfaces and the reactions on surfaces, which is benefited from the novel experimental techniques and the state of the art theoretical approaches. The advances in surface science immediately boost the development of semiconductor device fabrication (e.g. epitaxial growth [2], chemical vapor deposition [3] and atomic layer deposition [4]), self-assembled monolayer based molecular electronics [5, 6], catalysts [7], and fuel cells [8].

One central ingredient in a wide class of applications in surface science (such as heterogeneous catalysts and self-assembled monolayer) is the molecule-surface interaction. Notably, Gerhard Ertl’s contribution to the investigation of the CO molecules adsorbed on Pt surfaces earned him a Nobel Prize of Chemistry in 2007. Indeed, for the last decade adsorption of molecules on metal surfaces [9–12] and semiconductors [13, 14] gains a great deal of attention stimulated by their relevances in catalysis and molecular electronics. Meanwhile, we have seen considerably fewer studies of the molecule-insulator interfaces. Adsorption of organic molecules on wide-gap insulator surfaces is usually chemically inert and is treated as weak physisorption as long as the surface is free of defect. For instance, the features of the frontier molecular orbitals (MOs) of a pentacene molecule are preserved upon its adsorption on Cu-supported NaCl films as is resolved by scanning tunneling microscopy (STM) [15]. Due to the inertness of the wide-gap insulator surfaces, they are excellent candidates for the supporting substrates in chemical and technical applications.

Nevertheless, an intriguing separation process in the mining industry draws back our attention to revisit the interface between organic molecules and wide-gap insulators. It has been observed that the addition of certain organic molecules can trigger the separation of various minerals such as halite (NaCl), sylvite (KCl) and kieserite ($\text{MgSO}_4 \cdot \text{H}_2\text{O}$) effectively by electrostatic forces in an inhomogeneous electrical field. The electrostatic separation process is plausibly explained by a charge transfer model (sketched in Fig. 1.1). Without adsorbates, electronic excitation is practically impossible at room

temperature according to Fermi-Dirac statistics

$$f(\varepsilon) = \frac{1}{\exp[(\varepsilon - \mu)/k_B T] + 1}, \quad (1.1)$$

where k_B is the Boltzmann constant, T the temperature, and μ the chemical potential. We see that the occupation of electrons in the conduction band edge, or the probability of exciting an electron to the conduction band minimum (CBM) at room temperature is thus zero for an insulator with a band gap of 8 eV, typical for alkali chlorides. This situation, however, is changed by the unoccupied states brought by the adsorbate on the insulator surface as shown in Fig. 1.1(b). Depending on the position of the highest occupied molecular orbital (HOMO) with respect to the valence band maximum (VBM), electrons can be much more easily promoted to the lowest unoccupied molecular orbital (LUMO) either from HOMO or VBM since the effective energy gap is now much smaller than the band gap of the insulator surface. When the adsorbate covered surfaces are brought into contact, electrons can hop from the molecules of one side to the other if there is a difference in the Fermi energy of the surfaces, which is well-defined by the occupied and unoccupied states. The electron exchange vanishes until the thermal equilibrium is reached and the Fermi levels of both surfaces are aligned. A contact voltage drop $U = (\phi_B - \phi_A)/e$ appears across the interface as a result of the net charge transfer, where $\phi = E_{\text{vac}} - E_f$. The contact voltage is supposedly responsible for the electrostatic separation process.

While the model of charge transfer is sound and straightforward, it is simply a proof of concept and it deserves a much more careful thinking. One readily recognizes that in order to make this model work, a relatively small molecular HOMO-LUMO gap is necessary. In practice, industry uses phenolic benzoic acid molecules for the separation process. A naïve quantum chemistry calculation shows that the HOMO-LUMO energy gap is over 4.5 eV for these molecules, which is definitely too large for thermal excitations. One shall then naturally argue that the molecule-surface interaction should play an important role in this context. Although the perfect insulating surface are usually not reactive, defects on the surface evidently enhance the adsorption of the molecules [16–19]. As a matter of fact, a large number of various defects can be introduced inevitably because of entropic reasons during the mechanical grinding process of the minerals. Defects might not only alter the adsorption geometry but also impose significant changes in the electronic structure of the adsorbate system. Altogether, we find ourselves trapped in this simple charge transfer model because of our ignorance of the molecules, the surfaces, and their interfaces.

To this end, we realize that the molecule-insulator interface is the heart of the charge transfer model. Besides, it is also of great relevance to the molecular electronics and self-assembled monolayer on ultrathin insulator films at the atomic scale. Experimentally, the information of the occupied and unoccupied state of both molecules and extended systems can be accurately measured from various surface sensitive techniques, such as photoemission, absorption and energy loss spectroscopy. The adsorption geometry can be also derived precisely from diffraction and reflection methods such as normal incident X-ray standing wave [20], while thermal desorption experiment is able to evaluate the

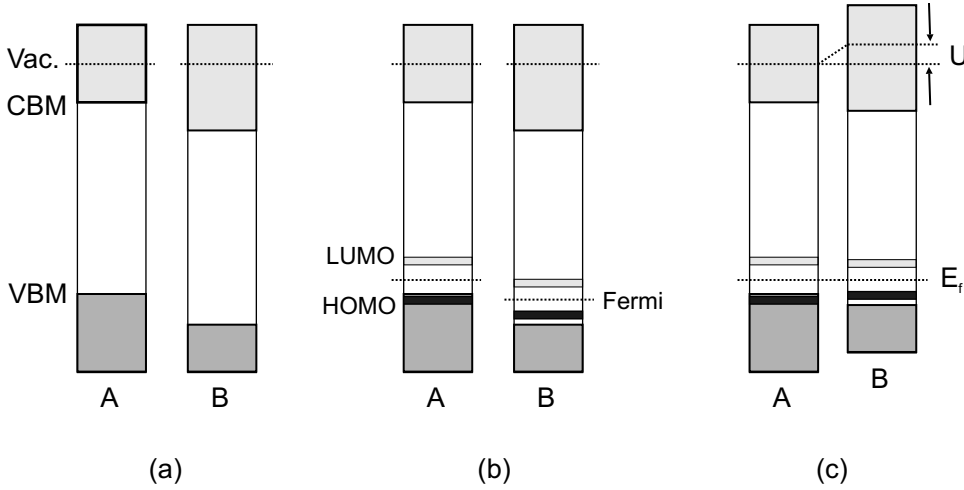


Figure 1.1: Charge transfer model in the presence of adsorbates on wide-gap insulators. (a) Without adsorbates, electronic excitations are suppressed due to the large band gap. (b) The adsorbate introduces unoccupied states within the gap of the insulator, enabling electronic excitations to the unoccupied state provided that the excitation energy is sufficiently small. (c) When two adsorbate systems are brought into contact, mobile electrons flow from A to B depending on the position of the Fermi level. When thermal equilibrium is reached, it results in the alignment of the Fermi level E_f . A contact voltage U then appears, which facilitates the electrostatic separation process.

adsorption energy. On the other hand, the atomic configuration and electronic structure are in principle directly accessible from quantum mechanics. The fast developing theories and boosting computational resources in first-principles community have made the theoretical calculation an indispensable piece of treasure for both explanatory and predictive purposes. An obvious advantage of first-principles approach is that the system of interest, for example, a specific type of defect on the surface, can be designed arbitrarily to get its quantitative properties, while it is much complicated experimentally. It also helps to understand the phenomena at the nanoscale found in experiment. In fact, the interpretation of STM images relies heavily on density functional theory (DFT) nowadays.

It should be borne in mind that the first-principles calculation is by no means a panacea to real-life problems. It will be shown in Part I that there is no universal method for all problems. We consider DFT as an illustration since it is prevalent in the predictions of ground-state properties. However, the semilocal nature of the standard functional approximations fails to correctly describe the *van der Waals* force in weakly bound systems [21]. DFT also tends to yield wrong magnetization of strongly correlated systems [22]. Moreover, the notorious band gap problem associated with self-interaction error and functional discontinuity refrains DFT from an accurate description of the electronic structure even at ground-state. As a static mean-field theory, DFT misses dynamic polarization effect as well [23]. Ultimately DFT is a ground-state theory so

one should resort to other methods for excitation properties. Indeed, the charge transfer model involves electronic excitation, and therefore theories beyond DFT are required for this work.

In this thesis, the molecule-insulator interface is extensively investigated by first-principles calculations within the framework of DFT and many-body perturbation theory. After a comprehensive introduction to the theoretical methods given in Part I, we examine the gas-phase benzoic acid and its phenolic derivatives, as well as the properties of bulk NaCl and KCl in Part II. Part III presents the adsorption of the selected benzoic acid molecules on the ideal alkali chlorine surfaces. The effect of various surface defects (e.g. color center and steps) on the adsorption configuration and electronic structure is also demonstrated. Finally, we discuss the implication of the results in the context of the charge transfer model in Ch. 14.

Part I

Theoretical Framework

2 Hartree-Fock Theory

2.1 Many-electron Wavefunction

The physical and chemical properties of any system at atomic scale can be fundamentally traced back to the many-body Hamiltonian, whose description is governed by quantum mechanics. Let us consider a system consisting of N electrons and K nuclei. We solve the time-independent Schrödinger's equation in terms of the many-body Hamiltonian operator \mathcal{H} and many-body wavefunction Ψ

$$\mathcal{H}\Psi(\mathbf{r}_i, \mathbf{R}_k) = E\Psi(\mathbf{r}_i, \mathbf{R}_k), \quad (2.1)$$

where \mathbf{r}_i and \mathbf{R}_k denote the coordinates of the electrons and nuclei, respectively. Casting the Hamiltonian into mathematical notation, we write¹

$$\mathcal{H} = -\frac{1}{2} \sum_{i=1}^N \nabla_i^2 - \frac{1}{2} \sum_{k=1}^K \nabla_k^2 - \sum_{i=1}^N \sum_{k=1}^K \frac{Z_k}{|\mathbf{r}_i - \mathbf{R}_k|} + \sum_{i < j} \frac{1}{|\mathbf{r}_i - \mathbf{r}_j|} + \sum_{k < l} \frac{Z_k Z_l}{|\mathbf{R}_k - \mathbf{R}_l|}, \quad (2.2)$$

where Z_k is the charge for the k -th nucleus. In most cases, the nuclei are moving much more slowly than the electrons as the nucleus is much more massive than the electron ($M_n \approx 1800m_e$). Therefore, it is convenient to decouple the motion of the electrons from that of the nuclei and calculate electronic energies for fixed nuclear positions. This is the *Born-Oppenheimer* approximation, where the *electronic* Schrödinger equation reads

$$\left(-\frac{1}{2} \sum_{i=1}^N \nabla_i^2 - \sum_{i=1}^N \sum_{k=1}^K \frac{Z_k}{|\mathbf{r}_i - \mathbf{R}_k|} + \sum_{i < j} \frac{1}{|\mathbf{r}_i - \mathbf{r}_j|} \right) \Psi_{\text{el}}(\mathbf{r}_i) = E_{\text{el}} \Psi_{\text{el}}(\mathbf{r}_i). \quad (2.3)$$

The Born-Oppenheimer approximation has profound consequences to the theoretical communities, leading to concepts like potential energy surface. The approximation is entirely justified in general, and it reduces the many-body problem to a tractable form.

Let us now examine the many-electron wavefunction $\Psi(\mathbf{x}_1, \mathbf{x}_2, \dots, \mathbf{x}_i, \dots)^2$, where $\mathbf{x}_i = (\mathbf{r}_i, \sigma_i)$ are combined *spin-orbital coordinates*. Electrons are *fermions*, and since a wavefunction of identical fermions is anti-symmetric, the electronic wavefunction must change sign whenever the coordinates \mathbf{x}_i of two electrons are swapped:

$$\begin{aligned} \mathcal{P}_{ij}\Psi(\mathbf{r}_1, \mathbf{r}_2, \dots, \mathbf{r}_i, \dots, \mathbf{r}_j, \dots) &= \Psi(\mathbf{r}_1, \mathbf{r}_2, \dots, \mathbf{r}_j, \dots, \mathbf{r}_i, \dots) \\ &= -\Psi(\mathbf{r}_1, \mathbf{r}_2, \dots, \mathbf{r}_i, \dots, \mathbf{r}_j, \dots), \end{aligned} \quad (2.4)$$

¹Hartree atomic unit $\hbar = m_e = 4\pi\epsilon_0 = e^2 = 1$ is used throughout this thesis by default.

²The subscript 'el' is omitted since most of the time we are dealing with the electronic wavefunction.

where \mathcal{P}_{ij} is a permutation operator interchanging the coordinates of electrons i and j . This is another proof of Pauli exclusion principle, namely two fermions cannot occupy the same state because $\Psi = 0$ if we let $\mathbf{r}_i = \mathbf{r}_j$ in Eq. (2.4).

In an early attempt to construct the many-electron wavefunction Ψ , it is written as products (*i.e.* Hartree-product) of one-electron eigenstates $\psi_i(\mathbf{x}_i)$ in an independent particle picture:

$$\Psi_{\text{HP}}(\mathbf{x}_1, \mathbf{x}_2, \dots, \mathbf{x}_N) = \psi_1(\mathbf{x}_1)\psi_2(\mathbf{x}_2)\cdots\psi_N(\mathbf{x}_N), \quad (2.5)$$

and the independent one-electron Hamiltonian is

$$\mathcal{H}_{\text{IP}} = \sum_{i=1}^N \left[-\frac{1}{2}\nabla_i^2 - \sum_{k=1}^K \frac{Z_k}{|\mathbf{r}_i - \mathbf{R}_k|} \right], \quad (2.6)$$

where the electron-electron interaction is fully neglected. The construction in Eq. (2.5) suggests that the electrons are *uncorrelated*, and the eigenvalue of Ψ is thus the sum of the one-electron eigenvalues $\sum_{i=1}^N \varepsilon_i$.

However, the Hartree-product obviously violates Pauli principle, because the wavefunction in Eq. (2.5) is symmetric when the coordinates of two electrons are interchanged. A simple and correct ansatz for the many-electron wavefunction is given by the Slater determinants [24]

$$\Psi(\mathbf{x}_1, \mathbf{x}_2, \dots, \mathbf{x}_N) = \frac{1}{\sqrt{N!}} \begin{vmatrix} \psi_1(\mathbf{x}_1) & \psi_2(\mathbf{x}_1) & \cdots & \psi_N(\mathbf{x}_1) \\ \psi_1(\mathbf{x}_2) & \psi_2(\mathbf{x}_2) & \cdots & \psi_N(\mathbf{x}_2) \\ \vdots & \vdots & \ddots & \vdots \\ \psi_N(\mathbf{x}_N) & \psi_2(\mathbf{x}_N) & \cdots & \psi_N(\mathbf{x}_N) \end{vmatrix} \quad (2.7)$$

The prefactor reflects the $N!$ permutations of N electrons on the set of N coordinates. By the *variational principle*, the ground-state energy of a system can be approximated.

2.2 Hartree Equation

Using the Hartree-product wavefunction in Eq. (2.5), we obtain the expectation value of the electronic Hamiltonian in Eq. (2.3), *i.e.* the ground-state energy

$$\begin{aligned} \langle \Psi_{\text{HP}} | \mathcal{H} | \Psi_{\text{HP}} \rangle &= \sum_{i=1}^N \int d^3r \psi_i^*(\mathbf{r}) \left(-\frac{1}{2}\nabla_i^2 + v_{\text{ext}} \right) \psi_i(\mathbf{r}) \\ &\quad + \frac{1}{2} \sum_{i,j}^N \int d^3r d^3r' \frac{|\psi_i(\mathbf{r})|^2 |\psi_j(\mathbf{r}')|^2}{|\mathbf{r} - \mathbf{r}'|}, \end{aligned} \quad (2.8)$$

where v_{ext} is the external potential for the electron due to the nuclei. The expectation value can be minimized with respect to the one-electron function ψ_i under the constraint

that the wavefunctions are normalized via Lagrange multipliers. The resulting set of equations are called the Hartree equations [25]

$$\left[-\frac{1}{2}\nabla^2 + v_{\text{ext}}(\mathbf{r}) + \sum_{j=1}^N \int d^3r' \frac{|\psi_j(\mathbf{r}')|^2}{|\mathbf{r} - \mathbf{r}'|} \right] \psi_i(\mathbf{r}) = \varepsilon_i \psi_i(\mathbf{r}), \quad (2.9)$$

where ε_i are the Lagrange multipliers. The third term in the Hamiltonian in Eq. (2.9) is the Hartree potential v_H since the electron density $n(\mathbf{r}) = \sum_{i=1}^N |\psi_i(\mathbf{r})|^2$. The one-electron Hartree Hamiltonian h_i includes the one-electron kinetic energy and its electrostatic interaction to the other electrons and nuclei

$$h_i = -\frac{1}{2}\nabla_i^2 + v_{\text{ext}} + v_H. \quad (2.10)$$

In this way, the original many-body problem is reduced to a single-particle problem. This is the essence of a *mean-field* theory. We combine the v_{ext} and v_H into an effective potential v_{eff} so that the Hartree equation has a simple form as

$$\left[-\frac{1}{2}\nabla^2 + v_{\text{eff}}(\mathbf{r}) \right] \psi_i(\mathbf{r}) = \varepsilon_i \psi_i(\mathbf{r}) \quad (2.11)$$

From Eq. (2.9), it is straightforward to write the expectation value of the total electronic energy in the Hartree equation as

$$\begin{aligned} E_H = \langle \Psi_{\text{HP}} | \mathcal{H} | \Psi_{\text{HP}} \rangle &= \sum_{i=1}^N \varepsilon_i - \frac{1}{2} \int d^3r d^3r' \frac{n(\mathbf{r})n(\mathbf{r}')}{|\mathbf{r} - \mathbf{r}'|} \\ &= \sum_{i=1}^N \varepsilon_i - V_H \end{aligned} \quad (2.12)$$

where V_H is the *Hartree energy*, a *mean-field* electrostatic energy of the electronic charge distribution. As the electronic repulsion is double-counted in the sum of the non-interacting one-electron eigenvalues, V_H has to be subtracted in Eq. (2.12).

Hartree Hamiltonian is dependent on the wavefunction, and therefore an iterative self-consistent field (SCF) scheme is usually employed to calculate the Hartree equation. During the SCF process, one guesses the wavefunctions $\psi^0(\mathbf{r})$ and constructs the one-electron Hamiltonian operator \mathcal{H}^0 . The Hartree equations are then solved, providing a new set of $\psi(\mathbf{r})$ presumably different from the initial guess. This process is repeated until the difference between the old wavefunction and the new one meets the convergence criterion. In practice, the new v_{eff} is by construction mixed with the one of the previous SCF step to speed up the convergence.

One problem with the Hartree equation is the spurious interaction of one electron with itself. This is evident from Eq. (2.9) when $i = j$. The *self-interaction* error is inherited from the unphysical symmetric behavior of the Hartree-product wavefunction discussed in Sec. 2.1. Therefore the results from Hartree equations are usually inaccurate. We will see that the self-interaction is canceled exactly by an exchange potential if a single Slater determinant is used as the many-electron wavefunction in the next section.

2.3 Hartree-Fock Method

Fock extended the Hartree equation to the anti-symmetric Slater determinant wavefunctions shown in Eq. (2.7) [26]. A new term, *i.e.* the *exchange* term appears in the *Hartree-Fock* (HF) equations for the one-electron wavefunction

$$\left[-\frac{1}{2}\nabla^2 + v_{\text{ext}}(\mathbf{r}) + \sum_{j=1}^N \int d^3r' \frac{|\psi_j(\mathbf{r}')|^2}{|\mathbf{r} - \mathbf{r}'|} \right] \psi_i(\mathbf{r}) - \sum_{j=1}^N \int d^3r' \frac{1}{|\mathbf{r} - \mathbf{r}'|} \psi_j^*(\mathbf{r}') \psi_i(\mathbf{r}') \psi_j(\mathbf{r}) \delta_{\sigma_i \sigma_j} = \varepsilon_i \psi_i(\mathbf{r}). \quad (2.13)$$

An alternative definition of the non-interacting one-electron Fock operator \mathcal{F} for each electron i in the quantum chemistry community is

$$\mathcal{F} = -\frac{1}{2}\nabla_i^2 + v_{\text{ext}} + V_i^{\text{HF}}, \quad (2.14)$$

where the HF potential $V_i^{\text{HF}} = 2\mathcal{J}_i - \mathcal{K}_i$, and the \mathcal{J}_i and \mathcal{K}_i are the Coulomb operator and exchange operator, respectively. As is mentioned in Sec. 2.2, the HF method is also a *mean-field theory* like the Hartree equation. A practical route to solve the HF equations is the Roothaan SCF method independently proposed by Hall [27] and Roothaan [28], in which the HF orbitals are expanded via linear combinations of atomic orbitals (see Sec. 4.1.1). The eigenvalues ε_i of the HF equations are the orbital energies. Koopmans' theorem states that the orbital energy ε_i of the occupied orbital state ψ_i is equivalent to the negative value of the energy necessary to remove one electron from orbital ψ_i

$$\text{IP}(\psi_i) = -\varepsilon_i. \quad (2.15)$$

In the case of an one-electron system ($i = j$), the Hartree potential is exactly canceled by the exchange term, *i.e.* the *Fock exchange*. As a result, the HF method is *free of self-interaction*. The Fock exchange arises when the two electrons are of the same spin $\sigma_i = \sigma_j$, and the probability of finding two electrons of the same spin close to one another is therefore reduced. It can be visualized as a *exchange hole* around each electron.

Analogous to Eq. 2.12, the total energy in the HF method is

$$E_{\text{HF}} = \sum_{i=1}^N \varepsilon_i - V_{\text{H}} - E_{\text{x}}, \quad (2.16)$$

where E_{x} is the *exchange energy*. It turns out that the total energy in the HF equation differs from the Hartree equation by exactly the exchange energy. The Fock exchange introduces a great complexity to the calculations since the exchange is a *nonlocal* term, and it depends on the information of one wavefunction at both \mathbf{r} and \mathbf{r}' . In practice, it involves a rather tedious evaluation of the two-electron integrals, which scales as N^4 with respect to the number of basis functions.

While the *correlation effect* between electron with the same spin is included (and labeled as the *exchange effect*), in the HF method the electrons with opposite spin are yet not correlated. Indeed, the motion of each electron is correlated with every other so that the total energy is further reduced. Such *dynamic correlation* is absent in the HF theory because of the neglect of possible excited state configuration of the HF determinant. The difference between the exact energy of the system and the HF total energy is defined as the correlation energy. The correlation energy per electron can easily amount to more than 1 eV [12], and it is therefore of paramount importance for a reliable description of molecule-surface interactions.

The correlation effect can be included in the *post*-Hartree-Fock methods, in which the electronic correlations can be described as the virtual electronic excitations. In this way, the electrons do not feel the mean-field of other electrons. Rather, they are interacting with each other. The Møller-Plesset (MP) theory treats the excitations perturbatively to take into account of the correlation. The total energy of the popular second-order MP2 approximation is written as

$$E_{\text{MP2}} = E_{\text{HF}} - \sum_{l < m}^{\text{occ.}} \sum_{p < q}^{\text{unocc.}} \frac{[(lm|pq) - (lq|mp)]^2}{\varepsilon_l + \varepsilon_m - \varepsilon_p - \varepsilon_q}, \quad (2.17)$$

where the two-electron four-orbital integral is in the form of

$$(lm|pq) = \int d^3r d^3r' \psi_l^*(\mathbf{r}) \psi_m^*(\mathbf{r}) \frac{1}{|\mathbf{r} - \mathbf{r}'|} \psi_p(\mathbf{r}') \psi_q(\mathbf{r}'). \quad (2.18)$$

It should be noted that the MP n method is not variational, so it is likely that the correlation energy given by the perturbations are overestimated. The MP2 in particular fails to describe electronic repulsive terms at higher orders, which also leads to an overestimation of the correlation. Last but not least, the MP n energy might be divergent for a metallic system [29].

Instead of the perturbation method, the wavefunction can be reconstructed as a linear combination of multiple Slater determinants rather than a single HF determinant

$$\Psi = \Psi_{\text{HF}} + c_1 \Psi_1 + c_2 \Psi_2 + \cdots, \quad (2.19)$$

where the new Slater determinants Ψ_i represent the excited states by reorganizing the occupation of the orbitals of the HF determinant. Then the optimum wavefunction can be determined by the variational principle with respect to the coefficient c_i . This is the *configuration interaction* (CI) method. The CI method is extremely expensive, and it is rarely used for extended systems.

It is eminent at this point that we need a different theory than the HF method to give an appropriate description of the molecule-surface interaction including the exchange-correlation effect in an affordable way. This theory is the density functional theory (Chapter 3).

3 Density functional Theory

3.1 Early approximations

At a first glance at the Hartree-Fock method, we get the impression that it is really a complicated equation as the electronic wavefunction depends on three spatial and one spin coordinates of each electron. Moreover, despite the mathematical transparency of the wavefunction, the wavefunction itself is *not* a physical observable. The electron density $n(\mathbf{r})$, or the probability of finding one electrons at \mathbf{r} , on the other hand, is an observable. The integration of electron density over the whole space yields the number of electrons

$$\int d^3r n(\mathbf{r}) = N. \quad (3.1)$$

It is thus instructive to work on the electron density $n(\mathbf{r})$ instead of the wavefunction.

In the language of electron density, the electron-nuclei attraction in the potential of K nuclei is defined as

$$V_{\text{nucl-el}}[n(\mathbf{r})] = \sum_{k=1}^K \int d^3r \frac{Z_k}{|\mathbf{r} - \mathbf{R}_k|} n(\mathbf{r}), \quad (3.2)$$

and the electron-electron Coulomb repulsion is

$$V_{\text{el-el}}[n(\mathbf{r})] = \frac{1}{2} \int d^3r d^3r' \frac{n(\mathbf{r})n(\mathbf{r}')}{|\mathbf{r} - \mathbf{r}'|}. \quad (3.3)$$

The kinetic energy of a continuous electron distribution is less straightforward. In 1927, Thomas [30] and Fermi [31] derived the kinetic energy T for a jellium system¹

$$T_{\text{TF}}[n(\mathbf{r})] = \frac{3}{10} (3\pi^2)^{\frac{2}{3}} \int d^3r [n(\mathbf{r})]^{\frac{5}{3}} \quad (3.4)$$

The *Thomas-Fermi* (TF) equation along with Eq. (3.2) and (3.3) was the first attempt to define a density functional where the variable $n(\mathbf{r})$ is a function of the three-dimensional spatial coordinates.

What is again missing in the TF approximation is electronic exchange-correlation effect. Slater in 1951 proposed that the exchange energy can be determined as

$$E_{\text{x}}[n(\mathbf{r})] = -\frac{9\alpha}{8} \left(\frac{3}{\pi}\right)^{\frac{1}{3}} \int d^3r [n(\mathbf{r})]^{\frac{4}{3}}, \quad (3.5)$$

¹Jellium is a system characterized by an homogeneous electron gas moving in an infinite volume of a space consisting of a uniformly distributed positive charge.

and Eq. (3.5) defines the Slater exchange when $\alpha = 1$. Although these early approximations are far from being rigorous and accurate in terms of modern theories, these pioneer works are provocative and they lead to the successful establishment of density functional theory.

3.2 Hohenberg-Kohn Theorems

In an N -electron interacting system, electrons interact with one another and with the potential of nuclei as an external potential. One recognizes that there must be an one-to-one correspondence between the electron density $n(\mathbf{r})$ and the external potential v_{ext} in order for the DFT to be a legitimate first-principles method. The mapping from v_{ext} to $n(\mathbf{r})$ is explicit since it is always possible to solve the many-body Schrödinger equation from the external potential to obtain the many-body wavefunction and the electron density. The reverse mapping is proved by Hohenberg and Kohn in 1964 via *reductio ad absurdum*, which is now known as the Hohenberg-Kohn (HK) *existence theorem* [32]. The HK theorem states that for an N -electron interacting system in an external potential $v_{\text{ext}}(\mathbf{r})$, the ground-state energy E_0 is a universal functional of the density $n(\mathbf{r})$, *i.e.* every observable can be obtained from the density

$$n(\mathbf{r}) \Rightarrow v_{\text{ext}}(\mathbf{r}) \Rightarrow \mathcal{H} \Rightarrow E_0, \Psi_0. \quad (3.6)$$

The proof is generalized and extended to degenerate ground-states by Levy [33].

Hohenberg and Kohn showed in a second theorem that density obeys a variational principle, which provides evidence that the ground-state total energy can be obtained by minimization under arbitrary wavefunction variations. Here we demonstrate the density variational principle, following the *constraint search* approach of Levy [33]. The variational procedure is carried out in two stages. First, we minimize the energy $E[n]$ with respect to the wavefunctions for a given density n

$$E[n] = \min_{\psi} \langle \psi | \mathcal{H} | \psi \rangle. \quad (3.7)$$

If we separate the Hamiltonian into the Hamiltonian \mathcal{H}_0 for the homogeneous electron gas and the external potential, for a given density n , the functional $E[n]$ can be written as

$$E[n] = \min_{\psi} [\langle \psi | \mathcal{H}_0 | \psi \rangle] + \int d^3r v_{\text{ext}}(\mathbf{r}) n(\mathbf{r}), \quad (3.8)$$

where \mathcal{H}_0 has a kinetic contribution and an electron-electron interaction V_{ee} . We define a universal functional $F[n]$

$$F[n] = \min_{\psi} \langle \psi | \mathcal{H}_0 | \psi \rangle. \quad (3.9)$$

Then the ground-state energy can be obtained by the minimization with respect to the density n while v_{ext} is kept fixed

$$E[n] = F[n] + \int d^3r v_{\text{ext}}(\mathbf{r}) n(\mathbf{r}). \quad (3.10)$$

The minimization is subject to the constraint of a fixed N . The minimizing density is hence the ground-state density.

3.3 Kohn-Sham Formalism

The plain adoption of density functional does not simplify the calculation with respect to the Hartree-Fock equation due to the complicated nature of electronic interactions V_{ee} . In 1965 Kohn and Sham [34] proposed a groundbreaking method for calculating the ground-state energy of an *interacting* system in terms of a *fictitious* system of *non-interacting* electrons. The non-interacting electrons are in an effective potential v_{eff} so that the ground-state density of the *fictitious* system is the same as the *real* system. The KS-DFT total energy can be written as

$$E_{\text{KS}} = T_0[n] + E_{\text{ext}}[n] + E_{\text{H}}[n] + E_{\text{xc}}[n], \quad (3.11)$$

where the correction to the non-interacting kinetic energy T_0 and all *exchange* and *correlation* effects have been grouped into the exchange-correlation (XC) energy E_{xc} . Minimizing Eq. (3.11) by the variation principle, we have the Kohn-Sham (KS) one-electron equation

$$\left[-\frac{1}{2}\nabla_i^2 + v_{\text{ext}} + v_{\text{H}} + v_{\text{xc}} \right] \psi_i = \left[-\frac{1}{2}\nabla_i^2 + v_{\text{eff}} \right] \psi_i = \varepsilon_i \psi_i, \quad (3.12)$$

where the XC potential v_{xc} is the functional derivative of E_{xc}

$$v_{\text{xc}} = \frac{\partial E_{\text{xc}}}{\partial n}. \quad (3.13)$$

The single-particle energies ε_i appear as Lagrange multipliers to ensure the correct normalization to the number of particle N . The Kohn-Sham states have no specific physical interpretation except for the highest occupied state.

A comparison between Eq. (3.11) and (3.12) implies that the summation of the single-particle energies ε_i of the occupied states leads to a double-counting of the Hartree energy and there is also a difference in the exchange-correlation energy. The total energy in Eq. (3.11) then can be explicitly expressed as

$$E_{\text{KS}} = \sum_{i=1}^N \varepsilon_i - \frac{1}{2} \int d^3r d^3r' n(\mathbf{r}) \frac{1}{|\mathbf{r} - \mathbf{r}'|} n(\mathbf{r}') + E_{\text{xc}}[n] - \int d^3r v_{\text{xc}}[n(\mathbf{r})] n(\mathbf{r}) \quad (3.14)$$

Like the HF equations, KS-DFT calculations are also carried out self-consistently because v_{ext} is a functional of $n(\mathbf{r})$, while $n(\mathbf{r})$ depends on the one-particle wavefunction. We note that KS-DFT is an *exact* ground-state theory. Unfortunately, the exact form of E_{xc} with respect to $n(\mathbf{r})$ is unknown, and E_{xc} has to be approximated. The accuracy of KS-DFT, in this sense, is solely connected to the specific approximation of the XC functional.

3.4 Exchange-correlation Functionals

In order to provide physical insights into the exchange and correlation energies, we first define a non-negative coupling constant λ which controls the strength of inter-electronic

interaction V_{ee} in a many-electron system

$$\mathcal{H} = T + V_{\text{ext}}^\lambda + \lambda V_{ee}. \quad (3.15)$$

The system corresponds to a non-interacting system when $\lambda = 0$, or a fully-interacting one when $\lambda = 1$. Varying λ at fixed $n(\mathbf{r})$, we have a *real* external potential for $\lambda = 1$, and a KS effective potential for $\lambda = 0$. The coupling constant λ therefore acts like a switch that smoothly converts a non-interacting KS reference system to an interacting system in an *adiabatic connection* as λ is increased from 0 to 1. The exchange-correlation energy E_{xc} , as the sum of exchange energy E_x and correlation energy E_c , then can be written as

$$\begin{aligned} E_{xc}[n] &= \langle \psi_n^{\text{min},\lambda} | T + \lambda V_{ee} | \psi_n^{\text{min},\lambda} \rangle |_{\lambda=1} - \langle \psi_n^{\text{min},\lambda} | T + \lambda V_{ee} | \psi_n^{\text{min},\lambda} \rangle |_{\lambda=0} - E_H \\ &= \int_0^1 d\lambda \frac{d}{d\lambda} \langle \psi_n^{\text{min},\lambda} | T + \lambda V_{ee} | \psi_n^{\text{min},\lambda} \rangle - E_H, \end{aligned} \quad (3.16)$$

where $\psi_n^{\text{min},\lambda}$ is the interacting ground-state wavefunction for density n when $\lambda = 1$, and the non-interacting (or the KS) wavefunction for the same density when $\lambda = 0$.

The exchange-correlation functional $E_{xc}[n(\mathbf{r})]$ is connected to the *exchange-correlation energy density* (energy per particle) $\varepsilon_{xc}[n(\mathbf{r})]$ via

$$E_{xc}[n(\mathbf{r})] = \int d^3r n(\mathbf{r}) \varepsilon_{xc}[n(\mathbf{r})]. \quad (3.17)$$

It is convenient to introduce the exchange-correlation hole distribution n_{xc}

$$n_{xc}(\mathbf{r}, \mathbf{r}') = g(\mathbf{r}, \mathbf{r}') - n(\mathbf{r}'), \quad (3.18)$$

where $g(\mathbf{r}, \mathbf{r}')$ is the probability of finding an electron at \mathbf{r}' if there is an electron at \mathbf{r} . Integrating over \mathbf{r}' , we find that

$$\int d^3r' n_{xc}(\mathbf{r}, \mathbf{r}') = \int d^3r' g(\mathbf{r}, \mathbf{r}') - \int d^3r' n(\mathbf{r}') = N - 1 - N = -1, \quad (3.19)$$

which implies that when an electron is definitely at \mathbf{r} , it is absent elsewhere. The exchange-correlation hole vanishes for large separations, and for $|\mathbf{r}| \rightarrow \infty$,

$$\int d^3r' \frac{n_{xc}(\mathbf{r}, \mathbf{r}')}{|\mathbf{r} - \mathbf{r}'|} \rightarrow -\frac{1}{|\mathbf{r}|}. \quad (3.20)$$

3.4.1 Local Density Approximation

In the local density approximation (LDA), the exchange-correlation energy depends on the *local* value of electron density at \mathbf{r} exclusively²

$$E_{xc}^{\text{LDA}}[n(\mathbf{r})] = \int d^3r n(\mathbf{r}) \varepsilon_{xc}^{\text{LDA}}[n(\mathbf{r})], \quad (3.21)$$

²The spin dependence for spin-polarized system is suppressed in this thesis.

where $\varepsilon_{xc}^{\text{LDA}}[n(\mathbf{r})]$ is the exchange-correlation density of a homogeneous electron gas. The exchange part of LDA can be derived from, e.g., the Slater exchange for a homogeneous electron gas in Eq. (3.5). As for the correlation energy, one often resorts to quantum Monte Carlo techniques to calculate the total energy for uniform electron gases accurately [35].

LDA is by construction accurate for homogeneous systems, as well as for systems with very slow varying densities. In particular, LDA satisfies the important sum rule in Eq. (3.19). While it is the simplest exchange-correlation functional, LDA is also surprisingly useful in a wide range of bulk and surface problems [36]. A possible explanation of the seemingly success of LDA is due to the error-cancellation in the exchange and correlation energy [37]. Nevertheless, LDA tends to predict smaller lattice constant and higher cohesive energy. As for adsorbate systems, the binding energy from LDA is *over-estimated* in general. Indeed, the *over-binding* in LDA leads to spurious binding energy in weakly bound systems [21]. Moreover, LDA suffers from the self-interaction and it lacks functional derivative discontinuity, which as a result yields much smaller fundamental band gaps of insulators and semiconductors. We will discuss these two issues after the generalized gradient approximation.

3.4.2 Generalized Gradient Approximation

The first step to improve the LDA is to approximate the exchange-correlation energy by a Taylor expansion. The exchange-correlation functional is expanded in terms of both the local density n and its gradient ∇n [38]. This *gradient expansion approximation*, however, violates the sum rule in Eq. (3.19), and does not produce consistent improvement over the LDA since in real systems the gradients are too large.

The *generalized gradient approximation* (GGA) modifies the behavior of the exchange-correlation functional at large gradients to preserve some properties such as the sum rule and the scaling laws [39]. Analogous to the LDA, the exchange-correlation energy in GGA can be expressed as

$$\begin{aligned} E_{xc}^{\text{GGA}}[n(\mathbf{r})] &= \int d^3r n(\mathbf{r}) \varepsilon_{xc}^{\text{GGA}}[n(\mathbf{r}), \nabla n(\mathbf{r})] \\ &= \int d^3r n(\mathbf{r}) \varepsilon_x^{\text{hom}}[n(\mathbf{r})] F_{xc}[n(\mathbf{r}), \nabla n(\mathbf{r})], \end{aligned} \quad (3.22)$$

where $\varepsilon_x^{\text{hom}}$ is the exchange energy density of the unpolarized homogeneous electron gas, and the enhancement factor F_{xc} is a dimensionless term. The GGA functional is usually referred to as a *semilocal* functional. Different constructions of F_{xc} lead to various flavors of GGA functionals, noticeably the Perdew and Wang (PW91) [40] and the Perdew-Burke-Ernzerhof (PBE) functional [41]. The GGA provides a much better agreement with experiment than the LDA. It reduces the over-binding in the LDA, predicting more realistic properties for both the bulk and surface systems. There has been constant development of the GGA functionals over the recent years. These new functionals are designed for the specific systems, such as the revised PBE (RPBE) for

the chemical reactivity on surfaces [42], and the PBEsol for the improved equilibrium properties of solids and surfaces [43].

As mentioned in Sec. 3.4.1, the self-interaction cannot be canceled by the exchange energy in either GGA or LDA, in contrast to the Hartree-Fock theory where the Hartree-Fock exchange cancels exactly the self-interaction (see Sec. 2.3). This spurious self-interaction of one electron with itself might lead to an incorrect description of the electronic structure since the self-interaction tends to put the eigenvalues of the localized states too high in energy [37]. In other words, the self-interaction favors the *delocalization* of electrons [44]. We will see this in Chapter 6 where the molecular orbitals of a benzoic acid are incorrectly ordered by LDA. In addition, the XC potential of the local and semilocal functionals exhibits exponential decays for large distances r , while the asymptotic form of the exact potential follows r^{-1} . As a consequence, Rydberg states are not properly treated by the LDA and GGA functionals [37].

Another problem associated with the failures of LDA and GGA is the absence of functional derivative discontinuity [37]. According to Janak's theorem [45], the eigenvalue of an orbital ε_i can be derived from the variation of the total energy with respect to the occupation number of that orbital

$$\varepsilon_i = \frac{\partial E}{\partial n_i}. \quad (3.23)$$

For an N -electron system with nuclear charge Z , the highest (partially) occupied KS orbital eigenvalue ε_{HO} is the chemical potential $\mu = \partial E / \partial N$. Varying N in the vicinity of Z , we have [46]

$$\varepsilon_{\text{HO}} = \begin{cases} -I = E(Z) - E(Z-1) & (Z-1 < N < Z) \\ -A = E(Z+1) - E(Z) & (Z < N < Z+1) \end{cases}, \quad (3.24)$$

where I and A are the ionization energy and the electron affinity of the Z -electron system. The difference between $-I$ and $-A$ arises from a discontinuous jump in the derivative of the total energy with respect to the electron number. Since the functional derivative of the external potential and Hartree potential are both continuous with respect to $n(\mathbf{r})$, there must be a discontinuity in the exchange-correlation functional derivative Δ_{xc} as N crosses the integer Z . However, as the LDA and GGA exchange-correlation potentials are continuous in the density and its gradient, they do not exhibit the derivative discontinuity. Instead, the LDA and GGA averages over the discontinuity [47], so that the highest occupied KS eigenvalue given in the LDA and GGA differs $-I$ by $\Delta_{\text{xc}} = \frac{1}{2}(I - A)$.

The absence of the derivative discontinuity is intimately responsible for the significantly underestimated band gap in KS-DFT. We see this by defining the *real* band gap (fundamental gap) as the ground-state energy difference between the N and $N \pm 1$ systems:

$$E_g = I - A = E(N+1) + E(N-1) - 2E(N). \quad (3.25)$$

The KS gap is the difference between the highest occupied and lowest unoccupied states of the N -electron system:

$$\begin{aligned} \varepsilon_{N+1}^{\text{KS}}(N) - \varepsilon_N^{\text{KS}}(N) &= [\varepsilon_{N+1}^{\text{KS}}(N+1) - \varepsilon_N^{\text{KS}}(N)] - [\varepsilon_{N+1}^{\text{KS}}(N+1) - \varepsilon_{N+1}^{\text{KS}}(N)] \\ &= E_g - \Delta_{\text{xc}}. \end{aligned} \quad (3.26)$$

Thus, the KS gap is always smaller by Δ_{xc} even if the exchange-correlation energy is exact. For the bulk NaCl, the GGA-PW91 functional predicts a KS gap of 5.4 eV, while the experimental gap amounts to 8.5 eV.

Apart from the gap problem, the local and semilocal nature of the LDA and GGA fails to describe the long-range *van der Waals* (vdW) forces. The vdW interactions are particularly important for weakly bound systems, such as molecules on perfect ionic surfaces. The implementation of vdW in the framework of DFT will be discussed in Sec. 3.5. The self-interaction error and derivative discontinuity, however, can be intuitively remedied to some extent by the introduction of Hartree-Fock exchange into the DFT.

3.4.3 Hybrid Functional

We resume the adiabatic connection in Eq. (3.16), which can be simplified according to the Hellmann-Feynman theorem³

$$\begin{aligned} E_{\text{xc}} &= \int_0^1 d\lambda \langle \psi^{\text{min},\lambda} | V_{\text{ee}} | \psi^{\text{min},\lambda} \rangle - E_{\text{H}} \\ &= \int_0^1 d\lambda \langle \psi^{\text{min},\lambda} | V_{\text{xc}} | \psi^{\text{min},\lambda} \rangle. \end{aligned} \quad (3.27)$$

In the non-interacting limit when $\lambda = 0$, V_{xc} in Eq. (3.27) reduces to the HF exchange V_{x}^{HF} using the KS orbitals. We then decompose Eq. (3.27) into two parts

$$\begin{aligned} E_{\text{xc}} &= \int_0^1 d\lambda \langle \psi^{\text{min},0} | V_{\text{x}}^{\text{HF}} | \psi^{\text{min},0} \rangle + \int_0^1 d\lambda \langle \psi^{\text{min},\lambda} | V_{\text{xc}} - V_{\text{x}}^{\text{HF}} | \psi^{\text{min},\lambda} \rangle \\ &= E_{\text{x}}^{\text{HF}} + z(E_{\text{xc}}^{\text{KS}} - E_{\text{x}}^{\text{HF}}) \\ &= \alpha E_{\text{x}}^{\text{HF}} + (1 - \alpha) E_{\text{xc}}^{\text{KS}}, \end{aligned} \quad (3.28)$$

where α is between 0 and 1. The exchange-correlation in this form is called a *hybrid functional* as it includes both exact HF exchange and KS-DFT exchange-correlation⁴. The incorporation of HF exchange effectively remedies the self-interaction error and derivative discontinuity in the exchange-correlation functional within KS-DFT. The structural parameters, as well as the molecular energy gap and band gap of solids are usually much improved by hybrid functionals [48–51]. As is pointed out by Yang *et al.* [52], the correct prediction of the band gap relies on the fact that the exact energy varies linearly as a function of the electron number between two adjacent integer numbers. This is a natural consequence from the functional discontinuity mentioned in the last section. However, it has been shown that the semilocal and local functionals exhibit a convex manner, while HF curves are concave rather than straight. The band gaps from (semi)local DFT and HF calculations are therefore either too small or too large. The band gaps can benefit

³The Hellmann-Feynman states that for $E_{\lambda} = \langle \psi_{\lambda} | \mathcal{H}_{\lambda} | \psi_{\lambda} \rangle$, $\frac{dE_{\lambda}}{d\lambda} = \langle \psi_{\lambda} | \frac{d\mathcal{H}_{\lambda}}{d\lambda} | \psi_{\lambda} \rangle$.

⁴Hybrid functional is considered as one of the orbital-dependent density functional because the KS orbitals are explicitly expressed in E_{xc} .

from the mixing of the exact exchange due to the fact that the straight line behavior can be recovered to some extent. We will use the PW1PW hybrid functional [48] primarily for the adsorbate calculation in this thesis, which mixes 20% exchange exchange with the PW91 XC functional. Another widely used hybrid functional for condensed matter is the PBE0 functional, and it usually incorporates 25% exact exchange based on perturbation theory argument [53]. We note that the value α is tunable and it is often dependent on the system under investigation.

Hybrid functional has been quite popular within the quantum chemistry community for a long time, but it is until recently that it has been adopted in solid state physics. One of the main obstacle is that the exact exchange is *nonlocal*, and it is extremely ineffective to evaluate the exact exchange in the reciprocal space expanded by plane-wave basis sets compared to that computed in localized Gaussian-type orbitals in the real-space formalism. Since the long-range exchange interaction in insulators decays exponentially with respect to the energy gap [54], one can benefit from the truncation of the Coulomb repulsion in the slow-varying long-range tail. This gives rise to the *screened* hybrid functionals. In the Heyd-Scuseria-Ernzerhof (HSE) screened functional, the exchange is divided into the short-range (sr) and long-range (lr) components [49]

$$E_{xc}^{\text{HSE}} = \alpha E_x^{\text{HF},\text{sr}}(\mu) + (1 - \alpha) E_x^{\text{PBE},\text{sr}}(\mu) + E_x^{\text{PBE},\text{lr}}(\mu) + E_c^{\text{PBE}}, \quad (3.29)$$

where the screening parameter μ determines the separation of the short-range and long-range parts

$$\frac{1}{r} = \text{sr}(r) + \text{lr}(r) = \frac{1 - \text{erf}(\mu r)}{r} + \frac{\text{erf}(\mu r)}{r}. \quad (3.30)$$

In one limit when $\mu = 0$, the long-range term is zero and HSE reduces to the unscreened PBE0 functional. For $\mu \rightarrow \infty$, HSE is identical to GGA-PBE since the whole exact exchange is screened. The range-separated functional sees an increasing interest from the solid state physics community as it usually requires a less dense \mathbf{k} -point sampling than its unscreened counterpart in reciprocal space. Moreover, for metallic systems the screened Coulomb interaction avoids the singularity in the derivative of the orbital energy with respect to \mathbf{k} arising from the Fourier transform $4\pi/k$ of the $1/r$ Coulomb potential. Nevertheless, screened hybrid functionals are not panacea either, and sometimes HSE results are not on par with GGA calculations for many metals [50, 51].

3.5 van der Waals Interactions in Density Functional Theory

Generally speaking, the van der Waals force includes contributions between two permanent dipoles, between a permanent dipole and a induced dipole, and between two instantaneously induced dipoles. In this thesis, we restrict the term to the last contribution, *i.e.* the London dispersion force due to the instantaneous dipoles. This attractive dispersion force arises when charge fluctuations in one part of an atomic system is correlated with that in another, and hence it is a truly *nonlocal* correlation effect. The vdW interaction, while being relatively small compared to ionic and covalent interactions, is very important in sparse matters and weakly bound systems. The vdW interaction

energy follows the R^{-6} asymptotic form for atoms and molecules, and the R^{-4} form for insulating sheets [21].

As is mentioned in Sec. 3.4.1, one important issue in KS-DFT is that the standard functional approximations are incapable of describing the long-range correlation effects, such as the *vdW* interaction. In this thesis, we apply two different approaches to account for the *vdW* interaction in the DFT calculations: the empirical DFT-D method and the *ab initio* *vdW* density functional (*vdW*-DF). In the DFT-D method proposed by Grimme [55], the long-range dispersion is taken into account by an additional pair-wise interaction term

$$E_{\text{DFT-D}} = E_{\text{KS-DFT}} - s_6 \sum_{i=1}^{N-1} \sum_{j=i+1}^N \frac{C_{ij}^6}{R_{ij}^6} f_{\text{damp}}(R_{ij}), \quad (3.31)$$

where C_{ij} and R_{ij} are the dispersion coefficients and inter-atomic distances for atom pair ij , respectively. s_6 is a global scaling factor, which is empirically set to 0.75 for the PBE functional. The damping function f_{damp} given by

$$f_{\text{damp}}(R_{ij}) = \frac{1}{1 + e^{-\alpha(R_{ij}/R_0 - 1)}} \quad (3.32)$$

serves to cut off the unphysical behavior of the asymptotic *vdW* interaction for small R_{ij} . R_0 is the sum of modified atomic *vdW* radii, and α is a global parameter.

The *vdW*-DF proposed by Dion *et al.* is another attempt to describe the long-range dispersion force seamlessly within KS-DFT without any empirical fitting parameters [56]. The *vdW*-DF XC energy is expressed as

$$E_{\text{vdW-DF}} = E_{\text{x}}^{\text{GGA}} + E_{\text{c}}^{\text{LDA}} + E_{\text{c}}^{\text{nl}}, \quad (3.33)$$

where the energy terms on the right-hand side represent the GGA exchange, LDA correlation and nonlocal correlation energy, respectively. The dynamical long range dispersion is therefore explicitly included as the nonlocal correlation effect. In this thesis, the revPBE exchange is chosen as the GGA exchange because it is close to the Hartree-Fock exchange and it suffers least from the erroneous over-binding due to exchange alone compared to other exchange functionals [21, 56]⁵. The nonlocal correlation energy E_{c}^{nl} is expressed in terms of the interaction kernel $\phi(\mathbf{r}, \mathbf{r}')$

$$E_{\text{c}}^{\text{nl}} = \frac{1}{2} \int d^3r d^3r' n(\mathbf{r}) \phi(\mathbf{r}, \mathbf{r}') n(\mathbf{r}'). \quad (3.34)$$

The nonlocal kernel is derived from the adiabatic connection fluctuation-dissipation theorem (ACFDT) with several approximations, and it is computationally more feasible than other *ab initio* techniques, such as exact exchange and random phase approximation (EXX/RPA) [58–60]. Both methods allow self-consistent calculations, although it is straightforward to see that DFT-D is computationally much faster than the *vdW*-DF method. In this thesis, the algorithms proposed by Soler *et al.* is used for the SCF *vdW*-DF calculations [61].

⁵The search for an optimized exchange in *vdW*-DF is still in progress. See Ref.[57] for example.

4 Implementations of Density Functional Theory

4.1 Basis Sets

The choice of basis set is central to the first-principles calculations. The basic idea of a basis set is to expand the information of an atom in terms of a mathematical form. It is common to expand a basis set in either a localized atomic-like form, or a plane-wave. In this section, a concise introduction of these two basis sets will be given in the context of periodic systems.

4.1.1 Atomic-like orbitals

The atomic-centered basis set, or the linear combination of atomic orbitals (LCAO) method is prevalent in the quantum chemistry of solids. In LCAO, each crystalline orbital $\psi_i(\mathbf{r}; \mathbf{k})$ is a linear combination of a set of Bloch functions $\phi_\mu(\mathbf{r}; \mathbf{k})$

$$\psi_i(\mathbf{r}; \mathbf{k}) = \sum_{\mu} a_{\mu,i}(\mathbf{k}) \phi_{\mu}(\mathbf{r}; \mathbf{k}), \quad (4.1)$$

where $a_{\mu,i}$ are the coefficients to be optimized. The Bloch functions are defined in terms of atomic-centered functions $\varphi_{\mu}(\mathbf{r})$

$$\phi_{\mu}(\mathbf{r}; \mathbf{k}) = \sum_{\mathbf{R}} \varphi_{\mu}(\mathbf{r} - \mathbf{A}_{\mu} - \mathbf{R}) e^{i\mathbf{k} \cdot \mathbf{R}}, \quad (4.2)$$

where \mathbf{R} is the lattice translation vector, and \mathbf{A}_{μ} is the coordinates of the nucleus in the zero reference cell where φ_{μ} is centered. The atomic orbital φ_{μ} is expanded by a set (*contracted*) of individually normalized Gaussian-type functions (GTFs) g_j at the same center¹, with *fixed* coefficients d_j and exponents α_j

$$\varphi_{\mu}(\mathbf{r} - \mathbf{A}_{\mu} - \mathbf{R}) = \sum_j d_j g_j(\alpha_j; \mathbf{r} - \mathbf{A}_{\mu} - \mathbf{R}), \quad (4.3)$$

and the Gaussian primitives can be written in terms of spherical harmonics

$$g_j(\alpha_j; \mathbf{r}; l, m) = N_{lm}(\alpha) r^l Y_{lm}(\theta, \phi) e^{-\alpha_j r^2}, \quad (4.4)$$

¹Although the atomic orbitals are typically Slater orbitals, it is numerically more convenient to write a Slater orbital by a linear combination of Gaussians and operate the Gaussians. For example, one advantage of using Gaussian-type functions is that the product of two Gaussians is another Gaussian.

where l and m are angular quantum numbers. The expansion coefficients $a_{\mu,i}(\mathbf{k})$ are determined by the solution of the generalized eigenvalue equation for each reciprocal lattice vector \mathbf{k}

$$\mathbf{F}(\mathbf{k})\mathbf{C}(\mathbf{k}) = \mathbf{S}(\mathbf{k})\mathbf{C}(\mathbf{k})E(\mathbf{k}) \quad (4.5)$$

where \mathbf{S} is the overlap matrix, \mathbf{F} the Fock matrix, \mathbf{C} the coefficient matrix, and E the diagonal energy matrix.

A minimal basis set is known as a single- ζ basis set, and for each *shell*² there is *only* one corresponding basis function. The STO-3G basis set is a minimal basis set. The core and valence shells described by the STO-3G basis set are each constructed by a linear combination of 3 primitive Gaussian-type functions. One problem related to the minimal basis sets is the transferability because alteration of basis orbitals is not allowed. A more versatile construction of a basis set is the *split-valence* scheme, in which the valence electrons are treated with two or more basis functions for each atomic orbital. The core electrons can still be described by a single- ζ basis set since the core electrons are less affected by the environment. For example, in the 6-31G basis set, the core shell is the sum of 6 primitive Gaussians, and the valence shells are described by a linear combination of two basis functions, one of which has 3 primitive Gaussians and the second would simply be the normalized primitive. Basis sets like 6-31G are double- ζ basis. Accordingly, a triple- ζ basis describes the valence shells in terms of three basis functions. The different orbitals in the split-valence scheme allow the electron density to adapt the chemical environment so that split-valence basis sets have a high transferability.

It is common to include *polarization functions* to improve the accuracy of a basis set. For example, a d function can be added to the basis of atoms without d electrons in the 6-31G(d) basis set. In case of a carbon atom, a p -orbital centered on the atom can be polarized away from the nucleus by the additional d -orbital. The lowered symmetry gives rise to a more accurate description of chemical reactions. One can also add *diffuse functions* to provide more accurate descriptions of anions, or neutral molecules with lone-pair electrons. A diffuse function has a small exponent, and it improves the basis set at the *tails* of atomic orbitals which is faraway from the nucleus. However, in periodic systems, a diffuse basis set might give rise to a convergence problem and one should avoid using a basis set which is too diffuse.

It should be borne in mind that due to the incompleteness of the basis set that are usually used, the *basis set superposition error* (BSSE) arises when one tries to evaluate the binding energy of two interacting fragments in atomic-centered basis sets. In a system comprising two fragments A and B, if the basis sets are not complete, the energy of A will be improved by the basis sets of B, and vice versa. Since the total energy of isolated fragments are described by their own basis set, the binding energy in the presence of the BSSE is *overestimated*. A common technique to correct the spurious binding due to the basis set incompleteness is the *counterpoise* method by Boys [62]. The energy of a separated fragment are calculated in the presence of the “host” basis set of the other fragment. The energy difference referenced to the calculation using the individual basis

²The nomenclature *shell* implies a group of atomic orbitals with the same quantum number n and l .

set of the fragment is the correction to the BSSE. The counterpoise method is necessary for an accurate prediction of molecular adsorption on surfaces with the localized basis sets.

4.1.2 Plane-wave Basis Set

In periodic systems, it is natural to write a basis set in a plane-wave basis set. We see this by rewriting the Schrödinger equation in reciprocal space. Since the potential V is periodic, it can be expanded as a Fourier series in the reciprocal vectors \mathbf{G}

$$V(\mathbf{r}) = \sum_{\mathbf{G}} e^{i\mathbf{G}\cdot\mathbf{r}} V_{\mathbf{G}}. \quad (4.6)$$

Similarly, under the periodic boundary condition, an arbitrary wavefunction can be expanded as a Fourier series with wave vectors \mathbf{q}

$$\psi(\mathbf{r}) = \sum_{\mathbf{q}} e^{i\mathbf{q}\cdot\mathbf{r}} C_{\mathbf{q}}. \quad (4.7)$$

Then we have the central equation in the reciprocal space by writing $\mathbf{q} = \mathbf{k} + \mathbf{G}$

$$\left[\frac{1}{2}(\mathbf{k} + \mathbf{G})^2 - \varepsilon \right] C_{\mathbf{k}+\mathbf{G}} + \sum_{\mathbf{G}'} V_{\mathbf{G}-\mathbf{G}'} C_{\mathbf{k}+\mathbf{G}'} = 0 \quad (4.8)$$

For each wave vector \mathbf{k} , we can solve the central equation (4.8), and obtain the eigenvalues ε and eigenvectors with components $C_{\mathbf{k}+\mathbf{G}}$. The eigenvectors are the Bloch functions, which can be expressed as the product of a plane-wave times a periodic function with the periodicity of the lattice \mathbf{R}

$$\psi_{\mathbf{k},n}(\mathbf{r}) = \left(\sum_{\mathbf{G}} C_{\mathbf{k}+\mathbf{G},n} e^{i\mathbf{G}\cdot\mathbf{r}} \right) e^{i\mathbf{k}\cdot\mathbf{r}} = u_{\mathbf{k},n}(\mathbf{r}) e^{i\mathbf{k}\cdot\mathbf{r}}, \quad (4.9)$$

where n represents the band index, and $u_{\mathbf{k},n}(\mathbf{r}) = u_{\mathbf{k},n}(\mathbf{r} + \mathbf{R})$. The sums over wave vector \mathbf{k} can be performed over the irreducible Brillouin zone (IBZ) using certain sampling schemes, e.g. the Monkhorst-Pack sampling [63].

The plane-waves are orthonormal and independent of the position of the atoms, so that they do not suffer from the BSSE. Plane-waves are diagonal in any powers of the momentum \mathbf{p} , so they are eigenfunctions of the kinetic energy operator. The kinetic energy can be written as

$$T = \frac{1}{2} \sum_{\mathbf{k},n} \sum_{\mathbf{G}} f(\varepsilon_{\mathbf{k},n}) |C_{\mathbf{k}+\mathbf{G},n}|^2 |\mathbf{k} + \mathbf{G}|^2, \quad (4.10)$$

where $f(\varepsilon_{\mathbf{k},n})$ is the occupation number. In practice, one cannot do an infinite summation over the reciprocal lattice vectors and the kinetic energy is truncated to a cut-off energy

$$\frac{1}{2} |\mathbf{k} + \mathbf{G}|^2 \leq E_{\text{cut}}. \quad (4.11)$$

As another example, the Hartree energy can be expressed in the reciprocal space as

$$E_H = \frac{\Omega}{2} \sum_{\mathbf{G}} v_H(\mathbf{G}) n(\mathbf{G}), \quad (4.12)$$

where Ω denotes the volume of the unit cell. The Hartree potential is obtained using Poisson's equation³

$$v_H(\mathbf{G}) = \frac{4\pi n(\mathbf{G})}{|\mathbf{G}|^2}. \quad (4.13)$$

The expansion in plane-waves in reciprocal space is computationally very efficient thanks to the fast Fourier transformation on modern computers.

In practice, the number of plane-waves could be an order of magnitude larger than that of localized basis set. Since in the core region the valence electron wavefunctions must be orthogonal to those of the core, the wavefunction has rapid oscillation near the core, which requires a huge number of plane-wave functions. This can be circumvented either using a localized atomic-centered basis set in the core region, such as the muffin-tin sphere in the linearized augmented-plane-wave (LAPW) method [64], or employing a pseudopotential which replaces the potential near the core with a smooth part. For the plane-wave calculations involved in this work, we use the pseudopotential method.

4.2 Pseudopotentials

The essence of the pseudopotential method is to replace the strong core potential by a smoothly varied potential. The ground-state wavefunction ψ^{PS} of the pseudopotential reproduces the all electron valence wavefunction outside the core radius r_c . In the core region where $r < r_c$,⁴ the wavefunction becomes smooth instead of exhibiting rapid oscillation as in the all-electron wavefunction. In this way, the pseudo-wavefunction ψ^{PS} can be represented by a low number of $|\mathbf{G}|$ plane-waves.

4.2.1 Norm-conserving Pseudopotentials

A good pseudopotential should be both accurate and *transferable*, thereby ensuring that the pseudopotential generated from atomic calculations can be applied to different applications, such as ions, molecules, and condensed matter. We start with the concept of *norm-conserving* pseudopotential (NCP) [65], the pioneer of modern *ab initio* pseudopotentials. *Norm-conservation* requires that inside r_c the norm of the pseudo-wavefunction ψ^{PS} is constrained to the true wavefunction

$$\int_0^{r_c} dr r^2 |\psi^{\text{PS}}(\mathbf{r})|^2 = \int_0^{r_c} dr r^2 |\psi(\mathbf{r})|^2, \quad (4.14)$$

³Although the Hartree potential diverges when $\mathbf{G} = 0$, the sum of the Hartree potential, the electron-nucleus interaction energy and the nucleus-nucleus energy is a constant for a neutral system.

⁴The frozen core approximation is often applied to a pseudopotential as the core states are not changed by the environment in most cases.

where the spherical symmetry is implied. As the eigenvalue and wavefunction are angular momentum l -dependent, pseudopotentials of this type are *semilocal*.

The conservation ensures that the total charge in the core region is correct, and the normalized pseudo-wavefunction outside r_c is equal to the true wavefunction⁵. These conditions are prerequisites for a correct description of the pseudo-wavefunction and potential in the valence region where bonding occurs when the NCPP is applied to a molecule or solid.

A good measure of the pseudopotential transferability is provided by the logarithmic derivatives and its first energy derivative at r_c of the all-electron and pseudo-wavefunction. We first see that the equality for $r > r_c$ ensures that the logarithmic derivatives at r_c of ψ^{PS} agrees with that of ψ

$$\frac{1}{\psi^{\text{PS}}(r, E)} \frac{d\psi^{\text{PS}}(r, E)}{dr} \Big|_{r=r_c} = \frac{1}{\psi(r, E)} \frac{d\psi(r, E)}{dr} \Big|_{r=r_c}, \quad (4.15)$$

where E is the atomic reference energy. In addition, using Green's theorem, we have the first energy derivative of the logarithmic derivatives

$$-\frac{\partial}{\partial E} \frac{\partial}{\partial r} \ln \psi(r, E) \Big|_{r=r_c} = \frac{1}{r_c^2 |\psi(r_c, E)|^2} \int_0^{r_c} dr r^2 |\psi(r, E)|^2. \quad (4.16)$$

Thus, norm-conservation also ensures that the first derivative of the logarithmic derivatives with respect to E matches between the true and pseudo-wavefunction.

Constructing a pseudopotential requires one to determine the core radius r_c . A large r_c makes a *soft* pseudopotential, which needs a small number of plane-waves. But a soft pseudopotential is usually less transferable than a hard potential, while the latter requires more plane-waves.

It should be noted that pseudopotentials in a semilocal form, like the NCPP, are not very efficient. We may write the pseudopotential in terms of each atomic l value

$$V^{\text{PS}}(\mathbf{r}) = V^{\text{loc}}(\mathbf{r}) + \sum_{l=0}^{l_{\text{max}}} V_l^{\text{PS}}(\mathbf{r}) \mathcal{P}_l, \quad (4.17)$$

where V^{loc} is a local (l -independent) potential, and \mathcal{P}_l is an angular momentum projection operator. The nonlocal component of the pseudopotential is denoted by V_l^{PS} . When a pseudopotential in the form of Eq. (4.17) is expanded with a plane-wave basis, the calculation becomes unpleasant because a huge number of integrals arising from the \mathbf{k} -dependence needed to be calculated due to the nonlocality [64]. Kleinman and Bylander realized this problem and managed to construct a *separable* pseudopotential operator [66]. The construction begins by adding and subtracting a local function V^{L}

$$\sum_l V_l^{\text{PS}}(\mathbf{r}) \mathcal{P}_l = V^{\text{L}}(\mathbf{r}) + \sum_{lm} |Y_{lm}\rangle \delta V_l(\mathbf{r}) \langle Y_{lm}|, \quad (4.18)$$

⁵Equality is not applied to nonlocal potentials like the Hartree-Fock exchange potential.

where $\delta V_l = V_l^{\text{PS}} - V_l^{\text{L}}$, and the projection operator is expressed by spheric harmonics. A nonlocal pseudopotential operator V^{NL} is used to replace the second term on the right hand side (RHS) of Eq. (4.18), *i.e.* the semilocal term V^{SL}

$$V^{\text{NL}} = \sum_{lm} \frac{|\delta V_l \psi_{lm}^{\text{PS}}\rangle \langle \psi_{lm}^{\text{PS}} \delta V_l|}{\langle \psi_{lm}^{\text{PS}} | \delta V_l | \psi_{lm}^{\text{PS}} \rangle}. \quad (4.19)$$

Unlike the semilocal V^{SL} , V^{NL} is fully nonlocal in both angular momentum (l and m) and radius r . It is readily shown that when operating on the reference atom states $|\psi_{lm}^{\text{PS}}\rangle$, V^{NL} and V^{SL} are equivalent. With this separable form, the matrix element is indeed much easier to operate with as it can be written as the product of projection operations

$$\langle \psi_i | V^{\text{NL}} | \psi_i \rangle = \sum_{lm} \frac{\langle \psi_i | \delta V_l \psi_{lm}^{\text{PS}} \rangle \langle \delta V_l \psi_{lm}^{\text{PS}} | \psi_i \rangle}{\langle \psi_{lm}^{\text{PS}} | \delta V_l | \psi_{lm}^{\text{PS}} \rangle} \quad (4.20)$$

From the perspective of numerical efficiency, this offers a significant improvement over the semilocal form, where integrals for each pair of ψ_i and ψ_j are involved.

We note here that the success of pseudopotential relies on the linearization of the exchange-correlation functional V_{xc} with respect to density n . However, in pseudopotential calculations for alkali and transition metals, because there is significant overlap between core and valence electron densities, the linearization might result in systematic errors. One straightforward method is to include *semi-core* electrons as valence electrons. Alternatively, one can resort to *non-linear core correction* [67] to explicitly treat the non-linear exchange-correlation interaction between core and valence electron densities

$$\tilde{V}_{\text{xc}} = V_{\text{xc}}(n^{\text{PS}}) + [V_{\text{xc}}(n^{\text{PS}} + n^{\text{core}}) - V_{\text{xc}}(n^{\text{PS}})]. \quad (4.21)$$

4.2.2 Ultrasoft Pseudopotentials

A different approach by Vanderbilt *et al.*, known as *ultrasoft pseudopotential* (USPP) [68], is able to achieve the same accuracy as the NCPP while making the pseudopotential more smooth by abandoning the norm-conservation inside the core region. In ultrasoft pseudopotential approach, the total energy is expressed as

$$E = \sum_{\text{occ}} \langle \tilde{\psi}_j | T + V^{\text{NL}} | \tilde{\psi}_j \rangle + \int d^3r V^{\text{L}}(\mathbf{r}) \tilde{n}(\mathbf{r}) + E_{\text{H}} + E_{\text{xc}} + E_{\text{nucl-nucl}}. \quad (4.22)$$

The nonlocal separable pseudopotential V^{NL} is a projection operator

$$V^{\text{NL}} = \sum_{mn} D_{nm}^{(0)} |\beta_n\rangle \langle \beta_m|, \quad (4.23)$$

where β_m are represented by the product of spherical harmonics and radial functions. We have the pseudo-charge density

$$\tilde{n}(\mathbf{r}) = \sum_{\text{occ}} \left[\tilde{\psi}_j^*(\mathbf{r}) \tilde{\psi}_j(\mathbf{r}) + \sum_{mn} Q_{nm}(\mathbf{r}) \langle \tilde{\psi}_j | \beta_n \rangle \langle \beta_m | \tilde{\psi}_j \rangle \right], \quad (4.24)$$

where Q_{nm} are local functions. The pseudo-wavefunction $\tilde{\psi}$ can be obtained by solving the secular equation by the variational principle

$$[\mathcal{H} - \varepsilon_j \mathcal{S}] \tilde{\psi}_j = 0, \quad (4.25)$$

with

$$\mathcal{H} = T + V_{\text{xc}} + V_{\text{H}} + V^{\text{L}} + \sum_{mn} D_{nm} |\beta_n\rangle \langle \beta_m|, \quad (4.26)$$

$$\mathcal{S} = \mathbf{1} + \sum_{mn} \int_{r < r_c} d^3r Q_{nm}(\mathbf{r}) |\beta_n\rangle \langle \beta_m|, \quad (4.27)$$

and

$$D_{nm} = D_{nm}^{(0)} + \int_{r < r_c} d^3r [V^{\text{L}}(\mathbf{r}) + V_{\text{xc}} + V_{\text{H}}] Q_{nm}(\mathbf{r}). \quad (4.28)$$

4.2.3 Projector Augmented Wave Method

Finally, we brief sketch the basic concept of the *projector augmented wave* (PAW) method by Blöchl [69], which will be heavily used throughout this work. The PAW method is similar to the ultrasoft pseudopotential method, but it keeps the full all-electron wavefunction as in the APW method. We define an auxiliary smooth wavefunction $|\tilde{\psi}_n\rangle$, which can be transformed to the true wavefunction $|\psi_n\rangle$ through a linear transformation operator \mathcal{T}

$$|\psi_n\rangle = \mathcal{T} |\tilde{\psi}_n\rangle. \quad (4.29)$$

The Schrödinger equation is then transformed in terms of the auxiliary wavefunctions

$$\mathcal{T}^\dagger \mathcal{H} \mathcal{T} |\tilde{\psi}_n\rangle = \varepsilon_n \mathcal{T}^\dagger \mathcal{T} |\tilde{\psi}_n\rangle. \quad (4.30)$$

Now we need to find a suitable transformation \mathcal{T} to make the auxiliary wavefunctions well behaved.

Since the true valence wavefunction is smooth, the transformation has no effect outside the core sphere centered on the nucleus

$$\mathcal{T} = \mathbf{1} + \mathcal{T}_0. \quad (4.31)$$

Within the sphere, each smooth function $|\tilde{\psi}\rangle$ can be expanded by partial waves $|\tilde{\phi}_m\rangle$

$$|\tilde{\psi}_n\rangle = \sum_m c_m |\tilde{\phi}_m\rangle. \quad (4.32)$$

Analogously, we define partial waves $|\phi_m\rangle$ to expand the true wavefunction in the sphere

$$|\psi_n\rangle = \mathcal{T} |\tilde{\psi}_n\rangle = \sum_m c_m |\phi_m\rangle. \quad (4.33)$$

Thus the all-electron wavefunction can be rewritten as

$$|\psi_n\rangle = |\tilde{\psi}_n\rangle + \sum_m c_m [|\phi_m\rangle - |\tilde{\phi}_m\rangle] \quad (4.34)$$

As \mathcal{T} is a linear operator, the coefficients c_m must be linear functionals of $|\tilde{\psi}_n\rangle$

$$c_m = \langle \tilde{p}_m | \tilde{\psi}_n \rangle \quad (4.35)$$

for some smooth projector functions $|\tilde{p}_m\rangle$. The one-center expansion $\sum_m |\tilde{\phi}_m\rangle \langle \tilde{p}_m | \tilde{\psi}_n \rangle$ of the smooth function $|\tilde{\psi}_n\rangle$ reduces to itself if the smooth projector functions are orthonormal to the partial waves inside the augmentation sphere

$$\langle \tilde{p}_m | \tilde{\phi}_{m'} \rangle = \delta_{mm'}. \quad (4.36)$$

Using the condition (4.36), we see that the transformation \mathcal{T} involves the all-electron wavefunction

$$\mathcal{T} = \mathbf{1} + \sum_m \left[|\phi_m\rangle - |\tilde{\phi}_m\rangle \right] \langle \tilde{p}_m|. \quad (4.37)$$

The true all-electron wavefunction $\psi_n(\mathbf{r}) = \langle \mathbf{r} | \psi_n \rangle$ can therefore be obtained from the transformation operator in Eq. (4.37)

$$\begin{aligned} \psi_n(\mathbf{r}) &= \tilde{\psi}_n(\mathbf{r}) + \sum_m \left[\phi_m(\mathbf{r}) - \tilde{\phi}_m(\mathbf{r}) \right] \langle \tilde{p}_m | \tilde{\psi}_n \rangle \\ &= \tilde{\psi}_n(\mathbf{r}) + \psi_n(\mathbf{r} - \mathbf{R}) - \tilde{\psi}_n(\mathbf{r} - \mathbf{R}), \end{aligned} \quad (4.38)$$

where \mathbf{R} is the coordinates of the nucleus. The all-electron wavefunction now can be considered as a superposition of three contributions: the auxiliary wavefunctions which are smooth everywhere, the rapid oscillating part within the core sphere (*i.e.* on-site), and the smooth wavefunctions within the sphere which are subtracted from the all-electron wavefunctions.

In general, for an arbitrary operator \mathcal{A} in the all-electron wavefunctions problem, it is possible to transform it to $\tilde{\mathcal{A}}$ that operate on the smooth functions

$$\tilde{\mathcal{A}} = \mathcal{T}^\dagger \mathcal{A} \mathcal{T}, \quad (4.39)$$

where \mathcal{T} is in the form of Eq. (4.37). We can derive the density in this way and it has a similar form as in Eq. (4.38)

$$n(\mathbf{r}) = \tilde{n}(\mathbf{r}) + n^1(\mathbf{r}) - \tilde{n}^1(\mathbf{r}), \quad (4.40)$$

where the superscript 1 denotes the localized density within the augmentation sphere.

To summarize, we note that the PAW method is as efficient as the ultrasoft pseudopotential, and it is superior in the way that the core states information is not lost. Therefore, unlike NCPP and ultrasoft pseudopotential, non-linear core correction is not necessary for the PAW method since the explicit non-linear dependence of the total energy on the one-center density is properly taken into account.

5 Many-body Perturbation Theory

We are facing a paradox with the density functional theory: DFT is in principle *exact*, which implies that it should be able to treat the properties of a many-electron system exactly. But unfortunately we do not have access to the exact exchange-correlation functional. It is thus desirable to climb up towards the highest rung of the “Jacob’s ladder” of exchange-correlation functional¹ to achieve the highest chemical accuracy. On the other hand, DFT is essentially a static ground-state theory, although it can be applied to excited states with a proper choice of the exchange-correlation functional. The most relevant deficiency is the gap problem associated with the derivative discontinuity mentioned in Sec. 3.4.2. Long-range correlations (such as vdW and dynamic polarization) are neither captured by standard DFT approximations.

The static DFT can be extended to the time-dependent DFT (TDDFT) [70], where time-dependence is introduced to the exchange-correlation potential and the electron density. An analogous approach based on the Green’s functions, *i.e.* many-body perturbation theory (MBPT) [71], achieved much success in solid-state physics in recent years. In this thesis, Hedin’s *GW* approximation is used to correct the fundamental gap from DFT calculations, followed by the two-particle Bethe-Salpeter equation for the bound electron-hole (*e-h*) interaction in the excited state.

5.1 Green’s Function Theory

Green’s functions are extraordinarily useful for perturbation problems. Let us begin with the one-particle Schrödinger equation

$$[\mathcal{H}_0(\mathbf{r}) + V(\mathbf{r})]\psi_E = E\psi_E, \quad (5.1)$$

where the external potential V is treated as a perturbation. We define the corresponding Green’s function by the differential equation

$$[E - \mathcal{H}_0(\mathbf{r})]G_0(\mathbf{r}, \mathbf{r}', E) = \delta(\mathbf{r} - \mathbf{r}'). \quad (5.2)$$

The Schrödinger equation can be rewritten as

$$[G_0^{-1}(\mathbf{r}, E) - V(\mathbf{r})]\psi_E = 0, \quad (5.3)$$

and the solution for the system under some perturbation is

$$\psi_E(\mathbf{r}) = \psi_E^0(\mathbf{r}) + \int d\mathbf{r}' G_0(\mathbf{r}, \mathbf{r}', E) V(\mathbf{r}') \psi_E(\mathbf{r}'), \quad (5.4)$$

¹A good example of the highest rung of a Jacob’s ladder is the EXX/RPA functional.

where $\psi_E^0(\mathbf{r})$ is the eigenfunction of \mathcal{H}_0 .

This can be extended to the time-dependent equation

$$[i\partial_t - \mathcal{H}_0(\mathbf{r}) - V(\mathbf{r})]\psi(\mathbf{r}, t) = 0, \quad (5.5)$$

and the related Green's functions are defined by

$$[i\partial_t - \mathcal{H}_0(\mathbf{r})]G_0(\mathbf{r}t, \mathbf{r}'t') = \delta(\mathbf{r} - \mathbf{r}')\delta(t - t') \quad (5.6)$$

$$[i\partial_t - \mathcal{H}_0(\mathbf{r}) - V(\mathbf{r})]G(\mathbf{r}t, \mathbf{r}'t') = \delta(\mathbf{r} - \mathbf{r}')\delta(t - t'). \quad (5.7)$$

Analogous to the static equation, the eigenstates can be expressed in terms of G_0 and G

$$\psi(\mathbf{r}, t) = \psi^0(\mathbf{r}, t) + \int d\mathbf{r}' dt' G_0(\mathbf{r}t, \mathbf{r}'t') V(\mathbf{r}') \psi(\mathbf{r}', t') \quad (5.8)$$

$$\psi(\mathbf{r}, t) = \psi^0(\mathbf{r}, t) + \int d\mathbf{r}' dt' G(\mathbf{r}t, \mathbf{r}'t') V(\mathbf{r}') \psi^0(\mathbf{r}', t') \quad (5.9)$$

By iterating Eq. (5.2) and comparing it to Eq. (5.9), a Dyson-like equation can be derived

$$G = G_0 + G_0 V G, \quad (5.10)$$

and it corresponds to a sum over the Feynman diagrams (cf. Fig. 5.1). We can see that Green's function method is indeed extremely useful since the full and the unperturbed Green's functions can be connected directly through the Dyson equation.

We now define the one-electron Green's function as the expectation value with respect to the many-body ground-state $|N\rangle$

$$G(\mathbf{r}t, \mathbf{r}'t') = -i\langle N | \mathcal{T} \psi(\mathbf{r}t) \psi^\dagger(\mathbf{r}'t') | N \rangle = \begin{cases} -i\langle N | \psi(\mathbf{r}t) \psi^\dagger(\mathbf{r}'t') | N \rangle & \text{for } t > t' \\ i\langle N | \psi^\dagger(\mathbf{r}'t') \psi(\mathbf{r}t) | N \rangle & \text{for } t < t', \end{cases} \quad (5.11)$$

where \mathcal{T} is the time-ordering operator, and $\psi(\mathbf{r}t)$ is the field operator in the Heisenberg picture which annihilates an electron at point \mathbf{r} and time t . $\psi^\dagger(\mathbf{r}'t')$ is the field operator that creates an electron at (\mathbf{r}', t') . When $t > t'$, G describes the propagation of an electron which was added at \mathbf{r}' to \mathbf{r} . When $t < t'$, G is interpreted as the probability amplitude that a hole created at \mathbf{r} will propagate to \mathbf{r}' . Therefore, the Green's function describes either the propagation of an electron ($t > t'$) or a hole ($t < t'$).²

G is intimately related to not only the expectation value of any single-particle operator in the ground-state (e.g. charge density and ground-state energy), but also the one-electron excitation spectrum in photoemission and inverse photoemission. In the photoemission process (PES), a photon $h\nu$ is absorbed by a system and an electron is emitted with a kinetic energy E_{kin} . The binding energy of the electron is thus

$$\varepsilon_i = h\nu - E_{\text{kin}}. \quad (5.12)$$

In the inverse photoemission (IPES), the process is reversed and the final state energy of the electron is

$$\varepsilon_f = E_{\text{kin}} - h\nu. \quad (5.13)$$

²The Green's function is also called *retarded* if $t > t'$, or *advanced* if $t < t'$.

The photoemission current observed in experiment is described by Fermi's golden rule, and it is related to the *spectral function*

$$A(\mathbf{r}, \mathbf{r}', \omega) = \sum_s f_s(\mathbf{r}) f_s^*(\mathbf{r}') \delta(\omega - E_s), \quad (5.14)$$

where s represents the excited state. The electron removal energy E_s in PES and the transition amplitude $f_s(\mathbf{r})$ are defined by the N - and $(N - 1)$ -electron states

$$f_s(\mathbf{r}) = \langle N - 1, s | \psi(\mathbf{r}) | N \rangle \quad (5.15)$$

$$E_s = E(N) - E(N - 1, s) < \mu, \quad (5.16)$$

where μ is the chemical potential. The electron addition energy in IPES can be defined analogously

$$f_s(\mathbf{r}) = \langle N | \psi(\mathbf{r}) | N + 1, s \rangle \quad (5.17)$$

$$E_s = E(N + 1, s) - E(N) > \mu. \quad (5.18)$$

Inserting a complete set of $(N \pm 1)$ -electron states by the closure relation $\sum |N \pm 1\rangle \langle N \pm 1| = 1$ between the field operators in Eq. (5.11), we have the Green's function in the Lehmann representation

$$G(\mathbf{r}, \mathbf{r}', \omega) = \sum_s \frac{f_s(\mathbf{r}) f_s^*(\mathbf{r}')}{\omega - E_s \pm i\eta}, \quad (5.19)$$

where $i\eta$ is an infinitesimal imaginary part needed for the convergence of the Fourier transform to frequency domain. The poles of the Green's function G then are the one-electron addition and removal energies. The spectral function is given by the imaginary part of the Green's function

$$A(\mathbf{r}, \mathbf{r}', \omega) = \frac{1}{\pi} |\text{Im} G(\mathbf{r}, \mathbf{r}', \omega)| \quad (5.20)$$

In the non-interacting system, each δ peak in the spectral function corresponds to the excitation of a single particle. When interactions are present, the peaks of the spectral function are broadened as a result of the finite lifetime of the peak. Nevertheless, one can still treat those broadened peaks as particle-like as long as their main profile are identifiable. This gives rise to the concept of a *quasiparticle* (QP).

5.2 Hedin's GW Approximation

We see from Eq. (5.2) that the Green's function can generally be expressed as

$$G(\omega) = [\omega - \mathcal{H}]^{-1} \quad (5.21)$$

It is always possible to separate the fully-interacting \mathcal{H} into a non-interacting \mathcal{H}_0 , and a nonlocal and energy-dependent *self-energy* operator Σ

$$\mathcal{H}(\mathbf{r}, \mathbf{r}', \omega) = \mathcal{H}_0(\mathbf{r}) + \Sigma(\mathbf{r}, \mathbf{r}', \omega) \quad (5.22)$$

with

$$\mathcal{H}_0(\mathbf{r}) = -\frac{1}{2}\nabla^2 + v_{\text{ext}}(\mathbf{r}) + v_{\text{H}}(\mathbf{r}). \quad (5.23)$$

The problem of solving the many-electron system is now corresponding to the solution of the one-particle QP equation

$$\mathcal{H}_0\psi_i^{\text{QP}}(\mathbf{r}) + \int d\mathbf{r}' \Sigma(\mathbf{r}, \mathbf{r}', \varepsilon_i^{\text{QP}}) \psi_i^{\text{QP}}(\mathbf{r}') = \varepsilon_i^{\text{QP}} \psi_i^{\text{QP}}(\mathbf{r}). \quad (5.24)$$

While it looks similar to the one-particle mean field theories like DFT or Hartree-Fock theory, Eq. (5.24) is essentially a *dynamic* formulation, and the energy and wavefunction are not single-particle quantities but are related to quasiparticles.

The Green's function G_0 of the non-interacting \mathcal{H}_0 can be cast into the Lehmann representation³

$$G_0(\mathbf{r}, \mathbf{r}', \omega) = \sum_i \frac{\psi_i(\mathbf{r})\psi_i^*(\mathbf{r}')}{\omega - E_i + i\eta \text{sgn}(E_i - \mu)}, \quad (5.25)$$

where ψ_i is the one-particle wavefunction, and E_i the eigenvalue of the non-interacting Hamiltonian. It is illuminating from Eq. (5.10) that the interacting one-particle Green's function G and the non-interacting G_0 should also be connected by the Dyson equation, as is proposed by Hedin [72].

$$G(12) = G_0(12) + \int d3d4 G_0(13)\Sigma(34)G(42). \quad (5.26)$$

Hedin's simplified notation $1 \equiv (\mathbf{r}_1, \sigma_1, t_1)$ is used to represent a group of the space, spin and time variables. 1^+ denotes $t_1 + \eta$ where η is a positive infinitesimal, and $\int d1 = \Sigma_\sigma \int d\mathbf{r}_1 \int dt_1$. The Feynman diagram for the Green's function $G(12)$ is shown in Fig. 5.1.

The self-energy Σ is obtained by self-consistently solving a set of coupled integro-differential equations involving the vertex Γ , the polarization P , the bare (v) and screened Coulomb interaction W

$$\Sigma(12) = i \int d3d4 G(14)W(1^+3)\Gamma(42; 3) \quad (5.27)$$

$$\Gamma(12; 3) = \delta(12)\delta(13) + \int d4d5d6d7 \frac{\delta\Sigma(12)}{\delta G(45)} G(46)G(75)\Gamma(67; 3) \quad (5.28)$$

$$W(12) = v(12) + \int d3d4 W(13)P(34)v(42) \quad (5.29)$$

$$P(12) = -i \int d3d4 G(23)G(42^+)\Gamma(34; 1). \quad (5.30)$$

The screened potential W is another Dyson-like equation like the Green's function. While G_0 and G are the propagators for electrons or holes, v and W can be understood as the propagations of the quantum particles of the electric field. The polarization P

³The notation of G and G_0 in this section differs from Sec. 5.1.

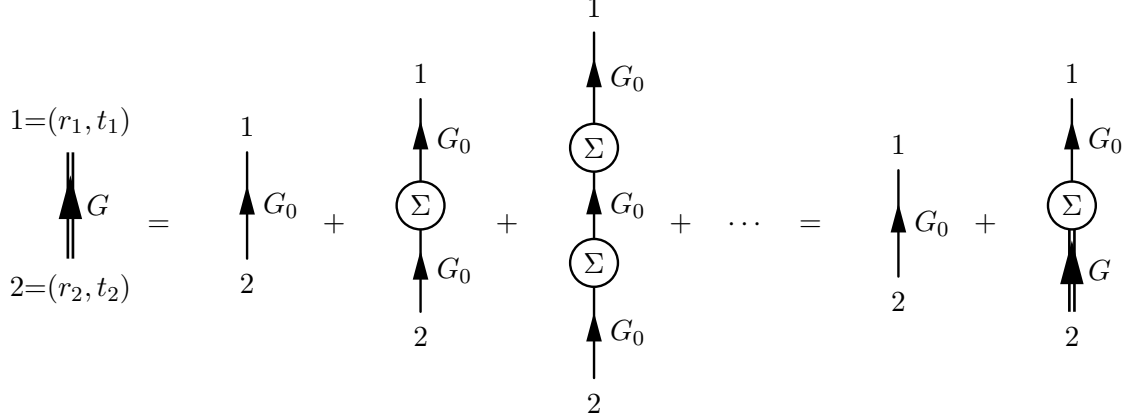


Figure 5.1: Feynman diagram of the Dyson equation for the Green's function $G(12)$. The heavy double line and the plain line denote the propagation of an interacting electron and of a non-interacting electron, respectively.

is the response of the system to the additional electron or hole, which is built up by the creations of electron-hole pairs. In other words, the polarization acts like the self-energy for the electric field particles, and it converts the bare Coulomb potential into the screened potential. Indeed, we see that P and Σ share the same structure, which contains two propagators connected via the vertex function Γ . The vertex Γ is a three-point kernel that contains the information of the electron-hole interactions. It is the most complicated term in Hedin's equation, and it cannot in general be evaluated numerically since it includes a functional derivative. Hedin approximated the vertex by neglecting the variation of the self-energy with respect to the Green's function, which leads to a much simplified form of Γ

$$\Gamma(12; 3) = \delta(12)\delta(13). \quad (5.31)$$

The polarization is accordingly reduced to the form of the random phase approximation (RPA) [73, 74]

$$P(12) = -iG(12^+)G(21). \quad (5.32)$$

For example, using the non-interacting G_0 in Eq. (5.25), we have the polarizability P^0 in the independent particle (IP) form

$$P^0(\mathbf{r}, \mathbf{r}', \omega) = \sum_{ij} (f_i - f_j) \frac{\psi_i(\mathbf{r})\psi_j^*(\mathbf{r})\psi_j(\mathbf{r}')\psi_i^*(\mathbf{r}')}{\omega - (\varepsilon_j - \varepsilon_i) + i\eta}, \quad (5.33)$$

where f_i are occupation numbers. The self-energy becomes the simple product of G and W

$$\Sigma(12) = iG(12)W(1^+2). \quad (5.34)$$

This is Hedin's GW approximation for self-energy, which can be visualized by the diagram in Fig. 5.2 as a series of scattering processes in RPA.

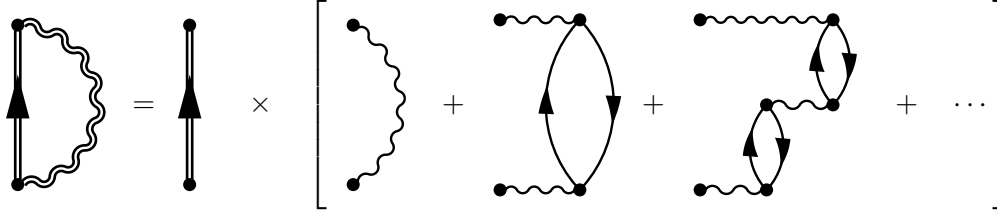


Figure 5.2: Feynman diagram for the self-energy in the GW approximation. The double wiggly line is the screened Coulomb interaction in the RPA form. The zigzag lines represent the bare Coulomb interaction. The bubble refers to an electron-hole pair. The self-energy in the RPA is an infinite summation containing scattering of all orders with the most divergent term.

In practice, G is constructed using single-particle KS-DFT orbitals. The single-particle orbitals and eigenvalues can be considered as a zeroth-order approximation to the QP amplitudes and energies. The QP energies in Eq. (5.24) then can be approximated as a first-order perturbation

$$\varepsilon_i^{\text{QP}} = \varepsilon_i^{\text{KS}} + Z_i \langle \psi_i^{\text{KS}} | \Sigma(\varepsilon_i^{\text{KS}}) - V_{\text{xc}}^{\text{KS}} | \psi_i^{\text{KS}} \rangle, \quad (5.35)$$

where the renormalization factor Z_i is defined as

$$Z_i^{-1} = 1 - \langle \psi_i^{\text{KS}} | \left. \frac{\partial \Sigma}{\partial \varepsilon} \right|_{\varepsilon=\varepsilon_i^{\text{KS}}} | \psi_i^{\text{KS}} \rangle. \quad (5.36)$$

Instead of using the full Green's function, it is customary to use the non-interacting Green's function G_0 in Eq. (5.25) and screened interaction W_0 in the so-called one-shot G_0W_0 method. Iterating both G and W in the self-consistent GW calculations is not straightforward since Σ is non-Hermitian and energy dependent, and it does not guarantee a systematic improvement over the G_0W_0 method without vertex corrections [75–77]. With vertex corrections, self-consistent GW is able to achieve very accurate band gaps [78], but the calculation is formidable for large systems. It is often sufficient to start the GW calculations with the LDA orbitals, whereas for certain systems (such as transition-metal oxides) hybrid functionals are preferred [79].

The GW self-energy can be decomposed into exchange and correlation parts by writing the screened interaction W into $W - v + v$

$$\Sigma = iG_0^{\text{KS}}W = iG_0^{\text{KS}}v + iG_0^{\text{KS}}(W - v) = \Sigma_x + \Sigma_c. \quad (5.37)$$

The exchange part can be evaluated analytically in a form of the Hartree-Fock exchange. The correlation self-energy needs to be calculated numerically. One central quantity is the evaluation of the full dielectric response of the system, which connects the bare and

screened Coulomb interaction ⁴

$$W(\mathbf{r}, \mathbf{r}', \omega) = \int d\mathbf{r} \varepsilon^{-1}(\mathbf{r}, \mathbf{r}'', \omega) v(\mathbf{r}'', \mathbf{r}') \quad (5.38)$$

$$W_{\mathbf{G}\mathbf{G}'}(\mathbf{q}, \omega) = \varepsilon_{\mathbf{G}\mathbf{G}'}^{-1}(\mathbf{q}, \omega) v(\mathbf{q} + \mathbf{G}'), \quad (5.39)$$

where \mathbf{q} is a vector in the first Brillouin zone, and the bare Coulomb potential $v(\mathbf{q})$ in the momentum space is given by $4\pi/(\Omega|\mathbf{q}|^2)$. The local field effect, which is due to the local inhomogeneities of the electronic system, is taken into account by the off-diagonal components with $\mathbf{G} \neq \mathbf{G}'$. In GW approximation, the dielectric function is related to the polarizability by

$$\varepsilon_{\mathbf{G}\mathbf{G}'}(\mathbf{q}, \omega) = \delta_{\mathbf{G}\mathbf{G}'} - v(\mathbf{q} + \mathbf{G})P_{\mathbf{G}\mathbf{G}'}(\mathbf{q}, \omega). \quad (5.40)$$

When P is zero, there is no polarization and the total potential V_{tot} is equal to the external potential V_{ext} according to the linear response relations

$$V_{\text{tot}} = V_{\text{ext}} + V_{\text{ind}}, \quad (5.41)$$

$$V_{\text{ext}} = \varepsilon V_{\text{tot}}, \quad (5.42)$$

$$V_{\text{tot}} = \varepsilon^{-1} V_{\text{ext}}, \quad (5.43)$$

$$\rho_{\text{ind}} = \chi V_{\text{ext}} = P V_{\text{tot}}, \quad (5.44)$$

where V_{ind} is the induced potential by external perturbations, and the induced charge ρ_{ind} is connect to the external potential via the reducible polarizability χ . The inverse dielectric function can be expressed in terms of v and χ

$$\varepsilon_{\mathbf{G}\mathbf{G}'}^{-1}(\mathbf{q}, \omega) = \delta_{\mathbf{G}\mathbf{G}'} + v(\mathbf{q} + \mathbf{G})\chi_{\mathbf{G}\mathbf{G}'}(\mathbf{q}, \omega). \quad (5.45)$$

The reducible polarizability χ is linked to the irreducible polarizability P by a Dyson-like equation

$$\chi = P + P v \chi. \quad (5.46)$$

The inverse dielectric function is of great significance to determine the excitation spectra. The electron-energy-loss spectra (EELS) are accessible from its imaginary part $-\Im[\varepsilon^{-1}(\mathbf{q}, \omega)]$. In optical absorption experiment, the spectra are described by the imaginary part of the *macroscopic dielectric function* ε_{M}

$$\varepsilon_{\text{M}}(\omega) \equiv \lim_{\mathbf{q} \rightarrow 0} \frac{1}{\varepsilon_{00}(\mathbf{q}, \omega)}. \quad (5.47)$$

Alternatively, the macroscopic dielectric function can be expressed in a more useful form in terms of a modified polarizability \tilde{P}

$$\varepsilon_{\text{M}}(\omega) \equiv 1 - \lim_{\mathbf{q} \rightarrow 0} \left[v(\mathbf{q}) \tilde{P}_{00}(\mathbf{q}, \omega) \right], \quad (5.48)$$

⁴ $\varepsilon_{\mathbf{G}\mathbf{G}'}(\mathbf{q}, \omega) \equiv \varepsilon(\mathbf{q} + \mathbf{G}, \mathbf{q} + \mathbf{G}', \omega)$.

with

$$\tilde{P} = P + P\tilde{v}P. \quad (5.49)$$

The modified \tilde{v} is nothing but the bare Coulomb interaction v except that \tilde{v} vanishes for the long-range contribution ($\mathbf{G} = 0$).

The evaluation of the dielectric function is cumbersome and it requires a full integration in ω along the imaginary axis [80], or by a real-axis integration [81, 82]. However, it is noticed that in most cases $\varepsilon_{\mathbf{G}\mathbf{G}'}(\mathbf{q}, \omega)$ is characterized by a strong peak corresponding to a plasmon excitation at the plasmon frequency, which can be described by a single-pole function. In the *plasmon-pole approximation*, the position and strength of the pole can be determined by sum rules [83] or by reproducing the dielectric function at two imaginary energies [84]. The plasmon-pole approximation is reasonable as the details of the energy dependence in $\varepsilon_{\mathbf{G}\mathbf{G}'}(\mathbf{q}, \omega)$ are not critical. It works well when the screening is dominated by a small number of poles at high energies. Nevertheless, the lifetime of a quasiparticle cannot be obtained by the plasmon-pole approximation because the imaginary part of the self-energy is zero outside the poles.

5.3 Two-particle Bethe-Salpeter Equation

In the *GW* method, the vertex Γ , as the linear response of the self-energy to a change in the total potential, is approximated to δ , and the two Green's functions are no longer coupled in the polarizability P . The decoupling implies that the bound electron-hole interaction, *i.e.* the *excitonic* effect is neglected in the absorption spectra. Indeed, it has been found that the polarizability in the IP-RPA form (Eq. 5.33) even with *GW* corrections yields a blue-shift of the absorption peak for several insulators and metallic systems [85–89]. In the context of this work where the creation of mobile electron is involved, it is apparent that the electron-hole attraction is important in determining the effective excitation energy.

The inclusion of the excitonic effect through the vertex corrections is achieved in a second iteration of Hedin's equation from Eq. (5.27) to (5.30), assuming the self-energy is in the *GW* approximation. The vertex function can be formally written as the derivative of the inverse Green's function with respect to the total potential

$$\Gamma(12; 3) = -\frac{\delta G^{-1}(12)}{\delta V(3)} = \delta(12)\delta(13) + i\frac{\delta[G(12)W(1^+2)]}{\delta V(3)}. \quad (5.50)$$

Neglecting the change in screening due to the excitation, we have

$$\Gamma(12; 3) = \delta(12)\delta(13) + iW(1^+2)\frac{\delta G(12)}{\delta V(3)} \quad (5.51)$$

From the identity

$$\frac{\delta G(12)}{\delta V(3)} = -\int d4d5 G(14)\frac{\delta G^{-1}(45)}{\delta V(3)}G(52), \quad (5.52)$$

we reach an integral equation for the vertex

$$\Gamma(12; 3) = \delta(12)\delta(13) + iW(1^+2) \int d67G(16)G(72)\Gamma(673). \quad (5.53)$$

This is the *Bethe-Salpeter* equation (BSE) [90] for the irreducible vertex function. We now define a three-point polarizability P in terms of the Γ

$$P(312) = -i \int d67G(16)G(72)\Gamma(673). \quad (5.54)$$

Multiplying with $-iG(41)G(25)$ on the left, the polarization can be expressed as

$$P(345) = -iG(43)G(35) + i \int d12G(41)G(25)W(1^+2)P(312), \quad (5.55)$$

where the kernel GGW is a four-point function. We then introduce a four-point screened interaction

$$W(1234) \equiv W(12)\delta(13)\delta(24), \quad (5.56)$$

and the four-point P and W are connect by a Dyson equation as

$$P = P^0 - PWP^0, \quad (5.57)$$

where P^0 is the four-point IP-RPA polarizability. As for the modified polarizability in Eq. (5.48), there is an analogous *Bethe-Salpeter* equation for the four-point \tilde{P}

$$\tilde{P} = P^0 + P^0 K \tilde{P}. \quad (5.58)$$

The kernel K comprises the bare electron-hole exchange \tilde{v} and the screened electron-hole attraction $-W$ ⁵

$$K(1234) = \delta(12)\delta(34)\tilde{v}(13) - \delta(13)\delta(24)W(12). \quad (5.59)$$

The solution of the four-point \tilde{P} can be transformed to an eigenvalue problem associated with an *effective two-particle Hamiltonian*

$$\mathcal{H}_{(n_1 n_2)(n_3 n_4)} \equiv (\varepsilon_{n_2} - \varepsilon_{n_1})\delta_{n_1 n_3}\delta_{n_2 n_4} + (f_{n_1} - f_{n_2})K_{(n_1 n_2)(n_3 n_4)}, \quad (5.60)$$

where n_i refer to energy indexes of one-particle KS states. In practice, the static screening is used and the two-particle equation is reduced to

$$\begin{aligned} \sum_{n_3 n_4} \{(\varepsilon_{n_2} - \varepsilon_{n_1})\delta_{n_1 n_3}\delta_{n_2 n_4} + (f_{n_1} - f_{n_2}) [\tilde{v}_{(n_1 n_2)(n_3 n_4)} - W_{(n_1 n_2)(n_3 n_4)}]\} A_{\lambda}^{(n_3 n_4)} \\ = E_{\lambda} A_{\lambda}^{(n_3 n_4)}, \end{aligned} \quad (5.61)$$

where E_{λ} is the excitation energy.

⁵When the spin is considered, $K = 2\tilde{v} - W$.

It has been shown that the two-particle excitonic Hamiltonian can be formally separated into four blocks [71]

$$\mathcal{H}^{\text{exc}} = \begin{pmatrix} \mathcal{H}^{\text{res}} & \mathcal{H}^{\text{cpl}} \\ -[\mathcal{H}^{\text{cpl}}]^* & -[\mathcal{H}^{\text{res}}]^* \end{pmatrix}. \quad (5.62)$$

The resonance part \mathcal{H}^{res} contains the transitions at positive absorption energies ω , which is defined as

$$\mathcal{H}_{(vc)(v'c')}^{\text{res}} = (\varepsilon_c - \varepsilon_v)\delta_{vv'}\delta_{cc'} + K_{(vc)(v'c')}, \quad (5.63)$$

where c and v denote the conduction and valence states, respectively. The coupling part is symmetric, and it describes the interaction between the resonant and antiresonant parts, *i.e.* the electron-hole pairs at both positive and negative energies

$$\mathcal{H}_{(vc)(v'c')}^{\text{cpl}} = K_{(vc)(\overline{v'c'})}, \quad (5.64)$$

where the electron-hole antipairs are denoted by $\overline{v'c'}$. While the two-particle \mathcal{H}^{exc} is generally not Hermitian, the resonant part is Hermitian. Therefore in the *Tamm-Dancoff approximation* (TDA), the \mathcal{H}^{exc} is approximated by its resonant part and the effect of the coupling is neglected. The macroscopic dielectric function in the TDA can be expressed as

$$\varepsilon_{\text{M}}(\omega) \equiv 1 - \lim_{\mathbf{q} \rightarrow 0} \sum_{\lambda} \frac{\left| \sum_{vc, \mathbf{k}} \langle v, \mathbf{k} - \mathbf{q} | e^{-i\mathbf{q}\mathbf{r}} | c, \mathbf{k} \rangle A_{\lambda}^{vc, \mathbf{k}} \right|^2}{E_{\lambda} - \omega}. \quad (5.65)$$

Although the TDA is now becoming a standard method to study excitations in nanostructures [91–93], defects in solids [94] and molecules [95], the neglect of the coupling part might shift the absorption peak to higher energy [96], and the TDA could eventually break down for nanostructures where the confined optical excitation has a mixed excitonic-plasmonic behavior [97]. Hence, full BSE calculations including the coupling part are always desirable.

To this point, we have reviewed all the first-principles techniques that are used to study the molecule-surface interfaces in this thesis. Before preceding to the results, we should be aware of the fact that there is no *all-in-one* first-principles method for all types of properties in realistic calculations. One will be definitely thwarted by the huge and unrealistic amount of computation time and memory if everything is carried out with the highest level of theory. We now sketch the basic strategy in dealing with different properties with the corresponding level of theory. The ground-state properties, such as structural parameters and adsorption geometries can already be well described within the KS-DFT using hybrid functionals. The long-range dispersion force in weakly bound systems are taken into account by either DFT-D or vdW-DF. The *GW* approximation, being a dynamical theory, is able to provide an accurate prediction of the fundamental band gap and dynamic correlations. Finally, the BSE is an indispensable tool to include the electron-hole interaction for the excitation properties.

Part II

**Gas-phase Molecules and Bulk
Insulators**

6 Benzoic Acid and Its Phenolic Derivatives

6.1 Ground-state Geometries

The representative organic molecules studied in this work is benzoic acid and its phenolic derivatives. Their molecular structures are shown in Fig. 6.1. Benzoic acid ($\text{C}_6\text{H}_5\text{COOH}$) is the simplest aromatic carboxylic acid, with one carboxylic group attached to an aromatic ring. BA can be functionalized to hydroxybenzoic acids, namely salicylic acid (SA) or *para*-salicylic acid (*p*-SA) by attaching one phenolic group to the *ortho*- or *para*- position with respect to the carboxylic group¹. All molecules are flat due to sp^2 hybridization over the benzene, carboxylic and phenolic groups.

The ground-state structural parameters of these molecules are calculated with the PW1PW hybrid functional (See Sec. 3.4.3) in the localized basis set as implemented in CRYSTAL06 [98]. The C, O, and H atoms of the molecules are expanded by Pople-type 6-31G(*d*) basis sets². The values for the intramolecular bond lengths are given in Table 6.1. The results given by the PW1PW hybrid functional are in accord with the experimental values.

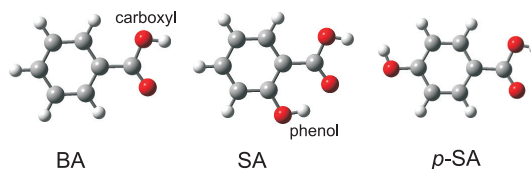


Figure 6.1: Structures of benzoic acid, salicylic acid, and *para*-salicylic acid. The red (black), gray, and small white atom represent oxygen, carbon, and hydrogen, respectively.

6.2 Electronic Structures

Apparently, the electronic properties of the benzoic acid should be affected by the presence of the phenolic group. This is evidenced experimentally by the occupied electronic states of these acids in condensed films as resolved by ultra-violet photoemission spectroscopy (UPS) [101]. We show in Table 6.2 both PW1PW calculations and UPS results of the frontier orbital energies. A first impression from the comparison is that the separation between HOMO and HOMO-1 by PW1PW functional is in agreement with UPS, whereas the discrepancy becomes larger for the HOMO-3 energy with respect to the HOMO. In addition, the presence of phenolic OH in SA and *p*-SA changes the intramolecular interaction and leads to a larger separation between HOMO and HOMO-1

¹The alternative (IUPAC) names for SA and *p*-SA are 2- and 4-hydroxybenzoic acid, respectively.

²One can refer to Appendix E for a detailed description of the basis set.

Table 6.1: Intramolecular bond lengths (Å) of benzoic acid, salicylic acid and *para*-salicylic acid. The C–C is the average values of the six bond lengths between neighboring carbon atoms over the aromatic ring.

	BA		SA		<i>p</i> -SA
	PW1PW	Expt. ¹	PW1PW	Expt. ²	PW1PW
C–C	1.394	1.388	1.399	1.385	1.395
C–C _{carb.}	1.482	1.484	1.460	1.457	1.475
C _{carb.} –O _{carb.}	1.351		1.341	1.307	1.353
C _{carb.} =O _{carb.}	1.213		1.231	1.234	1.214
O _{carb.} –H	0.974		0.974	1.000	0.973
C–O _{phenol}			1.336	1.358	1.354
O _{phenol} –H			0.990	1.029	0.968

¹ Reference [99].² Reference [100].**Table 6.2:** Frontier molecular orbital energies (eV) of BA, SA and *p*-SA calculated with the PW1PW hybrid functional. The energies are shifted so that the HOMO energy is zero.

	BA		SA		<i>p</i> -SA	
	PW1PW	Expt. ¹	PW1PW	Expt. ¹	PW1PW	Expt. ¹
LUMO	5.81		4.79		5.36	
HOMO	0.00	0.00	0.00	0.00	0.00	0.00
HOMO-1	-0.05	-0.18	-1.04	-1.00	-0.81	-0.73
HOMO-2	-0.37		-1.67		-0.97	
HOMO-3	-1.55	-2.36	-2.82	-3.10	-2.10	-2.58

¹ Reference [101].

than that of BA. While the unoccupied states are not accessible from UPS, the PW1PW calculations suggest that SA has the smallest HOMO-LUMO gap among all three acids, and the gap for *p*-SA is the largest.

However, in the absence of experimental data of the gap, it is unclear how reliable the PW1PW functional is for the electronic structure of hydroxybenzoic acids. It is thus tempting to extend the calculations to the *GW* approximation since in principle an accurate energy gap can be obtained by the quasiparticle energies from *GW* calculations. Here we briefly introduce the scheme and parameters for the one-shot G_0W_0 calculations. The LDA orbitals and eigenvalues are used as the input to the quasiparticle corrections. The LDA calculations are performed in a plane-wave basis set with norm-conserving pseudopotentials implemented in ABINIT [102]. The molecules are confined in a box with the dimension of $30.0 \times 30.0 \times 24.0$ Bohr³, which is repeated periodically in *x*, *y* and *z* directions. The \mathbf{k} point is sampled at the Γ point, and the cut-off energy for the kinetic energy is 70 Ry (952 eV). In the subsequent G_0W_0 calculations, the slowly decaying Coulomb potential between the periodic images is corrected with a box-like cutoff ($20.0 \times 20.0 \times 10.0$ Bohr³) [103]. We include over 450 empty states in the evaluation of the polarizability and the Green's function for the self-energy. 2×10^5 reciprocal lattice \mathbf{G} vectors (equivalent to a cut-off energy of about 68 Ry) are included in the calculation of the exchange self-energy. The plasmon pole approximation is used to calculate the RPA response function, and 3000 \mathbf{G} vectors (4 Ry) are included to account for the local-field effect. The quasiparticle gap is converged within 0.1 eV with these parameters. The *GW* (and BSE) calculations are carried out with the YAMBO package [104].

The molecular orbital energies from LDA, PW1PW and $G_0W_0^{\text{LDA}}$ are compiled in Fig. 6.2. It is not surprising that LDA predicts too small HOMO-LUMO gap for all molecules. More seriously, LDA gives a wrong order of the three highest occupied orbitals of BA when compared to the hybrid functional and G_0W_0 calculations. Both PW1PW and G_0W_0 predict that the HOMO and HOMO-1 are delocalized bonding-states of the cyclic benzene ring for all the three molecules. These two orbital levels are almost degenerate, which is very similar to the benzene molecule. However, LDA instead predicts the highest occupied state as a non-bonding state, where the electron density is localized around the carboxylic group. This is indeed the consequence of the *self-interaction* in the local and semilocal approximations of KS-DFT, which is discussed in Sec. 3.4.2. The self-interaction in LDA has a tendency to delocalize the electrons, and as a result the localized electronic states are often put too high in energy. In fact, we see from Fig. 6.2 that the energy separation between the two highest π orbitals can be well described at the level of LDA because the delocalized states are usually much less influenced by the self-interaction error. On the other hand, the LDA orbital energies of the localized state at the carboxylic group, *i.e.* the HOMO-2 in the PW1PW and G_0W_0 calculation, are consistently blue shifted by about 0.6 eV for all the three molecules. This is clearly an effect of the self-interaction.

It is a relief to see that the Hartree-Fock exchange in the PW1PW hybrid functional indeed improves the spurious self-interaction, and the PW1PW orbital characteristics and the energies for the occupied states are in line with the G_0W_0 results. Being a

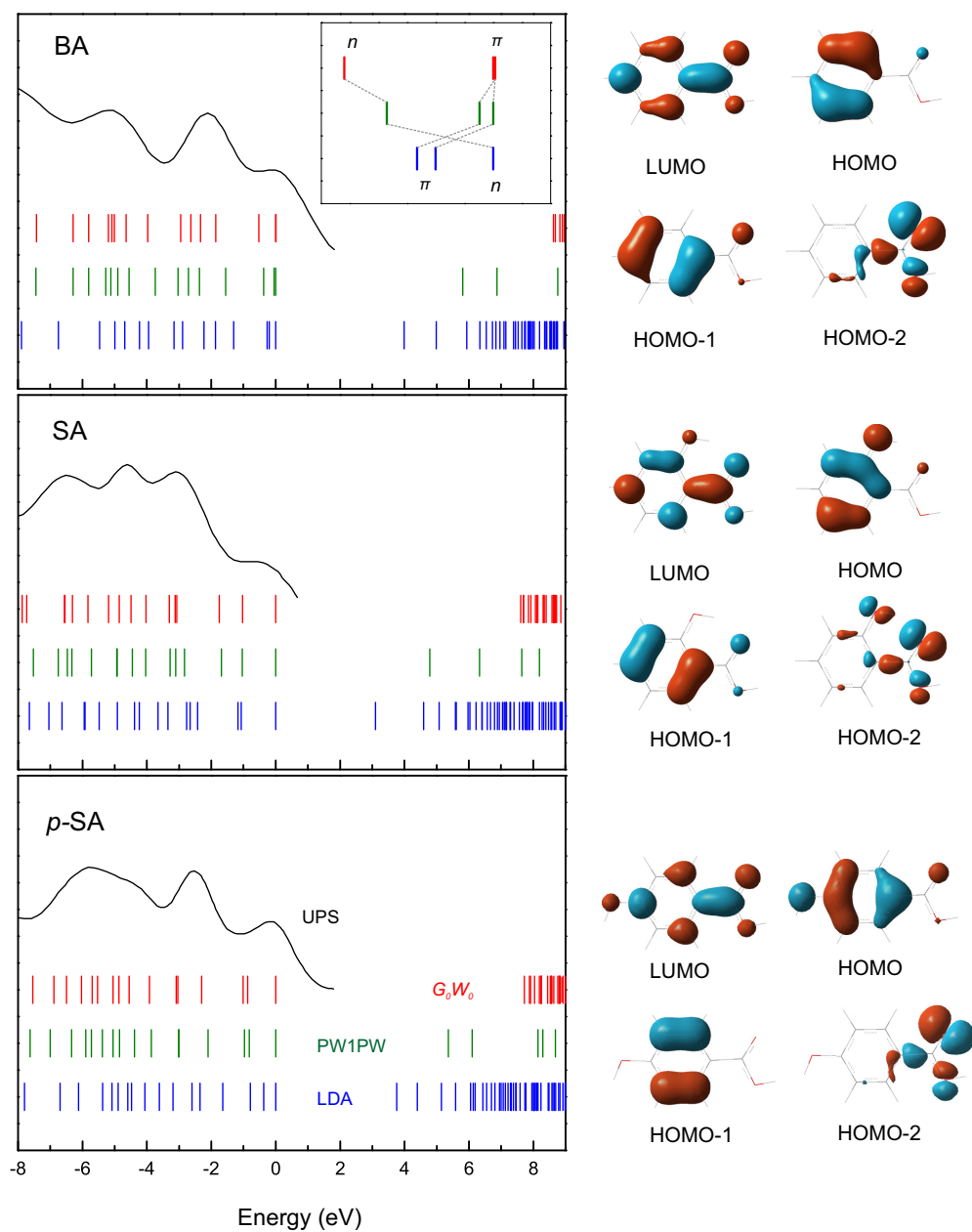


Figure 6.2: Molecular orbital energies of various hydroxybenzoic acids calculated with PW1PW, LDA and $G_0W_0^{LDA}$. The three highest occupied states for BA are highlighted in the inset. The UPS data is from Ref. [101]. The highest occupied states are aligned to zero energy. The electron density of LUMO and three highest occupied MOs from hybrid functional calculations are presented in the right panel.

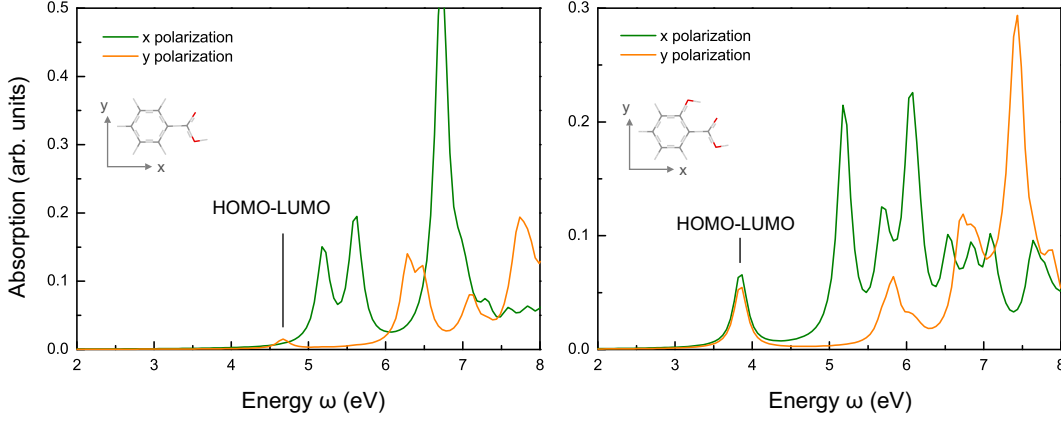


Figure 6.3: Optical absorption spectra $\Im m \epsilon_M(\omega)$ for BA (left) and SA (right) molecules. The spectra are broadened by an artificial Lorentzian of 0.1 eV.

dynamic theory, the G_0W_0 yields quasiparticle energies in quantitative agreement with the UPS experiment. In particular, the HOMO–3 levels for all molecules by $G_0W_0^{LDA}$ align well with the UPS peaks. The HOMO–3 is also a localized non-bonding state at the carboxylic group, with a different molecular orbital symmetry than the HOMO–2. Hence, it is reasonable to assert that the self-interaction error is further suppressed in GW calculations. Nevertheless, in overall PW1PW gives a good account of the occupied states.

Moving to the unoccupied states, we find the quasiparticle energy corrections to the HOMO and LUMO are rather substantial. An interesting observation is that the quasiparticle correction to the LUMO+2 is about 2 eV smaller than the LUMO and LUMO+1 in the present calculations. Instead of the π^* anti-bonding character of the LUMO and LUMO+1, the wavefunction of the LUMO+2 is largely delocalized away from the molecule, a sign of a Rydberg orbital. We mentioned in Sec. 3.4.2 that the Rydberg state is not correctly described by the LDA because of the unrealistic exponential decay of the potential in the long-range. As a result, for the BA and the *p*-SA, the quasiparticle energy of the LUMO is marginally higher than that of the LUMO+2. The quasiparticle energy gap, *i.e.* the difference between the electron removal and affinity energy now amounts to 8.63, 7.62, and 7.88 eV for BA, SA, and *p*-SA, respectively. These values are about twice as large as the LDA gap, and even the PW1PW hybrid functional underestimates the fundamental gap to a large extent when referenced to the G_0W_0 gap (See Table 6.2). To wrap up, we find that LDA not only gives a too small HOMO-LUMO gap but could also distort the spectrum for the occupied orbitals. Therefore, hybrid functional is necessary for physical interpretations of the molecules.

6.3 Molecular Excitonic Effect

When comparing the GW gaps of the molecules to the lowest optical peaks from the available UV/visible optical spectra, one finds that the discrepancies are enormous. For example, the lowest two excitation states of BA appear at 4.55 and 5.38 eV in optical spectra [105]. However, the quasiparticle gap from GW approximation reaches over 9 eV. As for SA, the quasiparticle energy gap is also much larger than the observed optical peak around 4.0 eV [106]. These findings lead to an assumption that the bound electron-hole interaction must play an important role in the optical absorption if the GW fundamental gap is reasonable. Therefore, we conduct the two-particle BS equation within the Green's function method to explicitly evaluate the *excitonic effect* in the optical process of these molecules. We take BA and SA as the subjects because a direct comparison to experiment is possible. The BSE calculation requires the quasiparticle corrections of the $G_0W_0^{\text{LDA}}$ results. The two-particle excitonic Hamiltonian includes both resonant and coupling parts, as the Tamm-Dancoff approximation using only the resonant part of the excitonic Hamiltonian has been found to affect the excitonic peak position and the spectral lineshape in molecular systems [96, 97]. In the present study, we find that the lowest excitation peak using the TDA tends to shift to higher energy by about 0.1 eV with respect to the full BSE calculation. A comparison between the TDA and the full BSE calculation on the optical absorption of BA and SA is given in Appendix A. The static screened Coulomb potential (with a cut-off of 4 Ry) is used as the effective electron-hole interaction in the BSE calculations. We use a cut-off of 2 Ry (about 1000 \mathbf{G} vectors) for the screened interaction W , and a cut-off of 68 Ry (2×10^5 \mathbf{G} vectors) for the exchange component \tilde{v} . Electron-hole pairs involving the transitions in an energy window of 33.2 eV are considered in the BSE kernel (Eq. 5.60), and this ensures that the absorption spectra are well converged.

The absorption spectra $\text{Im}\epsilon_{\text{M}}(\omega)$ in Fig. 6.3 indeed show excellent agreement with optical spectra in terms of the lowest excitation peak. The difference between the BSE calculations and experimental optical peaks are within 0.15 eV. The lowest excited states for both BA and SA correspond to the singlet excitations from HOMO to LUMO, *i.e.* the transitions from the bonding state to the antibonding state of the aromatic ring. This can be visualized by the excitonic wavefunction in Fig. 6.4, as the excitonic wavefunction resembles to that of the LUMO (Fig. 6.2) if an electron is removed from the HOMO.

The binding energy E_{b} of the bound electron-hole is defined as the energy difference between the continuum state and the exciton state

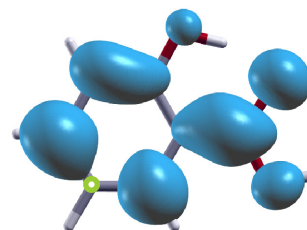


Figure 6.4: Excitonic wavefunction of the lowest singlet exciton of SA molecule. The position of the hole (*i.e.* the removed electron) is indicated by a circle.

$$E_{\text{b}} = E_{\text{g}} - E_{\text{exc}}, \quad (6.1)$$

where E_g is the quasiparticle energy gap, and E_{exc} refers to the exciton energy. The exciton binding energy of the lowest excited state of BA is $8.8 - 4.6 = 4.2$ eV³, and it amounts to $7.6 - 3.8 = 3.8$ eV for SA. Therefore, both molecules show substantial exciton binding energies, whose magnitudes are about half of the fundamental gap. The electron-hole pair is thus very strongly bound, and the exciton is spatially localized at the aromatic benzene ring. The strong excitonic effect is an important feature of the benzoic acid and its phenolic derivatives.

³Here 8.8 eV is the quasiparticle energy difference between the π and π^* states.

7 NaCl and KCl

7.1 Structural Parameters

In this section, we first examine the bulk properties of NaCl. The NaCl crystal structure is face-centered cubic (space group $Fm\bar{3}m$). The equilibrium lattice constant (a_0), bulk modulus (B_0) and lattice energy (E_l) are calculated and compared to experiment, which are summarized in Table 7.1. We use the 8-511G and 86-311G split-valence basis sets for Na and Cl [107], respectively.¹ The cell parameters of bulk NaCl have been fully optimized using the Broyden-Fletcher-Goldfarb-Shanno (BFGS) algorithm. A fine Monkhorst-Pack (MP) \mathbf{k} -point mesh of $8 \times 8 \times 8$ was employed, corresponding to 29 k -points in the IBZ of the primitive unit cell. The energy convergence criteria for self-consistent field (SCF) calculation is 10^{-7} hartree. Geometry optimizations is considered as converged when the residual force is below 0.0003 Hartree/Bohr.

The lattice constant and bulk modulus are calculated with several functionals, including HF method, GGA-PW91 functional, and two hybrid functionals, namely B3LYP [108] and PW1PW. It is found that the lattice constant predicted by PW1PW (5.68 Å) is closest to experiment with a slight overestimation of 0.7%. It should be kept in mind that the experimental a_0 measured at room temperature includes zero-point phonon effects, which usually show an expansion of 1% compared to the 0 K value for the ionic solids [109]. The bulk modulus is obtained by fitting the curve $E(V)$ with a strain (ϵ) matrix. PW1PW gives a more accurate description of the bulk modulus among all the methods, although the value is still underestimated by 6.0%. The lattice energy (E_l) of NaCl at zero Kelvin is defined as

$$E_l = E_{\text{NaCl}} - E_{\text{Na}^+} - E_{\text{Cl}^-}, \quad (7.1)$$

where E_{NaCl} , E_{Na^+} and E_{Cl^-} refer to the total energy of bulk NaCl, isolated Na and Cl ions, respectively. We see that although all methods are able to obtain reasonable lattice energies, the E_l calculated by PW1PW (8.00 eV) is again closest to the experimental value.

KCl shares the same crystal structure as NaCl. PW1PW hybrid function using the 86-511G basis sets for K yields a lattice constant $a_0 = 6.48$ Å, which is about 4.5% larger than experiment (6.20 Å) [113]. GGA-PBE² slightly improves over PW1PW, but the lattice constant is still about 4.1% too large. Hence, we find that the lattice constants of both NaCl and KCl are overestimated by GGA and hybrid functionals.

¹The detailed information of the basis sets is presented in Appendix E.

²The PBE calculations are performed using the PAW potential in a plane-wave basis set.

Table 7.1: Calculated equilibrium lattice constant (a_0), bulk modulus (B_0), lattice energy (E_l) and band gap (E_g) of NaCl.

Parameters	HF	PW91	B3LYP	PW1PW	Expt.
a_0 (Å)	5.79	5.72	5.73	5.68	5.64 ¹
B_0 (GPa)	22.9	24.2	24.9	25.0	26.6 ²
E_l (eV)	7.71	7.98	7.82	8.00	8.20 ³
E_g (eV)	14.00	5.40	7.00	7.15	8.5 ³

¹ Reference [110].² Reference [111].³ Reference [112].

7.2 Band Structure

7.2.1 KS-DFT Electronic Structure

Both NaCl and KCl are direct band-gap insulators. We show the band structure of NaCl in Fig. 7.1 as an illustration. From Table 7.1 we see that the band gap obtained with HF or the GGA functional is either far too wide or too narrow. Hybrid functionals are able to improve the band gap value, although it is still somehow underestimated. In particular, PW1PW yielded a band gap of 7.15 eV for bulk NaCl, which is in better agreement with experiment than B3LYP. The density of states (DOS) plotted in Fig. 7.1(b) gives some insights into the electronic structure. The projected density of states (PDOS) $\rho_m(\varepsilon)$ are defined as the projection of the KS eigenstates $|\psi_{n,k}\rangle$ onto a set of orthonormal state $|\phi_m\rangle$

$$\rho_m(\varepsilon) = \sum_{n,k} w_k |\langle \phi_m | \psi_{n,k} \rangle|^2 \delta(\varepsilon - \varepsilon_{n,k}), \quad (7.2)$$

where w_k is the \mathbf{k} -point weight, and the summation is performed over the band index n and \mathbf{k} -point index k . The NaCl valence band is essentially formed by 3p states of Cl atom, whereas the conduction band minimum is of Cl 4s character. The 3s states of Na has only marginal contribution to the conduction band. While this is on the contrary to common belief that the conduction band of NaCl consists of Na s state solely, recent calculations proved that the conduction band indeed has a predominant chlorine character [114]. The valence band width is 1.97 eV by PW1PW functional, comparable to the experimental value of 1.8 eV. The small band dispersion is an indication of strong ionic bonding between Na and Cl atoms. The ionic nature can also be evidenced by a Mulliken population analysis, in which the net atomic charges of Na and Cl are +0.972 and -0.972 e , respectively.

The band structure of KCl predicted by PW1PW closely resembles that of bulk NaCl. The valence band is mostly of Cl 3p character, and the lowest conduction band sees a mixture of the K 4s, and more significantly, the Cl 4s states. The PW1PW band gap amounts to 8.00 eV, about 0.7 eV smaller than experiment. GGA-PBE functional, on the other hand, severely underestimates the gap ($E_g^{\text{PBE}} = 5.04$ eV). Therefore, the

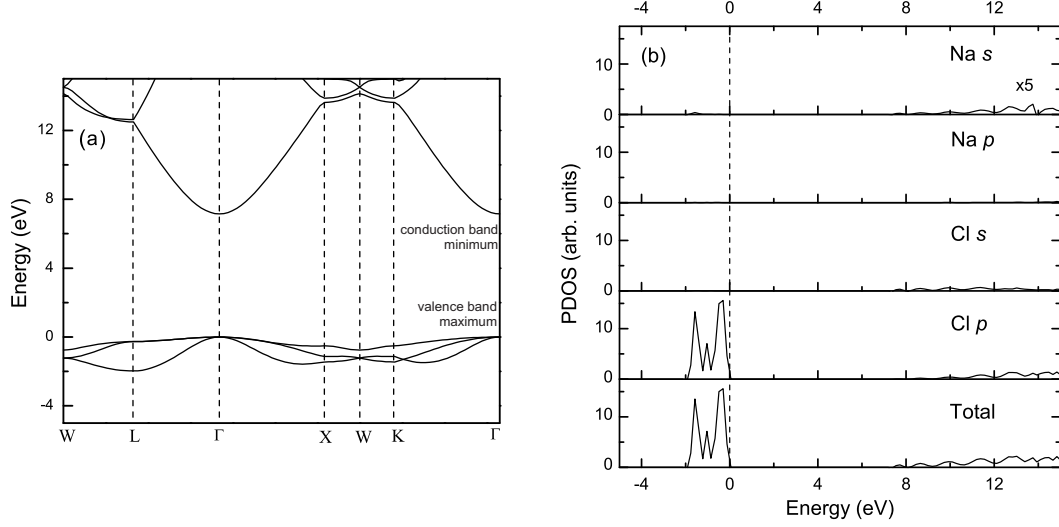


Figure 7.1: (a) Band structure of bulk NaCl and (b) total DOS and projected density of states (PDOS) onto the s and p states of Na and Cl, calculated with PW1PW functional. The top of the valence band is set to zero energy.

addition of the nonlocal HF exchange to the GGA exchange manages to correct the band gap to some extent, leading to a much closer agreement with experiment. We note that the valence bandwidth of KCl is 0.94 eV as predicted by PW1PW, about 1 eV smaller than that of NaCl. As the valence bandwidth is determined by second-neighbor p - p overlap, the smaller dispersion of the KCl valence band is a result of partial screening of the overlap, which stems from the higher degree of ionic bonding due to the higher electropositivity of K. This is also evidenced by the Mulliken population analysis that results in an absolute net atomic charge of KCl of 1.004 e for the ions, which is larger than that of bulk NaCl.

7.2.2 Quasiparticle Band Gap

Following the gas-phase molecules, we calculate the quasiparticle band structure of NaCl in G_0W_0 approximation on top of LDA eigenvalues and orbitals. The Na norm-conserving pseudopotential includes non-linear core correction. We use a cut-off energy of 80 Ry (1088 eV), and a $6 \times 6 \times 6$ MP \mathbf{k} -point mesh equivalent to 16 \mathbf{k} points in the IBZ. The LDA optimized $a_0 = 5.54$ Å is adopted as the lattice constant. The resulting band gap from LDA exchange-correlation functional is 4.95 eV.

In the subsequent G_0W_0 calculations, the state summation in the calculation of self-energy includes 124 empty bands, *i.e.* those states up to 112 eV above the VBM using LDA. Local field effect is taken into account via 230 \mathbf{G} vectors (with a cut-off energy of 12 Ry) in the RPA response function calculations. The $G_0W_0^{\text{LDA}}$ significantly corrects the underestimated band gap by the LDA exchange-correlation functional, shifting the VBM downward by 2.07 eV, and the CBM upward by 1.05 eV. This consequently gives

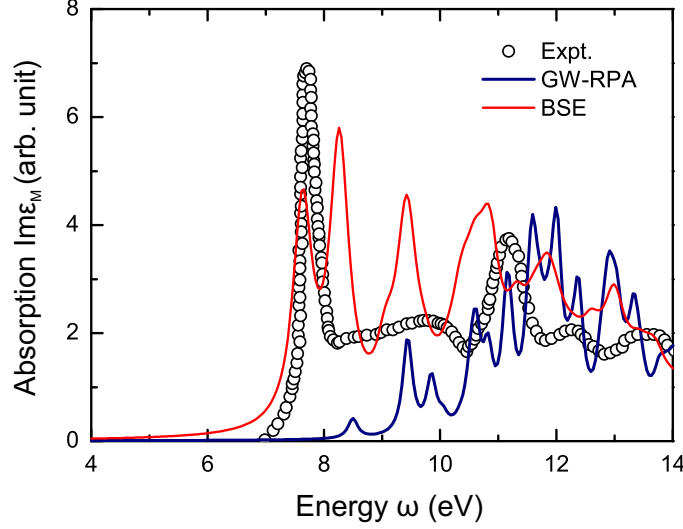


Figure 7.2: Absorption spectra of bulk NaCl calculated with independent particle RPA and BSE. The quasiparticle energies are obtained by rigid scissors shifts of the LDA eigenvalues to reproduce the experimental gap. A broadening of 0.1 eV is applied.

rise to a quasiparticle gap of 8.06 eV, about 0.4 eV smaller than the experimental gap. This is in accord to the general trend of the G_0W_0 calculations on top of LDA eigenvalues that the quasiparticle gaps are usually slightly underestimated [78].

7.3 Excitonic Effect

The lowest energy exciton in alkali halides is known as a tightly bound Frenkel exciton localized at the anion because of the small screening in between the electron-hole pair [115]. We calculate the macroscopic dielectric function of NaCl as an example in both independent particle RPA and two-particle BSE. The excitonic peak is dependent on the fundamental gap, and due to the underestimation of the quasiparticle gap by $G_0W_0^{\text{LDA}}$, we apply rigid scissors shifts to both the conduction band and valence band and reproduce the experimental band gap of 8.5 eV. We include 4 valence bands and 28 conduction bands in the evaluation of the BSE kernel, with 230 \mathbf{G} vectors (12 Ry) in the screened interaction and 4200 \mathbf{G} vectors (90 Ry) in the exchange interaction. The static dielectric function includes 530 \mathbf{G} vectors (23 Ry). It is obvious from Fig. 7.2 that the independent particle RPA using the shifted eigenvalues exhibits a blue-shift of the lowest excitation peak, which corresponds to the fundamental gap of NaCl. The BSE calculation correctly captures the lowest exciton peak as compared to the experimental room temperature spectrum [116], with calculated exciton binding energy of 0.9 eV. Apart from the position of the peak, the intensity and lineshape also change from the independent particle to the two-particle equation. Similar results have been also identified by Bechstedt [117]. At larger energies, the optical peaks from BSE calculations

deviate from the experimental peaks by a rigid shift of about 0.5 eV, which is possibly as a result of the crude scissors operation. We note that the optical spectra can be well described by the Tamm-Dancoff approximation (TDA) including only the positive energy electron-hole pairs in the excitonic Hamiltonian. The difference between the TDA and full BSE calculation in the absorption spectra is negligible.

Part III

Organic Molecules on Wide-gap Insulator Surfaces

8 Hydroxybenzoic Acids on Ideal NaCl(100)

After discussing the properties of the isolated molecules and alkali halides insulators, we now turn to the investigation of the molecule-insulator interfaces. This chapter is devoted to the adsorption of organic molecules, specifically the hydroxybenzoic acids on the perfect (100) surfaces of NaCl and KCl. As a first step, we will present the adsorption on NaCl(100) surface, discussing the properties of the surface, the adsorption configurations, and the roles of the long-range vdW interaction.

8.1 Properties of NaCl(100) Surface

We start with the surface energy calculation because it is the most basic thermodynamic quantity of a surface, and it is a good benchmark for various theoretical methods. The surface energy can be expressed as [118]

$$\gamma = \lim_{n \rightarrow \infty} E_s(n) = \lim_{n \rightarrow \infty} \frac{E(n) - n[E(n) - E(n-1)]}{2A}, \quad (8.1)$$

where $E(n)$ is the total energy of an n -layer slab, and A is the area of the primitive surface cell. The factor 2 accounts for the upper and lower surfaces of the slab. Thus $E_s(n)$ is the energy per unit cell area needed to form the surface from the bulk, and it converges to the surface energy per unit area as more layers are added. In this study up to 12 layers have been used to check the surface energy convergence, as is illustrated in Fig. 8.1. The calculated γ is 12.25 meV/Å², consistent with the results obtained by other functionals and earlier experiments [119]. The E_s shows a rapid convergence after three and more layers have been put together. In fact, the E_s difference between a 5-layer and 12-layer slab is only 0.08% of the γ value.

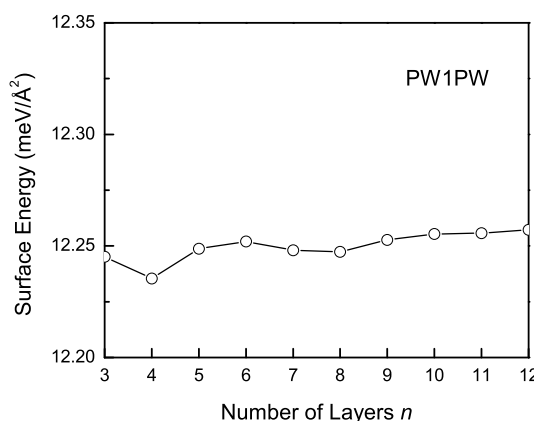


Figure 8.1: Surface energy of NaCl(100) calculated for various numbers of layers by PW1PW functional. The surface energy is well converged with 5 and more layers.

Table 8.1: The relaxation of the NaCl(100) surface with a 5-layer and 12 layer slab. The subscripts 1, 2 and 3 designate the first, second and third layer, respectively.

	Δz (Å)					
	Na ₁	Cl ₁	Na ₂	Cl ₂	Na ₃	Cl ₃
5-layer slab	−0.023	0.019	0.002	−0.003	0.000	0.000
12-layer slab	−0.023	0.020	0.003	−0.003	0.001	0.001

	Δ_i (Å)				
	1(Na–Cl)	2(Na–Cl)	3(Na–Cl)	Δ_{12} (%)	Δ_{23} (%)
5-layer slab	−0.021	0.003	0.000	−0.05	−0.02
12-layer slab	−0.022	0.003	0.000	−0.04	−0.03
Expt. ¹	−0.07	0.01	0.00	−1.4	0.1

¹ Reference [120].

The relaxation of NaCl(100) surface (see Tab. 8.1) induces small vertical displacements of Na and Cl atoms in the first and second layer of the slab, whereas there is almost no change for atoms in deeper layers. The average rumpling of the surface is calculated using the following relation

$$\Delta_i = \frac{1}{2}(\Delta_{z,\text{Na}(i)} - \Delta_{z,\text{Cl}(i)}) \quad (8.2)$$

where $\Delta_{z,\text{Na}(i)}$ and $\Delta_{z,\text{Cl}(i)}$ is the vertical displacement of Na and Cl in the i -th layer. It can be seen from the calculation that in the top layer the Na atom tends to move towards the bulk by 0.023 Å while the Cl atom relaxes away from the bulk by about 0.020 Å. The buckling of the surface atoms was also found in a low-energy electron diffraction (LEED) experiment [120], but the rumpling observed by LEED is larger. It is obvious that the buckling of surface atoms also affects the interlayer distance. The change of the interlayer distance $\Delta_{i,i+1}$ is defined as

$$\Delta_{i,i+1} = \frac{\Delta_{z,\text{Na}(i)} + \Delta_{z,\text{Cl}(i)} - \Delta_{z,\text{Na}(i+1)} - \Delta_{z,\text{Cl}(i+1)}}{a_0}, \quad (8.3)$$

where a_0 is the equilibrium lattice constant of NaCl. According to both the calculation and LEED the distance between the upper two layers is reduced after relaxation. Small buckling of atoms in the second and third layer leads to much smaller changes in the interlayer spacing between these two layers. In addition, the results obtained from the 5-layer slab agree quite well to the 12-layer slab. Therefore we will use a 5-layer supercell slab for the study of adsorption on perfect NaCl(100).

Before proceeding to the next section, we give a glimpse into the electronic structure of NaCl(100) surface. Fig. 8.2(a) shows the band structure of NaCl(100) obtained from a relaxed 5-layer slab. The unrelaxed (100) slab exhibits a very similar electronic structure

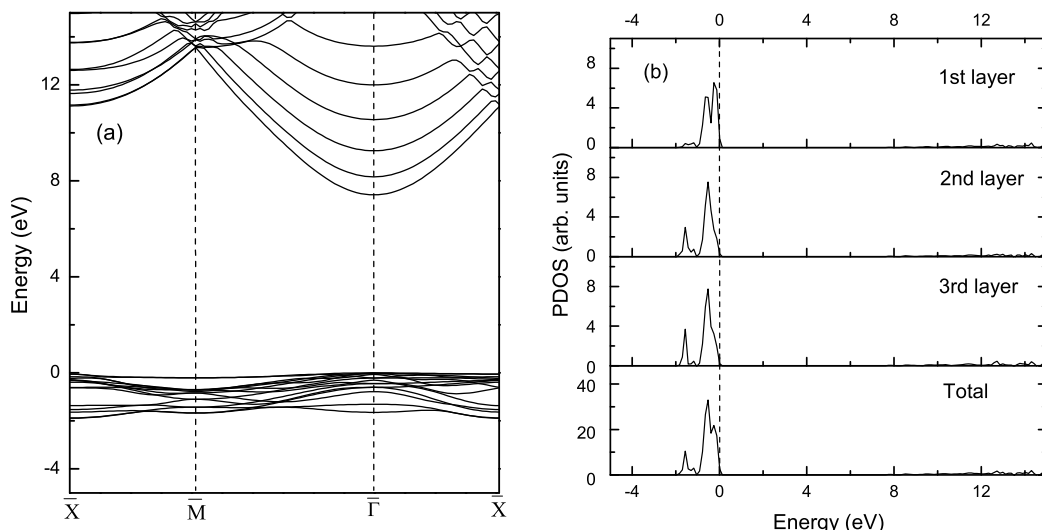


Figure 8.2: (a) Band structure and (b) DOS of a 5 layer NaCl(100) slab calculated using the PW1PW functional. The top of the valence band is shifted to energy zero.

because of the small relaxation and rumpling at the surface. The electronic structure of NaCl(100) surface is qualitatively identical to that of the bulk. The calculated surface band gaps are 7.41 eV and 7.20 eV obtained from the 5-layer and 12-layer slab, respectively. This, however, is contradictory to the common belief that band gap of the ionic surface should be smaller than that of the bulk due to the decreased Madelung potential at the surface. For reference, we calculated the electronic structure of a thicker slab consisting of 30 layers of atoms, and obtained a band gap of 7.15 eV, the same as the bulk value. This is in agreement with previous DFT calculations based on the plane wave pseudo-potential approach, where the band gaps for both the bulk and the (100) surface were found to be identical [119]. One can see from the layer-resolved DOS of a 5-layer slab in Fig. 8.2(b) the narrowing of the valence band width in the first layer, as well as a small shift of the peaks to the valence band maximum. The second and third layers, however, already exhibit bulk-like electronic properties.

8.2 Adsorption of Benzoic Acid and Its Phenolic Derivatives on NaCl(100)

8.2.1 Adsorption Configurations

The adsorption geometries of various benzoic acids on NaCl(100) are obtained from an initial configuration where the molecules are placed at different positions on the surface with a vertical separation distance of about 2.5 Å, followed by subsequent BFGS updates. It is reasonable to start the optimization from a parallel configuration with a molecule lying flat on the surface, as is suggested by previous experiments [16, 101].

Table 8.2: Adsorption energies, representative bond lengths and charge transfer to the adsorbates for adsorption on NaCl(100). The subscripts c and p denote atoms in carboxylic and phenolic group, respectively (see Fig. 8.3).

	Bond lengths d (Å)				
	Na–O _{1,c}	Na–O _{2,c}	Na–O _p	Cl–H _c	Cl–H _p
BA	2.74	2.37		2.18	
SA	3.25	2.37	2.50	2.31	2.97
p -SA	3.16	2.32		2.44	

	Adsorption Energy (eV)		Charge (e)
	E_{ads}	$E_{\text{ads}}^{\text{BSSE}}$	
BA	-0.60	-0.43	0.021
SA	-0.70	-0.48	0.001
p -SA	-0.61	-0.41	0.016

The adsorption is modeled by a two-sided adsorption on a 3×3 supercell with five-layer-thick slab including 90 atoms. The final adsorption geometries for BA, SA and p -SA on NaCl(100) are shown in Fig. 8.3. The adsorption energy, which is given in Table 8.2, is calculated according to the definition

$$E_{\text{ads}} = E_{\text{M/NaCl}} - E_{\text{NaCl}} - E_{\text{M}}, \quad (8.4)$$

where $E_{\text{M/NaCl}}$, E_{NaCl} and E_{M} denote the total energy of the adsorbed system, NaCl(100) and the isolated molecule, respectively. It is necessary to include the basis set superposition error (BSSE) correction for the adsorption energy in all calculations using the localized basis set. The BSSE corrected adsorption energy calculated using the usual counterpoise scheme is expressed as [62]

$$E_{\text{ads}}^{\text{BSSE}} = E_{\text{ads}} + (E_{\text{NaCl}} - E_{\text{NaCl}||\text{M}}) + (E_{\text{M}} - E_{\text{M}||\text{NaCl}}), \quad (8.5)$$

where E_{ads} (E_{NaCl}) is the energy of the NaCl(100) surface (adsorbate molecule) at its optimized adsorption geometry, and $E_{\text{NaCl}||\text{M}}$ ($E_{\text{M}||\text{NaCl}}$) is the energy of NaCl(100) (adsorbate molecule) with optimized geometry including ghost basis functions on the molecule (surface). As shown in Table 8.2, the BSSE correction to the adsorption energy amounts to about 0.2 eV, nearly 30% of the uncorrected adsorption energy.

We see from Fig. 8.3 that all three molecules bind to the surface through the interaction between a surface Na atom and the carboxylic oxygen. For SA, an additional bonding between Na and the phenolic oxygen is present. Moreover, the carboxylic hydrogen points downward to the surface Cl as a result of the interaction between these two atoms. Some representative bond lengths for the adsorption geometries are presented in Table 8.2. Overall, the bindings between various benzoic acids and NaCl(100) surface are quite weak. The adsorption energy for SA (0.48 eV) is largest among these three

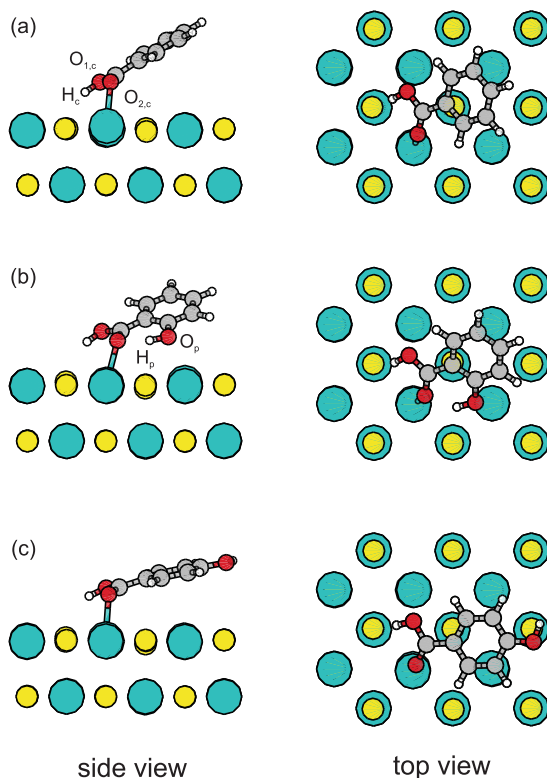


Figure 8.3: Adsorption geometries of (a)BA, (b)SA and (c)*p*-SA on the NaCl(100) surface. Only the top two layers of NaCl(100) are shown in the side views. Sodium and chlorine atoms are shown in green (dark grey) and yellow (light grey), whereas oxygen, carbon and hydrogen atoms of the adsorbates are shown in red (black), grey and white, respectively.

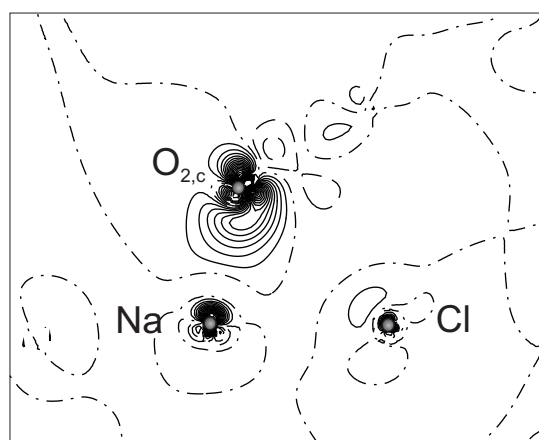
molecules because of the additional interaction between phenolic oxygen and surface sodium atoms. Indeed this additional Na-O interaction makes the SA tilted so that the aromatic ring is slightly rotated. It is noteworthy that all molecules still remain planar upon adsorption, and the intramolecular structure distortion shown in Table 8.3 is very small, which is in accord to experiment [16]. The contraction or expansion of the intramolecular bond lengths reflect how the molecule interacts with the surface. For instance, the expansion of the intramolecular hydrogen bond $O_{2,c} - H_p$ is a consequence of the interactions between $Na - O_{2,c}$ as well as $Cl - H_p$. In addition, we find that the dissociative adsorption where the carboxylic hydrogen is detached from the molecule is thermodynamically unfavorable compared to the molecular adsorption.

The charge density difference map shown in Fig. 8.4 reveals more details of the bonding between functionalized benzoic acids and NaCl(100). Here we use SA as an example and the nature of the bonding is qualitatively the same for both BA and *p*-SA. In Fig. 8.4 major electron accumulation can be seen in the region between the carboxylic O atom and the surface Na atom. Yet, most of the electrons forming the bond are

Table 8.3: Changes of intramolecular bond lengths Δd (in %) for various benzoic acids adsorbed on NaCl(100).

	carboxyl			phenol		
	C–O ₁	C–O ₂	O ₁ –H	C–O	O–H	O ₂ –H _p
BA	0.64	-0.57	1.58			
SA	0.42	-0.84	1.22	0.98	-0.01	1.93
<i>p</i> -SA	0.77	-0.79	1.00	-0.30	0.02	

contributed by the lone-pair electrons from carboxylic oxygen, which makes the bonding character *covalent*, or more specifically, a dative bond. The charge transfer is evaluated by Mulliken population analysis, as given in Table 8.2. It shows that there is a very small amount of electrons transferred to the benzoic acids upon adsorption. Although the partition of electrons based on the Mulliken population is rather arbitrary and basis set dependent, this small charge transfer is still expected in the context of the small intramolecular distortion of these molecules as well as of their low binding energies to the surface. Meanwhile, one should also recognize that the ionic contribution, *i.e.* the electrostatic interaction must take place in between the Na cation and the carboxylic O of the molecule. In the next section, we discuss the nature of the (short-ranged) binding in terms of the projected density of states and the renormalizations of the molecular orbitals upon adsorption.

**Figure 8.4:** Change in electron density for Na–O bonding after SA adsorption on NaCl(100). The solid and dashed lines represent electron accumulation and depletion, respectively. The dashed-dotted line indicates zero. The difference between adjacent lines is 0.015 e/Bohr^3 .

One important aspect missing so far is the long-range dispersion forces between the delocalized π electrons from the molecules and the surface. As pointed out in Sec. 3.5,

this is out of scope of the semilocal PW91 correlation functional. We will discuss the effect of the vdW interaction in Ch. 9, but at this moment we should be aware of the fact that the short-ranged chemical interactions (either covalent or electrostatic interaction) are not affected by the vdW force for the adsorption of benzoic acids on NaCl(100).

8.2.2 Electronic and Binding Properties

The effect of various benzoic acids on the electronic structure of the adsorbed NaCl(100) is illustrated in Fig. 8.5. It is evident from the band structures that the effective band gap of the adsorbed surface is now dependent on the distance between the HOMO and LUMO of the adsorbate. The calculated band gaps are 5.68, 4.86 and 5.16 eV for BA, SA and *p*-SA adsorbed NaCl(100), respectively. Another eminent feature shown in the PDOS in Fig. 8.5 is the broadening and splitting of some occupied molecular orbitals of the adsorbate. In order to get a closer view of the electronic properties, a blow-up of the DOS projected on SA upon its adsorption on NaCl(100) is given in Fig. 8.6. It is evident that molecular orbital splitting occurs for HOMO-1, HOMO-2 and HOMO-3 of the adsorbate, while HOMO-2 exhibits a large band broadening. As clearly seen from the electron density isosurfaces, the electrons of HOMO-2 and HOMO-3 are mainly located at the in-plane p_{xy} and out-of-plane p_z orbitals of the carboxylic O atom. Apart from the appreciable π electron density of the benzene ring, HOMO-1 also exhibits a small but non-negligible electron density on the carboxylic O atom. These broadenings and splittings are the signals of the *rehybridizations* in the frontier orbitals including HOMO-2, HOMO-3, and to some extent HOMO-1 during the covalent interactions. Similar features have been found when 4-hydroxy-thiophenol is adsorbed on NaCl(100) [121].

The molecular orbital shifts and broadenings of the adsorbate are addressed in the Newns-Anderson model [122, 123]. In principle, the Newns-Anderson model applies to the adsorption of atoms and molecules on metallic surfaces, but we will see that this also applies to the BA-NaCl interface. The projected density of states $n_a(\varepsilon)$ onto a single valence state of an adatom (or a molecule) according to the Newns-Anderson model can be expressed as

$$n_a(\varepsilon) = \frac{1}{\pi} \frac{\Delta(\varepsilon)}{[\varepsilon - \varepsilon_a - \Lambda(\varepsilon)]^2 + \Delta^2(\varepsilon)}, \quad (8.6)$$

with

$$\Delta(\varepsilon) = \pi \sum_k |V_{ak}|^2 \delta(\varepsilon - \varepsilon_k) \quad (8.7)$$

and

$$\Lambda(\varepsilon) = \frac{1}{\pi} \mathcal{P} \int d\varepsilon' \frac{\Delta(\varepsilon')}{\varepsilon - \varepsilon'}. \quad (8.8)$$

Here, the subscripts a and k refer to the adatom and the surface, respectively. V_{ak} is the interaction between the surface and adatom states. \mathcal{P} denotes the Cauchy principle value. In case of the *weak chemisorption*, the interaction V_{ak} is much smaller than the

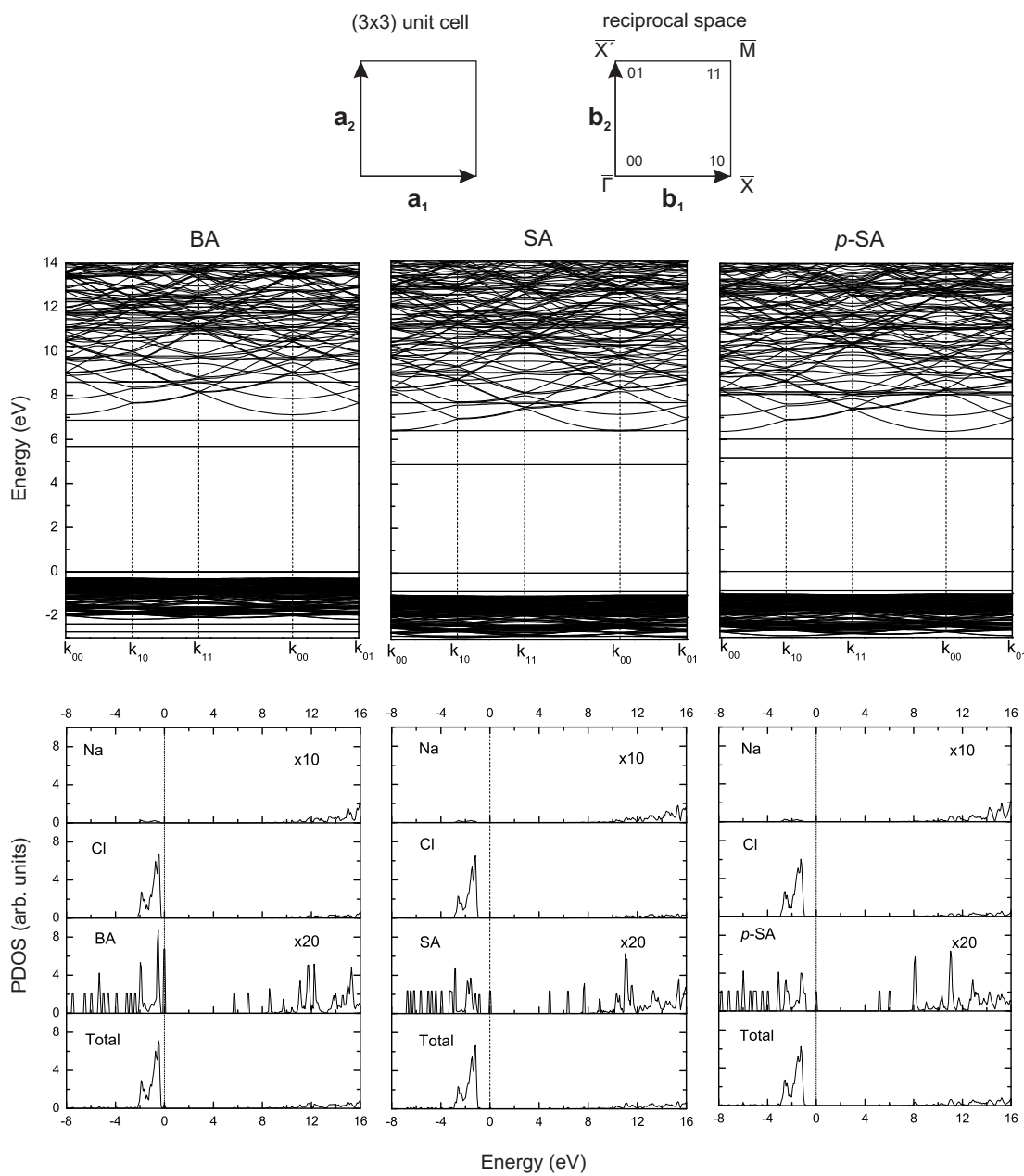


Figure 8.5: Band structures (top row) and PDOS (bottom row) of BA, SA and *p*-SA adsorbed on NaCl(100) using the PW1PW functional. The respective HOMOs are set to energy zero.

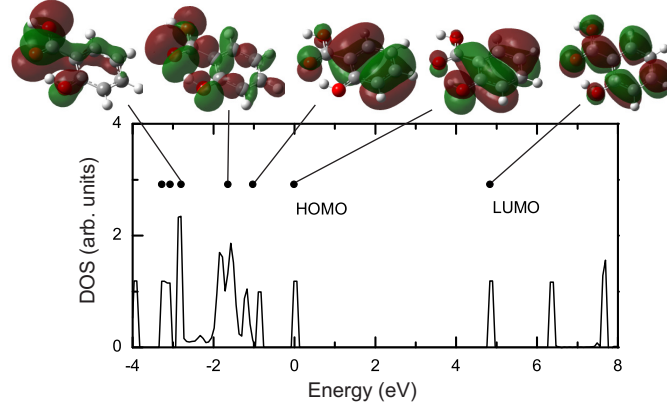


Figure 8.6: PDOS of SA upon adsorption on NaCl(100). The solid dots correspond to the energy levels of an isolated SA molecule at the adsorption geometry for direct comparison. The electron density isosurfaces of five frontier orbitals are also given. The HOMO is aligned to energy zero.

bandwidth of the surface W , and we have

$$\Delta(\varepsilon) \approx \pi \sum_k |V_0|^2 \delta(\varepsilon - \varepsilon_k) = \pi V_0^2 n_k(\varepsilon), \quad (8.9)$$

where V_0 is the averaged value of V_{ak} , and $n_k(\varepsilon)$ is the density of states of the unperturbed surface. n_k and accordingly Λ can be considered as energy-independent, and n_a turns into a Lorentzian broadening of the valence states centered on ε_a . In other words, the single valence state of the adsorbate is broadened into a *resonance* with a finite lifetime Δ^{-1} . When the adatom-surface coupling increases and $V_{ak} > W$, two localized states appear outside the continuous spectrum, which are given by the roots of $\varepsilon - \varepsilon_a - \Lambda(\varepsilon) = 0$. This is equivalent to the splitting of the adsorbate valence state into a bonding and antibonding state. We can see that these features are also present for the hydroxybenzoic acid adsorbates on wide-gap insulators. The evolutions of HOMO-1, HOMO-2 and HOMO-3 upon adsorption are indeed due to the covalent interaction between the Na atoms at the surface and the carboxylic (and phenolic if present) O atoms. In fact, outside the Na 3s valence states, the molecular orbitals of the adsorbates remain sharp and there is no coupling between these orbitals and the surface (see Fig. 8.5). Within the Na 3s states window, pronounced broadening and splittings of the adsorbate molecule orbitals arise as a result of the resonances.

However, we find that the covalent interaction does *not* contribute to the binding energy because all bonding and antibonding states of the adsorbate are still fully filled. This is reasonable since there is nearly no charge transfer between the surface and adsorbate. Physically, this implies that the covalent interaction acts like a repulsive Pauli barrier, where the electrons feel repulsion due to exclusion principle. Therefore, it is plausible to conclude that attractive interaction predicted by KS-DFT is attributed to the electrostatic interaction as in physisorption. Nevertheless, the covalent interaction

has a predominant role in determining the adsorption geometry because the orientation and tilting angle of the adsorbate molecule rely on the symmetry of the molecular orbital involved in the rehybridizations. This will be demonstrated in the next chapter where vdW interaction is introduced.

9 The Effect of van der Waals Interaction

In the preceding chapter, we find that the short-range ionic and covalent contributions at the benzoic acid-NaCl(100) interface give rise to an average adsorption energy of about 0.5 eV. It is interesting to see how the long-range dispersion force affects the binding energy and the adsorption geometry in the context of aromatic organic molecules on wide-gap insulators. Before presenting the effect of the dispersion force, we first review several theoretical studies on the vdW interactions in some organic molecule and insulator interfaces. Chakarova-Käck *et. al.* investigated the adsorption of phenol and α -Al₂O₃(0001) by vdW-DF¹ [124]. They found the binding was governed by the short-range interaction between the phenolic O atom and a surface Al atom, whereas the vdW contribution was secondary yet not negligible (about 20% of total binding energy). This is in contrast to the adsorption of phenol on graphite(0001), in which the interaction is purely nonlocal and long-ranged [125]. Using vdW-DF, Moses *et. al.* found a predominant contribution from the vdW interaction in the adsorption of aromatic and conjugated molecules on the basal plane of MoS₂ [126]. Pakarinen *et. al.* addressed the role of vdW forces in the adsorption and diffusion of PTCDA molecules on a nanostructured KBr(001) surface in terms of vdW-DF as well [127]. It was found that at some sites on the surface, most of the molecular binding is provided by vdW interactions, and the ionic contribution only accounts of 15% of the total binding energy. In light of these results we find that the effect of the dispersion force is indeed system-dependent. Without any quantitative calculations, it is an open question as to whether DFT calculations of conjugated molecules on insulators are reliable in the absence of the ubiquitous vdW forces.

In this chapter, we demonstrate the role of the vdW interaction in the binding of conjugated molecules and insulating surfaces by investigating the adsorption of SA molecule on NaCl(001) surface using vdW-DF within the framework of KS-DFT. The semi-empirical DFT-D provides a very similar picture of the binding energy and adsorption configuration. A comparison between the vdW-DF and the DFT-D method will be given in the next chapter.

9.1 Roles of vdW Forces in the Adsorption Energy

In order to measure the binding strength to the surface and to study the influence of chemical and vdW contributions, two quantities, the adsorption (E_{ads}) and interaction

¹The term vdW-DF in this thesis refers to the vdW-DF 04 version which uses the revPBE exchange functional.

Table 9.1: Calculated adsorption and interaction energies of the SA adsorbed on the NaCl(001) surface for the tilted adsorption configuration obtained with various exchange-correlation functionals. The superscript PBE indicates that the value reported is the single point energy evaluated by the corresponding XC functional at the PBE optimized geometry. All energies are given in eV.

	PW1PW	PBE	revPBE ^{PBE}	vdW-DF ^{PBE}	revPBE	SC vdW-DF
E_{ads}	-0.48	-0.45	-0.02	-0.72	-0.14	-0.82
E_{int}		-0.66	-0.28	-0.96	-0.31	-0.97

energies (E_{int}) are introduced. They are defined as

$$E_{\text{ads/int}} = E_{\text{system}}^{\text{relaxed}} - E_{\text{surface}}^{\text{relaxed/rigid}} - E_{\text{SA}}^{\text{relaxed/rigid}} \quad (9.1)$$

where E^{relaxed} or E^{rigid} indicate whether the corresponding structure is optimized or kept fixed at the optimized surface-adsorbate system coordinates. Thus E_{ads} is a thermodynamic quantity which refers to the different reference systems, whereas E_{int} is a non-adiabatic interaction energy between the different parts of the system.

We start with standard DFT calculations using the PBE exchange-correlation (XC) functional [41, 128] and the PAW method [69] as implemented in VASP [129, 130]. The plane-wave basis set kinetic cutoff energy is 450 eV and the Brillouin zone is sampled with a $2 \times 2 \times 1$ Monkhorst-Pack k -point mesh. The NaCl(001) surface is modeled using a (4×4) surface unit cell with a thickness of three atomic layers. This corresponds to a cell side length of 15.99 Å, taking the equilibrium NaCl lattice constant as 5.65 Å. The periodically repeated images of the slab are separated by a vacuum region with a thickness of 18 Å. A large unit cell is therefore constructed to ensure that the intermolecular interaction is minimized. The calculated adsorption energies are converged within 1 meV with the chosen computational parameters. The upper two NaCl slab layers and the molecule are allowed to relax until the atomic forces are less than 0.02 eV/Å.

The optimization within PBE-GGA DFT results in a non-parallel configuration as shown in Fig.9.1, as we have seen in the Sec. 8.2.1. The bond length between carboxylic O and Na atoms is 2.35 Å, while the average SA-NaCl(001) distance is about 3.5 Å. The optimal tilt angle between the SA and the surface is 30.2°. The adsorption geometry, and E_{ads} of -0.45 eV (see Table 9.1) are in agreement with previous PW1PW hybrid functional calculations.

In the next step, the vdW interaction is included as a post-GGA perturbation utilizing the self-consistent GGA electronic density with the vdW-DF method implemented in the grid based real space PAW code GPAW [131]. We choose a grid spacing of 0.20 Å in all GPAW calculations. In order to evaluate the contribution from the vdW interaction, which depends mostly only on the separation of the molecules from the surface, an artificial flat adsorption geometry is generated in addition to the tilted configuration by fixing the z coordinate of the molecule at a distance of 3.0 Å above the surface. The

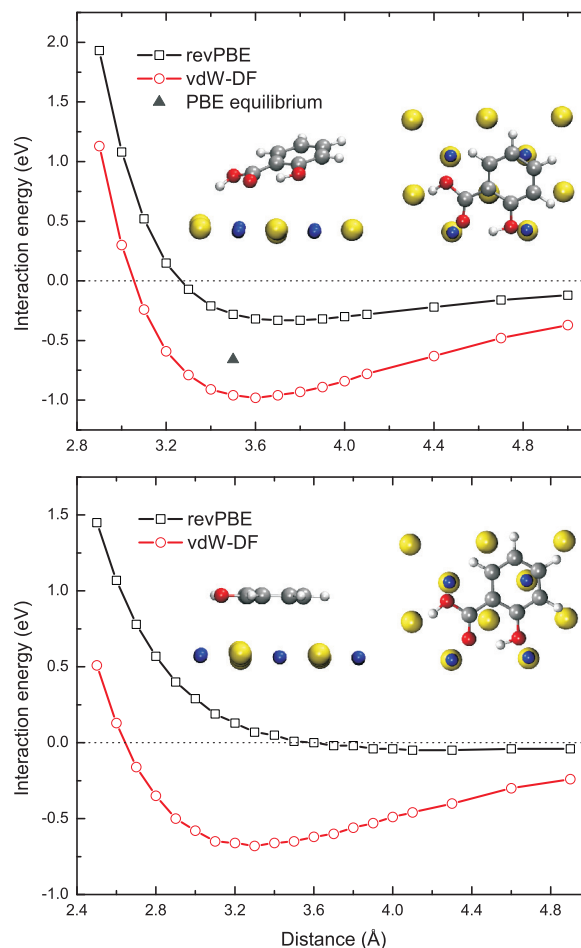


Figure 9.1: Interaction energies between the SA molecule and NaCl(001) surface as a function of average separation for the tilted (top) and parallel (bottom) adsorption configuration. The inset shows the adsorption geometries viewed from the side (left) and the top (right). Sodium and chlorine atoms are represented by the blue (black) and yellow (large light grey) balls, whereas carbon, oxygen and hydrogen atoms are shown in grey, red (dark grey) and white, respectively.

binding site is then determined by the in-plane x and y position of the molecule which is optimized within the PBE-GGA in VASP.

We show in Fig.9.1 the *interaction* energy curve of the adsorbate system calculated with both revPBE XC and vdW-DF as a function of the average distance between the molecule and surface. The geometrical structures of the molecule and surface were kept fixed at the values optimized with the PBE. As can be seen from the tilted adsorption configuration, the revPBE gives much lower interaction energies than the PBE (see Table 9.1 for the adsorption energy). This is in accordance with the general picture that the PBE and PW91 functionals tend to overestimate the binding energy [42, 132]. The revPBE has been shown to improve the chemisorption energy for atoms and molecules on transition metal surfaces [42]. It is also shown in Fig. 9.1 that the revPBE favors a larger separation between the SA and NaCl surface by 0.25 Å compared to the PBE functional. After the nonlocal correlation energy is taken into account, E_{int} exhibits a significant increase up to -0.96 eV. The nonlocal part now accounts for 70% of the total interaction energy. The vdW-DF predicts an equilibrium average distance of 3.6 Å, 0.15 Å shorter than that of the revPBE calculation since the nature of the vdW forces is attractive.

Turning to the parallel adsorption configuration, Fig. 9.1 shows that revPBE yields a very weak bond (less than 0.05eV). The vdW-DF, on the contrary, gives rise to an interaction energy of -0.68 eV at a distance of 3.3 Å. It is clear that the binding for this flat configuration purely originates from the vdW interaction. Note that E_{int} is about 0.3 eV smaller than that of the tilted configuration, which implies that the Na-O chemical interactions are also important and the final adsorption geometry with the inclusion of vdW interactions should be still non-parallel.

9.2 The Effect on the Adsorption Geometry and Electronic Structure

Based on these findings, we finally perform a self-consistent vdW-DF calculation in an attempt to obtain the most accurate adsorption properties for the SA-NaCl(001) system. The initial geometrical structure is pre-optimized within the revPBE in GPAW, since the vdW-DF also uses the revPBE exchange. The revPBE predicts a configuration similar to the PBE although the separation of the SA molecule and surface is 0.2 Å larger. E_{ads} is -0.14 eV, which amounts to one third of the PBE value. Then the vdW-DF forces are evaluated self-consistently for the adsorbate system in order to reach the equilibrium adsorption geometry.

To our surprise, the vdW-DF optimized structure turns out to be almost the *same* as in the revPBE calculations. The SA molecule is now slightly more parallel to the surface as a result of the attractive vdW forces. The tilt angle found is 0.5° smaller than that of the revPBE calculation, which corresponds to a decreased average distance of 0.1 Å between the SA and the surface. It is noteworthy that the bond distance between the carboxylic O and surface Na atoms remains unaltered. The self-consistent vdW-DF calculated E_{ads} is -0.82 eV (Table 9.1), which is 0.10 eV stronger than that of the

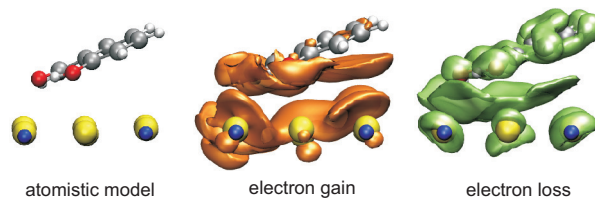


Figure 9.2: The change in electron density difference after inclusion of the nonlocal term ($\Delta\rho^{\text{vdW-DF}} - \Delta\rho^{\text{revPBE}}$). The absolute isovalue is 2×10^{-4} electrons/ \AA^3 .

PBE optimized structure. Yet the difference of E_{int} between the SC vdW-DF and the perturbative correction based on the PBE geometry is negligible.

The sheer change in the adsorption geometry of the adsorbate reveals that *the short-ranged contributions between the carboxylic O atom and surface Na atom still plays a central role in the final adsorption configuration*. We have already seen in Sec. 8.2.2 that the Na–O covalent interaction acts effectively as a Coulomb repulsion, and the equilibrium Na–O bond distance is determined by the joint effect of the repulsive covalent interaction and attractive ionic contribution. The tilting angle of the molecule, on the other hand, is a consequence of the symmetry of the molecular orbitals involved in the rehybridizations with the surface. This can be readily rationalized in a simple tight-binding picture, in which the HOMO-2 and HOMO-3 of the adsorbate are interacting with the 3s states of the Na atoms. The out-of-plane p_z orbital in the HOMO-3 (see Fig. 8.6) favors a more parallel orientation referenced to the surface due to the s - p_z σ bond, whereas the overlap between the in-plane p_{xy} orbital in the HOMO-2 and the s orbital of Na is benefited from a more perpendicular molecular orientation. These two competing factors thus give rise to a tilted adsorption configuration. The vdW contribution are delocalized and extended to the whole molecule, including the carboxylic group and the aromatic benzene ring. The usual effect of including the vdW interaction is to bring the molecule closer to the surface as a result of electronic correlations. In the context of the present molecule-insulator interface, we see that the energy gain by further decreasing the molecule-surface distance is *counterbalanced* by the Coulomb repulsion. Meanwhile, the adsorbate molecule remains planar after the dispersion force is included because of the strong intramolecular sp^2 hybridizations. In other words, the energy cost to bend the sp^2 C–C bond in between the carboxylic group and the aromatic ring is much higher than the energy gain from the vdW attractive contribution by bringing the aromatic ring closer to the surface. As a result, the molecule is refrained from a sizeable tilt or shift toward to the surface when the vdW interaction is switched on. The motion due to the vdW force is indeed restricted by the short-range interactions.

The nature of the vdW interaction can be visualized by the change in electron density difference after the inclusion of the nonlocal correlation functional (see Fig. 9.2). The electron density difference $\Delta\rho$ is expressed as

$$\Delta\rho = \rho_{\text{system}} - \rho_{\text{molecule}} - \rho_{\text{surface}}, \quad (9.2)$$

where ρ_{system} , ρ_{molecule} and ρ_{surface} represent the electron density of the relaxed system,

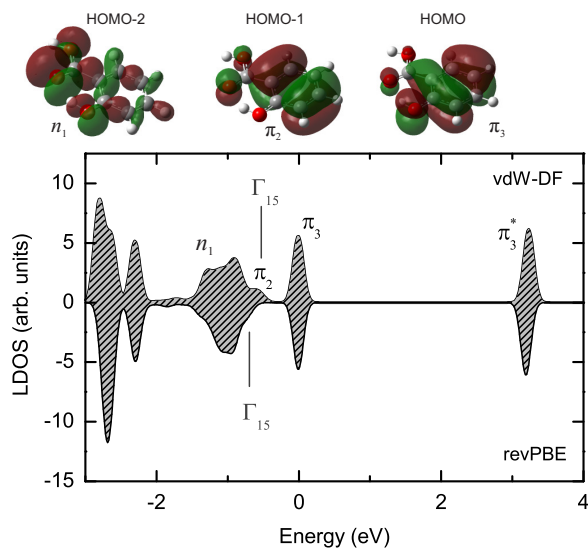


Figure 9.3: Local density of states (LDOS) of the SA adsorbed on NaCl(001) calculated with the SC vdW-DF and revPBE methods. The LDOS is convoluted with a 0.1 eV wide Gaussian function. The three uppermost occupied molecular orbitals are depicted on the top panel.

the isolated molecule and surface being in the same atomic configurations as in the relaxed system, respectively. Thus the electron density difference gives a clear indication of the bonding mechanism. As depicted in Fig. 9.2, the electron density moves from around the nuclei to the region between the aromatic ring and NaCl surface after the nonlocal correlation functional is switched on. The charge redistribution, albeit relatively small, accounts for the enhanced binding energy in terms of the changes in the Coulomb forces acting on the nuclei. This falls into line with the concept of the vdW force within the classical picture [133–135]. While the vdW-DF is central to the spirit of the long-range correlations from electronic motions, it is clear that this functional is capable of providing a coherent and unified picture of the dispersion force.

The electronic structure of the adsorbate system is also affected by the inclusion of vdW interactions. In Fig. 9.3, we plot the local density of states (LDOS) of the SA molecule for the revPBE and vdW-DF methods. In both cases the splitting and broadening of the HOMO-2 and HOMO-1 can be observed. The splitting of HOMO-2 can be ascribed to the hybridization of the σ electrons at the carboxylic group and surface Na s bands, while the broadening of the HOMO-1 arises mainly due to the interaction between the π electrons and the surface. Such broadenings have also been seen in previous ultra-violet photoemission spectroscopy (UPS) spectra of condensed SA on NaCl(001) [101]. It is clear that the SC vdW-DF yields a broader π_2 resonance than the revPBE-GGA functional as a result of stronger hybridizations between the p_z electrons delocalized over the aromatic ring and surface valence states. Nevertheless, when the vdW-DF is applied to the revPBE optimized structure, the resultant LDOS

is similar to that of the revPBE-GGA. Thus, it is mainly the slightly closer proximity between the SA and NaCl surface that induces the larger broadening of the π_2 band. Furthermore, the resonance between the HOMO-1 of the SA molecule and surface valence states pins the valence band maximum Γ_{15} 0.15 eV closer to the HOMO of the SA after the inclusion of vdW interaction, resulting in a HOMO- Γ_{15} separation of 0.5 eV. Experimentally UPS measurements found the HOMO of the SA (π_3) 0.1 eV above the Γ_{15} point of NaCl(001) [101]. Although the vdW-DF predicted value is yet not in perfect agreement with the experiment, the relative shift of the HOMO towards the Γ_{15} proves that the vdW interaction plays a significant role in the adsorption of the SA on NaCl(001) surface.

We have shown that the vdW dispersion forces play a dominant role in the binding between aromatic carboxylic acids and wide band gap insulators. The inclusion of the nonlocal correlation functional significantly enhances the adsorption energy of the SA molecule on NaCl(001) to -0.8 eV. Accordingly, the vdW forces *must be taken into account* when treating adsorption energies of aromatic and conjugated molecules on inert surfaces. As for the bonding configuration, however, we find that short-range interactions still play a crucial role. As demonstrated here, although their relative contribution to binding is not very large, their strong variation with bond angles, bonding sites and distances turns out to be decisive for the optimal bonding geometry of SA on the NaCl(001) surface, i.e. the local chemical bonds between the carboxylic and phenolic O and surface Na atoms are crucial for the adsorption configuration. In addition, vdW interactions have an influence on orbital alignment and broadening, as also demonstrated by our calculations. This proves that vdW interaction is essential and it plays an important part in both the adsorption energetics and electronic structure of the aromatic carboxylic acids on insulators.

10 Generic Aspects of Adsorption on Alkali Halide (100) Surfaces

We have addressed the binding energy, adsorption configuration, and the effect on the electronic structure of various benzoic acid molecules on the perfect (100) surface of NaCl in the last two chapters. In this chapter, a comprehensive study is dedicated to the adsorption on the KCl surface, including all the ingredients discussed in the earlier chapters. We concentrate here on a comparison of adsorption geometries and electronic structures on the ideal (100) surface between KCl and NaCl, so that a detailed picture of the interaction between the hydroxybenzoic acids and alkali halide surfaces can be obtained from first-principle calculations. The computational methods and parameters follow the descriptions in the preceding chapters.

10.1 Adsorption Geometries

The adsorption study starts with the investigation of various hydroxybenzoic acids on the ideal KCl(100) surface, shown in Fig. 10.1. The electronic structure of KCl(100) surface is, as expected, very close to that of the bulk with no traces of surface states. The calculated surface energy is 9.25 meV/Å with the PW1PW functional, which falls in line with other theoretical values and experiments [136, 137].

In 10.1 calculated adsorption and interaction energies are presented for the various adsorption systems on KCl(100), as well as on NaCl(100) for comparison. As seen there, the standard DFT methods employing the PW1PW hybrid functional and the PBE GGA functional yield quite similar E_{ads} since the two flavors of GGA, *i.e.* the PW91 functional in PW1PW and PBE are generally equivalent for many properties.[42, 132, 138] The adsorption energies on both surfaces are also very close, although on NaCl E_{ads} values are slightly larger.

The adsorption on KCl(100) follows the same configuration as that on NaCl(100) through the electrostatic interaction between the K-O and Cl-H bonds. The dominant chemical bonding occurs between the double bonded carboxylic O and surface K atoms, with an average bond length of 2.8 Å and 2.7 Å by PW1PW and PBE, respectively. The partially covalent character of the K-O bond can be revealed by the charge density difference map (not shown) where the electrons are localized in the region between the two atoms joined by the bond. This is supported by the projected density of states (PDOS) in Fig. 10.2 where the HOMO-1 and HOMO-2 of the adsorbate are smeared out as a result of the hybridizations between the $p_{x,y}$ (HOMO-2), p_z (HOMO-1) electrons of the molecule (see Fig. 10.3) and the 4s band of surface K atoms. This can be qualitatively described within the Newns-Anderson model of adsorption in the weak chemisorption

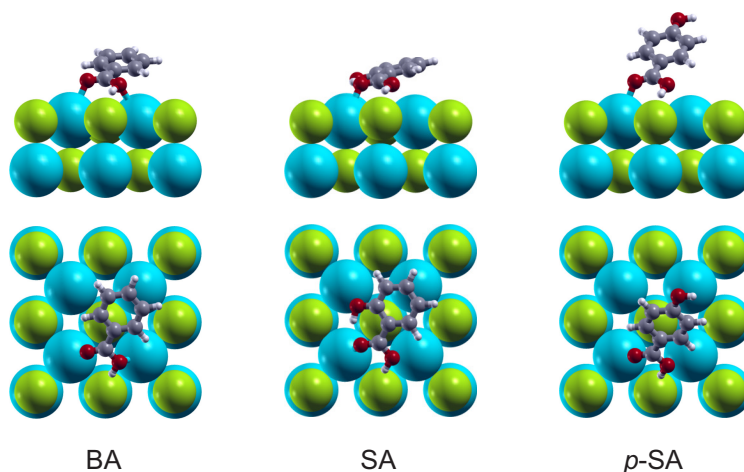


Figure 10.1: Side view (top panel) and top view (bottom) schematics of the adsorption of BA, SA and *p*-SA on KCl(100) surface. Potassium atoms: blue, chlorine atoms: green, oxygen atoms: red, carbon atoms: grey, hydrogen atoms: white.

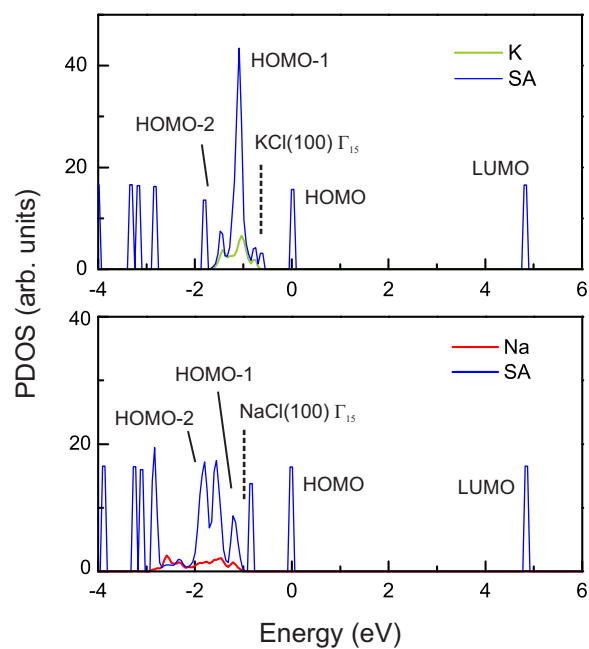


Figure 10.2: Comparison of the density of states projected onto the SA molecule and onto the cations for adsorption on KCl (top) and NaCl(100) (bottom) surfaces calculated with the PW1PW functional. The energy zero is shifted to the HOMO of SA.

Table 10.1: The adsorption energies and interaction energies (in parentheses) of BA, SA and *p*-SA on KCl and NaCl(100) surfaces. All energies are given in eV.

Adsorbate	PW1PW ¹	PBE-D			vdW-DF		
		PBE	Total	PBE	vdW ²	Total	revPBE XC Diff. ³
On KCl(100)							
BA	-0.40	-0.44	-0.72 (-0.84)	-0.41 (-0.53)	-0.31	(-0.77)	(-0.50)
SA	-0.43	-0.43	-0.84 (-1.04)	-0.43 (-0.63)	-0.41	(-0.99)	(-0.68)
<i>p</i> -SA	-0.44	-0.44	-0.62 (-0.71)	-0.44 (-0.53)	-0.18	(-0.67)	(-0.31)
On NaCl(100)							
BA	-0.43	-0.44	-0.82 (-0.96)	-0.41 (-0.56)	-0.40	(-0.77)	(-0.52)
SA	-0.48	-0.45	-0.98 (-1.19)	-0.45 (-0.66)	-0.53	(-0.94)	(-0.69)
<i>p</i> -SA	-0.45	-0.45	-0.81 (-0.93)	-0.45 (-0.56)	-0.37	(-0.78)	(-0.51)

¹ The reported energies have been corrected for the basis set superposition error (BSSE).

² The vdW contributions to the adsorption energy and interaction energy are the same.

³ $\Delta E_{xc} = E_{LDA,c} + E_c^{nl} - E_{revPBE,x}$.

Table 10.2: The relaxed geometric parameters of BA, SA and *p*-SA on KCl and NaCl(100). The separation R (in Å) is the distance between the geometric center of the molecule and the averaged position of the (100) surface. The tilt angle ϕ_{tilt} (in $^\circ$) is defined as the dihedral angle between the benzene ring and the (100) plane. $d_{\text{K(Na)-O}}$ (in Å) represents the distance from the carboxylic O to the nearest K(Na) atom. The interatomic distance between carboxylic H and Cl atoms is denoted by ($d_{\text{Cl-H}}$). The additional bond distance between phenolic O and surface K is shown in parentheses for the SA adsorbate system.

Adsorbate	PW1PW				PBE				PBE-D			
	R	ϕ_{tilt}	$d_{\text{K(Na)-O}}$	$d_{\text{Cl-H}}$	R	ϕ_{tilt}	$d_{\text{K(Na)-O}}$	$d_{\text{Cl-H}}$	R	ϕ_{tilt}	$d_{\text{K(Na)-O}}$	$d_{\text{Cl-H}}$
On KCl(100)												
BA	3.53	21.5	2.81	2.26	3.89	30.2	2.67	2.10	3.81	29.7	2.67	2.09
			2.88				3.12				3.06	
SA	3.15	14.4	2.79	2.30	3.46	23.2	2.76	2.23	3.44	23.2	2.75	2.21
			2.99				3.28				3.20	
			(3.06)				(2.98)				(2.94)	
p -SA	4.55	42.6	2.76	2.17	5.08	46.4	2.73	2.17	5.08	46.4	2.73	2.17
			2.99				3.85				3.85	
On NaCl(100)												
BA	3.82	30.5	2.37	2.18	3.86	29.9	2.32	2.10	3.80	30.9	2.36	2.03
			2.74				2.97				2.66	
SA	3.49	31.3	2.37	2.31	3.45	29.2	2.38	2.16	3.41	28.6	2.38	2.12
			3.25				3.22				3.01	
			(2.50)				(2.57)				(2.54)	
p -SA	3.89	29.1	2.37	2.19	4.01	29.9	2.31	2.10	4.00	30.2	2.32	2.08
			2.70				3.00				2.86	

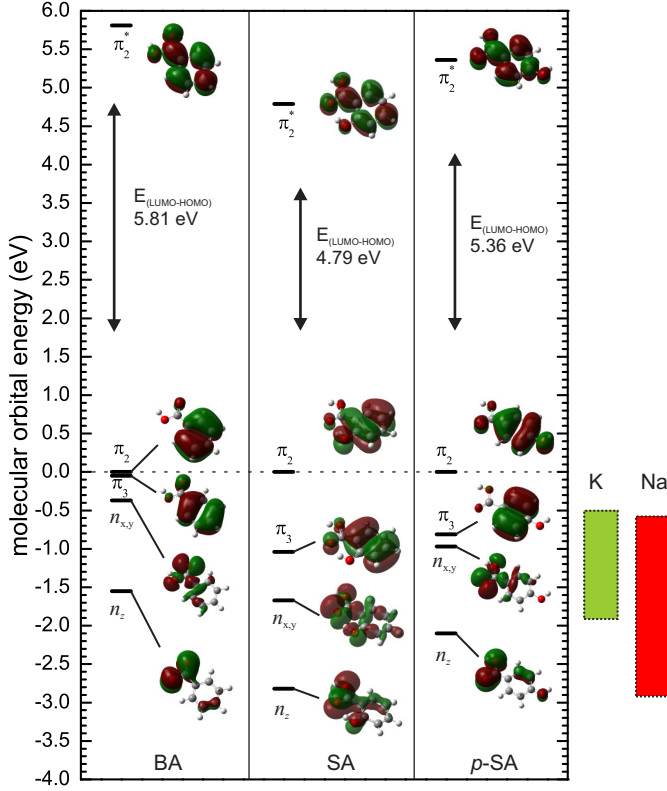


Figure 10.3: Diagrams of highest occupied and lowest unoccupied molecular orbital energy levels for BA, SA and *p*-SA molecules calculated by PW1PW. The *s* valence state bandwidths of the respective cations and their alignments with the molecular orbitals are illustrated.

limit, *i.e.* a single valence level of the molecule is broadened into a resonance with a finite lifetime [122, 123, 139]. Consequently, the carboxylic group is slightly rotated along the C=C bond with respect to the benzene ring. Moreover, the hybridization between the in-plane $p_{x,y}$ orbital of the carboxylic group and K 4*s* valence states gives rise to a tilted molecular adsorption configuration.

Interestingly, it is clearly seen in Fig. 10.1 and Table 10.2 that on KCl(100) the adsorbed *p*-SA is significantly more rotated out of the surface plane as compared to both BA and SA. Inspecting the PDOS (not shown), one sees a rather pronounced broadening of both the HOMO-2 and HOMO-1 of *p*-SA. This strong HOMO-2 resonance in *p*-SA, which gives rise to a more upright adsorption configuration on KCl(100), is essentially caused by the small separation between the HOMO-1 and HOMO-2 (0.16 eV) as shown in Fig. 10.3. Indeed, we find that the tilt angle for adsorption on KCl(100) is directly related to the energetic difference between the HOMO-1 and HOMO-2 of the adsorbate molecule: the smaller the separation between the HOMO-1 and HOMO-2 is, the more the molecule is tilted out of the surface plane. On the NaCl(100) surface, due to the broader Na 3*s* valence band and a more equal distribution of resonance states for all three molecules, the tilt angle dependence is thus absent. The role of covalent resonances also explains the difference of the molecule tilting angles when we move from the NaCl to the KCl substrate. For example in case of SA, it is seen in Fig. 10.3 that using the PW1PW hybrid functional, both the p_z and $p_{x,y}$ orbitals come into resonance with

the NaCl surface, while on the KCl surface the dominating resonance is between the p_z orbital (HOMO-1) and the surface s orbital, thus making the adsorbate molecule more parallel to the surface on KCl.

In the next step, geometric optimizations are performed within the dispersion-corrected PBE-D calculations to account for the missing vdW contribution in standard DFT approximations. Nevertheless, the final adsorption configurations for all molecules are very close to those obtained without dispersion corrections (see 10.2). This is in accordance with our previous self-consistent vdW-DF study on the SA-NaCl(100) system, which shows that the local interaction turns out to be decisive for the optimal bonding geometry (Sec. 9.2). A close inspection shows a systematic decrease of the distance between the singly bound carboxylic O and surface K atoms after the dispersion is included, while the bond length between the doubly bound carboxylic O and K atoms is unaltered (see the first row of d_{K-O} in 10.2). One can also see that the PBE parts of the adsorption energy in PBE-D calculations are equivalent to the descriptions without dispersion. Specifically, a very small decrease (0.03 eV) of the PBE E_{ads} for the BA adsorbate system is found after the vdW interaction is taken into account. This suggests that the final optimal geometry is stabilized by the interplay of the local chemical interaction and long range dispersion. In general, the whole molecule is closer to the surface as a result of the attractive vdW forces, but the change is rather subtle.

Although the effect on the adsorption geometry of the vdW interaction is small, it greatly enhances the binding to the surface. As seen from 10.1, the total E_{ads} increases by -0.2 to -0.5 eV due to the vdW contribution. Thus the strength of the vdW interaction is comparable to the chemical interaction. Only for the p -SA+KCl(100) system the magnitude of the vdW contribution is much smaller because the aromatic ring is further away from the surface. When the vdW-DF is applied to the PBE-D optimized structure, it yields E_{int} values close to the PBE-D values. This should not be considered as a coincidence, as the PBE-D and vdW-DF are constructed from qualitatively different approaches. The well-known trend is also found that revPBE systematically yields smaller binding energies than PBE and PW91 [42, 140]. It should be pointed out that while the choice of the revPBE exchange in the vdW-DF is generally appropriate, in some cases such as for the hydrogen-bonded complexes it may underestimate the binding. Nevertheless, we show that the overall interaction energies agree well with the PBE-D method when the revPBE exchange is combined with the nonlocal correlation energy. It is thus reasonable to expect that both PBE-D and vdW-DF are capable of describing the long range dispersion between the conjugated molecules and ionic insulators. In addition, we find that the SA adsorbate systems yield the largest dispersion. Since the π electrons are delocalized over the whole molecule from the aromatic ring to the carboxylic and phenolic group, the enhanced vdW interaction can be explained by the contribution from the additional phenolic group in SA. The phenolic group in the p -SA adsorbate system, on the other hand, is positioned quite far away from the surface, thus imposing a smaller effect on the interaction energy.

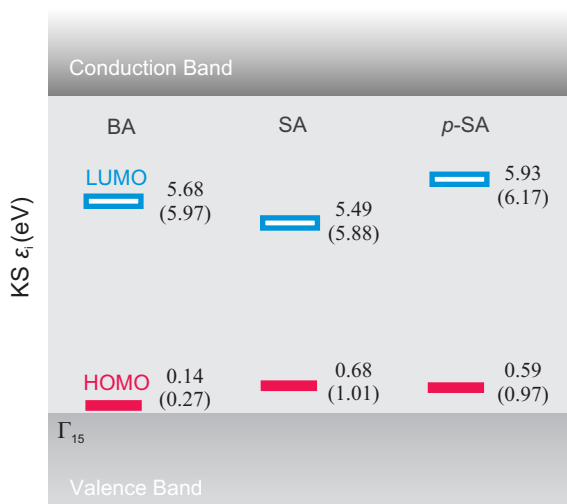


Figure 10.4: Band diagram of BA, SA and *p*-SA adsorbed on KCl(100) surface with the PW1PW functional. The valence band maximum of the surface defines energy zero. Values of adsorbate systems on NaCl(100) are also reported in parentheses.

10.2 Effective Kohn-Sham Gap and Molecular Orbital Alignment

To address the effect of various hydroxybenzoic acids on the electronic structure of the adsorbate systems, the Kohn-Sham energy levels for adsorptions on KCl and NaCl(100) are compiled and presented in Fig. 10.4. One should note that although the PW1PW functional is used here for the prediction of the electronic structure, the overall picture is still valid, since we have shown in Ch. 9 that the inclusion of long range dispersion has a limited effect on the band alignment between the adsorbate MOs and surface electronic states. We see a systematic trend that the HOMO and LUMO of the adsorbate on KCl(100) surface is 0.2 to 0.4 eV closer to the valence band maximum (VBM) (Γ_{15} point) of the surface as compared to the adsorption on NaCl(100). Such a difference can be rationalized by the PDOS of the different surfaces given in Fig. 10.2. We use the SA adsorbed system as an example, but an analogous discussion can be applied to the other systems. As we have mentioned, the valence *s* states bandwidth of Na is broader than that of K. For adsorption on NaCl(100), the HOMO-2 couples more strongly to the surface Na valence band than the HOMO-1, while on KCl(100) the broadening of the HOMO-1 is more pronounced. The rehybridization between HOMO-1 and K valence band shifts the whole MOs of the molecule with respect to the surface, giving rise to a closer alignment between the HOMO and Γ_{15} on KCl(100). In fact, this is in accord to the larger tilt angle of SA on NaCl(100) shown in Table 10.2 because of the strong resonance the HOMO-2 develops on NaCl(100). Nevertheless, it is clear from the diagram that the effective KS gaps for all systems are determined by the HOMO-LUMO separation. The HOMO-LUMO gaps stay almost identical after adsorption on KCl and NaCl, *i.e.* they do not deviate significantly from the isolated state as a result of weak interactions. For both NaCl and KCl, we show that the additional molecular levels introduced by the various hydroxybenzoic acid adsorbates can reduce the effective Kohn-Sham band gap to the HOMO-LUMO gap of the adsorbate.

10.3 Insights From Kohn-Sham DFT

In the last few chapters, we have investigated the adsorption of various hydroxybenzoic acids on flat (100) surface of KCl and NaCl within the framework of Kohn-Sham DFT. The adsorption configurations are governed by a complex interplay between the ionic contribution, covalent interaction and long-range vdW interaction.

- The ionic contribution arises simply from the electrostatic attraction between the carboxylic oxygen and the cation at the surface (and between the hydrogen and chlorine to some extent), which is responsible for the molecule-surface binding in the short range.
- The covalent interaction, while it behaves as a repulsive Coulomb interaction, has a fundamental impact on the adsorption geometry and the alignment of the molecular orbital with respect to the VBM. This is evidenced by the observed difference in the molecular orientation and the alignment of the HOMO with respect to the VBM upon adsorption on NaCl and KCl (100) surfaces.
- The vdW dispersion force, being a nonlocal polarization effect, considerably stabilizes the binding between the molecule and the surface of wide-gap insulators. In the present work, the vdW interaction accounts for about half of the total adsorption energy. However, we find that the dispersion force has little influence on the adsorption geometry. Both vdW-DF and PBE-D give equivalent description of the vdW part in the molecule-surface interaction, affirming the validity of both methods in the context of the current work.

Our calculations suggest that upon molecular adsorption on the *ideal* alkali halide (100) surface, the features of the molecular orbitals are generally preserved. The chemical inertness of the ideal surface facilitates the use of alkali halides as supporting templates for a wide variety of applications [127]. However, we note that this scenario does *not* necessarily hold for all organic-insulator systems. In Appendix B, we show that when a gluconic acid is adsorbed on the $\text{MgSO}_4 \cdot \text{H}_2\text{O}$ (100) non-polar surface, the molecular frontier orbitals undergo significant changes due to the rehybridizations. This is also a result of the peculiar covalent interaction.

We close this chapter by restating that the band gap obtained from KS-DFT, while being able to track the trend of various adsorbate systems, is usually underestimated and is thus inaccurate in its absolute value even when hybrid functionals are used. This has already been demonstrated by the gas-phase molecules and bulk insulators in Ch. 6 and 7. Moreover, some dynamic effects are clearly beyond the description of a mean-field theory such as KS-DFT. For instance, when a molecule is near a surface, the HOMO and LUMO experience the image potential due to the image charge in the surface, leading to a renormalization of the energy level positions of these two orbitals. This polarization effect is a dynamic and nonlocal correlation effect, and it is not captured by KS-DFT with standard exchange-correlation functionals. The properties of the electronic excitation are further altered if the electron-hole interaction is taken into account. In the next

chapter, we first resort to the GW approximation to correct the quasiparticle energies and to include the polarization effect in the molecule-insulator systems.

11 Polarization Induced Renormalization of Molecular Energy Levels

In this chapter, we will see how the long-ranged dynamic correlation due to the image charge potential influences the energy levels of the HOMO and LUMO of the molecular adsorbate on wide-gap insulators. The renormalization of the HOMO and LUMO has been observed in photoemission spectra [141] and electron transport measurements [15, 142]. Notably, Repp *et al.* observed that when a pentacene is adsorbed on NaCl(100)/Cu surface, the energy gap of the molecule exhibits sizeable reduction as the thickness of the NaCl film decreases [15], which is a direct indication of the renormalization of molecular levels due to the surface polarization effect. Using model *GW* calculations, Neaton *et al.* found a pronounced quasiparticle energy gap reduction (3.3 eV) of a benzene molecule upon its physisorption on graphite (0001) [23]. Later, they analyzed the C₆₀-Au(Ag) interfaces based on a constrained DFT calculation and a *GW* approximation of an Anderson impurity model, and a similar renormalization of energy levels is shown [143]. Thygesen and co-workers systematically investigated the renormalization of molecular levels at metallic and semiconducting surfaces through *GW* calculations [144, 145]. It was found that both local (semilocal) and hybrid exchange-correlation potentials fail to describe the polarization effect. Therefore, the Kohn-Sham eigenvalues of physisorbed species are not affected by the substrate. To illustrate to what extent the affinity and ionization levels of the benzoic acid adsorbates are shifted due to the surface polarization effect, we carry out *G*₀*W*₀ calculations for the BA and SA molecules adsorbed on NaCl(100) surface. We first discuss the classical image charge theory, which has been shown to be capable of qualitatively capturing the essence of the polarization effect.

11.1 Classical Image Charge Theory

In the classical model, a point charge q outside a substrate will induce an image charge inside the substrate. The image charge then subsequently creates an image potential V_{im} for the point charge [146, 147]

$$V_{\text{im}} = -\frac{1}{4} \frac{\varepsilon - 1}{\varepsilon + 1} \frac{q^2}{z - z_0}, \quad (11.1)$$

where ε is the static dielectric constant of the substrate. z and z_0 refer to the position of the point charge and image plane, respectively. Now think of a molecule on a substrate. The HOMO level of the molecule is related to the ionization potential, *i.e.* the energy required to remove an electron (or add a hole) from (to) the molecule. The additional

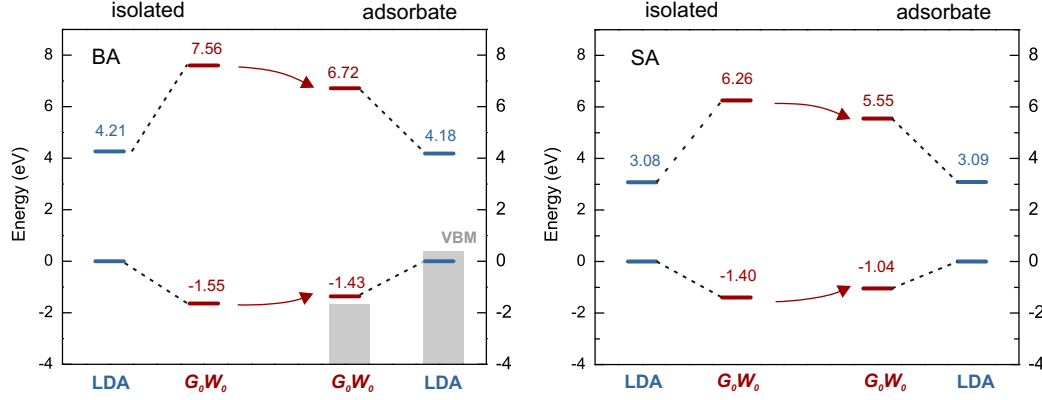


Figure 11.1: The evolution of the $\pi - \pi^*$ energy gap of the BA and SA molecules upon adsorption on NaCl(100). The π orbital of the molecule is aligned to energy zero.

hole now sees the image potential due to its image charge in the substrate. The effect of the image potential can be evaluated as the work done by the image force $-\partial V_{\text{im}}/\partial z$ to bring a hole from infinity to z

$$I_{\text{im}} = \int_{+\infty}^z dz' \left[-\frac{1}{4} \frac{\varepsilon - 1}{\varepsilon + 1} \frac{1}{(z' - z_0)^2} \right] = \frac{1}{4} \frac{\varepsilon - 1}{\varepsilon + 1} \frac{1}{z - z_0}. \quad (11.2)$$

Hence, the effective ionization energy in the presence of the image potential is given by

$$I_{\text{eff}} = I - \frac{1}{4} \frac{\varepsilon - 1}{\varepsilon + 1} \frac{1}{z - z_0}. \quad (11.3)$$

This implies that the ionization level will move upwards by $|V_{\text{im}}|$ because of the image potential. In analogous to the ionization energy, the effective electron affinity increase by $|V_{\text{im}}|$ due to the attractive interaction between the additional electron and its image. The electron affinity level accordingly moves down by $|V_{\text{im}}|$

$$A_{\text{eff}} = A + \frac{1}{4} \frac{\varepsilon - 1}{\varepsilon + 1} \frac{1}{z - z_0}. \quad (11.4)$$

The energy gap, which is the difference between the ionization energy and the electron affinity, is therefore reduced by $2|V_{\text{im}}|$ as a result of the image potential. As can be seen in Eq. (11.1), the magnitude of the gap reduction is proportional to the dielectric constant ε of the surface. On wide-gap insulator surfaces, the effect of the polarization effect is thus much less pronounced than that on metal surfaces.

11.2 Renormalization of Electronic Levels at Benzoic Acids/NaCl(100) Interfaces

The G_0W_0 quasiparticle energy is calculated using a four-layer (2×2) NaCl(100) supercell with molecules adsorbed on it, which represents an adsorption coverage of a full

Table 11.1: Calculated $\pi - \pi^*$ energy gaps (in eV) of BA, SA, and *p*-SA molecules on NaCl(100) by LDA and $G_0W_0^{\text{LDA}}$. The isolated molecule refers to the molecule detached from the surface while its geometry is kept fixed as that of the adsorbate.

	BA		SA		<i>p</i> -SA	
	LDA	$G_0W_0^{\text{LDA}}$	LDA	$G_0W_0^{\text{LDA}}$	LDA	$G_0W_0^{\text{LDA}}$
Adsorbate	4.18	8.15	3.09	6.59	3.58	6.97
Isolated	4.21	9.11	3.08	7.66	3.77	8.38

monolayer. While the unit cell is relatively small, the lateral intermolecular interaction is still suppressed, as the LDA calculations of an isolated molecule in the unit cell show limited energy level dispersions of the HOMO and LUMO with respect to the \mathbf{k} -point. The dispersions of the corresponding quasiparticle energy levels from GW calculations are still very small, about 0.03 eV.¹ The adsorption geometry optimized by the LDA functional is justified as the influence of the vdW interaction has been shown to be negligible. We include a total number of 512 and 960 bands for the self-energy calculation of the isolated molecule and the adsorbate system, respectively. A Γ centered 3×3 MP \mathbf{k} -point mesh (5 \mathbf{k} -points in the IBZ) is used throughout this section. The exchange self-energy includes over 10^5 \mathbf{G} vectors (60 Ry), and about 2000 \mathbf{G} vectors (4 Ry) are taken into account in the evaluation of the response function. The spurious long-range Coulomb interaction between the periodic images is truncated by a box-shape cutoff in the direction normal to the (100) surface. In Table 11.1 the results for all the three hydroxybenzoic acids are given.

An obvious *reduction* of the molecular energy gap can be found for all molecules when adsorbed on NaCl(100) according to the G_0W_0 calculations. This is clearly different from the LDA calculations where a slight change in the HOMO-LUMO gap is involved. In particular, we find that LDA predicts that the HOMO of BA is below the VBM of the surface (see Fig. 11.1), which is opposed to what have been found by the PW1PW hybrid functional (Fig. 8.5) and the G_0W_0 approximation. This is essentially a consequence of the distorted ordering of the frontier orbitals stemming from the spurious self-interaction error discussed in Ch. 6. Accordingly, in Table 11.1, the reported $\pi - \pi^*$ gap for BA refers to the LDA (HOMO-1)-LUMO gap, while for SA and *p*-SA the $\pi - \pi^*$ gap is the plain HOMO-LUMO gap. LDA yields nearly identical energy gaps due to the effective potential of the surface since the polarization effect cannot be described by the KS-DFT energy gap. We see in Fig. 11.1 that the G_0W_0 approximation tends to shift the HOMO and LUMO of an adsorbate to the mid-gap, thus decreasing the quasiparticle energy gap. For example, the ionization energy level moves up by 0.36 eV whereas the electron affinity level moves down by 0.71 eV when a SA molecule is adsorbed on the NaCl(100), corresponding to a gap reduction of 1.07 eV. Moreover, the renormalization of the G_0W_0 energy level should in principle inherit all the static ground-state effect from KS-DFT.

¹Note the dispersion of some unoccupied levels could be substantial due to the overlap of the electronic states.

Hence, the change in the energy gap upon adsorption given by G_0W_0 includes the effect described by KS-DFT

$$\Delta E_g^{G_0W_0} = \Delta E_g^{\text{pol}} + \Delta E_g^{\text{KS-DFT}} \quad (11.5)$$

where $\Delta E_g^{\text{KS-DFT}}$ is due to the polarization effect. Accordingly, the renormalization of the quasiparticle energy gap due to the polarization in the surface amounts to 1.1 and 1.2 eV for the SA and p -SA adsorbed systems, respectively. When it comes to the BA, we should be aware of the fact that the quasiparticle ionization energy level of the molecule does not correspond to the LDA HOMO anymore. Instead, it is the HOMO-1 level from the LDA calculations (cf. Fig. 6.2). Nevertheless, the results of the SA and p -SA suggest that $\Delta E_g^{\text{KS-DFT}}$ is negligible, and thus the polarization effect accounts for the G_0W_0 energy gap renormalization observed for all three molecules.

If we decompose the self-energy into the bare (Fock) exchange (Σ_x) and correlation (Σ_c) parts as in Eq. 5.37, we find that the renormalization of the HOMO and LUMO indeed arises from the change in the correlation energy ($\Delta\Sigma_c$). The change $\Delta\Sigma_x$ is rather small (0.2 eV), which is nearly equal to the change in the DFT exchange-correlation energy (ΔE_{xc}). For the HOMO, $\Delta\Sigma_c \approx 0.5$ eV, while for the LUMO $\Delta\Sigma_c \approx -0.8$ eV. From this, we see that it is indeed the change in the correlation part of self-energy that is responsible for the renormalization of the molecular energy gap. However, the asymmetric shift of Σ_c for the HOMO and LUMO suggests that the renormalization in the present case does not strictly follow the classical image potential theory. This is not unexpected in a full monolayer coverage as polarizations between the molecules are likely to take place.

To this end, it is demonstrated from the GW calculations that the adsorption of organic molecules on wide-gap insulator surface renormalizes the energy gap of the molecular adsorbate by about 1 eV. We show in Appendix B a similar polarization induced renormalization when a gluconic acid is adsorbed on a $\text{MgSO}_4 \cdot \text{H}_2\text{O}$ (100) surface. The effect of the polarization in the surface is to reduce the HOMO-LUMO gap. In the presence of a metallic surface, the KS-DFT using hybrid functionals (or even local and semilocal functionals) can occasionally reproduce the quasiparticle energy gap from a GW calculation [145]. This is simply an error cancellation due to the spurious self-interaction and the neglect of functional derivative discontinuity and polarization effect. For adsorption on wide-gap insulators, the discrepancy in the energy gap between a GW and a KS-DFT calculation will always be very pronounced. This imposes an important restriction on KS-DFT for the description of molecule-insulator interfaces.

12 Excitonic Effect at Molecule-Insulator Interface

In Sec. 6.3 sizeable molecular excitonic effects have been observed for the gas-phase hydroxybenzoic acids. The presence of the bound e - h pair reduces the effective excitation energy of an electron to nearly half of the HOMO-LUMO energy gap. It thus tempting to see how the excitonic effect behaves at the molecule-insulator interface using the two-particle BSE. The BSE calculation has been a rather formidable for the extended systems because of the extreme requirement in the memory when solving the excitonic Hamiltonian. It is until very recently that the excitonic effect is exploited for molecular adsorption on surfaces in terms of MBPT. In this chapter, we reveal the electron-hole interaction at the interface between the hydroxybenzoic acids and NaCl(100) surface. To the best of our knowledge, this is the first attempt to investigate the excitonic effect for a conjugated organic molecule adsorbed on an insulating surface.

The BSE calculations follow the adsorption of one-monolayer benzoic acids on a (2×2) unit cell as in Ch. 11, and use the quasiparticle energies from the G_0W_0 calculations. We are restricted to include the e - h pairs with energies up to 33 eV in the response function of the BS kernel using the full Hamiltonian.¹ The exciton energies are expected to be converged within 0.2 eV using this number of e - h pairs. For the statically screened Coulomb interaction and the exchange part of the BS kernel, about 1000 (3 Ry) and 20000 (20 Ry) \mathbf{G} vectors have been found sufficient for a well converged spectrum, respectively. The iterative Lanczos-Haydock recursive method is used to solve the full non-Hermitian excitonic Hamiltonian [97].

We first consider the absorption spectra in the TDA shown in Fig. 12.1. The first excitation peak appears at around 4.1 eV for both the BA and SA adsorbate systems. This peak is assigned to the HOMO-LUMO transition, *i.e.* the $\pi - \pi^*$ transition at the aromatic benzene ring according to a full diagonalization of the Hamiltonian². Going from the parallel perturbing field ($\theta = 0^\circ$) to the perpendicular polarization ($\theta = 90^\circ$), we see that the intensity of the $\pi - \pi^*$ peak does not change much because the molecules are tilted on the surface. This lowest singlet exciton energy is equivalent to the gas-phase molecule for the SA, whereas it is about 0.4 eV smaller than the isolated molecule for the BA. Nevertheless, this lowest molecular exciton state is barely affected by the underlying substrate. Moving to higher photon energies, we find the second lowest peak

¹ The size of the excitonic Hamiltonian is proportion to $N_v \times N_c \times N_k$, where N_v , N_c , and N_k denote the number of the valence bands, the conduction bands, and the \mathbf{k} -points, respectively. The inclusion of the whole 90 occupied states and 70 unoccupied states already results in a memory consumption of around 10 GB per process.

² A smaller number of e - h pairs with energies up to 20 eV is included due to the extremely cumbersome procedure of diagonalization.

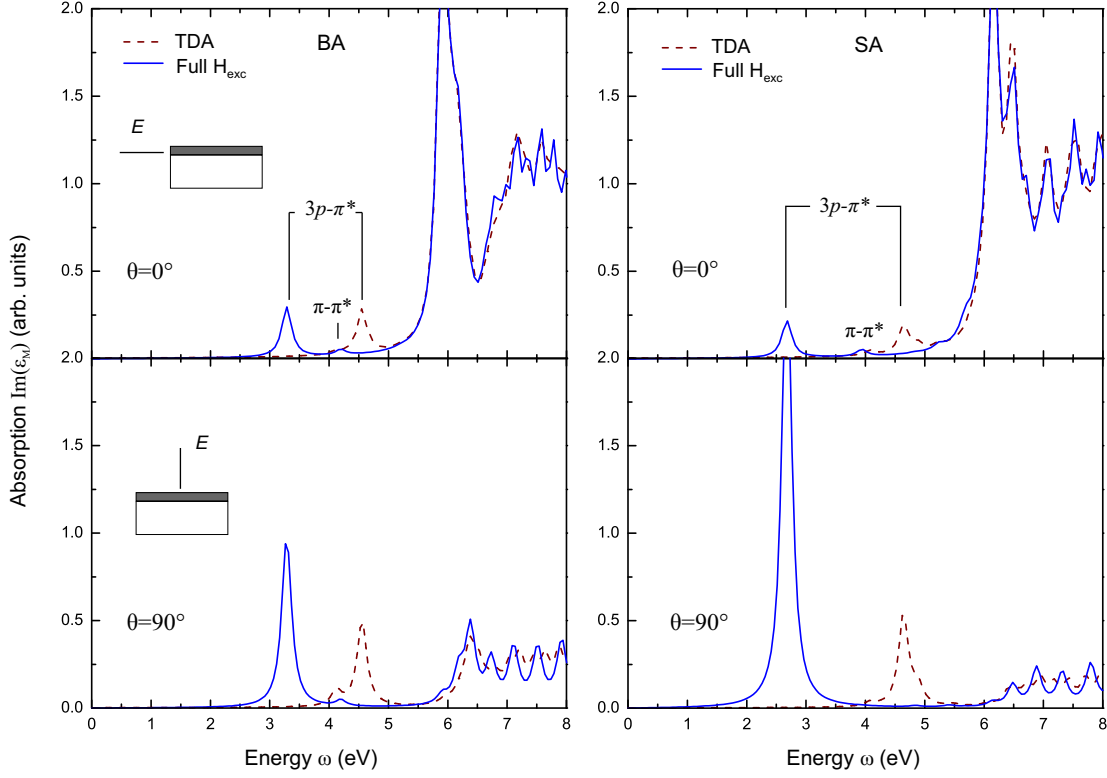


Figure 12.1: Absorption spectra of the BA and SA molecules adsorbed on NaCl(100) calculated within the Tamm-Dancoff approximation (TDA) and full excitonic Hamiltonian. The perturbative polarization direction with respect to the surface is denoted by θ . The spectra are broadened by a 0.1 eV Lorentzian.

occurs at 4.6-4.7 eV for both molecules, which is assigned to the transition from the VBM (Cl 3p) to the anti-bonding π^* state of the adsorbate. This peak thus is attributed to a charge transfer exciton, which in principle arises from the overlap between the surface VBM and the delocalized π^* orbital of the molecule. The presence of the charge transfer exciton is somehow surprising since in the ground state there is nearly no charge transfer from the molecule to the surface. At 6.0-6.1 eV the most strong absorption peak appears in the parallel polarization due to the surface exciton of the four-layer NaCl(100) slab. The surface exciton is much smaller than the bulk exciton (7.6 eV from the G_0W_0 eigenvalues), in line with the results of some other wide-gap materials [148, 149]. The peak related to the surface exciton is nearly fully suppressed for the transverse field ($\theta = 90^\circ$).

When the coupling part is switched on in the full Hamiltonian calculation, a sizeable *red-shift* of the $3p - \pi^*$ absorption peak can be witnessed in Fig. 12.1 for both molecules. The shift amounts to 1.3 and 2.0 eV for the BA and SA adsorbates, respectively. Remarkably, not only the excitation energy shifts, but the intensity of the $3p \rightarrow \pi^*$ transition also grows much stronger when $\theta = 90^\circ$. Such large perpendicular

transition dipole moment further evidences that the exciton is along the direction normal to the surface. The much stronger oscillating strength of this peak for the adsorbed SA molecule is benefitted from its adsorption configuration, as the SA molecule is more parallel and closer to the surface, resulting in a stronger overlap between the VBM and the π^* state. On the other hand, the lowest singlet molecular excited state and the surface excited state are not much influenced by the coupling part. We have already seen this in Sec. 6.3 and 7.3 that the TDA yields reliable energies for the lowest singlet exciton of the molecules and the bulk exciton of NaCl. As a consequence, the lowest exciton state for the adsorbate system is now related to the $3p - \pi^*$ transition. The $e-h$ antipair introduced by the coupling between the resonant and antiresonant part of the excitonic Hamiltonian must be responsible for the dramatic shift of the *surface-molecule* transition. Within the TDA where the excitonic Hamiltonian is approximated by the resonant term, the excitons are the $e-h$ pairs propagating forward in time because the resonant part contains the $v \rightarrow c$ transitions of positive energy, while the antiresonant part contains the $c \rightarrow v$ transitions of negative energy. The coupling part between the resonant and the antiresonant part hence includes the $e-h$ antipairs which propagate backward in time. Therefore, the full BSE calculation involves the oscillation of the $e-h$ pairs back and forth in time. As the coupling is simply the exchange term (bare and screened) of the $e-h$ interaction, it is speculated that the prominent red shift of the $3p-\pi^*$ peak arises from the sizeable *exchange interaction* between the electron and hole. In addition, we can see from Fig. 12.1 that the $3p - \pi^*$ peak becomes much stronger when the light polarization is changed from the parallel to the perpendicular direction to the surface. This is in accordance with the fact that the excitation is spatially confined at the molecule-surface interface.

It has been shown that the TDA fails describe the plasmonic excitation in the EELS of bulk Si [150] and some confined systems [97]. When applied to some isolated molecules, the TDA can lead to a substantial shift of the lowest excitation energy [151]. Here we find that in an extended system where an organic molecule is adsorbed on an insulating surface, the TDA can be also insufficient in describing the excitonic effect when the exchange interaction of the $e-h$ pair for some specific transitions is important. As for the BA and SA adsorbates on the NaCl(100) surface, the presence of the excitation at the molecule-surface interface revealed in the full BSE calculation further reduces the excitation energy to 3.3 and 2.7 eV, respectively. While the intramolecular excitonic effect is still preserved upon adsorption, the coupling between the conjugated molecule and wide-gap insulator surface offers a more effective channel for the electronic excitation.

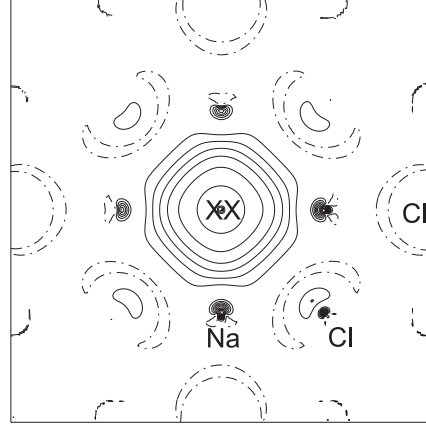
13 Roles of Surface Defects

The preceding chapters are devoted to the discussion on *ideal* alkali halide (100) surfaces. While these calculations are informative for the understanding of the molecule-surface interaction, one prefers a more realistic modeling of the system where surface defects are present. In fact, ideal surfaces with complete translation symmetry do not exist for entropy reasons. Even on pristine NaCl(100) surface, monatomic steps and kinks are also present inevitably. These surface defects are often decisive in chemical reactivity on insulator surfaces, and they play an important role in both the adsorption geometry and the electronic structure. For example, a few experiments and theoretical studies suggest dissociative adsorption of water at the color center on NaCl(100) [17, 152, 153]. Malaske *et al.* studied the adsorption of SA on the perfect NaCl(100) surface and at surface color center with EELS and UPS [16], and it was found that the binding of SA at the color center is much stronger than on undistorted surfaces. In this chapter, we shed light on the effect of surface defects by presenting two types of surface defects, namely the surface color center (F_s center) and the stepped surface. These results, together with the adsorption on ideal surfaces, provide a complete picture of the molecule-insulator interaction.

13.1 Adsorption at Surface Color Centers

In this section, the influence of NaCl(100) surface anion vacancies on the adsorption of various benzoic acid molecules is discussed. The anion vacancy, *i.e.* the color center (F center), is one of the most common point defects in ionic insulators. The term originates from the experimental observed coloration of the otherwise transparent crystals in the presence of the anion vacancies [154]. For example, the absorption peak associated with the F center at 465 nm renders the NaCl crystal yellow [155–157]. The neutral anion monovacancy is the simplest form of the F center, with a single bound electron in the vacancy center. An eminent application of anion vacancies in alkali halides is the color center laser first demonstrated in 1965 by Fritz and Menke [158]. We present in Appendix C a comprehensive description of the F center in bulk NaCl using hybrid functionals. The hybrid functionals have been shown to give a better account of the lattice relaxation for the defect systems than the GGA functional due to the reduced self-interaction. As for the adsorption at surface F_s center, we use the PW1PW hybrid functional in spin-polarized DFT calculations.

Figure 13.1: Electron-spin density of an F_s centers at NaCl(100) in the (100) plane. XX represents the anion vacancy. The lines are drawn in intervals of $0.01 e/\text{Bohr}^3$. The solid, dashed and dot-dashed lines indicate positive, negative and zero values, respectively.



13.1.1 Surface Color Center at NaCl(100)

The neutral F_s center is created from the five-layer-thick NaCl(100) slab with a (3×3) unit cell used in Sec. 8.2. One Cl atom is removed from the surface to form the anion vacancy. One unpaired electron is left in the vacancy center, whose electronic wavefunction is expanded by a *ghost* basis set. The ghost basis set is the same as that for Cl atoms. The geometry relaxation shows that the four Na atoms closest to the F_s center in the top layer shift towards the vacancy by 0.021 \AA , and the displacement of the Na atom beneath the F_s center in the second layer towards the defect is 0.29 \AA . The four second shell Cl neighbors in the top layer also show displacements of 0.021 \AA towards the vacancy. It is noteworthy that the inward relaxation of the nearest cations around the cavity is quite different from what has been found for other wide band gap ionic insulators, like MgO and LiF [159–161]. To understand this discrepancy, geometry relaxations have been calculated within the HF and DFT GGA theory, respectively. While the HF theory also predicts an inward displacement of the surface neighboring Na atoms of 0.15 \AA , the PW91 functional, however, shows an outward relaxation of 0.002 \AA . It is well-known that DFT tends to delocalize the electrons, whereas the HF favors more electron localization. The larger degree of delocalization of the unpaired electron gives rise to an effective positive electrostatic potential at the vacancy, which slightly pushes away the neighboring Na atoms. Moreover, if we remove the ghost basis function at the vacancy and add a diffuse function to the neighboring Na atoms for an adequate description of the unpaired electron, it turns out that an outward relaxation can also be achieved with the hybrid PW1PW functional. Despite the ambiguities of the relaxation behavior, the geometry perturbation induced by the F_s center is very small overall.

As shown in the spin density map in Fig. 13.1, the unpaired electron is well localized in the vacancy center. The trapping is stabilized by the Madelung potential and the effective positive charge on the vacancy. The calculation with the PW1PW functional showed a spin charge of $0.786 e$ for the *ghost* vacancy atom (XX). The rest of the spin density is spread over the nearest Na ions. The unpaired electron in the vacancy center also introduces singly occupied state in the band gap of NaCl(100). This new electron level lies 2.4 eV below the bottom of the conduction band, which is comparable to earlier

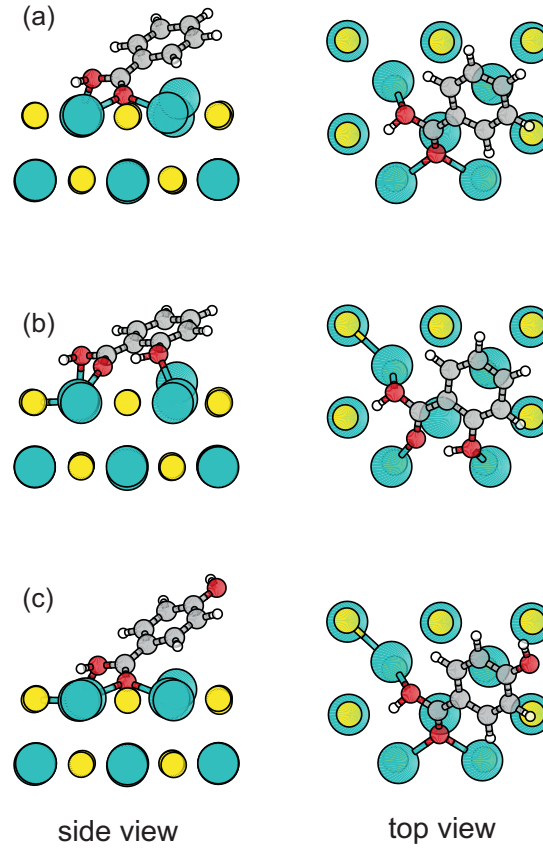


Figure 13.2: Adsorption geometries of (a)BA, (b)SA and (c)*p*-SA at an NaCl(100) F_s center. The color scheme is the same as in Fig. 8.3.

EELS results [16, 162].

The formation energy E_f of an F_s center as the energy required to extract a Cl atom is given by

$$E_f = E_d + E_{\text{Cl}} - E_{\text{NaCl}(100)} \quad (13.1)$$

where E_d and E_{Cl} are the total energy of the NaCl(100) with an F_s center and the atomic energy of an isolated Cl atom, respectively. The computed E_f for an anion vacancy is 5.79 eV at the HF level, while PW1PW gives a higher formation energy of 6.47 eV. Nevertheless, these values are in agreement with other theoretical studies.[163, 164]

13.1.2 Adsorption at Surface Color Center

The optimized adsorption geometries of various benzoic acids at NaCl(100) F_s center are given in Fig. 13.2. The ghost atom was kept fixed during the relaxation. It is evident that all molecules bind to the surface via the interaction between O atom and Na atom. For BA and *p*-SA, one carboxylic O atom forms a bond with surface Na, while the other carboxylic O atom binds to the surface in a bridging configuration across two Na atoms.

Table 13.1: Adsorption energies, representative bond lengths and spin density $\rho^{\alpha-\beta}$ of the adsorbates for adsorption at an NaCl(100) F_s center. The BSSE corrected adsorption energy is given in parenthesis. The subscripts follow the convention in Fig. 8.3.

	E_{ads} (eV)	Bond lengths d (Å)				Spin density (e)
		Na–O _{1,c}	Na ₁ –O _{2,c}	Na ₂ –O _{2,c}	Na–O _p	
BA	-1.98	2.25	2.32	2.36	0.992	
SA	-2.03 (-1.39)	2.31	2.19		2.28	1.000
<i>p</i> -SA	-1.79	2.24	2.32	2.32		0.995

Table 13.2: Changes of intramolecular bond lengths, Δd (in %), for various benzoic acids adsorbed at the NaCl(100) F_s center.

	carboxyl			phenol		
	C–O ₁	C–O ₂	O ₁ –H	C–O	O–H	O ₂ –H _p
BA	3.2	6.0	0.3			
SA	3.2	4.7	0.5	2.4	1.9	-7.0
<i>p</i> -SA	3.6	6.5	0.3	0.9	0.0	

Similar to the adsorption on NaCl(100), there is an additional bonding for the adsorption of SA through the interaction between the phenolic O and the surface Na, which makes its binding energy the largest of all three, as shown in Table 13.1. The BSSE corrected values are not included in Table 13.1 as BSSE correction gives rise to a large degree of overcorrection in the interaction energy due to the presence of the ghost basis function at the vacancy center. Alternatively, single point energy calculations at the previously optimized structures are performed without the ghost atom so that the counterpoise scheme can be applied. An additional diffuse function is added to the neighboring Na atoms around the vacancy to give an equivalent description of the F_s center. The basis set for the adsorbate molecule is also improved with the 6-311G(d,p) basis set. For SA, this results in an adsorption energy of 1.39 eV after BSSE correction, which agrees well with our calculations based on the plane-wave basis set. This implies that the real binding energy should be smaller than the values in Table 13.1 by about 0.6 eV. It is evident that the adsorption energies at the vacancy site are much higher than those on the ideal NaCl(100) surface. The increased adsorption energy is partly contributed by the stronger Na–O interactions, which is accompanied by a smaller Na–O bond lengths compared to the values on the flat NaCl(100) surface. This stronger interaction can be also seen in the intramolecular distortion of the molecules, as shown in Table 13.2. The expansions of the C–O bonds in both carboxylic and phenolic groups are much larger compared to the intramolecular distortions on NaCl(100) without defects. Nonetheless, the calculation suggests that dissociative adsorption energy of benzoic acids at the F_s center is higher by about 0.6 eV than in molecular adsorption. This is different from the

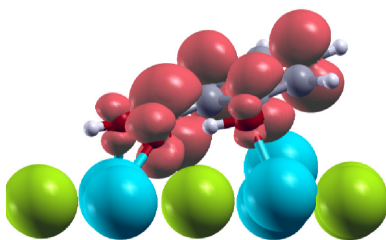


Figure 13.3: Electron spin density $\rho^{\alpha-\beta}$ isosurface for adsorption of SA at the NaCl(100) F_s center. The isovalue is $0.002 \text{ e}/\text{Bohr}^3$.

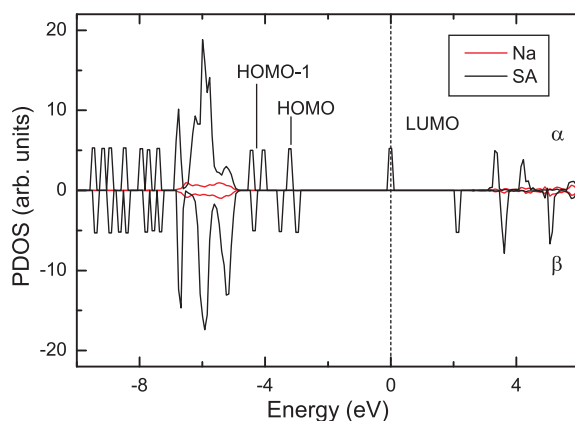


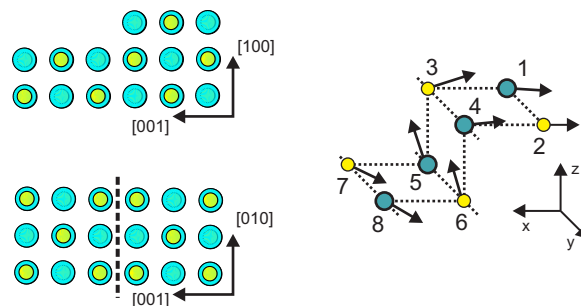
Figure 13.4: Density of states projected onto the Na atoms at the surface and the SA molecule upon adsorption at the F_s center. The LUMO is aligned to energy zero.

conclusion that dissociative adsorption of water at the surface color center is energetically favored [16, 17, 152]. Earlier experiments also revealed that SA is intact after adsorption at F_s centers on NaCl(100) [16], which agrees with our calculations.

While the vdW interaction is relatively important for the weakly bound system, it is of less importance to the adsorption at the F_s center. Without an explicit calculation of the long-range contribution, we might assume that the magnitude of the vdW interaction should be similar to that on ideal (100) surface, which is about half eV. The anion vacancy turns out to be chemically quite reactive, leading to the chemisorption of the benzoic acid molecules. This is clearly depicted in the spin density shown in Fig. 13.3, where the unpaired electron is now transferred to the carboxylic group and the aromatic ring of the SA molecule upon adsorption at the vacancy. In other words, adsorption at the vacancy causes a local *magnetization* of the adsorbate molecule. This large charge transfer is indeed the origin of the enhanced binding energy. It can be seen from Fig. 13.2 that the surface Na^+ cation is attracted by the increased electron density delocalized on the aromatic ring, and consequently it shows a small displacement towards the molecule.

Due to the pronounced charge transfer, the spin-resolved PDOS in Fig. 13.4 shows that the LUMO for the SA molecule is now partly occupied. Meanwhile, the HOMO

Figure 13.5: Slab model (left) and geometric relaxation (right) of [001] step on NaCl(100). Only the [001] step and two underlying NaCl(100) layers are shown. The arrows represent the directions of the atomic displacements. The white and black circles on the right denote Na and Cl atoms, respectively.



and the HOMO-1, which are mainly located at the aromatic ring, are now split. Apart from the broadening due to the resonance, the HOMO-2 also exhibits spin-polarized behavior due to the spin density at the carboxylic group. It turns out that the electronic properties of the organic molecule adsorbed at the color center are largely altered. This is also consistent with the sizeable changes in the intramolecular structure.

To summarize, the adsorption at the surface color center is in contrast to that on the ideal (100) surface. The charge transfer of the unpaired electron at the vacancy to the molecule gives rise to a chemisorption of the molecule with a large binding energy and a pronounced intramolecular distortion. Most notably, the energy gap of the molecule-insulator interface is no longer determined by the HOMO-LUMO gap of the molecule.

13.2 Effect of Non-Polar Stepped Surface

A step is an important line defect, in which the ledge separates two terraces from each other. In case of alkali halide surfaces, monatomic steps, *i.e.* steps of single atomic height prevail. Steps on NaCl(100) have been found to enhance the adsorption of H_2O [17, 153, 165] and CO_2 [166]. The electronic structures of ionic materials are also dependent on the properties of the steps on the surfaces [167]. In this section, we first examine the properties of a non-polar stepped surface, namely the [001]-oriented step on NaCl(100) surface.

13.2.1 Bare [001]-oriented Step

The [001] monatomic step, presented in Fig. 13.5, is created from a NaCl(301) vicinal surface. The monatomic step is separated by (100) terraces with a width of three anion-cation interatomic distances. Calculations are performed with the PW1PW hybrid functional in localized basis sets, using a 4×4 \mathbf{k} -point mesh corresponding to 10 \mathbf{k} -points in the IBZ. The geometry relaxation reveals that the atoms near the step edge tend to move towards their first neighbors, which is illustrated in Fig. 13.5. Due to symmetry reasons, there is no atomic displacement in the direction parallel to the step edges. From Table 13.3, we find that the most under-coordinated atoms, *i.e.* the edge atoms (Cl_3 and Na_4 in Fig. 13.5) show the largest displacement. The lower edge atoms (Na_5 and Cl_6) move out of the (100) plane to get closer to their first neighbors, which can be seen as bond contractions in Table 13.3. Further, the bond contraction is much

Table 13.3: Geometric relaxation of the atoms at the [001] step edge site. The subscripts of the atoms are the same as in Fig. 13.5. The color scheme follows the convention as Fig. 8.3.

	Displacement (Å)	
	Δx	Δz
Na ₁	-0.11	-0.03
Cl ₂	-0.12	0.00
Cl ₃	-0.20	0.14
Na ₄	-0.26	0.10
Na ₅	0.08	0.15
Cl ₆	0.07	0.13
Cl ₇	-0.01	-0.08
Na ₈	-0.02	-0.14

	Changes of interatomic distances	
	Δd (Å)	Δd (%)
Na ₁ -Cl ₃	-0.14	-5.1
Cl ₂ -Na ₄	-0.16	-3.7
Cl ₃ -Na ₅	-0.05	-1.7
Na ₄ -Cl ₆	-0.01	-0.5
Na ₅ -Cl ₇	-0.05	-1.9
Cl ₆ -Na ₈	-0.05	-1.6

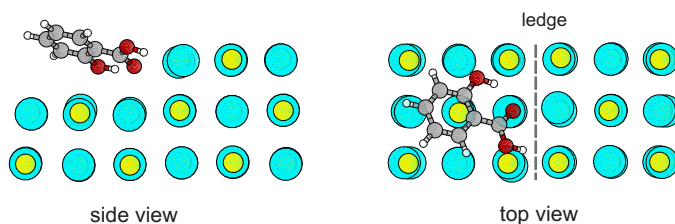
stronger when the coordination number (Z) of the atom connected to the edge atom is smaller. For instance, the distance between the edge atom Na₄ and step terrace atom Cl₂ ($Z=5$) is 2.696 Å, while the lower edge atom Cl₆ ($Z=6$) is 2.792 Å away from Na₄. Generally the Madelung potential acting on the under-coordinated atoms decreases as the coordination number of their first neighbors decreases. The bond contraction can be regarded as a compensation of the Madelung potential, and thus it becomes larger in the presence of more under-coordinated atoms. However, the overall atomic displacements and bond contractions for the [001] step are still quite limited.

The ledge formation energy can be expressed as

$$E_{\text{ledge}} = \frac{E_{\text{step}} - nE_{\text{bulk}} - 2\gamma A}{mL}, \quad (13.2)$$

where E_{step} is the total energy of the stepped slab which includes n formula units of NaCl. γ , A and L represent the surface energy of NaCl(100), surface area and step length, respectively. The factor m , accounting for the number of ledges in the unit cell, is 4 for the [001] step. The calculated ledge energy is 67 meV/Å for the rigid stepped surface. Geometric relaxation further decreases the ledge energy to 51 meV/Å. It should be borne in mind that the ledge energy consists of the step energy which is required to

Figure 13.6: Adsorption geometry of SA at the [001] step edge on the NaCl(100) surface. The color scheme follows the convention as Fig. 8.3.



form the step, and the step-step interaction which depends on the separation of the steps [119, 168]. Nonetheless, the actual step energy should be slightly lower than the ledge energy since the inter-step interaction only has a small contribution to the ledge energy [119].

The band structure of the NaCl(301) stepped surface is very close to that of the flat surface. The small perturbations of Madelung potentials around the step site are effectively compensated through geometric relaxation. The computed band gap of 7.46 eV is comparable to that of the flat NaCl(100) surface, in agreement with experiment [169].

13.2.2 Adsorption at the [001] Step

We show here the adsorption of SA as an example, whose most stable adsorption geometry at the [001] step is presented in Fig. 13.6. At the optimized adsorption configuration, the carboxylic O atom of C=O group prefers to bind to the surface at a bridge adsorption site, where it interacts with both the Na atom at the step edge and the Na atom of NaCl(100). Since the step edge atoms are more under-coordinated, the binding of carboxylic O to the step edge Na is stronger than that to the surface Na atom. This can be manifested by the shorter bond length to the step edge Na atom (2.48 Å) than to the surface Na atom (2.61 Å). Likewise the bond length between carboxylic H atom and step edge Cl atom (2.13 Å) is contracted compared to that on the ideal NaCl(100) (see Table 8.2). In addition, the phenolic O atom also interacts with the surface Na atom with an interatomic separation of 2.75 Å. The charge gain on SA after adsorption is 0.02 e according to the Mulliken population analysis. The PW1PW binding energy including BSSE correction is 0.72 eV, which is 0.24 eV larger than on flat NaCl(100) surface. This affirms that steps are preferred binding sites for molecular adsorption on NaCl surface.

The electronic structure of benzoic acids adsorbed at the [001] step is, not surprisingly, similar to the adsorption on the flat NaCl(100) surface because of the identical bonding mechanisms. The calculated PW1PW gap for SA adsorbed at the [001] step edge is 4.75 eV, nearly identical to the band gap on NaCl(100) surface. The alignment of the HOMO and the VBM is also consistent with the result on ideal surface. While vdW interaction is not included in PW1PW calculations, its impact on the electronic structure should be rather limited according to the discussion on the ideal surface. Hence, when a molecule is exposed to a non-polar stepped surface, the step edge provides a preferred binding site, while the electronic structure of the adsorbate system does not vary much from that of the molecular adsorption on the ideal surface.

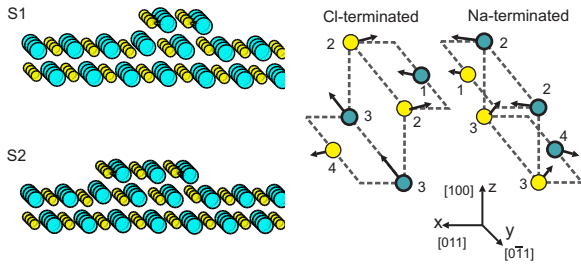


Figure 13.7: Schematics of relaxed geometries for the $[011]$ step on $\text{NaCl}(100)$ with a step width of 4 (S1) and 6 (S2) atomic rows. The inset shows the displacement directions of the atoms at the step edge site based on the S2 model. The color scheme follows the convention in Fig. 8.3.

13.3 Roles of Polar Steps

13.3.1 Bare $[011]$ Step

Polar steps are often very different from the non-polar ones in terms of the structural parameters and the electronic properties because of the varied electrostatic environment. In Fig. 13.7, two stoichiometric NaCl $[011]$ -oriented step models with different step terrace widths are presented. Unlike the $[011]$ step, the edge of the $[011]$ step is either terminated with Cl or Na atomic rows. Such alternating atomic rows generate a net dipole moment along $[01\bar{1}]$ arising from the nonzero electrical field between the two neighboring atomic rows [170–173]. The total dipole moment is thus clearly proportional to the number of the atomic rows along the step direction. This implies that the S2 model is more polar than the S1.

The $[011]$ step edge atoms is three-fold coordinated, making them even more under-coordinated than the step edge atoms of the $[001]$ step. The values of atomic charges at the step edge are smaller than those at the step terrace and on the regular surface according to the Mulliken analysis, which corresponds to a lower ionicity at the step edge. Therefore a much larger geometric relaxation is expected, as is presented in Table 13.4, especially for the edge atoms which have the largest displacements and move towards their nearest neighbors in order to compensate for the reduced Madelung potential. Similar to the $[001]$ step, the upper edge atoms tend to retract from step within their layer, in contrast to the lower edge atoms. It is also found that at the Na-terminated step site, the step edge Na atom shows a larger relaxation than the step edge atom at the Cl-terminated site. Generally both stepped surfaces exhibit almost the same geometric relaxation, and the displacements of step edge atoms in the S2 model are slightly larger due to its higher polarity. Similar behaviors are expected for KCl stepped surface.

The ledge energy of the NaCl $[011]$ step, as calculated from Eq. (13.2) with $m=2$, is substantially higher than that of the $[001]$ step. The rigid $[011]$ step shows ledge energies of 339 and 406 meV/Å for the S1 and S2, respectively¹ Relaxation effects significantly lower the ledge energy to 180 and 209 meV/Å, nearly half of the value of the rigid step. The higher ledge energy for the S2 is consistent with its larger atomic displacements of the step edge atoms, as a consequence of the higher polarity along the step direction.

¹ We do not attempt to correct the artificial dipole moment stemming from the periodic repetition of the slab model in the two-dimensional direction. After all, the model proposed here is hypothetical and the total energy correction to the dipole moment does not affect the observed trend.

Table 13.4: Geometric relaxation of the atoms at the NaCl [011] step site. The subscripts of the atoms are illustrated in Fig. 13.7.

	S1		S2	
	Δx (Å)	Δz (Å)	Δx (Å)	Δz (Å)
Cl-terminated				
Na ₁	0.22	0.15	0.13	0.14
Cl ₂	-0.21	0.12	-0.27	0.16
Na ₃	0.26	0.36	0.25	0.41
Cl ₄	0.13	-0.12	0.16	-0.10
Na-terminated				
Cl ₁	-0.07	0.21	0.03	0.21
Na ₂	0.42	0.01	0.48	0.01
Cl ₃	-0.21	0.28	-0.22	0.32
Na ₄	-0.16	-0.16	-0.20	-0.14
	S1		S2	
	Δd (Å)	Δd (%)	Δd (Å)	Δd (%)
Cl-terminated				
Na ₁ -Cl ₂	-0.29	-10.1	-0.27	-9.4
Cl ₂ -Na ₃	-0.19	-6.8	-0.20	-7.1
Na ₃ -Cl ₄	-0.05	-1.6	-0.02	-0.8
Na-terminated				
Cl ₁ -Na ₂	-0.31	-11.0	-0.29	-10.4
Na ₂ -Cl ₃	-0.20	-7.0	-0.21	-7.5
Cl ₃ -Na ₄	-0.00	-0.1	0.02	0.8

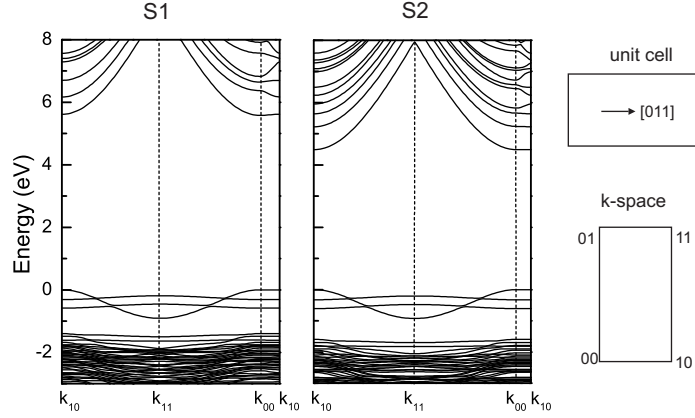


Figure 13.8: Band structures of the relaxed NaCl [011] stepped surface constructed by two slab models. The VBM is aligned to energy zero. The lattice vectors of the real-space and the reciprocal-space unit cells are not to scale.

As for the relaxed KCl [011] step, the calculated PW1PW ledge energy amounts to 199 meV/Å using the S2 model.

The electronic structure, particularly the band gap of a stepped surface, is explicitly dependent on the local electronic environment of the step edge atoms. For ionic insulators like NaCl, the VBM is mostly of Cl p character, whereas the CBM has a contribution from Na s state. The separation of the VBM and CBM is therefore sensitive to the anion-cation interaction. Generally, a weaker Madelung potential is corresponding to a smaller gap width. Indeed, we find that the PW1PW band gap of a rigid [011] step (S1) is merely 2.81 eV. Geometric relaxation compensates the Madelung potential by bond contractions around the step edge atoms, shifting the Na and Cl energy levels towards higher and lower energies, respectively. This results in a substantial recovery of the band gap to 5.58 eV after relaxation, but it is still about 2 eV smaller than that of the flat surface. An interesting feature in the band structure (Fig. 13.8) is the splitting of the VBM. The states that appear near the valence band edge are localized around the Cl atoms at the step edge, a consequence of the lowered electrostatic potential. Moreover, the S2 model shows a smaller gap width of 4.52 eV, associated with a larger split of the VBM because of the higher polarity. The dispersion of the VBM along $k_{10} - k_{11}$ and $k_{10} - k_{00}$ indicates a strong inter-atomic interaction between the step edge Cl atoms.

The effect of the polar step on the electronic structure is also present for the KCl [011] stepped surface. The calculated PW1PW band gap based on the S2 model is reduced by 3.7 eV compared to the bulk value. To conclude, we find that the reduced Madelung potential acting on the under-coordinated [011] step edge atoms results in much larger relaxation than on a surface with [001] steps. As a result, the band gap is significant reduced due to the shift of the energy levels of step edge anions towards mid-gap.

Figure 13.9: Adsorption geometry of SA at the Cl-terminated side of the [011] step on NaCl(100). The color code follows the convention as Fig. 8.3.

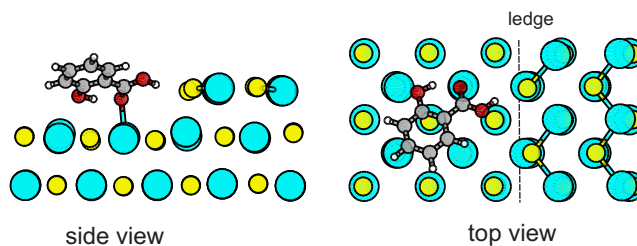
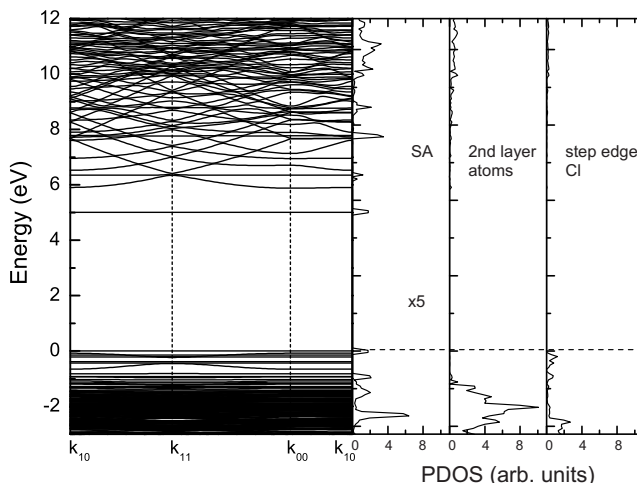


Figure 13.10: Band structure (left) and PDOS (right) of SA adsorbed at the Cl-terminated side of a [011] step on NaCl(100) obtained from the S1 surface model. The highest occupied state is shifted to energy zero.



13.3.2 Adsorption at the [011] Step

The stoichiometric [011] stepped surface provides two potential adsorption sites, one at the Cl-terminated step edge and the other on the Na-terminated side. We first briefly discuss the adsorption at the Cl-terminated site, using the SA molecule adsorbed at the NaCl [011] step (S1) as an example. The choice of the slab model is not critical and it shall not influence the general conclusion since the two models differ from each other by a rigid shift of the VBM and CBM.

The adsorption geometry optimized with the PW1PW functional is depicted in Fig. 13.9, where a carboxylic H atom binds to the step edge Cl atom with a bond length of 2.17/Å. Meanwhile, we see carboxylic and phenolic O atoms interact with the Na cations on the (100) terrace in the same fashion as the adsorption on (100) surface. The PW1PW adsorption energy is -0.80 eV including BSSE correction. The intramolecular distortion is comparable to that on the flat surface, and nearly no charge transfer is observed upon adsorption.

The PW1PW band structure and PDOS shown in Fig. 13.10 reveals that the effective band gap corresponds to the HOMO-LUMO separation of the SA molecule upon adsorption at the Cl-terminated step edge of the [011] step. Analogous to the adsorption on (100) surface discussed in Sec. 8.2.2, the alignment of the molecular orbital with respect to the stepped surface is indeed dominated by the interaction between the HOMO-2 and the Na 3s states. Accordingly, the whole molecular orbitals are shifted relative to the effective potential of the surface. We note that due to the small separation between

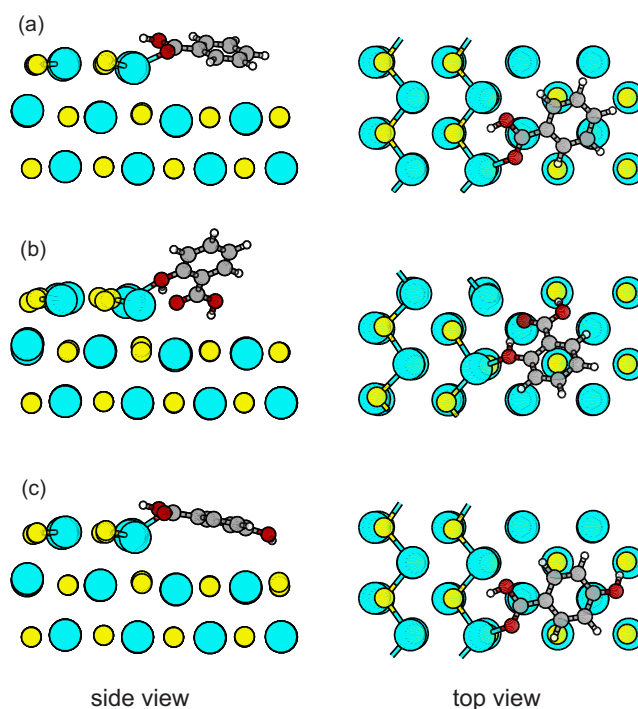


Figure 13.11: Adsorption geometries of (a) BA, (b) SA and (c) *p*-SA bound to the Na-terminated step edge of the [011] step on NaCl(100).

the HOMO and HOMO-2 for the BA molecule (cf. Table 6.2), a different alignment occurs where the HOMO of the BA adsorbate lies marginally below the VBM of the stepped surface. Nevertheless, the overall band gaps for all three benzoic acids adsorbed at Cl-terminated step edge are of the similar magnitude as those obtained on the ideal (100) surfaces.

Now we move the adsorption site from the Cl-terminated site to the Na-terminated step edge. As a first step, we show the adsorption configurations of the benzoic acid molecules at the NaCl [011] stepped surface.

The adsorption geometries optimized with the PW1PW hybrid functional are illustrated in Fig. 13.11. All configurations share a common Na–O bond and a less influential Cl–H bond, whereas an additional Na–O bond takes place for the SA adsorbate from the phenolic O atom. From Table 13.5, we see that the average Na–O bond length is shorter than that on the ideal NaCl(100) surface. This indicates that the binding between the O atom and the under-coordinated Na atom at the step edge is stronger, in accordance to the larger adsorption energy shown in Table 13.5. Hence, the molecules are more likely to be found at the Na-terminated step edge site.

We now extend the study to the adsorption at KCl [011] stepped surface. To address the influence of the vdW interaction, the semi-empirical PBE-D method is employed. In Fig. 13.12, some representative adsorption configurations of the BA and SA adsorbate systems are illustrated with the long-range dispersion correction. The corresponding

Table 13.5: Adsorption energies and representative bond lengths for adsorption at the Na-terminated step edge of the [011] step on NaCl(100) (S1). The subscripts c and p denote atoms in carboxylic and phenolic group, respectively.

	Adsorption Energy (eV)		Bond lengths d (Å)			
	E_{ads}	E_{ads}^{BSSE}	Na–O _{1,c}	Na–O _{2,c}	Cl–H _c	Na–O _p
BA	-1.09	-0.87	2.47	2.26	2.46	
SA	-1.21	-0.99	3.59	2.40	2.09	2.28
p -SA	-1.18	-0.91	2.45	2.26	2.57	3.26

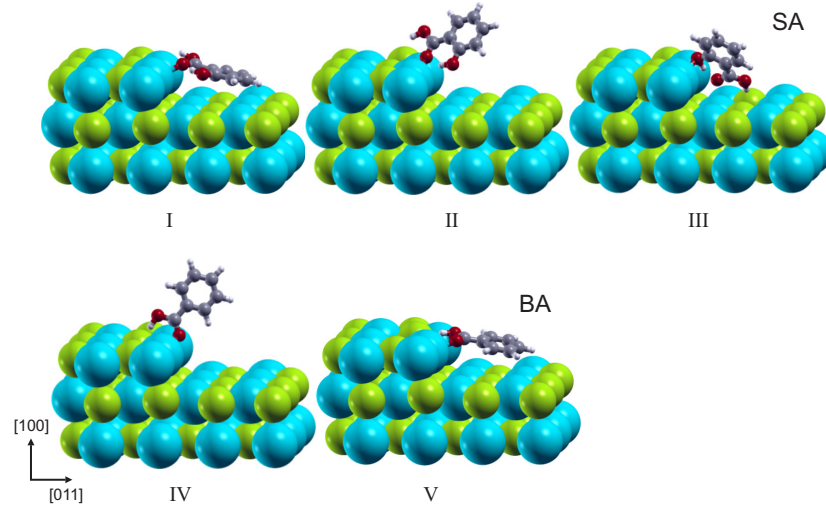


Figure 13.12: Adsorption sites of SA (I to III) and BA (IV and V) at the KCl [011] step with different configurations optimized by the semi-empirical PBE-D method with vdW interaction included.

Table 13.6: Molecular E_{ads} (in eV) for various adsorption configurations at the K-terminated step edge of the KCl [011] stepped surface calculated by the PBE-D method. The configurations refer to the structures in Fig. 13.12.

Configuration	Total E_{ads}	GGA-PBE	vdW
SA			
I	-0.68	-0.23	-0.45
II	-0.38	-0.15	-0.23
III	-1.10	-0.67	-0.43
BA			
IV	-0.99	-0.76	-0.23
V	-0.98	-0.47	-0.51

adsorption energies calculated with the PBE-D method are given in Table 13.6, including the contributions from the semilocal GGA-PBE functional and the vdW interaction. One readily identifies that the structure (III) in Fig. 13.12 is the preferred adsorption configuration for SA where the carboxylic group points towards the lower terrace of the (100) surface while the phenolic O is in close proximity to the under-coordinated K atom at the step edge. This coincides with the optimal adsorption geometry predicted by the PW1PW functional (cf. Fig. 13.11). While this configuration has the largest energy gain already from the GGA part, we see in Table 13.6 a sizeable contribution from the long-range vdW interaction. In structures (I) and (II), the vdW interaction is predominant for the molecular adsorption, whereas in (III) we find a larger ionic contribution to the adsorption energy. Thus the inclusion of vdW forces does not change the trends set by the hybrid functionals. As for the BA molecule, the GGA functional prefers the configuration (IV) in Fig. 13.12 in which the adsorbate binds to the step edge site in an upright configuration. The inclusion of dispersion, however, gives rise to another flat configuration on (100) terrace with almost the same adsorption energy as that of the standing up configuration (see Table 13.6). Obviously, opposed to structure (IV), the vdW interaction is now predominant due to the close proximity between the molecular plane and the low lying surface, which compensates for the smaller electrostatic interactions in the flat configuration. Therefore, at low coverage both configurations (IV and V) are energetically equivalent for the adsorption of BA at the [011]-stepped surface although their binding mechanisms differ. Nevertheless, as the adsorption on flat surfaces, the optimal adsorption geometry is still governed by the local electronic environment. Using the PW1PW1 hybrid functional, we find E_{ads} of -0.89, -0.97 and -0.94 eV for the BA, SA and *p*-SA adsorbate systems at the KCl [011] step edge including BSSE correction, respectively. These values are in line with those at the same step site on NaCl.

We now see in Fig. 13.13 that the presence of the polar step effectively reduces the PW1PW band gap of the adsorbate system when a molecule is adsorbed at the Na-

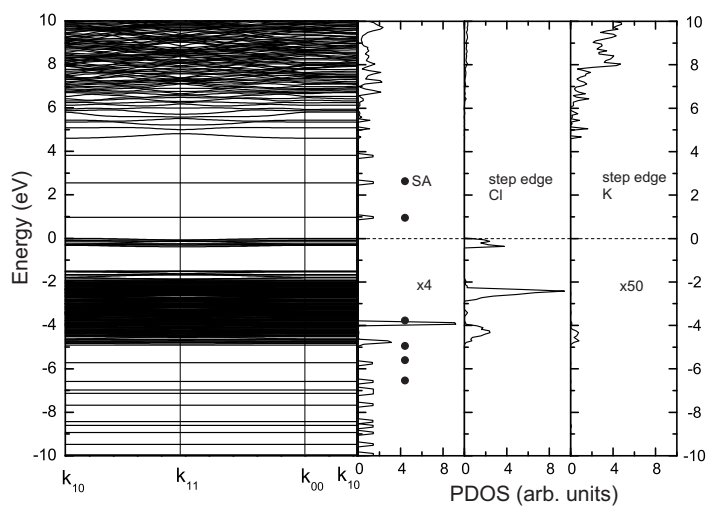


Figure 13.13: Band structure (left) and PDOS (right) of SA adsorbed at the K-terminated edge of the KCl [011] stepped surface calculated with the PW1PW functional. The dots give the molecular orbital energies of a gas-phase SA molecule. The HOMOs of the gas-phase and the adsorbed molecule are aligned. The top of the valence band is energy zero.

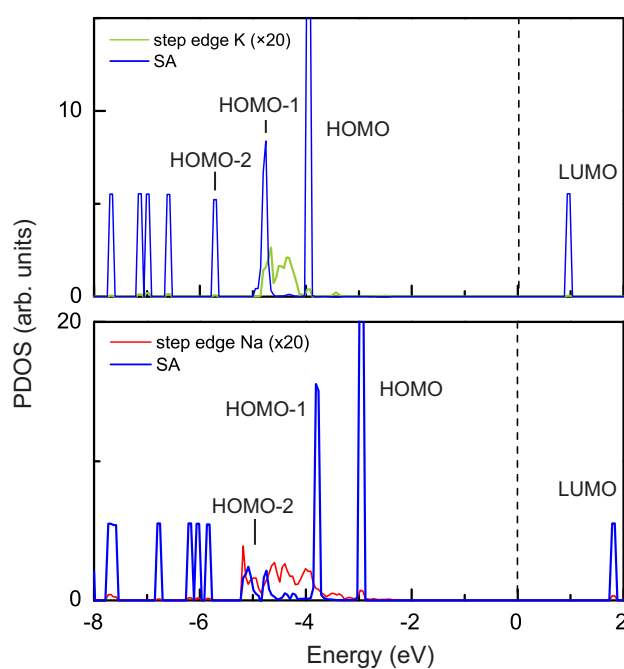


Figure 13.14: Projected density of states onto the SA molecule adsorbed at the cation step edge site of the KCl and NaCl [011] steps, using the PW1PW hybrid functional. The top of the stepped surface valence band is energy zero.

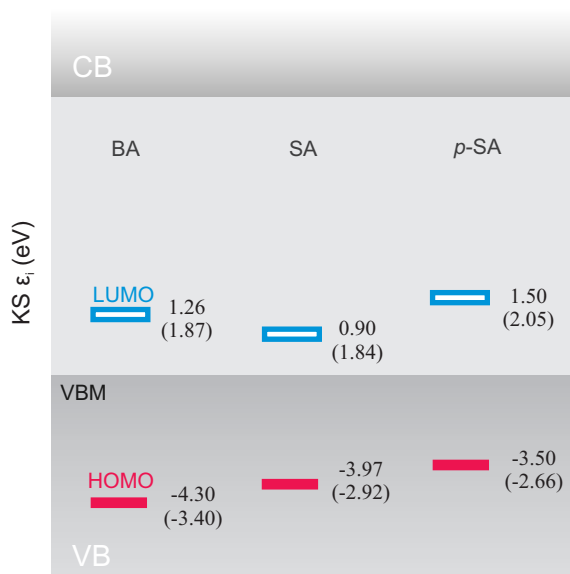


Figure 13.15: Band diagram of BA, SA, and *p*-SA adsorbed at the cation step edge of the KCl [011] stepped surface calculated with the PW1PW functional. The KS eigenvalues of the adsorbates are shifted with respect to the VBM of the stepped surface. The energy levels for adsorbates at the NaCl surface are shown in parentheses.

terminated step edge. The effective gap amounts to the separation between the LUMO and the VBM of the stepped surface. Most notably, the gap of the SA/KCl [011] stepped surface is about 1 eV smaller than the NaCl counterpart as is shown in Fig. 13.15. The origin of the discrepancy is revealed in the PDOS, as a consequence of the different resonance states of the adsorbate with the *s* states of the step edge cations. On the NaCl stepped surface, the HOMO-2 is broadened into resonance, whereas the HOMO-2 is apparently not coupling to the KCl [011] step, leaving the HOMO-1 in resonance with the valence states from the step edge cations. This is in agreement with what has been found on flat KCl (100) surface where the HOMO-1 exhibits more evident smearing than the HOMO-2 does. The different schemes of alignments on these two surfaces consequently shift the whole MOs and put the LUMO closer to the top of the valence band for the KCl stepped surface. It can be also seen in Fig. 13.13 that the relative distance between the MOs of the adsorbate agrees well with the isolated molecule.

In Fig. 13.15 the effective PW1PW band gaps of the three hydroxybenzoic acids adsorbed at the NaCl and KCl [011] stepped surface are given, along with the alignment of the MOs referenced to the VBM. As expected, the effective gaps for BA and *p*-SA adsorbed at the KCl polar step are about 0.6 eV smaller than those at the NaCl step. To this end, it is clear that the band gap of the adsorbate system is determined by both the *intrinsic* HOMO-LUMO gap and the *resonance* with respect to the surface, and it does not matter whether there is a surface defect or not. As a matter of fact, we always find that the KS band gaps for the SA adsorbed slabs have the smallest effective gap among the chosen benzoic acid molecules. This is not a coincidence provided with the similar characteristics of the MOs involved in the resonance (e.g. HOMO-2) and the HOMO-LUMO separations of the three molecules.

Due to the large size of the adsorbate on the polar stepped surface, the Green's function based MBPT calculation becomes formidable within the current computational

scheme. Although quantitative descriptions of the dynamic correlation effect and excitonic effect require the GW quasiparticle energies and BSE calculation, their influences can be implied from the previous calculations on flat surfaces. We first note that the quasiparticle correction for adsorption at the polar stepped surface will increase the PW1PW band gap. This is a reasonable assumption because the quasiparticle energy gaps of the molecules are much larger than the PW1PW gaps (Fig. 6.2). The alignment of the HOMO with respect to the VBM of the stepped surface, however, should be less modified by the quasiparticle energy correction since the valence states can be well described by the PW1PW hybrid functional. As a result, the G_0W_0 quasiparticle energy gap of the adsorbate system at the polar stepped surface should also be significantly smaller than that on the ideal flat surface. Moreover, it has been revealed in Ch. 11 that the polarization in the surface reduces the molecular energy gap of the adsorbate on the ideal (100) surface by about 1 eV. As the magnitude of the renormalization is related to the molecule-surface separation according to the classical image charge theory, a similar reduction of the molecular energy gap is expected at the stepped surface due to the surface polarization effect. The situation becomes more complex when the excitonic effect comes into play. It is unclear at this stage how the coupling between the molecule and the polar step edge could modify the electronic excitation spectra. In fact, the excitation at the stepped surface must be different from that on the ideal (100) surface presented in Ch. 12, because the VBM, *i.e.* the $3p$ valence states localized at the step edge Cl atoms are spatially separated from the adsorbate in the employed stepped surface model (Fig. 13.12). Thus, unlike the adsorption on (100) surface, it is doubtful that the transition can take place between the VBM of the stepped surface and the LUMO of the adsorbate. However, even without an explicit account of these higher-order dynamic correlation effect and excitonic effect, it turns out that while non-polar defects have a small effect on the electronic structure of the adsorbate system, polar defects can impose prominent influence on the alignment of the molecular orbitals with respect to the valence band of the substrate through tailoring the local electrostatic environment.

14 Summary and Perspectives

14.1 Discussion

When the present work was first initiated by the intriguing contact charging effect in technological applications, KS-DFT was the method of choice and the problem is reduced to the investigation on the electronic properties of the selected organic molecules. However, it soon became apparent that the interfaces of the organic molecules and wide-gap insulators are not as trivial as one would expect. The complex interaction at the interface imposes some interesting effect on the molecular adsorbate. Hence, the influence of the underlying substrate cannot be neglected anymore, and it is crucial to treat the coupled molecule and surface as a whole. In addition, we have shown in Part III that methods beyond KS-DFT are necessary for an accurate account of the energy gap and the dynamic correlation effect at the molecule-insulator interface. Even for a single gas-phase molecule, LDA in KS-DFT could predict distorted spectra for the occupied molecular orbitals, and the strong molecular excitonic effect addressed in Ch. 6 can only be taken into account in a state-of-art MBPT formalism. This work uncovers how our understanding of the molecule-insulator interface is refined through the gradually developed level of theory.

As mentioned in the Introduction, the puzzle behind the contact charge effect is intimately related to the electronic excitation. In a simplified picture where we just consider the electronic excitation on a single wide-gap insulator surface, the magnitude of the excitation energy has been found to be dependent on the intrinsic molecular energy gap of the hydroxybenzoic acid molecules. We first discuss the implications of the calculation to the single organic molecule. Using the PW1PW hybrid functional, we saw in Sec. 6.2 that the salicylic acid (SA) possesses the smallest HOMO-LUMO gap among all three molecules, while the benzoic acid (BA) molecule owns the largest gap. The quasiparticle correction to the HOMO and the LUMO in *GW* approximation does not alter the relative trend of the molecular energy gaps from the hybrid functional. The shift of the quasiparticle energy depends on the electronic localization of the orbital. This tendency is still maintained when the molecular excitonic effect is included in Sec. 6.3 as the exciton binding energy is proportional to the quasiparticle energy gap of the molecule. From the theoretical perspective, we feel the urge to at least use the hybrid functional even for the gas-phase conjugated molecules. The spurious self-interaction in the local (or semilocal) approximation of DFT exchange-correlation energy ruins the correct ordering the highest occupied molecular orbitals of the BA and *p*-SA molecule.

While the general features of the molecular orbitals are preserved when the hydroxybenzoic acid molecules are adsorbed on the ideal (100) surface of alkali chloride surfaces, the broadening of some interacting orbitals evolves an important signature of the

molecule-surface interaction. In Sec. 8.2.2, we find the covalent characteristic of the involved bonds mostly between the oxygen and surface cations. Although this covalent interaction does not contribute to the attractive binding energy, it is crucial in determining the adsorption geometry of the hydroxybenzoic acid molecules. The different adsorption configuration on NaCl and KCl(100) surfaces can be explained by the symmetry of the molecular orbitals, which are in resonance with the surface (Sec. 10.1). Even if the long-range vdW force is included, it can be seen in Sec. 9.2 that the tilting angle of the molecules and the distance between the molecule and surface are barely affected. This refreshes our knowledge of the role of the covalent contribution at the molecule-insulator interface. For a wide variety of carboxylic acids on a wide-gap insulating surface, there is no strict boundary between the physisorption and the chemisorption, because both electrostatic and covalent interactions are involved. We see that the binding energy for a single benzoic acid on NaCl or KCl(100) surface is about 0.4-0.5 eV from the short-range contributions, and about 0.5 eV from the long-range vdW interaction. The short-range attractive interaction comes from the ionic contribution, since the covalent interaction simply acts as a Pauli barrier.

The electronic structure of the benzoic acids on the ideal (100) surface in terms of the KS-DFT calculations does not reveal much excitement. The effective PW1PW energy gap is usually reduced to the HOMO-LUMO gap of the adsorbate because of the relative alignments of the frontier orbitals to the VBM of the surface. However, this scenario changes significantly if we include the dynamic correlation in the *GW* calculations in Sec. 11.2. Due to the polarization effect in the surface, the HOMO and LUMO experience sizeable renormalization and the quasiparticle energy gap exhibits a reduction of over 1 eV for the hydroxybenzoic acid molecules. This can be understood by the classical image charge theory, where the addition or removal of an electron in the molecule induces a corresponding image charge in the surface. Whereas the dielectric constant of the wide-gap insulator is relatively small, the *GW* calculations indicate that the reduction of the molecular energy gap can be still quite substantial.

The most striking feature appears in the Ch. 12 when the electron-hole interaction is taken into account for the adsorbate system. The BSE calculation using the full excitonic Hamiltonian finds a peculiar strong peak with an absorption energy in the vicinity of 3 eV when the light polarization is perpendicular to the surface. The excitation energy related to this peak, which is assigned to the transition from the VBM to the LUMO, is about 1 eV smaller than the molecular lowest singlet exciton energy of the π - π^* transition. In particular, we find that the position of this peak is shifted to higher energy if the electron-hole antipairs with negative frequencies are neglected in the Tamm-Dancoff approximation. This implies that this lowest excitation confined at the molecule-insulator interface has a substantial exchange of the *e-h* interaction. We show that for the conjugated molecule coupled to the wide-gap insulator, this intriguing excitonic effect can take place and it can only be accounted in a full BSE calculation. The presence of the molecule-surface exciton further reduces the excitation energy with respect to the gas-phase molecule.

Up to now, it has been quite a long journey from the KS-DFT to the Hedin's *GW* approximation, and ultimately to the two-particle BS equation during the adventure

of exploring the interface between the organic molecules and the wide-gap insulator surface. We recall that the KS-DFT with LDA gives an effective energy gap of about 3-4 eV for the various hydroxybenzoic acids adsorbed on NaCl and KCl(100) surfaces. Thus, the LDA gaps fortuitously coincide with the BSE excitation energies. This is, however, not too surprising because of the error cancellation in the LDA results. The LDA severely underestimates the band gap of the insulator and the HOMO-LUMO gap of the molecule. On the other hand, it totally misses the dynamic correlation effect and the excitonic effect, which tends to lower the excitation energy. Most notably, we show that the origin of the lowest excitation from the LDA and the BSE is fundamentally different.

In Ch. 13 we turn to study the influence of the surface defects because they are prevalent in real surfaces. Two kinds of defects, namely the surface color center and the polar step, have been shown to be decisive on the electronic structure of the adsorbate system. For adsorption at the surface color center, the most interesting feature is the charge transfer of the unpaired electron to the molecular adsorbate, which subsequently results in the magnetization of the adsorbate. The polar stepped surface is another example of band engineering through tailoring the electrostatic environment of the surface. We see in Sec. 13.3.2 that the effective KS-DFT gap can be decreased by over 2 eV when the hydroxybenzoic acid is adsorbed at the artificial [011]-oriented monatomic step edge. While this type of polar step is conceptual and it requires a high formation energy, these results demonstrate the possibility of controlling the alignment of the molecular orbitals with respect to the surface by such adsorption.

14.2 Outlook

In an effort to understand the microscopic mechanism in the separation process, this work provides a comprehensive insight into the molecule-surface adsorption geometry, interaction, and excitation properties. Meanwhile, the adsorption of aromatic carboxylic acid on wide-gap insulator offers an excellent playground to benchmark various *ab initio* methods for this specific system. The ever-increasing power in the contemporary supercomputers makes it possible to push the state of the art theoretical approaches to a new level in the first-principles calculations. We have already seen in this work that an accurate description of electronic excitations is accessible from the two-particle Green's function method, whereas it is beyond the scope of KS-DFT or even the *GW*-RPA method. In light of the interesting properties of the surface defects (e.g. the polar step), it is desirable to perform the BSE calculation when the molecules are adsorbed at these defect sites.

Last but not least, it is still not transparent how the contact charging effect is mediated between two insulators. For example, the separation output dependence on the relative humidity remains a mystery.¹ On the other hand, the charge transfer in between the insulators requires the knowledge of both insulators and their interface including the

¹It is tentatively shown in Appendix D that the adsorption of water molecules at the [011] step could recover the band gap.

adsorbed molecules. These are the directions that needed to be worked on in the future.

Appendices

Appendix A

Tamm-Dancoff Approximation to the Optical Absorption Spectra of Benzoic Acids

The optical absorption spectra $\Im(\epsilon_M)$ of the benzoic acid and salicylic acid molecules are calculated in terms of the Tamm-Dancoff approximation (resonant part only) and the full excitonic Hamiltonian (both resonant and coupling parts). The calculation parameters follow the description in Sec. 6.3. The resulting spectra are shown in Fig. A.1.

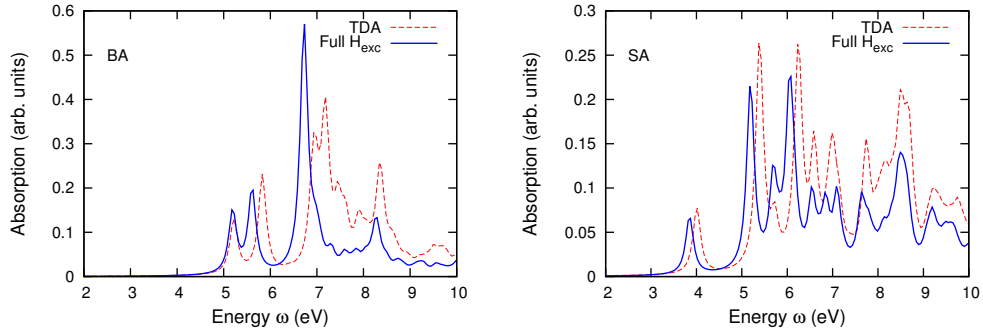


Figure A.1: Absorption spectra of the BA and SA molecules using the Tamm-Dancoff approximation and the full BSE Hamiltonian. The polarization direction is along the x axis illustrated in Fig. 6.3.

For both molecules, the optical absorption spectra exhibit blue-shifts with respect to the full BSE spectra. In particular, the shift for the lowest singlet excitation peak is quite insignificant. For example, the lowest $\pi \rightarrow \pi^*$ transition shifts by about 0.2 eV to higher energy for the SA (see Fig. 6.3), while the shift is less than 0.1 eV for the BA molecule. Hence, at least for the lowest excitation peak, the TDA is still a valid approximation for these benzoic acids. However, the discrepancies between the TDA and the full Hamiltonian becomes more substantial when one moves to the higher energy excitations. Not only the position of these peaks, but also the intensities are different from the full calculation. This can be understood by the large exchange interaction of the e - h pair [151]. It is suggested that the coupling between the e - h pairs and antipairs is important in reproducing the characteristics of the excitations at large energies for the benzoic acid molecules.

Appendix B

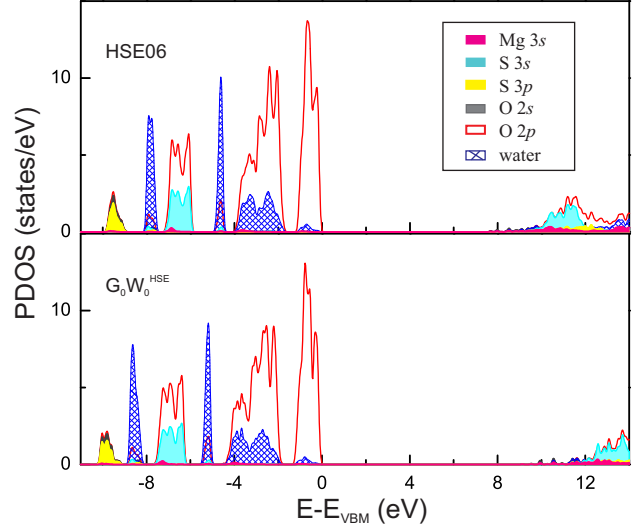
Gluconic Acid on $\text{MgSO}_4 \cdot \text{H}_2\text{O}$ (100)

The perfect non-polar surface of a wide band gap insulator, e.g. alkali halides is chemically inert with respect to organic molecules, and the features of the molecular orbitals are usually preserved upon adsorption. This has been resolved by scanning tunneling spectroscopy [15] and first principles calculations (Sec. 8.2.2). However, we show in the appendix that the molecular orbital of an organic molecule can also experience *strong variations* upon adsorption on a wide-gap insulating surface. The system under investigation is a gluconic acid (GA) molecule adsorbed on a $\text{MgSO}_4 \cdot \text{H}_2\text{O}$ (100) surface.

B.1 Bulk $\text{MgSO}_4 \cdot \text{H}_2\text{O}$

$\text{MgSO}_4 \cdot \text{H}_2\text{O}$ has a monoclinic structure (space group C_{2h}^6), and is chemically formed from MgSO_4 by incorporating one water molecule per unit. The crystal structure parameters were calculated with the PBE XC potential [41] within the generalized gradient approximation (GGA) as implemented in VASP [130]. The electron-ion interaction was described within the projector augmented wave method [174]. A kinetic energy cutoff of 500 eV and a $5 \times 5 \times 5$ \mathbf{k} -point mesh in the Brillouin zone are used. The convergence criterion of lattice parameter and atomic position relaxation is set to 0.02 eV/Å. The resultant lattice constants ($a = 6.79$ Å, $b = 7.79$ Å, $c = 7.69$ Å) and $\beta = 117.7^\circ$ are in good agreement with experiment and previous theoretical values [175]. The direct band gap at the Γ point is severely underestimated by the GGA-PBE (5.53 eV) and the local density approximation (LDA) (5.26 eV), compared to a surface sensitive experimental value (7.4 eV) [176]. A much more realistic gap of 7.41 eV is obtained with the screened hybrid functional HSE06 [49, 177] owing to the alleviation of the self-interaction error and derivative discontinuity problem by the nonlocal exact exchange. As resolved from the projected density of states (PDOS) in Fig. B.1, the valence band maximum (VBM) is of O-2p character and the conduction band minimum consists of Mg-3s and S-3s states. We also carry out the quasiparticle (QP) calculations according to Hedin's *GW* approximation [72, 178], which starts from the Kohn-Sham (KS) wavefunctions and adds QP corrections to the KS eigenvalues. We include 300 empty states with a $4 \times 4 \times 4$ \mathbf{k} -point mesh for the self-energy and a cutoff of 200 eV for the polarizability matrices. The QP correction substantially recovers the LDA gap to 8.36 eV, while the correction is much smaller (1.05 eV) to the HSE06 gap (see Fig. B.1). The projected density of states (PDOS) plot (Fig. B.1) given by HSE06 agrees quite well to the G_0W_0 calculation, which proves that the HSE06 hybrid functional is a good approximation for

Figure B.1: Projected density of states of bulk $\text{MgSO}_4 \cdot \text{H}_2\text{O}$ calculated with HSE06 hybrid functional (top panel) and G_0W_0 calculations using the HSE orbitals and eigenvalues (bottom panel).



the electronic properties of $\text{MgSO}_4 \cdot \text{H}_2\text{O}$. Another feature that is evident in Fig. B.1 is the hybridization between the molecular water $1b_1$ state and O $2p$ state, while the lower molecular orbitals of the incorporated water remain sharp. The pronounced broadening of the water $1b_1$ orbital is a consequence of the bonding to the neighboring Mg atoms.

B.2 Adsorption Geometry

We use a (1×2) $\text{MgSO}_4 \cdot \text{H}_2\text{O}(100)$ surface supercell with 14 atomic layers (72 atoms) for the adsorption studies. Test calculations using larger unit cells confirmed that the (1×2) supercell is adequate for various adsorption configurations while keeping the intermolecular interaction minimized. By construction, the (100) surface is cleaved in a way that the electrostatic dipoles between the Mg^{2+} and SO_4^{2-} are nearly within the surface plane. Hence, the macroscopic dipole moment is negligible along the surface normal, making this surface thermodynamically more favorable than other surface planes. The non-polar nature of the surface is also evidenced by the small displacements of the surface atoms during relaxations. A vacuum thickness of 14 Å was used to separate the adsorbate system from its periodic image. The calculations have been checked to converge well with respect to the slab thickness, \mathbf{k} -point mesh ($2 \times 4 \times 1$) and kinetic energy cutoff (400 eV). The PBE-D scheme [55] is employed to take into account the long-range vdW force. The electronic properties of the adsorbate system are evaluated with the HSE06 hybrid functional.

In Fig. B.2, the two configurations with the lowest E_{ads} (see Table B.1) are presented, both of which depict the fixture of the molecule via multiple localized Mg-O and O-H bonds. Such bonding type implies that an ordered structure can be achieved on $\text{MgSO}_4 \cdot \text{H}_2\text{O}(100)$ where the GA molecule is prone to lie flat on the surface along the [010] direction. Specifically, in Conf. I the molecule is stabilized via three Mg-O bonds from the carboxylic and hydroxylic O atoms with bond lengths ranging from 2.10 to 2.16

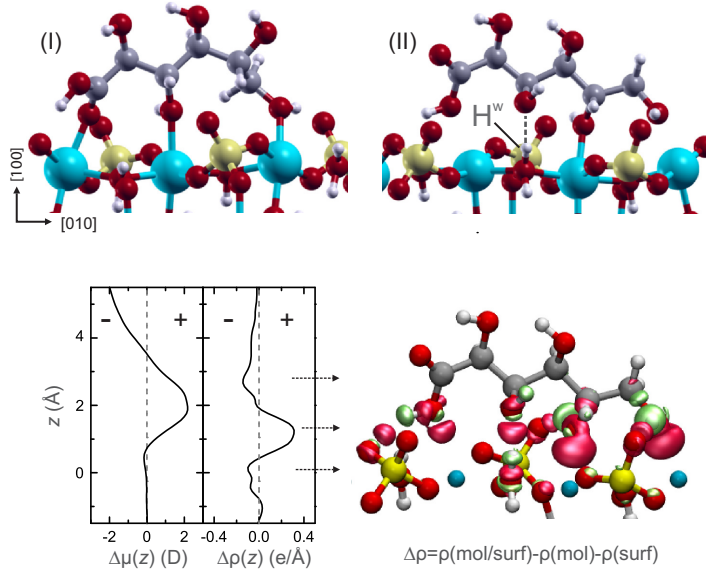


Figure B.2: Top: Two representative configurations of GA adsorbed on $\text{MgSO}_4 \cdot \text{H}_2\text{O}(100)$. Color code: Mg blue (large gray), S yellow (light gray), O red (black), C small gray, H white. Bottom: Adsorbate induced electron density difference $\Delta\rho$ for Conf. II obtained from HSE06 calculations along with the planar integrated $\Delta\rho(z)$ and accumulated induced dipole $\Delta\mu(z)$. The red (dark gray) and green (light gray) regions correspond to electron accumulation and depletion, respectively. The isosurface value is $\pm 0.03 \text{ e}/\text{\AA}^3$.

Table B.1: Adsorption (E_{ads}) and interaction energy (E_{int}) (in eV) for the two adsorption configurations optimized by PBE-D as shown in Fig. B.2. The GGA-PBE contributions to the E_{ads} (E_{int}) are explicitly listed. The deformation energy of the molecule is denoted by ΔE_{d} . The definitions of E_{ads} and E_{int} are given in Eq. (9.1).

Conf.	$E_{\text{ads}}^{\text{PBE-D}}$	$E_{\text{ads}}^{\text{PBE}}$	$E_{\text{int}}^{\text{PBE-D}}$	$E_{\text{int}}^{\text{PBE}}$	ΔE_{d}
I	-2.47	-1.63	-4.26	-3.42	0.77
II	-2.49	-1.53	-4.04	-3.09	0.53

Å. The incorporated water molecule at the surface is not interacting with the adsorbate. In the second configuration, we see a dominating Mg-O bond from the hydroxylic O (2.06 Å), accompanied by two weaker Mg-O bonds with larger bond lengths (2.22 and 2.55 Å). Besides, one of the hydroxylic O atom binds to the hydrogen of the water molecule at the surface (H^w). The difference in adsorption configurations has a direct influence on the binding energy as shown in Table B.1, where E_{int} calculated with GGA-PBE is 0.33 eV higher for Conf. I. While the vdW interaction ($E_{\text{int}}^{\text{PBE-D}} - E_{\text{int}}^{\text{PBE}}$) has been found substantial for both configurations (0.84 and 0.95 eV), it accounts for a relatively small portion (20-25%) of the total E_{int} compared to the short-range molecule-surface interactions. Hence, we conclude that the long-range vdW force does not play a predominant role in the adsorption of GA on $\text{MgSO}_4 \cdot \text{H}_2\text{O}(100)$.

Inspecting the charge density difference (Fig. B.2), one finds electron accumulations in between the bond region upon adsorption, as expected for covalent interactions. This is analogous to the BA/NaCl interface. Here, the dative covalent bond takes place through the donation from the lone-pair electrons of the O to the Mg atom. The strong interaction energy is still ascribed to the attractive electrostatic interaction. The adsorbate also has an effect on the dipole moment at the surface. The induced dipole moment is defined as [179]

$$\Delta\mu(z) = \int_{z_c}^z z \Delta\rho(z) dz, \quad (\text{B.1})$$

where $\rho(z)$ is the planar-integrated charge density difference, and z_c is the position of the slab center. The reference position is the top of the surface layer ($z = 0$). The upper limit of the integral $z > z_c$, and is chosen somewhere in the vacuum where the charge density difference is zero. In practice, we rewrite the adsorbate induced dipole as

$$\Delta\mu(z) = \Delta\mu(z - dz) + \frac{1}{2}[\Delta\rho(z - dz) + \Delta\rho(z)]dz, \quad (\text{B.2})$$

where dz is the z interval between two adjacent data. The calculated change in the surface dipole is -2.3 Debye due to the electron redistribution at the molecule-surface interface. Furthermore, the charge transfer is found to be small. For instance, a Bader analysis [180] predicts that 0.01 e are transferred to the molecule for Conf. II. This is expected as the energy gaps of both the surface and molecule are rather large.

An interesting indication of the large ΔE_d in Table B.1 is the pronounced intramolecular distortion from its equilibrium geometry upon adsorption. This feature stems partially from the intrinsic molecular structure of GA, and is not observed for some other organic molecules, e.g. hydroxybenzoic acid on $\text{MgSO}_4 \cdot \text{H}_2\text{O}(100)$ [175]. The sp^3 hybridization in the carbon chain makes the structure versatile through the rotation along the C-C bond with a small energy barrier, which can be easily overcome by the energy gain through the subsequent GA-surface interactions. An immediate consequence of this structural change can be manifested by the reduced gap of the adsorbate with respect to that of the gas phase molecule (Table B.2). In addition, our calculation on KCl(001) shows a minor deformation of the GA molecule with a much weaker E_{ads} (-0.4 eV excluding the vdW force), an indication that the intramolecular distortion is also related

Table B.2: Calculated energy gaps (in eV) of the GA molecule by DFT and *GW* approximation. The adsorbed molecule refers to the GA molecule adsorbed on $\text{MgSO}_4 \cdot \text{H}_2\text{O}(100)$ as in Conf. II, whereas the isolated molecule refers to the GA molecule detached from the surface while its geometry is kept fixed as that of the adsorbed molecule. The GA molecule in its equilibrium geometry is denoted by the gas phase molecule. The energy gaps of the SA adsorbed on $\text{MgSO}_4 \cdot \text{H}_2\text{O}(100)$ are given in parentheses for comparison.

	PBE	HSE06	LDA	$G_0W_0^{\text{LDA}}$
adsorbed	4.84 (3.21)	6.73 (4.30)	4.81	10.01
isolated	4.10 (3.37)	5.97 (4.49)	4.06	10.59
gas phase	4.46 (3.17)	6.39 (4.22)	4.43	10.94

to the surface. The higher reactivity of $\text{MgSO}_4 \cdot \text{H}_2\text{O}(100)$ is associated with its lower Madelung potential as the ions at the surface are more exposed to the environment.

B.3 Anomalous Molecular Orbital Variation

We now turn to the surface and adsorbate induced effect on the molecular orbital of the GA molecule. It is surprising to see from Fig. B.3 that, in Conf. II, the highest occupied molecular orbital (HOMO) experiences dramatic changes upon adsorption, even with the intramolecular structure kept intact. A detailed analysis reveals that the order of the HOMO and HOMO-1 is reversed after the molecule is attached to the surface. Consider the HOMO and HOMO-1 of GA in the gas phase are by no means degenerate, such *reordering* of the molecular orbitals is rather *unusual* on wide band gap insulators. This sends a signal that the adsorption can strongly modify the molecular orbitals even on pristine insulating surfaces. The interchange of HOMO and HOMO-1 subsequently increases the energy gap of the adsorbate by about 0.75 eV with respect to the isolated molecule (see Table B.2). We note that such gap variation shows no dependence of the XC functional used. The drastic modification of the HOMO, however, is absent for Conf. I where the electron density redistribution is considerably smaller. In Fig. B.4 two distinct behaviors of the frontier orbitals are perceivable when the GA molecule is lifted away from the surface while the intramolecular structure is fixed at its adsorbate state. In Conf. I, the gap between the HOMO and the lowest unoccupied molecular orbital (LUMO) experiences a small decrease relative to the isolated molecule. As the molecular HOMO in Conf. I lies within the surface band gap, there is no coupling between the HOMO and the surface valence band. Hence, the small gap reduction arises from the electrostatic potential of surface dipoles. This also holds true for the hydroxybenzoic acid (SA) adsorbate on $\text{MgSO}_4 \cdot \text{H}_2\text{O}(100)$ as well as the GA on alkali halide (001) surface. On the other hand, for Conf. II, the HOMO of the adsorbate is pinned below the surface VBM as a result of the resonance between the hydroxylic oxygen and H^{w} of the surface. Since the hydrogen bond weakens rapidly as the molecule is gradually

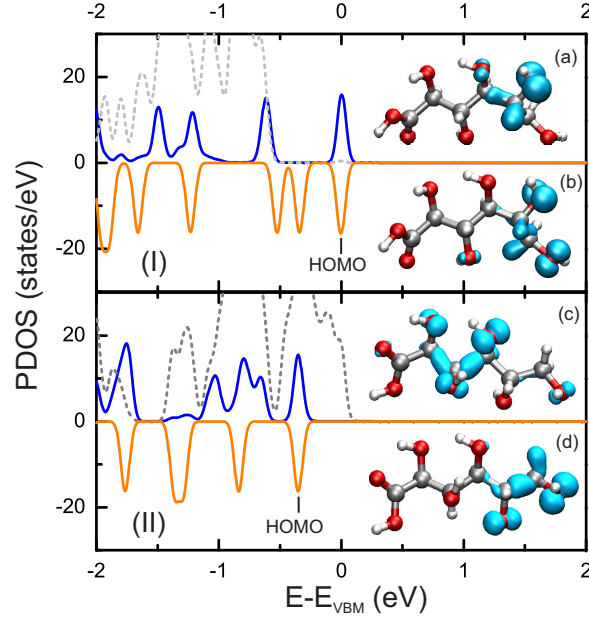


Figure B.3: Density of states projected onto the GA molecule (solid line) and surface (gray dashed line) calculated with the HSE06 functional for Conf. I and II. The adsorbed molecules are denoted by (a) and (c), and the isolated ones are given in (b) and (d). A Gaussian smearing of 0.05 eV has been applied. The HOMO of the isolated molecule is aligned to that of the adsorbate. The electron density distributions of HOMO for the adsorbed and isolated molecules are also illustrated.

detached from the surface, one can see the accelerated upshift of the HOMO against the VBM as well as the declining of the molecular energy gap in Fig. B.4. It is thus clear that the strong variations of the frontier orbitals upon molecular adsorption stem from the *rehybridizations*. The water molecule, which was usually thought to be inactive in $\text{MgSO}_4 \cdot \text{H}_2\text{O}$, however plays an important role in the electronic properties of the adsorbate.

We have seen up to this point that the frontier orbital of the adsorbate can be effectively influenced by the molecule-insulator interactions based on the KS-DFT. Following Ch. 11, we now illustrate the polarization effect on the electron affinity and ionization energy of the adsorbate upon adsorption on $\text{MgSO}_4 \cdot \text{H}_2\text{O}(100)$. Norm-conserving pseudopotentials, a cutoff energy of 816 eV (60 Ry) and a $2 \times 4 \times 1$ \mathbf{k} -point mesh are used for the LDA calculation. In the *GW* calculation, we include 200 and 400 empty bands for the isolated GA and adsorbate system in the evaluation of self-energy Σ , respectively. 3400 \mathbf{G} vectors are used for the local field effect in the response function. The slowly decaying Coulomb potential in the repeated-slab approach is corrected with a boxlike cutoff. The QP gap is converged within 0.1 eV with these parameters. The resulting QP gap from the $G_0W_0^{\text{LDA}}$ for the gas phase GA exhibits a much larger opening than the HSE06 HOMO-LUMO gap. When the molecule is brought into contact with the

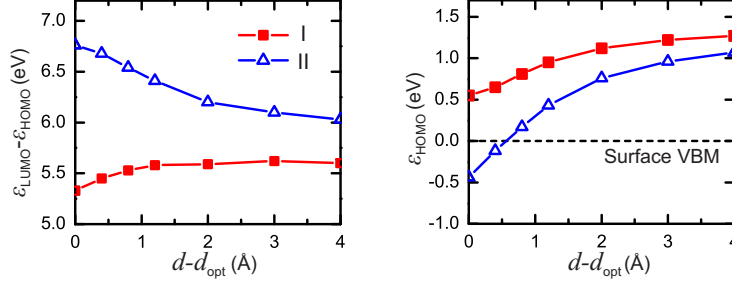


Figure B.4: The evolution of the HOMO-LUMO gap (left) and the HOMO energy (right) (within HSE06) of the GA adsorbate with respect to the distance to the surface d . d_{opt} is the separation between the molecule and surface at the optimized geometry.

surface, a pronounced gap reduction (0.58 eV) is obtained from the $G_0W_0^{\text{LDA}}$ calculation. This is clearly opposed to what has been found by DFT calculations. In fact, we find that $\Delta E_{\text{HOMO}}^{\text{QP}} = 0.6$ eV and $\Delta E_{\text{LUMO}}^{\text{QP}} = -0.7$ eV, corresponding to a gap reduction of 1.3 eV due to surface polarization. Note that apart from the polarization effect, the change in the energy gap upon adsorption given by G_0W_0 ($\Delta E_g^{G_0W_0}$) in Table B.2 also includes the contribution from the local interactions. Using Eq. (11.5), we find that $\Delta E_g^{\text{KS-DFT}} = (-0.58) - (-1.3) = 0.72$ eV, in excellent agreement with the HOMO-LUMO gap change upon adsorption from the DFT calculations (see Table B.2).

In summary, we have demonstrated in this appendix that upon adsorption to the surface of a wide band gap insulator, the molecular orbitals of the adsorbate can experience substantial changes as a result of the complex interplay of the sizeable electrostatic interaction and rehybridization. As the electronic properties are dictated by the energetic positions and characteristics of frontier orbitals of the adsorbate, one has to carefully assess the molecule-insulator interface when interpreting the transport and spectroscopic measurements.

Appendix C

Color Centers in NaCl

In this appendix, we investigate the anion (Cl) vacancy in NaCl in different charge states (-1, 0 and +1) by both semi-local and hybrid functionals, aiming for a better understanding of the F center in alkali halide and the performance of the hybrid functionals for localized defects. We note that the finite-size effect arises within the current modeling scheme for the vacancy. The common procedure for defect energetics calculation is to embed the defect into a supercell under periodic boundary condition (PBC). The advantage of using supercells instead of cluster methods is that the band structure of the host crystal is well-defined, as the cell is bulk-like [181]. However, tractable DFT calculations are usually constrained to about 1000 atoms, and the size of system is further limited for hybrid functionals in a plane-wave basis set. A single Cl vacancy in a 1000-atom NaCl supercell corresponds to a vacancy concentration of the order of 10^{20}cm^{-3} , which is much higher than those found in experiment (10^{15} to 10^{19}cm^{-3}). The periodic images of the point defects in a high density thus give rise to unrealistic defect-defect interactions, making the defect energetics dependent on the size of the supercells. The problem is even more serious for charged defects, as the neutralizing background slows the convergence of defect energies with respect to the supercell size [182]. Other sources of error for small supercells involve the elastic energy due to artificial relaxations of ions, and defect level dispersions introduced by defect-defect interactions. Corrections for the finite-size effect have been found indispensable in defect calculations for realistic interpretations [183–186], and they will be discussed and applied to the present study of Cl vacancies.

We first assess the performance of the hybrid functionals on the bulk properties of NaCl, and compare it to the GGA-PBE (Perdew-Burke-Ernzerhof) functional [41]. Both unscreened and screened hybrid functionals are employed. In the unscreened PBE0 functional, the exchange part of the XC energy E_{xc} is constructed by mixing a fraction (α) of non-local exact exchange E_x with PBE exchange E_x^{PBE} , while the correlation energy is simply taken from PBE, E_c^{PBE} :

$$E_{xc}^{\text{PBE0}} = \alpha E_x + (1 - \alpha) E_x^{\text{PBE}} + E_c^{\text{PBE}}. \quad (\text{C.1})$$

The amount of exact exchange α is a variable from 0 to 1, although conventionally $\alpha = 0.25$ is used as suggested by perturbation theory [53]. In practice α is usually varied to meet the experimental gap value. In a plane-wave basis set, the evaluation of the exact (HF) exchange is a hog to the computational resources and tends to be rather slow because of its truly non-local nature. The calculation can be accelerated

Table C.1: Calculated lattice constant (a_0), fundamental band gap at Γ (E_g), dielectric constant (ϵ_∞) and enthalpy of formation (ΔH_f) of rocksalt NaCl using various DFT functionals.

	$a_0(\text{\AA})$	$E_g(\text{eV})$	ϵ_∞	$\Delta H_f(\text{eV})$
GGA-PBE	5.69	5.00	2.33	-3.69
HSE06	5.65	6.43	2.13	-3.85
PBE0 ($\alpha = 0.25$)	5.64	7.19	1.98	-3.85
PBE0 ($\alpha = 0.40$)	5.62	8.47	1.86	-3.93
Expt.	5.57 ¹	8.5 ²	2.3 ³	-4.26 ¹

¹ Reference [187].

² Reference [188].

³ Reference [189].

by truncating the slowly decaying long-range part of the exact exchange as in the HSE (Heyd-Scuseria-Ernzerhof) hybrid functional [49]:

$$E_{xc}^{\text{HSE}} = \alpha E_x^{\text{sr}}(\mu) + (1 - \alpha) E_x^{\text{PBE,sr}}(\mu) + E_x^{\text{PBE,lr}}(\mu) + E_c^{\text{PBE}}. \quad (\text{C.2})$$

The screening parameter μ in Eq. (C.2) is given in Eq. (3.30). Here we use the optimized $\mu = 0.207 \text{ \AA}^{-1}$, following Ref. [177] along with $\alpha = 0.25$ and refer to this functional as HSE06.

In Table C.1 selected bulk properties of NaCl calculated using the GGA-PBE and hybrid functionals are summarized together with the experimental values. The calculations are carried out in the projector augmented wave (PAW) framework with the VASP code [130, 174, 190]. A semicore pseudopotential of Na is used, treating the $2p3s$ electrons as valence electrons. The kinetic cutoff energy for the plane-wave basis set is 500 eV. A Γ -centered $8 \times 8 \times 8$ Monkhorst-Pack \mathbf{k} -point mesh [63] is applied to the primitive cell containing one formula unit of NaCl. For HSE06 and PBE0 calculations, a down-sampled $4 \times 4 \times 4$ mesh is used to evaluate the non-local exact exchange. The down-sampling for the non-local exchange reduces the computing time significantly. It is generally necessary for the PBE0 to have a finer \mathbf{k} -point mesh than for the screened HSE functional to reach convergence.[50, 51] For the present case, the HF exchange using the PBE0 changes by roughly 15 meV per atom from the down-sampled $4 \times 4 \times 4$ to the full $8 \times 8 \times 8$, while the energy is already converged within 10^{-2} meV with the HSE06 functional. Nevertheless, the choice of the down-sampled \mathbf{k} -point for the PBE0 calculations is sufficient for the bulk properties. The lattice constant a is determined when the residual force is smaller than 5 meV/ \AA . The high frequency macroscopic dielectric constant ϵ_∞ can be calculated within a GW scheme using the random-phase approximation (RPA) with local field effect included. Around 90 empty bands are used for calculating the dielectric constant. The dielectric constant will also be referred to later for the finite-size corrections. Finally, the formation energy ΔH_f is defined as

$$\Delta H_f = E_{\text{NaCl(s)}} - E_{\text{Na(s)}} - \frac{1}{2} E_{\text{Cl}_2(\text{g})}. \quad (\text{C.3})$$

In Eq. (C.3), $E_{\text{NaCl(s)}}$ is the total energy of bulk NaCl. $E_{\text{Na(s)}}$ is the energy of bulk Na in a body centered cubic (bcc), which was optimized and calculated using the same \mathbf{k} -point mesh and cutoff energy as for bulk NaCl. $E_{\text{Cl}_2(\text{g})}$ refers to the energy of one gas phase Cl_2 molecule in a large tetragonal cell.

One immediately observes that the hybrid functionals improve not only the direct band gap ($\Gamma_{15} \rightarrow \Gamma_1$) but also the lattice constant and heat of formation compared to the GGA-PBE calculation in Table C.1, in agreement with earlier calculations [50, 51]. Yet, it is found the band gaps are still underestimated for the hybrid functionals with the original fraction (0.25) of exact exchange, and the PBE0 yields a much closer value to experiment than the HSE06. This implies that for wide gap insulators, as the electronic screening is quite weak, the unscreened exact exchange in PBE0 is preferred. For defect calculations, it is customary to tune the fraction of the exact exchange so that the experimental band gap can be reproduced [191, 192]. By increasing the amount of the non-local exchange from 0.25 to 0.40 within the PBE0, the band gap of NaCl recovers nearly to the experimental value, and the lattice constant and heat of formation are also reproduced best among the chosen functionals. We note that hybrid functionals tend to underestimate the dielectric constant of NaCl, a trend also found for semiconductors and other insulators [193]. An accurate description of the electronic dielectric constant with the hybrid functionals will require an explicit account of excitonic effects [78, 194].

To this end, we face several functionals for the subsequent calculations of the Cl vacancy in NaCl. The PBE0 ($\alpha = 0.40$) (we will refer it to mPBE0 hereafter) is apparently favored since it reproduces the experimental gap. However, as the choice of the fraction of the non-local exact exchange is empirical to some extent, its impact on the position of the deep defect level for wide gap insulators is still unknown. Meanwhile, the screened hybrid functional is of great interest as it shows considerable success in the prediction of defect energetics. Therefore it is plausible to also include the HSE06 functional with the original α , as well as the GGA-PBE for the defect calculations.

C.1 Electronic Structure of Chlorine Vacancies

In this section we briefly sketch out the single-particle Kohn-Sham (KS) eigenvalues of the Cl vacancy induced electronic levels. Supercells containing 64 atoms are employed for the calculations. The Brillouin zone is sampled with a $2 \times 2 \times 2$ \mathbf{k} -point mesh, and a plane-wave basis set cutoff energy of 450 eV is used. Further, the \mathbf{k} -point mesh for the non-local exact exchange is down-sampled to the Γ -point for HSE06, while a full $2 \times 2 \times 2$ \mathbf{k} -point mesh is necessary for well converged energies in PBE0 calculations. The convergence criterion for full relaxations is 0.01 eV/Å.

The removal of one Cl atom in a perfect NaCl crystal leaves a neutral vacancy V^0 with one electron bound to the vacancy center. The localized nature of the unpaired electron can be clearly identified in the charge density isosurface shown in Fig. C.1. The 1s characteristics of the wavefunction in the vacancy is contributed equally from the six neighboring Na atoms. The negligible displacement of the neighboring atoms around V^0 (see Table C.2) keeps the singly occupied a_{1g} level unshifted after relaxation. In

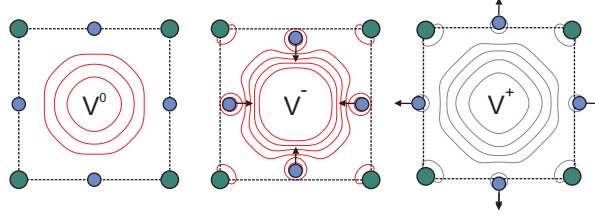


Figure C.1: The electron density (V^0 and V^-) and hole density (V^+) isosurface of the a_{1g} state in the (100) plane calculated with the mPBE0 functional. The lines are drawn in intervals of $0.01e/\text{\AA}^3$. The displacements of the nearest neighbor atoms around the Cl vacancy after relaxation are illustrated by the arrows. The blue and green circles represent the Na and Cl atoms, respectively.

Table C.2: Displacements (in the equilibrium bond length $0.5a_0$) of the nearest-neighbor Na atoms around the Cl vacancy calculated using the 64-atom cell. The positive value represents an outward relaxation against the vacancy, and vice versa. The values obtained with the 216-atom cell using the GGA-PBE are shown in parentheses.

	GGA-PBE	HSE06	mPBE0
V^+	+0.035 (+0.043)	+0.035	+0.036
V^0	-0.000 (-0.000)	-0.000	-0.000
V^-	-0.039 (-0.040)	-0.041	-0.044

the +1 charge state V^+ , the a_{1g} state is unoccupied and the polaronic hole is trapped in the vacancy. The nearest neighbor Na atoms tend to relax away from the vacancy because of the positive electrostatic potential inside the vacancy. The outward relaxation delocalizes the a_{1g} (see Fig. C.1), and shifts it to higher energy towards the CBM. In the -1 charge state V^- , the a_{1g} state becomes doubly-occupied. Upon relaxation the six nearest Na atoms show inward displacement towards the vacancy (Fig. C.1) as a polaronic distortion. As a consequence, the two electrons are more localized inside the vacancy site, shifting the a_{1g} state to lower energy. We note that the relaxations of the neighboring atoms around the anion vacancy follow the O_h symmetry for all charge states. No symmetry lowering (or Jahn-Teller distortion) is found since the defect level is either singly occupied for V^0 , or doubly occupied (unoccupied) for V^- (V^+). The reduced self-interaction in hybrid functionals also results in more pronounced atomic displacements for the charged defects as seen in Table C.2.

Table C.3 summarizes the KS energies of the Cl vacancies in various charge states for both rigid and relaxed defect structures. The choice of \mathbf{k} -point gives rise to a dispersion of the electronic level within the finite-size supercell scheme. The dispersion introduces a strong dependence on the supercell size of the energy level at the Γ -point ϵ^Γ . Thus we average the defect level energy over the Brillouin zone $\bar{\epsilon}$ since the averaged level shows a much better convergence than ϵ^Γ . [183] The dispersion also slightly pushes the host CBM to higher energies. The finite-size effect will be discussed in detail in Sec. C.2.1.

Table C.3: Energy levels (in eV) of the single-particle Kohn-Sham a_{1g} state of the Cl vacancy in a cubic 64-atom cell referenced to the VBM. The energy is averaged over the BZ. For V^0 , the positions of the a_1 state in spin-up (occupied) and spin-down (unoccupied) channels are given. The absolute positions of the host band edges are also given.

	PBE		HSE06		mPBE0	
	rigid	relaxed	rigid	relaxed	rigid	relaxed
$V^+(a_{1g}^0)$	3.74	5.02	4.90	6.25	6.81	8.25
$V^0(a_{1g}^1)_\uparrow$	4.09	4.10	4.83	4.83	5.30	5.30
$V^0(a_{1g}^1)_\downarrow$	4.85	4.86	6.13	6.13	8.12	8.12
$V^-(a_{1g}^2)$	5.04	4.37	6.07	5.22	6.87	5.69
ϵ_{VBM}	-0.76		-1.63		-2.78	
ϵ_{CBM}	4.24		4.80		5.69	

As predicted by all functionals, the a_{1g} states in all charged states lie within the upper half of the host band gap. We note that the absolute KS energies of the a_{1g} states [$\epsilon_{\text{KS}}(a_{1g}) + \epsilon_{\text{VBM}}$] are less affected when going from semi-local to hybrid functionals. In hybrid functionals, the VBM is lowered by 0.9 eV (HSE06) and 2.0 eV (mPBE0) with respect to the GGA-PBE as a result of the reduced self-interaction for the Cl $3p$ states. On the other hand, for rigid structures, the widening of the band gap in hybrid functionals tends to place the a_{1g} of V^- further away from the CBM compared to the semi-local functional, while the unoccupied a_{1g} state of V^+ is closer to the CBM when hybrid functionals are used.

C.2 Thermodynamic Transition Energies and Finite-Size Corrections

In general the single-particle energy level of the defect as calculated from the KS equation differs from the experimentally observed transition energies. [183] A rigorous approach to the transition energies, as discussed in this section, relies on the total energy difference of the defect energetics in various charged states.

A central quantity for the defect energetics is the formation energy E_f for a defect D in charge state q

$$E_f = E_D - E_H + \sum n_i \mu_i + q(\epsilon_{\text{VBM}} + \epsilon_F), \quad (\text{C.4})$$

where E_D and E_H are the total energy of the supercell with the defect D , and the host supercell without defects, respectively. n_i is the number of atoms removed from the supercell ($n_i = 1$ for the Cl monovacancy) or the number of impurities added ($n_i < 0$). μ_i refers to the chemical potential of the associated defect particle reservoir, and is subject to equilibrium conditions. For the present study, under extreme Cl-rich (or equivalently

Na-poor) conditions

$$\mu_{\text{Cl}} = \frac{1}{2}E_{\text{Cl}_2(\text{g})}. \quad (\text{C.5})$$

This places an upper limit on μ_{Cl} . The lower bound can be deduced from the following relation:

$$\mu_{\text{Na}} + \mu_{\text{Cl}} = E_{\text{NaCl}(\text{s})}. \quad (\text{C.6})$$

Therefore under Cl-poor (or Na-rich) conditions, which facilitate the formation of Cl vacancies,

$$\mu_{\text{Cl}} = E_{\text{NaCl}(\text{s})} - \mu_{\text{Na}(\text{s})} = \Delta H_f + \frac{1}{2}E_{\text{Cl}_2(\text{g})}, \quad (\text{C.7})$$

and this sets the lower limit of μ_{Cl} .

The remaining term $\epsilon_{\text{VBM}} + \epsilon_{\text{F}}$ in the formation energy [Eq. (C.4)] represents the chemical potential, or Fermi energy of the electrons in charged defects. The Fermi energy ϵ_{F} is varied within the band gap referenced to the energy of the host VBM ϵ_{VBM} ($0 \leq \epsilon_{\text{F}} \leq E_g$). Here ϵ_{VBM} is evaluated as the energy difference between a perfect host supercell and the same host supercell with one electron removed from the VBM:

$$\epsilon_{\text{VBM}} = E_{\text{H}}^0(n) - E_{\text{H}}^+(n-1), \quad (\text{C.8})$$

where n is the number of electrons in the host supercell. In principle, one needs a sufficiently large supercell with $n \rightarrow \infty$ corresponding to the dilute limit. In practice, a fractional charge q can be used along with a small supercell to obtain the ϵ_{VBM}

$$\epsilon_{\text{VBM}} = \lim_{q \rightarrow 0} \frac{E_{\text{H}}^0 - E_{\text{H}}^q}{q}. \quad (\text{C.9})$$

In the present case, the ϵ_{VBM} converges well within a 64-atom cell and a fraction charge of 0.001 e .

For charged defects, it is evident from Eq. (C.4) that the formation energy is dependent on the chemical potential of the exchanged electron. The thermodynamic transition energy $\epsilon(q/q')$ is defined as the Fermi energy at which the charge state q and q' of the defect system can be transformed spontaneously from one to the other. Therefore at the transition energy $\epsilon(q/q')$ these two charge states have the same formation energy. This gives the following form of the transition energy

$$\epsilon(q/q') = \frac{E_{\text{D}}(q) - E_{\text{D}}(q')}{q' - q} - \epsilon_{\text{VBM}}. \quad (\text{C.10})$$

C.2.1 Finite-Size Corrections

Before proceeding to the results, we shall discuss the correction methods for the finite-size effect, whose causes have been already identified in Introduction. For charged defects, the simplest correction is to align the electrostatic potential in the defect supercell to that of the host supercell. This is usually done by inspecting the potential difference ΔV between the core potentials of the atoms far from the defect center and that of the

bulk cell, and the energy correction term is essentially $\Delta E = q\Delta V$. This correction is rationalized by the fact that in periodic supercell calculations the zero of the electrostatic potential is chosen arbitrarily for each calculation, and the charged defect gives rise to a constant shift in the potential so that the bulk VBM cannot be applied directly to the defect supercell. However, due to the small size of the supercell used even the atoms farthest from the charged defect center are not bulk-like, making such correction scheme inaccurate. Recent study reveals that the potential alignment resembles the Makov-Payne scheme, [182] whereas the latter targets the correction of the unphysical defect-defect interactions. Indeed, Komsa and Rantala found that ΔV has the form $(\epsilon L)^{-1}$, where L is the lattice constant of a cubic supercell. [195] This is analogous to the Makov-Payne scheme to first order.

The popular Makov-Payne scheme for a charged defect in a cubic supercell in the dilute limit ($L \rightarrow \infty$) is expanded as

$$E_f(L) = E_f(L \rightarrow \infty) - \frac{\alpha_{\text{Md}} q^2}{2\epsilon L} - \frac{2\pi q Q}{3\epsilon L^3} + O(L^{-5}), \quad (\text{C.11})$$

where α_{Md} is the Madelung constant dependent on the lattice type, and q and Q the monopole and quadrupole moment of the defect charge, respectively [182]. The first order term, also called the Madelung energy, is thus the correction to the monopole-monopole interaction arising from the periodic image. The L^{-1} behavior of the artificial electrostatic interaction vanishes slowly, and this is usually the leading source of error. The higher order corrections have much smaller effects on the formation energy for ionic crystals, and it is usually accurate enough to include the corrections up to the quadrupole term. We note that in the Makov-Payne scheme the defect states are assumed to be localized, which is the case for the Cl vacancies in NaCl. For delocalized levels higher order corrections might become necessary. Although the Makov-Payne expansion is sound and accurate, it has been found that direct corrections using the Madelung energy and multipole interactions are prone to overshoot the formation energy, in particular for small supercells [196]. A more reliable approach is to employ a scaling method by performing a series of calculations using supercells of different sizes with the same symmetry. [197] The corrected formation energy $E_f(L \rightarrow \infty)$ then can be extrapolated to the dilute limit by fitting the calculated formation energies within finite-size cells to

$$E_f(L) = E_f(L \rightarrow \infty) + a_1 L^{-1} + a_3 L^{-3}, \quad (\text{C.12})$$

where a_n and $E_f(L \rightarrow \infty)$ are fitting parameters. It is clear that this scaling law method requires at least 4 supercells, and is rather computationally laborious.

In a recent work Freysoldt *et al.* proposed a general correction scheme (we will refer to it as the FNV scheme hereafter) for finite-size effect based on a single calculation of defect supercell without empirical parameters [198]:

$$E_f = E_f(L \rightarrow \infty) + E_q^{\text{latt}} - q\Delta_{q/b}, \quad (\text{C.13})$$

where E_q^{latt} is the macroscopically screened lattice energy of the defect charge q_d with compensating background, and $\Delta_{q/b}$ is an alignment term referenced to the bulk supercell

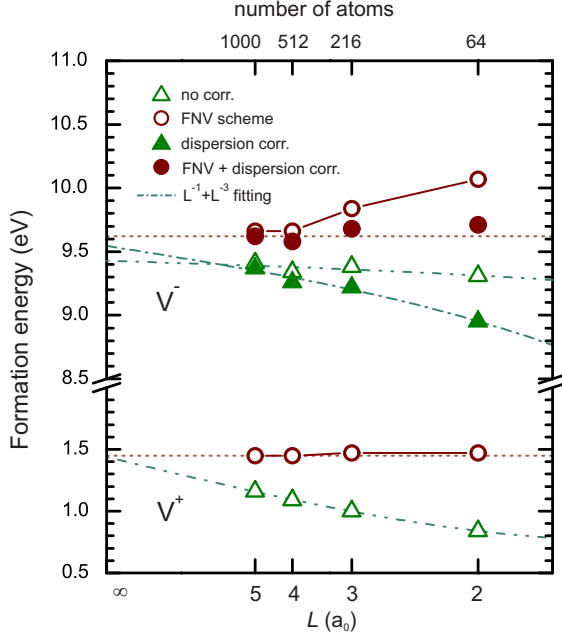


Figure C.2: Demonstration of the correction schemes for the formation energies of the Cl vacancy in the +1 and -1 charge states (in Cl-rich limit) with respect to the reciprocal supercell lattice constant L^{-1} . The calculations were performed with the GGA-PBE functional without structural relaxations.

to account for the microscopic screening. As the long-range E_q^{latt} scales as L^{-1} and the short-range alignment term as L^{-3} , the FNV scheme can be seen as an extension to the Makov-Payne expansion. It also allows for an explicit expression for the third-order L^{-3} energy term.

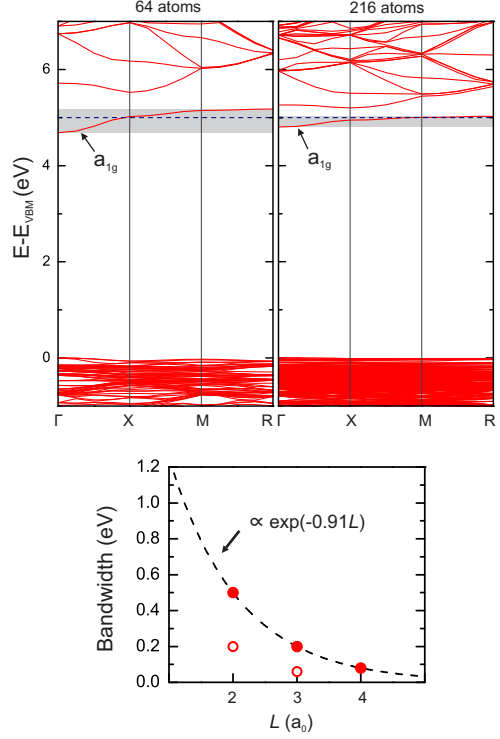
Now we apply both Makov-Payne scaling and FNV schemes to the formation energies of the charged Cl vacancies (V^+ and V^-) in NaCl. We refrain from including the potential alignment in these two schemes in order to avoid double-counting of the long-range L^{-1} term. Indeed Castleton *et al.* noticed that finite-size scaling with potential alignment resulted in wide error bars. [196] A series of simple cubic supercells containing 64, 216, 512 and 1000 atoms is chosen in the present study. The exceedingly large 1000-atom supercell restricts the calculations to the GGA-PBE functional, although we show that the obtained trend is applicable to hybrid functionals as well. For the 64- and 216-atom cells, the Brillouin zone is sampled with a $2 \times 2 \times 2$ \mathbf{k} -point mesh. For larger supercells, we use two special \mathbf{k} -points, *i.e.* Γ -point (0,0,0) and R -point (0.5,0.5,0.5) in reciprocal coordinates. Moreover, in the FNV scheme, the point charge q_d consists of an exponential decaying term and a localized contribution modeled by a Gaussian

$$q_d(r) = qxN_\gamma e^{-r/\gamma} + q(1-x)N_\beta e^{-r^2/\beta^2}, \quad (\text{C.14})$$

where N_γ and N_β are normalization constants, and x is the fraction of the relative amount of the exponential decay. In practice, the resulting corrected energy is insensitive to the choice of the specific parameters in Eq. (C.14) [198].

In Fig. C.2, we demonstrate the effects of finite-size corrections to the formation energies of Cl vacancies in +1 (V^+) and -1 (V^-) charge states. No relaxation is taken into account at this stage so as to exclude the finite-size effect of elastic energies. For V^+ ,

Figure C.3: Band structures (upper panel) of the Cl vacancy in the -1 charge state (V^-) in the unrelaxed 64- and 216-atom cells using the GGA-PBE functional. The shaded areas show the bandwidth of the doubly-occupied a_{1g} state induced by the negatively charged defect. The horizontal dashed line indicates the CBM of the perfect host without defects. In the bottom panel, the evolution of the bandwidth of the a_{1g} state (by closed circles \bullet) as a function of the supercell lattice constant is shown with an exponential fit curve for the unrelaxed structure. The band dispersion for the relaxed cell is also given by open circles \circ .



one first notices that the extrapolated formation energy from the Makov-Payne scaling law falls in line with that of the FNV scheme. The L^{-1} clearly dominates for the Makov-Payne fitted curve. The FNV scheme, on the other hand, shows a rapid convergence of the V^+ formation energy. We see that finite-size correction is indeed mandatory for an accurate description of formation energy of charged defects. For the smallest 64-atom cell, the uncorrected formation energy is underestimated by roughly 0.6 eV. Even for the 1000-atom cell, the formation energy without correction is still 0.2 eV too low.

Complexity arises when we move to the -1 charged Cl vacancy. The uncorrected formation energies in Fig. C.2 for V^- exhibit a zigzag evolution with respect to the increasing supercell size, making the Makov-Payne fit unreliable. Meanwhile, the FNV correction apparently yields a too high energy for small supercells, and the value does not appear to converge until we use the 512-atom cell. The source of such error is identified as the spurious dispersion of the defect levels as a result of the overlap between the wavefunctions of the defect and its periodic images. In the dilute limit, this localized defect level should be strictly a flat band. However, as shown in Fig. C.3, the Cl vacancy induced a_{1g} level within the band gap shows a prominent dispersion for small supercells. For hybrid functionals, the dispersion is less pronounced as the exact exchange favors a more localized electronic state in the vacancy. This artificial interaction tends to push the CBM of the host crystal to higher energies, or otherwise the CBM will become populated. The defect level dispersion has a short-range characteristics, as is evidenced by the exponential fit of the a_{1g} bandwidth with respect to the supercell lattice constant L for the 64-, 216- and 512-atom cells (in Fig. C.3). This short-ranged effect is not

included in either the Makov-Payne or FNV scheme, and thus one has to take it into account explicitly. We note that the dispersion correction is not necessary for V^+ since its a_{1g} level is unoccupied. Here the correction for the dispersion is considered by calculating the energy difference between the KS energy of the a_{1g} level at the Γ -point ϵ^Γ and the a_{1g} KS energy averaged over the sampled \mathbf{k} -points in the Brillouin zone $\bar{\epsilon}$. The FNV scheme based on the dispersion corrected formation energies is again able to yield converged results for small supercells, and the results are also comparable to the Makov-Payne method including the dispersion effect in the dilute limit.

For the neutral Cl vacancy V^0 , the situation becomes trouble-free since the electron is tightly bound to the vacancy center with a strongly localized electron density distribution as seen in Fig. C.1. The formation energy barely varies for the supercells considered, and therefore there is no need for finite-size corrections for V^0 .

We have shown the finite-size corrections for the charged defect supercells in rigid geometries with atoms fixed at their bulk positions. However, the introduction of a Cl vacancy inevitably changes the electrostatic potential of the local environment, resulting in atomic relaxations around the vacancy. The supercell approach, in this aspect, will lead to another error because the supercell employed in practice is usually not large enough for all local relaxations around the defect. This error can be partially alleviated by restricting the relaxations to the first two atomic shells around the defect, although it might underestimate the relaxation energy. Here we assess the finite-size effect on the elastic energy of the Cl vacancy in various charge states based on full relaxations using the GGA-PBE functional. We do not discuss the relaxations of the outer shell atoms since their displacements are much smaller than the first shell Na atoms and they contribute little to the formation energy. For the neutral vacancy V^0 , negligible inward relaxations of the six nearest neighbor Na atoms are found with supercells containing up to 216 atoms (see Table C.2). For V^- , the net negative potential induced by the excess electron added to the vacancy gives rise to an inward displacement of the neighboring cations. As discussed in Sec. C.1, this results in a more localized a_{1g} state, which consequently suppresses the dispersion of the a_{1g} with respect to the rigid structure (see Fig. C.3). Due to the finite-size of the supercell, Table C.2 shows that the displacement obtained from the 64-atom cell is 0.05 Å smaller than that from the 216-atom cell. The inability to fully relax in the 64-atom cell consequently gives a formation energy about 0.2 eV higher than that of the larger supercells. For the positively charged vacancy V^+ , the six nearest neighbor Na atoms experience an outward displacement due to the positive potential in the vacancy center. In contrast to V^- , the finite-size effect on the elastic energy is not significant for V^+ , as seen in Table C.2, since the atomic displacements using the 64- and 216-atom cells are of similar magnitude.

With all these comprehensive finite-size effects in mind, we now summarize the correction scheme applied in the present appendix. We restrict the calculations of formation energies with hybrid functionals to the use of the 64-atom supercell. Thanks to the localized nature of the defect state and negligible relaxation for V^0 , no correction is necessary. For V^+ we apply the FNV to the 64-atom cell and refrain from any correction for the elastic energy. For V^- the dispersion correction is applied to the 64-atom cell, followed by the FNV scheme. Further, the relaxation energies are aligned with those

Table C.4: Formation energies (in eV) of Cl vacancies in various charge states calculated with the GGA-PBE, HSE06 and mPBE0 functionals under Cl-rich and Cl-poor conditions. The Fermi energy is chosen at the VBM for charged defects. All values are corrected for finite-size effect.

	Cl-rich conditions			Cl-poor conditions		
	GGA-PBE	HSE06	mPBE0	GGA-PBE	HSE06	mPBE0
V^0						
rigid	4.44	4.63	4.71	0.75	0.78	0.78
relaxed	4.44	4.63	4.71	0.75	0.78	0.78
V^+						
rigid	1.47	0.75	-0.26	-2.22	-3.10	-4.19
relaxed	0.63	-0.10	-1.10	-3.05	-3.95	-5.03
V^-						
rigid	9.71	11.40	12.91	6.02	7.55	8.98
relaxed	9.55	11.01	12.50	5.86	7.16	8.57

obtained from the 216-atom cell, provided the latter already yields a converged elastic energy. In practice, due to the similar amount of atomic displacement, we use the PBE result as a reference for the hybrid functional, and subsequently lower the formation energies by 0.2 eV for the relaxed 64-atom supercells in the -1 charge state.

C.2.2 Chlorine Vacancy Thermodynamic Transition Energies

The calculated formation energies with finite-size corrections for the Cl vacancy in NaCl are shown in Table C.4, with the Fermi energy ϵ_F fixed at the VBM. For the neutral vacancy V^0 , the hybrid functionals yield higher formation energies than the GGA-PBE, although the energy differences are small. The functional dependence of formation energies for the charged states is much more prominent. With the hybrid functionals, we obtain higher formation energies for V^- and lower formation energies for V^+ . In particular, the negative formation energy of V^+ under Na-rich conditions suggests that the F^+ center could be predominating when the Fermi energy is close to the VBM.

To trace the source of the functional dependence of formation energy for charged vacancies, we may first rewrite the formation energy of V^+ in a rigid geometry with ϵ_F fixed at the VBM as

$$E_f(V^+) = (E_D^+ - E_D^0) + (E_D^0 - E_H^0 + \mu_{Cl}) + \epsilon_{VBM}, \quad (\text{C.15})$$

where the first term on the right-hand side is the electron ionization energy of V^0 (or equivalently the affinity energy of V^+), and the second term simply the formation energy of V^0 . By decomposing the formation energy into several contributions, it is clear that the discrepancies in $E_f(V^+)$ stem mostly from the different positions of the VBM by various functionals. We note that the ionization energy of V^0 shows very small changes

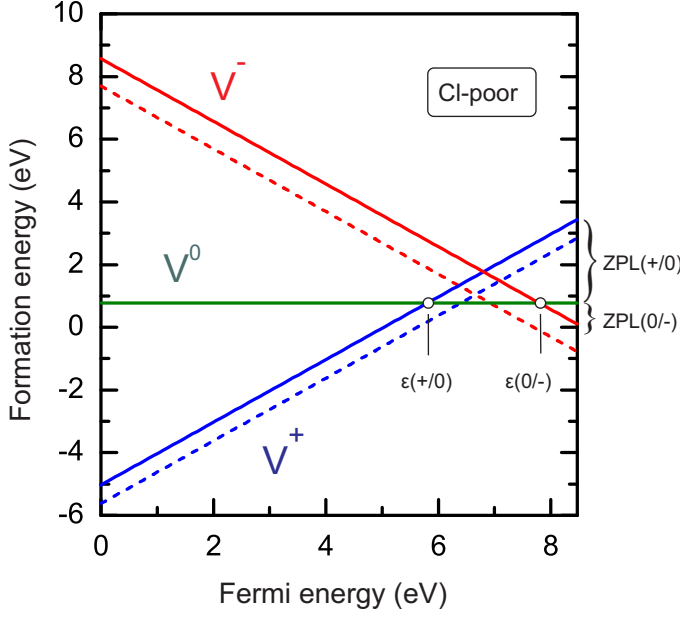


Figure C.4: Calculated mPBE0 formation energies of the Cl vacancy with full relaxations as a function of the Fermi energy under the Cl-poor condition. The solid lines represent the formation energies corrected for the finite-size effect. The thermodynamic transition levels and the zero-phonon lines (ZPL) are indicated. The uncorrected values are given in dashed lines for reference.

(within 0.05 eV) from semi-local to hybrid functionals, consistent with the similar absolute energy of the singly occupied a_{1g} state (see Table C.3). Analogously, the formation energy of V^- can be rewritten as

$$E_f(V^-) = (E_D^- - E_D^0) + (E_D^0 - E_H^0 + \mu_{\text{Cl}}) - \epsilon_{\text{VBM}}, \quad (\text{C.16})$$

where the first term on the right-hand side is now the (negative) electron affinity energy of V^0 (or the ionization energy of V^-). In contrast to the ionization energy, it is found that hybrid functionals tend to yield a smaller affinity energy of V^0 than semi-local functionals, and that the difference reaches up to 0.9 eV. Along with the ϵ_{VBM} , they explain the variations in the formation energy observed in Table C.4.

The atomic relaxation energy due to the polaronic electron or hole can be further extracted from Table C.4 as the difference between the rigid and relaxed structures. It is not surprising that the relaxation energies given by various functionals are consistent provided the atomic displacements are similar with these functionals (see Table C.2). The relaxation energy for V^+ is about 0.8 eV, while it ranges from 0.2 to 0.4 eV for V^- .

For a charged defect, the formation energy is a function of the Fermi energy as illustrated in Fig. C.4. The intersections of different charge states are the thermodynamic transition levels defined in Eq. (C.10). We see in Fig. C.4 that the transition levels $\epsilon(+/0)$ and $\epsilon(0/-)$ are both within the band gap. Therefore, the mPBE0 functional predicts that all charge states (-1, 0 and +1) of Cl vacancy could be thermodynamically stable when the Fermi energy is varied within the band gap. We note that although this is also qualitatively predicted by the uncorrected formation energies, the Fermi energy window for the neutral V^0 vacancy is much narrower.

The density functional dependence of the thermodynamic transition levels is illustrated in Fig. C.5(a). Both neutral and +1 charge states are predicted to be stable since

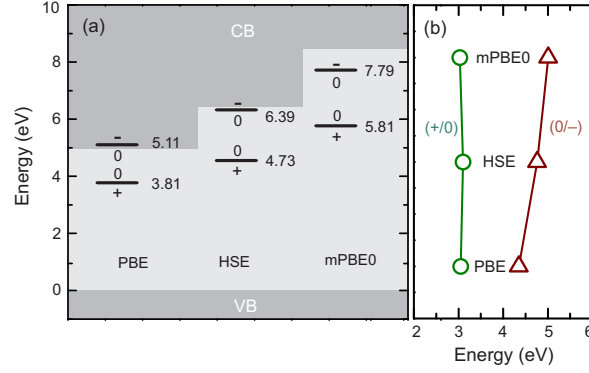


Figure C.5: (a) The thermodynamic transition levels of the Cl vacancy calculated with various functionals. The position of the VBM is aligned to energy zero. (b) The absolute values of the thermodynamic transition energies.

the $\epsilon(+/0)$ levels are within the band gap for all functionals, with transition energies increasing from 3.81 eV to 5.81 eV as the band gap widens from semi-local to hybrid functionals. On the other hand, the $\epsilon(0/-)$ is placed slightly above the CBM in the PBE, while its position falls into the band gap in HSE06 and is further shifted downwards with respect to the CBM in the mPBE0 calculations. Hence in contrast to the GGA-PBE, both the HSE06 and mPBE0 imply that the V^- is stable.

While the thermodynamic transition energy generally increases with respect to the VBM as the band gap enlarges, we see from Fig. C.5(b) that the absolute position $[\epsilon(q/q') + \epsilon_{\text{VBM}}]$ of the $\epsilon(+/0)$ level remains roughly unaffected from semi-local to hybrid functionals. This coincides with the findings by Alkauskas *et al.* that the calculated energy levels of localized defect are generally not tied to the position of the CBM [199]. The $\epsilon(0/-)$ levels are nevertheless more dispersed.

C.3 Optical Properties of the Color Center

The experimentally available optical properties of the F (V^0) and F' (V^-) center in NaCl serve as a benchmark for the assessment of the performance of the functionals. The optical processes are clearly marked in the configuration coordinate diagram in Fig. C.6 according to the Franck-Condon principle [200]. In the Franck-Condon approximation the electronic transition is assumed to occur very fast compared with the motion of nuclei in the lattice. Therefore, the optical excitation spectrum observed in experiment does not involve the relaxation of the defect structure, in contrast to the thermodynamic transition.

The optical absorption and emission can be described by vibronic (simultaneous vibrational and electronic) transitions, in which the lattice vibration mode is treated by a quantum harmonic oscillator. We first consider the excitation of an F center, which is a well-defined feature [155–157, 201]. By absorption of a photon, the unpaired electron is transferred to an excited electronic state (V^+ state) and an excited vibrational state.

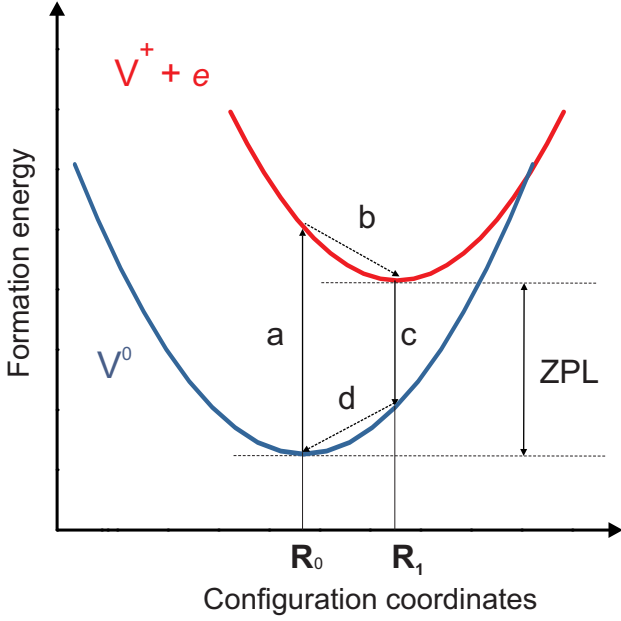


Figure C.6: Configuration coordinate diagram for the neutral and + charge state of Cl vacancy in NaCl. The Fermi energy is located at the CBM. The optical processes involved are the absorption (a), emission (c), Stokes (b) and anti-Stokes (d) shifts, and zero-phonon line (ZPL). The coordinates at the lowest vibrational state of the ground state and excited state are denoted by \mathbf{R}_0 and \mathbf{R}_+ , respectively. The zero-point energy is neglected in the diagram.

The excitation of an electron into the CBM is equivalent to bringing an electron to a reservoir with a chemical potential of $\epsilon_{\text{VBM}} + E_g$. The optical absorption energy E_a , as illustrated in Fig. C.6, is thus given by

$$E_a = E_f^{\mathbf{R}_0}(+; \epsilon_F = E_g) - E_f^{\mathbf{R}_0}(0), \quad (\text{C.17})$$

where the first term on the right-hand side is the formation energy of the unrelaxed +1 charge state (at coordinate \mathbf{R}_0) with the Fermi energy at the CBM, and the second term the formation energy of the relaxed neutral charge state (at \mathbf{R}_0). The excited state (F^+ center) subsequently relaxes to its zero-point vibration states. The energy gain due to the relaxation is the Stokes shift E_S between the vertical absorption and the zero-phonon line (ZPL). The ZPL is the transition energy from the lowest vibrational level (zero phonon mode) of the ground state to the lowest level of the excited state (at \mathbf{R}_1), without energy transfer to lattice phonons. In terms of thermodynamic transition energy, it is easy to see from Fig. C.4 that the ZPL can be expressed in terms of the difference between the band gap E_g and $\epsilon(+/0)$. In the present case, due to the identical formation energy between the rigid and relaxed V^0 , the Stokes shift reduces to the relaxation energy of the V^+ from the rigid structure. In the vertical emission (luminescence), the excited electron from the CBM recombines into the defect level and the emission energy E_e is given by

$$E_e = E_f^{\mathbf{R}_1}(+; \epsilon_F = E_g) - E_f^{\mathbf{R}_1}(0), \quad (\text{C.18})$$

where the defect structure in the neutral state is kept fixed as that in the relaxed +1 charge state. Finite-size correction on this relaxation energy is taken into account according to Sec. C.2.1. Once the electron is in the ground state, it relaxes to the bottom of the state with the relaxation energy E_{AS} (*i.e.* the anti-Stokes shift between the ZPL

Table C.5: Calculated vertical absorption (E_a) and emission (E_e) energies, zero-phonon line (ZPL) and the Stokes (E_S) and anti-Stokes (E_{AS}) shifts of the F and F' centers in NaCl. All values in eV.

	E_a	E_e	ZPL	E_S	E_{AS}
<i>F</i> center					
GGA-PBE	2.03	0.65	1.19	0.84	0.55
HSE06	2.56	1.07	1.70	0.85	0.63
mPBE0	3.50	1.88	2.66	0.84	0.78
Expt.	2.77 ¹	0.98 ²			
<i>F'</i> center					
GGA-PBE	0.76	-0.27	-0.11	0.87	0.16
HSE06	0.91	-0.34	0.04	0.86	0.38
mPBE0	2.03	0.27	0.68	1.35	0.41
Expt.	2.43 ³				

¹ Reference [202].² Reference [203].³ Reference [204].

and the vertical emission). The pronounced Stokes and anti-Stokes shifts (see Table C.5) are expected due to the large polaronic distortion.

The calculated vertical absorption and emission energies of the F center using the GGA-PBE and hybrid functionals are reported in Table C.5. The zero-point energy is not included since it is usually comparable for both the ground state and excited state. We find that the absorption and emission energies are underestimated by the GGA-PBE, and this is most likely related to the small band gap. As to the hybrid functionals, the mPBE0 yields too large values, about 0.8 eV higher for both the absorption and emission energies than the experimental values. The HSE06 hybrid functional apparently outperforms the GGA-PBE and the mPBE0 for the vertical transition energies, with deviations within 0.2 eV and 0.1 eV for the absorption and emission energies, respectively. The available experimental ZPLs for several F -aggregated centers (1.96 eV for R_2 band [205] and 1.48 eV for N band [206]) suggest the mPBE0 also gives a too large ZPL.

Analogously, we extend the calculation to the optical process of the F' center, which is formed when an electron is trapped at an F center by light absorption at low temperatures [157]. Instead of the sharp and bell-shaped curve of the F band, the F' center of NaCl gives rise to a broad F' absorption band, peaking at the longer wavelengths side of the F band [155–157]. It is seen in Table C.5 that all functionals now predict smaller absorption energies with respect to the experimental F' band peak. In accord with the F band absorption, the F' E_a increases from the semi-local functional to the hybrid functionals as the calculated band gap widens. The E_a values given by the GGA-PBE and HSE06 are well below the experimentally observed peak, whereas the mPBE0 yields

a value that is in better agreement with experiment. In addition, we find that the various functionals predict either a negative or a very small emission energy E_e from the excited F' state to the ground state. A negative emission energy in Table C.5 suggests that the configuration coordinate of the intersection lies between the coordinates of the minimum of the ground state and excited state. It is conceivable that in such case the excited state can return back to the ground state through a non-radiative process by vibrational relaxations, which leads to the luminescence quenching. The non-radiative path is also valid for a vibronic system with a small emission energy where the intersection is in the vicinity of the minimum of the excited state [207]. Experimentally, a radiative transition of an F' excited state is indeed absent [208].

C.4 Discussion

We have shown that, while hybrid functionals have been reported to be adequate for defects in some semiconductors [192, 209–214], the description of the localized anion vacancy in a wide gap insulator is less satisfactory by hybrid functionals when compared to the experimental optical absorption spectra. In this section, we aim to identify the possible origins of the failure of hybrid functionals for the description of the color centers in NaCl. It should be mentioned that the total energy difference scheme used to determine the absorption energy does not include the electron-hole interaction. Nonetheless, this should not affect the overall trend of the results because the presence of the exciton usually introduces a uniform redshift of the absorption energy irrespective of the density functionals.

We start with the discussion of the optical absorption since it is well-defined experimentally. The absorption energy of an F center in Eq. (C.17) can be rewritten as

$$\begin{aligned} E_a &= -\epsilon(+/0)^{\mathbf{R}_0} + E_g \\ &= \underbrace{[E_D^{\mathbf{R}_0}(+) - E_D^{\mathbf{R}_0}(0)]}_{\text{IP}(V^0)} + \underbrace{(\epsilon_{\text{VBM}} + E_g)}_{\epsilon_{\text{CBM}}}, \end{aligned} \quad (\text{C.19})$$

where $\epsilon(+/0)^{\mathbf{R}_0}$ refers to the vertical transition energy occurring at the geometry for the neutral vacancy, and $\text{IP}(V^0)$ is the ionization energy of V^0 . Therefore the absorption energy is solely dependent on the ionization of the neutral vacancy and the position of the band edge in a perfect supercell, and no structural relaxation is involved. As the ionization energy is not sensitive to the choice of the functional as discussed in Sec. C.2.2, it becomes obvious that the discrepancies in the absorption energy reported in Table C.5 mostly stem from the variations in the CBM energy. For instance, the GGA-PBE ϵ_{CBM} is 1.45 eV lower than the mPBE0 value as a result of the well-known band gap problem associated with the local and semi-local DFT functionals. While the energy gap can be reproduced by mixing 40% exact exchange in mPBE0, it is yet not clear whether the positions of the band edges are accurate.

In principle, the band gap problem can be overcome by quasiparticle (QP) self-energy calculations based on many-body perturbation theory. Here we follow the widely adopted

GW approximation for the electronic self-energy [72] and calculate the QP corrections to the Kohn-Sham eigenvalues. The GW approximation can be understood as the Hartree-Fock theory with a dynamically screened Coulomb interaction. The QP energies are calculated in a two-atom NaCl unit cell with a Γ centered $4 \times 4 \times 4$ \mathbf{k} -point mesh and an energy cutoff of 200 eV for the response function, and a total of 256 bands. The dynamic dielectric matrix is constructed with a frequency grid of 200 points.[215] We note that the QP gap of NaCl is closely related to the starting wavefunction and self-consistency. It is found that single shot G_0W_0 correction is too small when it is applied to the GGA-PBE eigenstates, whereas G_0W_0 on top of mPBE0 overestimates the QP gap. A fully self-consistent GW calculation also yields a too large QP gap irrespective of the initial eigenstates, as a result of the neglect of the attractive electron-hole interaction.[78] By updating the eigenvalues (four times) in the Green's function G and keeping the screened Coulomb interaction W at the RPA level within the initial PBE eigenvalues, the GW_0 @PBE scheme produces a QP gap of 8.43 eV, in agreement with experiment. The VBM is now lowered by 2.77 eV with respect to the PBE eigenvalue, and the CBM is lifted up by 0.66 eV, reaching to 4.90 eV by QP corrections. Compared to the GW_0 result, the mPBE0 CBM is placed 0.8 eV too high in energy, while the CBM energy calculated with the HSE06 functional coincides with that of the GW_0 (see Table C.3). A good agreement with the experiment F band absorption energy can be already obtained if the ϵ_{CBM} in Eq. (C.19) is naively replaced by the GW_0 value while keeping the ionization energy untouched. Therefore, the ionization energies of the neutral Cl vacancy V^0 calculated by semi-local and hybrid functionals are well described from the total energy difference (ΔSCF) method. In contrast, the calculated ionization energy of the negative charge system V^- is less satisfactory with GGA-PBE and is not much improved with the hybrid functionals based on the experimental F' band absorption peak and the GW_0 CBM energy. This is easily understood since the electronic correlations for the removal of a second electron from the a_{1g} level is beyond the scope of DFT [94]. These many-body effects are accessible from the many-body perturbation theory, e.g. in the GW approximation via the self-energy.

In the GW approximation, the QP energies of the highest occupied and lowest unoccupied level correspond to the electron removal and addition energies, respectively. It is then straightforward from Eq. (C.19) that the absorption energy can be calculated as the QP energy difference between the CBM and the lowest unoccupied state of the V^+ , provided the ionization potential of the neutral defect system is equivalent to the electron affinity of the positive charged system. For example, using a 64-atom supercell with a cutoff energy of 100 eV and a Γ point for the response function and 1024 total bands, the GW_0 @PBE method yields an F band absorption energy of 2.47 eV. We note that the two-particle excitonic effect in the optical absorption is not taken into account in the GW approximation either.

For shallow defects, it has been found that the hybrid functional shows great improvement over local or semi-local functionals in the defect transition energies [214]. This is mostly likely benefited from the fact that the position of the shallow defect follows the band edge (either CBM or VBM), which can be reproduced by hybrid functionals with tunable α . For deep levels as demonstrated in this study, we find that a reproduction of

a realistic band gap by an *ad hoc* tuning of the amount of the exact exchange in hybrid functionals does not guarantee an accurate description of the optical defect levels, and the thermodynamic charge transition levels as well. We see that the GGA-PBE is prone to an underestimation of the vertical transition energy, which is obviously impaired by a small band gap and a low conduction band edge. A significant shift for the band edges can be observed with the hybrid functionals. This leads to an increased vertical transition energy which is usually in better agreement with experiment, although the overestimation of the CBM energy by an increased fraction of the exact exchange in mPBE0 might give too high values (e.g. for the F band).

In addition to the electronic contributions (e.g. ionization energy and the position of the band edge), the structural relaxation also plays an important role in predicting the transition energies. The Frank-Condon shift (*i.e.* the difference between the absorption and emission energy) sheds light on the effect of the exact exchange on the lattice relaxations around the vacancy. By adopting the GW_0 CBM energy into the F band emission energy in Table C.5, we find that the lattice relaxation in presence of the electron-phonon interaction is best accounted by the mPBE0 hybrid functional as a result of the more localized electron density in the vacancy. The localization is proportional to the amount of the non-local exact exchange which reduces the self-interaction arising from the DFT XC functional. The localized nature of the trapped electron is further enhanced by a GW calculation, exhibiting an even smaller \mathbf{k} -dispersion of the a_{1g} level than the mPBE0 since the GW approximation is free of self-interaction. In this context, we expect the structural relaxation will also be more realistic within many-body perturbation theory.

The discussion of the vertical transition energies finally invokes us to return to the thermodynamic transition level presented in Sec. C.2.2. The thermodynamic transition level can be readily decomposed into the electronic and structural contributions as

$$\epsilon(+/0) = [E_g - E_a(F)] + \Delta E_D^+ \quad (\text{C.20})$$

and

$$\epsilon(0/-) = [E_g - E_a(F')] + \Delta E_D^0 \quad (\text{C.21})$$

where ΔE_D^+ and ΔE_D^0 are the relaxation energies from the initial geometry for the positive and neutral charge state, respectively. By incorporating the experimental vertical absorption energy and mPBE0 relaxation energy into Eq. (C.20) and (C.21), we come to the thermodynamic transition energies $\epsilon(+/0)=6.6$ eV and $\epsilon(0/-)=7.5$ eV. Therefore, the general picture of the Cl vacancy energetics by the adjusted hybrid functional so as to reproduce the experimental band gap remains qualitatively sound albeit not numerically accurate.

To wrap up, we find that the reduced self-interaction error alleviated by the exact exchange allows for a more accurate description of the atomic relaxations in the vicinity of the vacancy compared to the DFT results. Yet, hybrid functionals are unable to achieve quantitative agreement with experimental optical absorption peaks. We show that this is closely related to the overestimations of the band edges when the fundamental gap is reproduced by an empirical amount of exact exchange. Meanwhile, when the electronic correlation comes into play during the removal (addition) of a second electron

from (to) the localized defect level, the ionization (affinity) energy predicted within the framework of DFT is far from satisfactory. More elaborate methods (such as *GW* approximation [216–219] and two-particle Bethe-Salpeter equation [71, 94, 220, 221]) are thus necessary for more accurate descriptions of the optical process and defect energetics of the localized defects in wide gap insulators.

Appendix D

Passivation of the Polar Step by Water

It has been found in technological applications that in an environment with relatively high humidity, the output of the mineral separation process falls dramatically. We tentatively explain this phenomenon by utilizing the polar [011] monatomic step discussed in Sec. 13.3. The band structure in Fig. 13.8 shows a pronounced gap reduction due to the presence of the dipole and the under-coordinated step edge atoms. We now put one water molecule at the Cl-terminated side for each step edge Cl atoms. This gives a full coverage of the Cl step edge by the water molecules.

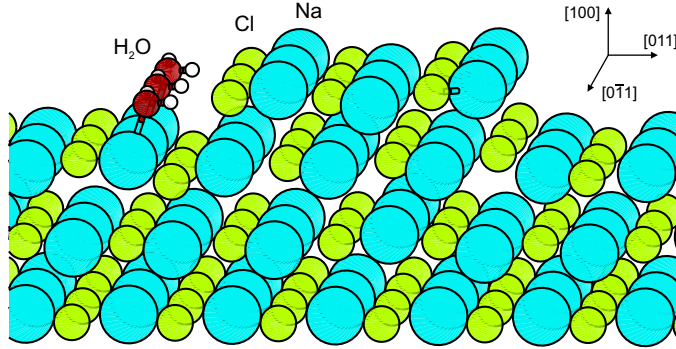


Figure D.1: Water molecules adsorbed at the Cl-terminated NaCl [011] stepped surface.

The optimized adsorption geometry based on the S2 model is illustrated in Fig. D.1, using the PW1PW hybrid functional. The water molecule sits on the (100) terrace with one hydrogen atom pointing at the Cl atom at the step edge. The H–Cl bond length is 2.32 Å, typical for a hydrogen bond.

It can be seen in Fig. D.2 that the band gap recovers to over 5 eV after the water molecule is adsorbed, which is about 0.5 eV larger than the band gap of the bare [011]-oriented stepped surface. The offset of the step edge Cl $3p$ states from the rest electronic states is also much smaller compared to the band structure in Fig. 13.8. Hence, the water adsorbate can effectively *passivate* the electronic states localized at the step edge Cl atoms. This is a consequence of the enhancement of the Madelung potential near the Cl atoms at the step edge, and the coordination number of these Cl atoms becomes larger.

If a hydroxybenzoic acid is now adsorbed at the Na-terminated side of the stepped surface, the effective gap of the adsorbate system will increase with respect to the ad-

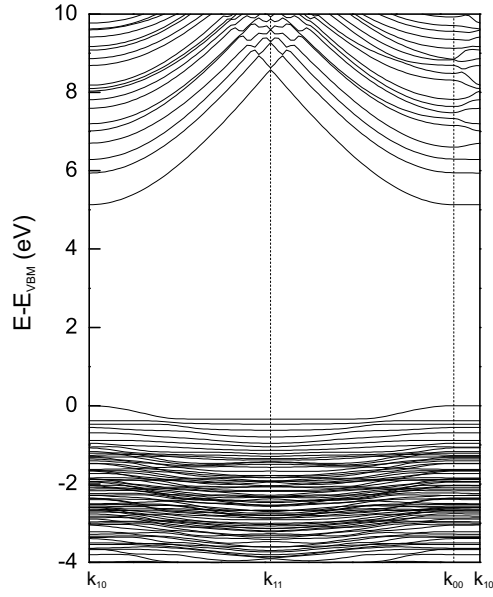


Figure D.2: Band structure of the NaCl [011] stepped surface with the water adsorbed at the Cl-terminated step edge.

sorption at the bare [011] step because the energy gap relies on the separation between the VBM and the LUMO. Due to the small offset of the step edge Cl $3p$ state, the HOMO-2 resonance state is closer to the VBM, which leads to a larger distance between the VBM and the LUMO. Therefore, in the high humidity condition, the effect of the polar steps in reducing the gap could be partially compensated by the water molecules.

Appendix E

Localized Basis Sets

The basis sets used in CRYSTAL calculations are provided in this appendix. The carbon, oxygen and hydrogen atoms of the molecules are described by 6-31G(*d*) basis sets. A test calculation with larger 6-311G(*d,p*) basis set yields an adsorption energy difference of 0.04 eV for the SA adsorbed on NaCl(100).

Carbon:

```
6 4
0 0 6 2.0 1.0
 3047.52490      0.183470000E-02
 457.369510     0.140373000E-01
 103.948690     0.688426000E-01
 29.2101550     0.232184400
 9.28666300     0.467941300
 3.16392700     0.362312000
0 1 3 4.0 1.0
 7.86827240    -0.119332400  0.689991000E-01
 1.88128850    -0.160854200  0.316424000
 0.544249300   1.143456400  0.744308300
0 1 1 0.0 1.0
 0.168714400   1.000000000  1.000000000
0 3 1 0.0 1.0
 0.800000000   1.000000000
```

Hydrogen:

```
1 2
0 0 3 1.0 1.0
 18.7311370     0.334946000E-01
 2.82539370     0.234726950
 0.640121700     0.813757330
0 0 1 0.0 1.0
 0.161277800     1.000000000
```

Oxygen:

```
8 4
0 0 6 2.0 1.0
  5484.67170      0.183110000E-02
  825.234950      0.139501000E-01
  188.046960      0.684451000E-01
  52.9645000      0.232714300
  16.8975700      0.470193000
  5.79963530      0.358520900
0 1 3 6.0 1.0
  15.5396160     -0.110777500      0.708743000E-01
  3.59993360     -0.148026300      0.339752800
  1.01376180      1.130767000      0.727158600
0 1 1 0.0 1.0
  0.270005800      1.000000000      1.000000000
0 3 1 0.0 1.0
  0.800000000      1.000000000
```

Using the O as an example, we see that the 1s electrons of O are expanded by a linear combination of 6 primitive Gaussians $0.0018e^{-5484.7r^2} + 0.14e^{-825.2r^2} + 0.068e^{-188.0r^2} + \dots + 0.36e^{-5.8r^2}$. The 2s valence electrons are expanded by two functions in a double- ζ scheme, namely $-0.11e^{-15.5r^2} - 0.15e^{-3.6r^2} + 1.1e^{-1.0r^2}$, and a normalized primitive $e^{-0.27r^2}$. Analogously, the 2p electrons are described by two functions: $0.07e^{-15.5r^2} + 0.34e^{-3.6r^2} + 0.73e^{-1.0r^2}$ and $e^{-0.27r^2}$. A 3d polarization Gaussian-type function $e^{-0.8r^2}$ is also appended to the atom.

For Na, K, and Cl atoms, the 8-511G, 86-511G and 86-311G split-valence basis sets are used in this work, respectively.

Sodium:

```
11 4
0 0 8 2.0 1.0
  56700.0000      0.000225
  8060.00000      0.001910
  1704.00000      0.011050
  443.600000      0.050060
  133.100000      0.169100
  45.8000000      0.365800
  17.7500000      0.399800
  7.38000000      0.149400
0 1 5 8.0 1.0
  119.000000     -0.006730      0.008030
  25.3300000     -0.079800      0.063900
```

7.80000000	-0.079300	0.207400
3.00000000	0.305600	0.339800
1.28900000	0.563900	0.372600
0 1 1 0.0 1.0		
0.57800000	1.000000	1.000000
0 1 1 0. 1.		
0.32300000	1.000000	1.000000

Potassium:

19 6		
0 0 8 2.0 1.0		
172500.0000	0.000220	
24320.00000	0.001920	
5140.000000	0.011090	
1343.900000	0.049920	
404.5000000	0.170200	
139.4000000	0.367900	
54.39000000	0.403600	
22.71000000	0.145900	
0 1 6 8.0 1.0		
402.0000000	-0.006030	0.008410
93.50000000	-0.080500	0.060200
30.75000000	-0.109400	0.211700
11.91000000	0.258000	0.372600
5.167000000	0.684000	0.402200
1.582000000	0.399000	0.186000
0 1 5 8. 1.		
17.35000000	-0.007400	-0.032100
7.550000000	-0.129000	-0.062000
2.939000000	-0.683400	0.169100
1.190000000	1.080000	1.500000
0.674000000	1.030000	1.060000
0 1 1 0.0 1.0		
0.389000000	1.000000	1.000000
0 1 1 0.0 1.0		
0.216000000	1.000000	1.000000
0 3 3 0.0 1.0		
3.940000000	0.160000	
1.072000000	0.313000	
0.394000000	0.406000	

Chlorine:

```
17 5
0 0 8 2.0 1.0
 135320.000 0.000225
 19440.0000 0.001910
 4130.00000 0.011100
 1074.00000 0.049890
 323.400000 0.170300
 111.100000 0.368300
 43.4000000 0.403600
 18.1800000 0.145900
0 1 6 8.0 1.0
 324.800000 -0.007630 0.008200
 73.0000000 -0.082900 0.060500
 23.7100000 -0.104600 0.211500
 9.13800000 0.254000 0.376500
 3.93000000 0.695000 0.396700
 1.32900000 0.399000 0.186000
0 1 3 8.0 1.0
 4.75500000 -0.374000 -0.034000
 1.75600000 -0.475400 0.161700
 0.78500000 1.340000 0.925000
0 1 1 0.0 1.0
 0.32000000 1.000000 1.000000
0 1 1 0.0 1.0
 0.12500000 1.000000 1.000000
```

Regarding the isolated Na^+ and Cl^- for the lattice energy calculations, the two most diffuse *sp* shells are re-optimized. The exponent of the most diffuse shell is also optimized (0.117 Bohr^{-2}) for calculations of the isolated Cl atom.

Bibliography

- [1] J. M. Thomas and W. J. Thomas, *Principles and Practice of Heterogeneous Catalysis* (WILEY-VCH Verlag, Weinheim, 1997)
- [2] M. Copel, M. C. Reuter, Efthimios Kaxiras, and R. M. Tromp, “Surfactants in epitaxial growth,” *Phys. Rev. Lett.* **63**, 632–635 (1989)
- [3] *Chemical Vapor Deposition: Principles and Applications*, 2nd ed., edited by M. L. Hitchman and K. F. Jensen (Academic Press, 1993)
- [4] Markku Leskelä and Mikko Ritala, “Atomic layer deposition (ALD): from precursors to thin film structures,” *Thin Solid Films* **409**, 138 – 146 (2002)
- [5] Jean-Marie Lehn, “Perspectives in Supramolecular Chemistry - From Molecular Recognition towards Molecular Information Processing and Self-Organization,” *Angew. Chem. Int. Ed.* **29**, 1304–1319 (1990)
- [6] R. Lloyd Carroll and Christopher B. Gorman, “The Genesis of Molecular Electronics,” *Angew. Chem. Int. Ed.* **41**, 4378–4400 (2002)
- [7] B. Hammer and J.K. Nørskov, “Theoretical surface science and catalysis—calculations and concepts,” *Impact of Surf. Sci. on Catalysis*, *Advances in Catalysis* **45**, 71 – 129 (2000)
- [8] Brian C. H. Steele and Angelika Heinzl, “Materials for fuel-cell technologies,” *Nature* **414**, 345–352 (2001)
- [9] Hisao Ishii, Kiyoshi Sugiyama, Eisuke Ito, and Kazuhiko Seki, “Energy Level Alignment and Interfacial Electronic Structures at Organic/Metal and Organic/Organic Interfaces,” *Adv. Mater.* **11**, 605–625 (1999)
- [10] Xavier Crispin, Victor Geskin, Annica Crispin, Jérôme Cornil, Roberto Lazzaroni, William R. Salaneck, and Jean-Luc Brédas, “Characterization of the Interface Dipole at Organic/ Metal Interfaces,” *J. Am. Chem. Soc.* **124**, 8131–8141 (2002)
- [11] *Chemical Bonding at Surfaces and Interfaces*, edited by Anders Nilsson, Lars Pettersson, and Jens Nørskov (Elsevier, 2007)
- [12] Axel Groß, *Theoretical Surf. Sci.: A Microscopic Perspective*, 2nd ed. (Springer, Berlin Heidelberg, 2009)

- [13] W.G. Schmidt, K. Seino, M. Preuss, A. Hermann, F. Ortmann, and F. Bechstedt, “Organic molecule adsorption on solid surfaces: chemical bonding, mutual polarisation and dispersion interaction,” *Appl. Phys. A: Materials Science & Processing* **85**, 387–397 (2006)
- [14] Jürgen Hafner, “Adsorption and reaction of organic molecules on solid surfaces - ab initio density functional investigations,” *Monatshefte für Chemie / Chemical Monthly* **139**, 373–387 (2008)
- [15] Jascha Repp, Gerhard Meyer, Sladjana M. Stojković, André Gourdon, and Christian Joachim, “Molecules on Insulating Films: Scanning-Tunneling Microscopy Imaging of Individual Molecular Orbitals,” *Phys. Rev. Lett.* **94**, 026803 (2005)
- [16] U. Malaske, C. Tegenkamp, M. Henzler, and H. Pfnür, “Defect-induced band gap states and the contact charging effect in wide band gap insulators,” *Surf. Sci.* **408**, 237–251 (1998)
- [17] A. Allouche, “Water dissociation on defective sites on the NaCl(100) surface. A quantum ab initio study,” *J. Phys. Chem. B.* **102**, 10223–10228 (1998)
- [18] X. Q. Gong, A. Selloni, M. Batzill, and U. Diebold, “Steps on anatase TiO₂(101),” *Nature Materials* **5**, 665–670 (2006)
- [19] J. Zhu, J. A. Farmer, N. Ruzycki, L. Xu, C. T. Campbell, and G. Henkelman, “Calcium adsorption on MgO(100): Energetics, structure, and role of defects,” *J. Am. Chem. Soc.* **130**, 2314–2322 (2008)
- [20] G. Mercurio, E. R. McNellis, I. Martin, S. Hagen, F. Leyssner, S. Soubatch, J. Meyer, M. Wolf, P. Tegeder, F. S. Tautz, and K. Reuter, “Structure and Energetics of Azobenzene on Ag(111): Benchmarking Semiempirical Dispersion Correction Approaches,” *Phys. Rev. Lett.* **104**, 036102 (2010)
- [21] D.C. Langreth, B.I. Lundqvist, S.D. Chakarova-Kack, V.R. Cooper, M. Dion, P. Hyldgaard, A. Kelkkanen, J. Kleis, Lingzhu Kong, Shen Li, P.G. Moses, E. Murray, A. Puzder, H. Rydberg, E. Schroder, and T. Thonhauser, “A density functional for sparse matter,” *J. Phys.: Condens. Matter* **21**, 084203 (2009)
- [22] A. I. Liechtenstein, V. I. Anisimov, and J. Zaanen, “Density-functional theory and strong interactions: Orbital ordering in Mott-Hubbard insulators,” *Phys. Rev. B* **52**, R5467–R5470 (1995)
- [23] J. B. Neaton, Mark S. Hybertsen, and Steven G. Louie, “Renormalization of Molecular Electronic Levels at Metal-Molecule Interfaces,” *Phys. Rev. Lett.* **97**, 216405 (2006)
- [24] J. C. Slater, “The Theory of Complex Spectra,” *Phys. Rev.* **34**, 1293–1322 (1929)
- [25] D. R. Hartree, “The Wave Mechanics of an Atom with a Non-Coulomb Central Field,” *Proc. Camb. Phil. Soc.* **24**, 89–110 (1928)

-
- [26] V. Fock, “Näherungsmethode zur Lösung des quantenmechanischen Mehrkörperproblems,” *Z. Physik* **61**, 126–148 (1930), 10.1007/BF01340294
- [27] G.G. Hall, “The Molecular Orbital Theory of Chemical Valency. VIII. A Method of Calculating Ionization Potentials,” *Proc. R. Soc. Lond. A*, 541–552(1951)
- [28] C. C. J. Roothaan, “New Developments in Molecular Orbital Theory,” *Rev. Mod. Phys.* **23**, 69–89 (1951)
- [29] Andreas Grüneis, Martijn Marsman, and Georg Kresse, “Second-order M[oller]ller–Plesset perturbation theory applied to extended systems. II. Structural and energetic properties,” *J. Chem. Phys.* **133**, 074107–11 (2010)
- [30] L. H. Thomas, “The calculation of atomic fields,” *Proc. Camb. Phil. Soc.* **23**, 542–548 (1927)
- [31] E. Fermi, “Un Metodo Statistico per la Determinazione di alcune Proprietà dell’Atomo,” *Rend. Accad. Naz. Lincei* **6**, 602–607 (1927)
- [32] P. Hohenberg and W. Kohn, “Inhomogeneous Electron Gas,” *Phys. Rev.* **136**, B864–B871 (1964)
- [33] Mel Levy, “Universal Variational Functionals of Electron Densities, First-Order Density Matrices, and Natural Spin-Orbitals and Solution of the v -Representability Problem,” *Proc. Nat. Acad. Sci.* **76**, 6062–6065 (1979)
- [34] W. Kohn and L. J. Sham, “Self-Consistent Equations Including Exchange and Correlation Effects,” *Phys. Rev.* **140**, A1133–A1138 (1965)
- [35] D. M. Ceperley and B. J. Alder, “Ground State of the Electron Gas by a Stochastic Method,” *Phys. Rev. Lett.* **45**, 566–569 (1980)
- [36] M. C. Payne, M. P. Teter, D. C. Allan, T. A. Arias, and J. D. Joannopoulos, “Iterative minimization techniques for ab initio total-energy calculations: molecular dynamics and conjugate gradients,” *Rev. Mod. Phys.* **64**, 1045–1097 (1992)
- [37] Stephan Kümmel and Leeor Kronik, “Orbital-dependent density functionals: Theory and applications,” *Rev. Mod. Phys.* **80**, 3–60 (2008)
- [38] Frank Herman, John P. Van Dyke, and Irene B. Ortenburger, “Improved Statistical Exchange Approximation for Inhomogeneous Many-Electron Systems,” *Phys. Rev. Lett.* **22**, 807–811 (1969)
- [39] Mel Levy, “Density-functional exchange correlation through coordinate scaling in adiabatic connection and correlation hole,” *Phys. Rev. A* **43**, 4637–4646 (1991)
- [40] John P. Perdew and Yue Wang, “Accurate and simple analytic representation of the electron-gas correlation energy,” *Phys. Rev. B* **45**, 13244–13249 (1992)

- [41] John P. Perdew, Kieron Burke, and Matthias Ernzerhof, “Generalized Gradient Approximation Made Simple,” *Phys. Rev. Lett.* **77**, 3865–3868 (1996)
- [42] B. Hammer, L. B. Hansen, and J. K. Nørskov, “Improved adsorption energetics within density-functional theory using revised Perdew-Burke-Ernzerhof functionals,” *Phys. Rev. B* **59**, 7413–7421 (1999)
- [43] John P. Perdew, Adrienn Ruzsinszky, Gábor I. Csonka, Oleg A. Vydrov, Gustavo E. Scuseria, Lucian A. Constantin, Xiaolan Zhou, and Kieron Burke, “Restoring the Density-Gradient Expansion for Exchange in Solids and Surfaces,” *Phys. Rev. Lett.* **100**, 136406 (2008)
- [44] Marcus Lundberg and Per E. M. Siegbahn, “Quantifying the effects of the self-interaction error in DFT: When do the delocalized states appear?” *J. Chem. Phys.* **122**, 224103 (2005)
- [45] J. F. Janak, “Proof that $\frac{\partial E}{\partial n_i} = \epsilon$ in density-functional theory,” *Phys. Rev. B* **18**, 7165–7168 (1978)
- [46] John P. Perdew, Robert G. Parr, Mel Levy, and Jose L. Balduz, “Density-Functional Theory for Fractional Particle Number: Derivative Discontinuities of the Energy,” *Phys. Rev. Lett.* **49**, 1691–1694 (1982)
- [47] John P. Perdew and Mel Levy, “Physical Content of the Exact Kohn-Sham Orbital Energies: Band Gaps and Derivative Discontinuities,” *Phys. Rev. Lett.* **51**, 1884–1887 (1983)
- [48] T. Bredow and A. R. Gerson, “Effect of exchange and correlation on bulk properties of MgO, NiO, and CoO,” *Phys. Rev. B* **61**, 5194–5201 (2000)
- [49] Jochen Heyd, Gustavo E. Scuseria, and Matthias Ernzerhof, “Hybrid functionals based on a screened Coulomb potential,” *J. Chem. Phys.* **118**, 8207–8215 (2003)
- [50] J. Paier, M. Marsman, K. Hummer, G. Kresse, I. C. Gerber, and J. G. Ángyán, “Screened hybrid density functionals applied to solids,” *J. Chem. Phys.* **124**, 154709 (2006)
- [51] J. Paier, M. Marsman, K. Hummer, G. Kresse, I. C. Gerber, and J. G. Ángyán, “Erratum: “Screened hybrid density functionals applied to solids” [*J. Chem. Phys.* **124**, 154709 (2006)],” *J. Chem. Phys.* **125**, 249901 (2006)
- [52] Aron J. Cohen, Paula Mori-Sánchez, and Weitao Yang, “Fractional charge perspective on the band gap in density-functional theory,” *Phys. Rev. B* **77**, 115123 (2008)
- [53] John P. Perdew, Matthias Ernzerhof, and Kieron Burke, “Rationale for mixing exact exchange with density functional approximations,” *J. Chem. Phys.* **105**, 9982–9985 (1996)

-
- [54] Kohn, “Density-functional theory for systems of very many atoms,” *Int. J. Quantum Chem.* **56**, 229 (1995)
- [55] Stefan Grimme, “Semiempirical GGA-type density functional constructed with a long-range dispersion correction,” *J. Comp. Chem.* **27**, 1787–1799 (2006)
- [56] M. Dion, H. Rydberg, E. Schröder, D. C. Langreth, and B. I. Lundqvist, “Van der Waals Density Functional for General Geometries,” *Phys. Rev. Lett.* **92**, 246401 (2004)
- [57] Kyuho Lee, Éamonn D. Murray, Lingzhu Kong, Bengt I. Lundqvist, and David C. Langreth, “Higher-accuracy van der Waals density functional,” *Phys. Rev. B* **82**, 081101 (2010)
- [58] Michael Rohlfing and Thomas Bredow, “Binding Energy of Adsorbates on a Noble-Metal Surface: Exchange and Correlation Effects,” *Phys. Rev. Lett.* **101**, 266106 (2008)
- [59] Judith Harl and Georg Kresse, “Accurate Bulk Properties from Approximate Many-Body Techniques,” *Phys. Rev. Lett.* **103**, 056401 (2009)
- [60] Xinguo Ren, Patrick Rinke, and Matthias Scheffler, “Exploring the random phase approximation: Application to CO adsorbed on Cu(111),” *Phys. Rev. B* **80**, 045402 (2009)
- [61] Guillermo Román-Pérez and José M. Soler, “Efficient Implementation of a van der Waals Density Functional: Application to Double-Wall Carbon Nanotubes,” *Phys. Rev. Lett.* **103**, 096102 (2009)
- [62] S. F. Boys and F. Bernardi, “Calculation of small molecular interaction by differences of separate total energies,” *Molecular Physics* **19**, 553 (1970)
- [63] Hendrik J. Monkhorst and James D. Pack, “Special points for Brillouin-zone integrations,” *Phys. Rev. B* **13**, 5188–5192 (1976)
- [64] *Plane waves, pseudopotentials and the LAPW method*, edited by David J. Singh and Lars Nordstrom (Kluwer Academic, 1994)
- [65] D. R. Hamann, M. Schlüter, and C. Chiang, “Norm-Conserving Pseudopotentials,” *Phys. Rev. Lett.* **43**, 1494–1497 (1979)
- [66] Leonard Kleinman and D. M. Bylander, “Efficacious Form for Model Pseudopotentials,” *Phys. Rev. Lett.* **48**, 1425–1428 (1982)
- [67] Steven G. Louie, Sverre Froyen, and Marvin L. Cohen, “Nonlinear ionic pseudopotentials in spin-density-functional calculations,” *Phys. Rev. B* **26**, 1738–1742 (1982)
- [68] David Vanderbilt, “Soft self-consistent pseudopotentials in a generalized eigenvalue formalism,” *Phys. Rev. B* **41**, 7892–7895 (1990)

- [69] P. E. Blöchl, “Projector augmented-wave method,” *Phys. Rev. B* **50**, 17953–17979 (1994)
- [70] Erich Runge and E. K. U. Gross, “Density-Functional Theory for Time-Dependent Systems,” *Phys. Rev. Lett.* **52**, 997 (1984)
- [71] Giovanni Onida, Lucia Reining, and Angel Rubio, “Electronic excitations: density-functional versus many-body Green’s-function approaches,” *Rev. Mod. Phys.* **74**, 601–659 (2002)
- [72] Lars Hedin, “New Method for Calculating the One-Particle Green’s Function with Application to the Electron-Gas Problem,” *Phys. Rev.* **139**, A796–A823 (1965)
- [73] Stephen L. Adler, “Quantum Theory of the Dielectric Constant in Real Solids,” *Phys. Rev.* **126**, 413–420 (1962)
- [74] Nathan Wiser, “Dielectric Constant with Local Field Effects Included,” *Phys. Rev.* **129**, 62–69 (1963)
- [75] B. Holm and U. von Barth, “Fully self-consistent *GW* self-energy of the electron gas,” *Phys. Rev. B* **57**, 2108–2117 (1998)
- [76] Wolf-Dieter Schöne and Adolfo G. Eguiluz, “Self-Consistent Calculations of Quasiparticle States in Metals and Semiconductors,” *Phys. Rev. Lett.* **81**, 1662–1665 (1998)
- [77] Wei Ku and Adolfo G. Eguiluz, “Band-Gap Problem in Semiconductors Revisited: Effects of Core States and Many-Body Self-Consistency,” *Phys. Rev. Lett.* **89**, 126401 (2002)
- [78] M. Shishkin, M. Marsman, and G. Kresse, “Accurate Quasiparticle Spectra from Self-Consistent *GW* Calculations with Vertex Corrections,” *Phys. Rev. Lett.* **99**, 246403 (2007)
- [79] C. Rödl, F. Fuchs, J. Furthmüller, and F. Bechstedt, “Quasiparticle band structures of the antiferromagnetic transition-metal oxides MnO, FeO, CoO, and NiO,” *Phys. Rev. B* **79**, 235114 (2009)
- [80] R. W. Godby, M. Schlüter, and L. J. Sham, “Self-energy operators and exchange-correlation potentials in semiconductors,” *Phys. Rev. B* **37**, 10159–10175 (1988)
- [81] F. Aryasetiawan, “Self-energy of ferromagnetic nickel in the *GW* approximation,” *Phys. Rev. B* **46**, 13051–13064 (1992)
- [82] A. Fleszar and W. Hanke, “Electronic excitations in beryllium chalcogenides from the *ab initio GW* approach,” *Phys. Rev. B* **62**, 2466–2474 (2000)
- [83] Mark S. Hybertsen and Steven G. Louie, “Electron correlation in semiconductors and insulators: Band gaps and quasiparticle energies,” *Phys. Rev. B* **34**, 5390–5413 (1986)

-
- [84] R. W. Godby and R. J. Needs, “Metal-insulator transition in Kohn-Sham theory and quasiparticle theory,” *Phys. Rev. Lett.* **62**, 1169–1172 (1989)
- [85] Giovanni Onida, Lucia Reining, R. W. Godby, R. Del Sole, and Wanda Andreoni, “Ab Initio Calculations of the Quasiparticle and Absorption Spectra of Clusters: The Sodium Tetramer,” *Phys. Rev. Lett.* **75**, 818–821 (1995)
- [86] Michael Rohlfing and Steven G. Louie, “Excitonic Effects and the Optical Absorption Spectrum of Hydrogenated Si Clusters,” *Phys. Rev. Lett.* **80**, 3320–3323 (1998)
- [87] Michael Rohlfing and Steven G. Louie, “Electron-Hole Excitations in Semiconductors and Insulators,” *Phys. Rev. Lett.* **81**, 2312–2315 (1998)
- [88] Stefan Albrecht, Lucia Reining, Rodolfo Del Sole, and Giovanni Onida, “Ab Initio Calculation of Excitonic Effects in the Optical Spectra of Semiconductors,” *Phys. Rev. Lett.* **80**, 4510–4513 (1998)
- [89] Andrea Marini and Rodolfo Del Sole, “Dynamical Excitonic Effects in Metals and Semiconductors,” *Phys. Rev. Lett.* **91**, 176402 (2003)
- [90] E. E. Salpeter and H. A. Bethe, “A Relativistic Equation for Bound-State Problems,” *Phys. Rev.* **84**, 1232–1242 (1951)
- [91] Marie Lopez del Puerto, Murilo L. Tiago, and James R. Chelikowsky, “Excitonic Effects and Optical Properties of Passivated CdSe Clusters,” *Phys. Rev. Lett.* **97**, 096401 (2006)
- [92] B. Arnaud, S. Lebègue, P. Rabiller, and M. Alouani, “Huge Excitonic Effects in Layered Hexagonal Boron Nitride,” *Phys. Rev. Lett.* **96**, 026402 (2006)
- [93] Ludger Wirtz, Andrea Marini, and Angel Rubio, “Excitons in Boron Nitride Nanotubes: Dimensionality Effects,” *Phys. Rev. Lett.* **96**, 126104 (2006)
- [94] Michel Bockstedte, Andrea Marini, Oleg Pankratov, and Angel Rubio, “Many-Body Effects in the Excitation Spectrum of a Defect in SiC,” *Phys. Rev. Lett.* **105**, 026401 (2010)
- [95] So Hirata and Martin Head-Gordon, “Time-dependent density functional theory within the Tamm-Dancoff approximation,” *Chem. Phys. Lett.* **314**, 291–299 (1999)
- [96] Maurizia Palummo, Conor Hogan, Francesco Sottile, Paolo Bagalá, and Angel Rubio, “Ab initio electronic and optical spectra of free-base porphyrins: The role of electronic correlation,” *J. Chem. Phys.* **131**, 084102 (2009)
- [97] Myrta Grüning, Andrea Marini, and Xavier Gonze, “Exciton-Plasmon States in Nanoscale Materials: Breakdown of the Tamm-Dancoff Approximation,” *Nano Lett.* **9**, 2820–2824 (2009)

- [98] Roberto Dovesi, Roberto Orlando, Bartolomeo Civalleri, Carla Roetti, Victor R. Saunders, and Claudio M. Zicovich-Wilson, “CRYSTAL: a computational tool for the ab initio study of the electronic properties of crystals,” *Zeitschrift für Kristallographie*, **220**, 571–573 (2005)
- [99] G. Bruno and L. Randaccio, “A Refinement of the benzoic-acid structure at room-temperature,” *Acta Crystallographica Section B-Structural Science* **36**, 1711–1712 (1980)
- [100] M Sundaral and L. H. Jensen, “Refinement of structure of salicylic acids,” *Acta Crystallographica* **18**, 1053 (1965)
- [101] C. Tegenkamp and H. Pfnür, “Adsorbate induced contact charging: pure and OH-substituted benzoic acids adsorbed on wide band gap insulators,” *Phys. Chem. Chem. Phys.* **4**, 2653–2659 (2002)
- [102] X. Gonze, B. Amadon, P.-M. Anglade, J.-M. Beuken, F. Bottin, P. Boulanger, F. Bruneval, D. Caliste, R. Caracas, M. Côté, T. Deutsch, L. Genovese, Ph. Ghosez, M. Giantomassi, S. Goedecker, D.R. Hamann, P. Hermet, F. Jollet, G. Jomard, S. Leroux, M. Mancini, S. Mazevet, M.J.T. Oliveira, G. Onida, Y. Pouillon, T. Rangel, G.-M. Rignanese, D. Sangalli, R. Shaltaf, M. Torrent, M.J. Verstraete, G. Zerah, and J.W. Zwanziger, “ABINIT: First-principles approach to material and nanosystem properties,” *40 YEARS OF CPC: A celebratory issue focused on quality software for high performance, grid and novel computing architectures*, *Comp. Phys. Comm.* **180**, 2582–2615 (2009)
- [103] Carlo A. Rozzi, Daniele Varsano, Andrea Marini, Eberhard K. U. Gross, and Angel Rubio, “Exact Coulomb cutoff technique for supercell calculations,” *Phys. Rev. B* **73**, 205119 (2006)
- [104] Andrea Marini, Conor Hogan, Myrta Grüning, and Daniele Varsano, “yambo: An ab initio tool for excited state calculations,” *Comp. Phys. Comm.* **180**, 1392–1403 (2009)
- [105] H. E. Ungnade and R. W. Lamb, “The absorption spectra of benzoic acid and esters,” *J. Am. Chem. Soc.* **74**, 3789–3794 (1952)
- [106] Z.L. Ernst and J. Menashi, “The spectrophotometric determination of the dissociation constants of some substituted salicylic acids,” *Trans. Faraday Soc.* **59**, 230–240 (1963)
- [107] M. Prencipe, A. Zupan, R. Dovesi, E. Apra, and V. R. Saunders, “Ab-initio study of the structural properties of LiF, NaF, KF, LiCl, NaCl, and KCl,” *Phys. Rev. B* **51**, 3391–3396 (1995)
- [108] A. D. Becke, “A new mixing of Hartree-Fock and local density-functional theories,” *J. Chem. Phys.* **98**, 1372–1377 (1993)

-
- [109] Gábor I. Csonka, John P. Perdew, Adrienn Ruzsinszky, Pier H. T. Philipsen, Sébastien Lebègue, Joachim Paier, Oleg A. Vydrov, and János G. Ángyán, “Assessing the performance of recent density functionals for bulk solids,” *Phys. Rev. B* **79**, 155107 (2009)
- [110] *CRC Handbook of Chemistry and Physics*, 87th ed. (CRC, Boca Raton, FL, 2006)
- [111] B. J. Marshall and Cleaveli.Cr, “Elastic constants of LiBr from 300 degrees to 4.2 degrees K,” *J. Phys. Chem. Solids* **30**, 1905 (1969)
- [112] Nuzio O. Lipari and A. Barry Kunz, “Energy Bands and Optical Properties of NaCl,” *Phys. Rev. B* **3**, 491–497 (1971)
- [113] *Crystal Structures*, 2nd ed., edited by W. G. Wyckoff, Vol. 1 (Wiley, New York, 1968)
- [114] P. K. de Boer and R. A. de Groot, “With a grain of salt,” *Phys. Lett. A* **256**, 227–229 (1999)
- [115] J. Frenkel, “On the Transformation of light into Heat in Solids. I,” *Phys. Rev.* **37**, 17–44 (1931)
- [116] D. M. Roessler and W. C. Walker, “Electronic Spectra of Crystalline NaCl and KCl,” *Phys. Rev.* **166**, 599–606 (1968)
- [117] F. Bechstedt, K. Seino, P. H. Hahn, and W. G. Schmidt, “Quasiparticle bands and optical spectra of highly ionic crystals: AlN and NaCl,” *Phys. Rev. B* **72**, 245114 (2005)
- [118] R. Dovesi, B. Civalleri, R. Orlando, C. Roetti, and V.R. Saunders, “Reviews in Computational Chemistry, Volume 21,” (John Wiley & Sons, Inc, New York, 2005) Chap. Ab Initio Quantum Simulation in Solid State Chemistry 1
- [119] B. Li, A. Michaelides, and M. Scheffler, “Density functional theory study of flat and stepped NaCl(001),” *Phys. Rev. B* **76**, 075401 (2007)
- [120] J. Vogt and H. Weiss, “The structure of NaCl(100) and KCl(100) single crystal surfaces: a tensor low energy electron diffraction analysis,” *Surf. Sci.* **491**, 155–168– (2001)
- [121] C. Tegenkamp and H. Pfnür, “Correlation of electronic and local structure of 4-hydroxy-thiophenol on NaCl(100) and Ag(100),” *J. Chem. Phys.* **118**, 7578–7584 (2003)
- [122] P. W. Anderson, “Localized Magnetic States in Metals,” *Phys. Rev.* **124**, 41–53 (1961)
- [123] D. M. Newns, “Self-Consistent Model of Hydrogen Chemisorption,” *Phys. Rev.* **178**, 1123–1135 (1969)

- [124] Svetla D. Chakarova-Käck, Elsebeth Schroder, Bengt I. Lundqvist, and David C. Langreth, “Application of van der Waals Density Functional to an Extended System: Adsorption of Benzene and Naphthalene on Graphite,” *Phys. Rev. Lett.* **96**, 146107 (2006)
- [125] Svetla D. Chakarova-Käck, Øyvind Borck, Elsebeth Schröder, and Bengt I. Lundqvist, “Adsorption of phenol on graphite(0001) and $\alpha - \text{Al}_2\text{O}_3(0001)$: Nature of van der Waals bonds from first-principles calculations,” *Phys. Rev. B* **74**, 155402 (2006)
- [126] Poul Georg Moses, Jens J. Mortensen, Bengt I. Lundqvist, and Jens K. Nørskov, “Density functional study of the adsorption and van der Waals binding of aromatic and conjugated compounds on the basal plane of MoS_2 ,” *J. Chem. Phys.* **130**, 104709 (2009)
- [127] O. H. Pakarinen, J. M. Mativetsky, A. Gulans, M. J. Puska, A. S. Foster, and P. Grutter, “Role of van der Waals forces in the adsorption and diffusion of organic molecules on an insulating surface,” *Phys. Rev. B* **80**, 085401 (2009)
- [128] John P. Perdew, Matthias Ernzerhof, Aleš Zupan, and Kieron Burke, “Nonlocality of the density functional for exchange and correlation: Physical origins and chemical consequences,” *J. Chem. Phys.* **108**, 1522–1531 (1998)
- [129] G. Kresse and J. Hafner, “Ab initio molecular-dynamics simulation of the liquid-metal amorphous-semiconductor transition in germanium,” *Phys. Rev. B* **49**, 14251–14269 (May 1994)
- [130] G. Kresse and J. Furthmüller, “Efficient iterative schemes for ab initio total-energy calculations using a plane-wave basis set,” *Phys. Rev. B* **54**, 11169–11186 (1996)
- [131] J. J. Mortensen, L. B. Hansen, and K. W. Jacobsen, “Real-space grid implementation of the projector augmented wave method,” *Phys. Rev. B* **71**, 035109 (2005)
- [132] Karen Johnston, Jesper Kleis, Bengt I. Lundqvist, and Risto M. Nieminen, “Influence of van der Waals forces on the adsorption structure of benzene on silicon studied using density functional theory,” *Phys. Rev. B* **77**, 121404 (2008)
- [133] R. P. Feynman, “Forces in Molecules,” *Phys. Rev.* **56**, 340–343 (1939)
- [134] Mark J. Allen and David J. Tozer, “Helium dimer dispersion forces and correlation potentials in density functional theory,” *J. Chem. Phys.* **117**, 11113–11120 (2002)
- [135] T. Thonhauser, Valentino R. Cooper, Shen Li, Aaron Puzder, Per Hyldgaard, and David C. Langreth, “Van der Waals density functional: Self-consistent potential and the nature of the van der Waals bond,” *Phys. Rev. B* **76**, 125112 (2007)
- [136] A. R. C. Westwood and T. T. Hitch, “Surface Energy of 100 Potassium Chloride,” *J. Appl. Phys.* **34**, 3085–3089 (1963)

-
- [137] P. W Tasker, “The surface energies, surface tensions and surface structure of the alkali halide crystals,” *Philosophical Magazine A* **39**, 119–136 (1979)
- [138] Ann E. Mattsson, Rickard Armiento, Peter A. Schultz, and Thomas R. Mattsson, “Nonequivalence of the generalized gradient approximations PBE and PW91,” *Phys. Rev. B* **73**, 195123 (2006)
- [139] J.W. Gadzuk, “Surface molecules and chemisorption: I. Adatom density of states,” *Surf. Sci.* **43**, 44 – 60 (1974)
- [140] Andris Gulans, Martti J. Puska, and Risto M. Nieminen, “Linear-scaling self-consistent implementation of the van der Waals density functional,” *Phys. Rev. B* **79**, 201105 (2009)
- [141] P. D. Johnson and S. L. Hulbert, “Inverse-photoemission studies of adsorbed diatomic molecules,” *Phys. Rev. B* **35**, 9427–9436 (1987)
- [142] Sergey Kubatkin, Andrey Danilov, Mattias Hjort, Jerome Cornil, Jean-Luc Bredas, Nicolai Stuhr-Hansen, Per Hedegard, and Thomas Bjornholm, “Single-electron transistor of a single organic molecule with access to several redox states,” *Nature* **425**, 698–701 (2003)
- [143] Jay D. Sau, J. B. Neaton, Hyoung Joon Choi, Steven G. Louie, and Marvin L. Cohen, “Electronic Energy Levels of Weakly Coupled Nanostructures: C_{60} -Metal Interfaces,” *Phys. Rev. Lett.* **101**, 026804 (2008)
- [144] Kristian S. Thygesen and Angel Rubio, “Renormalization of Molecular Quasiparticle Levels at Metal-Molecule Interfaces: Trends across Binding Regimes,” *Phys. Rev. Lett.* **102**, 046802 (2009)
- [145] J. M. Garcia-Lastra, C. Rostgaard, A. Rubio, and K. S. Thygesen, “Polarization-induced renormalization of molecular levels at metallic and semiconducting surfaces,” *Phys. Rev. B* **80**, 245427 (2009)
- [146] L.D. Landau and E.M. Lifshitz, *Electrodynamics of continuous media* (Pergamon Press, 1984)
- [147] Milton W. Cole and Morrel H. Cohen, “Image-Potential-Induced Surface Bands in Insulators,” *Phys. Rev. Lett.* **23**, 1238–1241 (1969)
- [148] Neng-Ping Wang, Michael Rohlfing, Peter Krüger, and Johannes Pollmann, “Quasiparticle band structure and optical spectrum of LiF(001),” *Phys. Rev. B* **67**, 115111 (2003)
- [149] Michael Rohlfing, Neng-Ping Wang, Peter Krüger, and Johannes Pollmann, “Image States and Excitons at Insulator Surfaces with Negative Electron Affinity,” *Phys. Rev. Lett.* **91**, 256802 (2003)

- [150] Valerio Olevano and Lucia Reining, “Excitonic Effects on the Silicon Plasmon Resonance,” *Phys. Rev. Lett.* **86**, 5962–5965 (2001)
- [151] Yuchen Ma, Michael Rohlfing, and Carla Molteni, “Excited states of biological chromophores studied using many-body perturbation theory: Effects of resonant-antiresonant coupling and dynamical screening,” *Phys. Rev. B* **80**, 241405 (2009)
- [152] S. Folsch and M. Henzler, “Water adsorption on the NaCl surface,” *14th International Seminar on Surface Physics*, *Surf. Sci.* **247**, 269–273 (1990)
- [153] B. Ahlswede and K. Jug, “MSINDO study of the adsorption of water molecules at defective NaCl(100) surfaces,” *Surf. Sci.* **439**, 86–94 (1999)
- [154] *Physics of Color Centers*, edited by W. B. Fowler (Academic Press, New York, 1968)
- [155] R. W. Pohl, “Electron conductivity and photochemical processes in alkali-halide crystals,” *Proc. Phys. Soc.* **49**, 3 (1937)
- [156] H. Pick, “Über den Einfluß der Temperatur auf die Erregung von Farbzentren,” *Ann. Physik* **423**, 365–376 (1938)
- [157] H. Pick, “Color centers in alkali halides,” *Nuovo Cimento Suppl.* **7**, 498–522 (1958)
- [158] B. Fritz and E. Menke, “Laser effect in KCl with FA(Li) centers,” *Solid State Commun.* **3**, 61 (1965)
- [159] G. Mallia, R. Orlando, C. Roetti, P. Uglieri, and R. Dovesi, “F center in LiF,” *Phys. Rev. B* **63**, 235102 (2001)
- [160] A.M. Ferrari and G. Pacchioni, “Electronic structure of F and V center on the MgO surface,” *J. Phys. Chem.* **99**, 17010 (1995)
- [161] C.A. Gilbert, R. Smith, and S.D. Kenny, “Ab-initio modelling of defects in MgO,” *Nuclear Instruments & Methods In Physics Research Section B* **255**, 166 (2007)
- [162] V. Zielasek, T. Hildebrandt, and M. Henzler, “Surface color centers on epitaxial NaCl films,” *Phys. Rev. B* **62**, 2912–2919 (2000)
- [163] W. C. Mackrodt and R. F. Stewart, “Defect properties of ionic solids .1. Point-defects at surfaces of face-centered cubic crystals,” *J. Phys. C: Solid State Physics* **10**, 1431–1446– (1977)
- [164] V. E. Puchin, A. L. Shluger, and N. Itoh, “Theoretical studies of atomic emission and defect formation by electronic excitation at the (100) surface of NaCl,” *Phys. Rev. B* **47**, 10760–10768 (1993)
- [165] Q. Dai, J. Hu, and M. Salmeron, “Adsorption of water on NaCl (100) surfaces: Role of atomic steps,” *J. Phys. Chem. B* **101**, 1994–1998 (1997)

-
- [166] C. Tegenkamp, W. Ernst, M. Eichmann, and H. Pfnür, “Stepped NaCl films grown epitaxially on Si-precovered vicinal Ge(100),” *Surf. Sci.* **466**, 41 – 53 (2000)
- [167] J. Goniakowski and C. Noguera, “Atomic and electronics structure of steps and kinks on MgO(100) and MgO(110),” *Surf. Sci.* **340**, 191–204 (1995)
- [168] E. D. Williams, “Surfaces steps and surface morphology - Understanding macroscopic phenomena from atomic observations,” *Surf. Sci.* **300**, 502–524 (1994)
- [169] Christoph Tegenkamp, “Vicinal surfaces for functional nanostructures,” *J. Phys.; Condens. Matter* **21**, 013002 (2009)
- [170] A. Pojani, F. Finocchi, J. Goniakowski, and C. Noguera, “A theoretical study of the stability and electronic structure of the polar 111 face of MgO,” *Surf. Sci.* **387**, 354 (1997)
- [171] C. Noguera, “Polar oxide surfaces,” *J. Phys.: Condens. Matter* **12**, R367 (2000)
- [172] G. Geneste, J. Morillo, F. Finocchi, and M. Hayoun, “Primary nucleation processes in binary oxide growth,” *Surf. Sci.* **601**, 5616 (2007)
- [173] J. Goniakowski, F. Finocchi, and C. Noguera, “Polarity of oxide surfaces and nanostructures,” *Rep. Prog. Phys.* **71**, 016501 (2008)
- [174] G. Kresse and D. Joubert, “From ultrasoft pseudopotentials to the projector augmented-wave method,” *Phys. Rev. B* **59**, 1758–1775 (1999)
- [175] Volodymyr Maslyuk, Christoph Tegenkamp, Herbert Pfnür, and Thomas Bredow, “Adsorption of Functionalized Benzoic Acids on $\text{MgSO}_4 \cdot \text{H}_2\text{O}$ (100),” *ChemPhysChem* **7**, 1055–1061 (2006)
- [176] V. V. Maslyuk, C. Tegenkamp, H. Pfnür, and T. Bredow, “Properties of Ternary Insulating Systems: The Electronic Structure of $\text{MgSO}_4 \cdot \text{H}_2\text{O}$,” *J. Phys. Chem. A* **109**, 4118–4124 (2005)
- [177] Aliaksandr V. Krukau, Oleg A. Vydrov, Artur F. Izmaylov, and Gustavo E. Scuseria, “Influence of the exchange screening parameter on the performance of screened hybrid functionals,” *J. Chem. Phys.* **125**, 224106 (2006)
- [178] F. Aryasetiawan and O. Gunnarsson, “The GW method,” *Rep. Prog. Phys.* **61**, 237–312 (1998)
- [179] A. Michaelides, P. Hu, M.-H. Lee, A. Alavi, and D. A. King, “Resolution of an Ancient Surf. Sci. Anomaly: Work Function Change Induced by N Adsorption on $\text{W}\{100\}$,” *Phys. Rev. Lett.* **90**, 246103 (2003)
- [180] W. Tang, E. Sanville, and G. Henkelman, “A grid-based Bader analysis algorithm without lattice bias,” *J. Phys.; Condens. Matter* **21**, 084204 (2009)

- [181] Chris G. Van de Walle and Jörg Neugebauer, “First-principles calculations for defects and impurities: Applications to III-nitrides,” *J. Appl. Phys.* **95**, 3851–3879 (2004)
- [182] G. Makov and M. C. Payne, “Periodic boundary conditions in ab initio calculations,” *Phys. Rev. B* **51**, 4014–4022 (1995)
- [183] Stephan Lany and Alex Zunger, “Assessment of correction methods for the band-gap problem and for finite-size effects in supercell defect calculations: Case studies for ZnO and GaAs,” *Phys. Rev. B* **78**, 235104 (2008)
- [184] Risto M Nieminen, “Issues in first-principles calculations for defects in semiconductors and oxides,” *Modelling Simul. Mater. Sci. Eng.* **17**, 084001 (2009)
- [185] Stephan Lany and Alex Zunger, “Accurate prediction of defect properties in density functional supercell calculations,” *Modelling Simul. Mater. Sci. Eng.* **17**, 084002–(2009)
- [186] C.W.M. Castleton, A Höglund, and S Mirbt, “Density functional theory calculations of defect energies using supercells,” *Modelling Simul. Mater. Sci. Eng.* **17**, 084003– (2009)
- [187] Joachim Paier, Martijn Marsman, and Georg Kresse, “Why does the B3LYP hybrid functional fail for metals?” *J. Chem. Phys.* **127**, 024103 (2007)
- [188] R. T. Poole, J. Liesegang, R. C. G. Leckey, and J. G. Jenkin, “Electronic band structure of the alkali halides. II. Critical survey of theoretical calculations,” *Phys. Rev. B* **11**, 5190–5196 (1975)
- [189] F. Bechstedt and R. Del Sole, “Analytical treatment of band-gap underestimates in the local-density approximation,” *Phys. Rev. B* **38**, 7710–7716 (1988)
- [190] Joachim Paier, Robin Hirschl, Martijn Marsman, and Georg Kresse, “The Perdew–Burke–Ernzerhof exchange–correlation functional applied to the G2-1 test set using a plane-wave basis set,” *J. Chem. Phys.* **122**, 234102 (2005)
- [191] Fumiyasu Oba, Atsushi Togo, Isao Tanaka, Joachim Paier, and Georg Kresse, “Defect energetics in ZnO: A hybrid Hartree-Fock density functional study,” *Phys. Rev. B* **77**, 245202 (2008)
- [192] A. Janotti, J. B. Varley, P. Rinke, N. Umezawa, G. Kresse, and C. G. Van de Walle, “Hybrid functional studies of the oxygen vacancy in TiO₂,” *Phys. Rev. B* **81**, 085212 (2010)
- [193] F. Fuchs, J. Furthmüller, F. Bechstedt, M. Shishkin, and G. Kresse, “Quasiparticle band structure based on a generalized Kohn-Sham scheme,” *Phys. Rev. B* **76**, 115109 (2007)

-
- [194] Joachim Paier, Martijn Marsman, and Georg Kresse, “Dielectric properties and excitons for extended systems from hybrid functionals,” *Phys. Rev. B* **78**, 121201 (2008)
- [195] Hannu-Pekka Komsa and Tapio T. Rantala, “Comparison of charged-defect finite-size supercell correction methods in a general framework,” (2009), arXiv:0906.1283v1
- [196] C. W. M. Castleton, A. Höglund, and S. Mirbt, “Managing the supercell approximation for charged defects in semiconductors: Finite-size scaling, charge correction factors, the band-gap problem, and the ab initio dielectric constant,” *Phys. Rev. B* **73**, 035215 (2006)
- [197] C. W. M. Castleton and S. Mirbt, “Finite-size scaling as a cure for supercell approximation errors in calculations of neutral native defects in *InP*,” *Phys. Rev. B* **70**, 195202 (2004)
- [198] Christoph Freysoldt, Jörg Neugebauer, and Chris G. Van de Walle, “Fully Ab Initio Finite-Size Corrections for Charged-Defect Supercell Calculations,” *Phys. Rev. Lett.* **102**, 016402 (2009)
- [199] Audrius Alkauskas, Peter Broqvist, and Alfredo Pasquarello, “Defect Energy Levels in Density Functional Calculations: Alignment and Band Gap Problem,” *Phys. Rev. Lett.* **101**, 046405 (2008)
- [200] Edward U. Condon, “Nuclear Motions Associated with Electron Transitions in Diatomic Molecules,” *Phys. Rev.* **32**, 858–872 (1928)
- [201] R. F. Wood and H. W. Joy, “Theory of the Absorption and Emission of the F Center in Alkali-Halide Crystals,” *Phys. Rev.* **136**, A451–A463 (1964)
- [202] R. H. Bartram, A. M. Stoneham, and Philip Gash, “Ion-Size Effects in Color Centers,” *Phys. Rev.* **176**, 1014–1024 (1968)
- [203] Chong Kim Ong and John M. Vail, “Theoretical survey of F centers in alkali halides with NaCl structure. II. Emission and the relaxed excited state,” *Phys. Rev. B* **18**, 6861–6864 (1978)
- [204] S. Y. La and R. H. Bartram, “Wave Functions for F' Centers in Alkali Halides,” *Phys. Rev.* **144**, 670–675 (1966)
- [205] D. B. Fitchen, R. H. Silsbee, T. A. Fulton, and E. L. Wolf, “Zero-Phonon Transitions of Color Centers in Alkali Halides,” *Phys. Rev. Lett.* **11**, 275–277 (1963)
- [206] C. B. Pierce, “Discrete Phonon and Zero-Phonon Optical Absorption Spectra in Alkali Halides,” *Phys. Rev.* **135**, A83–A86 (1964)
- [207] Mladen Georgiev, *F' Centers in Alkali Halides* (Springer Berlin Heidelberg, 1988)

- [208] S. Benci and M. Manfredi, “Luminescence Lifetime in KCl Crystals Containing α , F , and F' Centers,” *Phys. Rev. B* **7**, 1549–1553 (1973)
- [209] Hilkka Saal, Thomas Bredow, and Michael Binnewies, “Band gap engineering of ZnO via doping with manganese: effect of Mn clustering,” *Phys. Chem. Chem. Phys.* **11**, 3201–3209 (2009)
- [210] A. Stroppa and G. Kresse, “Unraveling the Jahn-Teller effect in Mn-doped GaN using the Heyd-Scuseria-Ernzerhof hybrid functional,” *Phys. Rev. B* **79**, 201201 (2009)
- [211] Adam Gali, Erik Janzén, Péter Deák, Georg Kresse, and Efthimios Kaxiras, “Theory of Spin-Conserving Excitation of the $N - V^-$ Center in Diamond,” *Phys. Rev. Lett.* **103**, 186404 (2009)
- [212] Péter Ágoston, Karsten Albe, Risto M. Nieminen, and Martti J. Puska, “Intrinsic n -Type Behavior in Transparent Conducting Oxides: A Comparative Hybrid-Functional Study of In_2O_3 , SnO_2 , and ZnO,” *Phys. Rev. Lett.* **103**, 245501 (2009)
- [213] David O. Scanlon, Benjamin J. Morgan, Graeme W. Watson, and Aron Walsh, “Acceptor Levels in p -Type Cu_2O : Rationalizing Theory and Experiment,” *Phys. Rev. Lett.* **103**, 096405 (2009)
- [214] Peter Deák, Bálint Aradi, Thomas Frauenheim, Erik Janzén, and Adam Gali, “Accurate defect levels obtained from the HSE06 range-separated hybrid functional,” *Phys. Rev. B* **81**, 153203 (2010)
- [215] M. Shishkin and G. Kresse, “Implementation and performance of the frequency-dependent GW method within the PAW framework,” *Phys. Rev. B* **74**, 035101 (2006)
- [216] Michael P. Surh, Hélio Chacham, and Steven G. Louie, “Quasiparticle excitation energies for the F-center defect in LiCl,” *Phys. Rev. B* **51**, 7464–7470 (1995)
- [217] Patrick Rinke, Anderson Janotti, Matthias Scheffler, and Chris G. Van de Walle, “Defect Formation Energies without the Band-Gap Problem: Combining Density-Functional Theory and the GW Approach for the Silicon Self-Interstitial,” *Phys. Rev. Lett.* **102**, 026402 (2009)
- [218] L. Martin-Samos, G. Roma, P. Rinke, and Y. Limoge, “Charged Oxygen Defects in SiO_2 : Going beyond Local and Semilocal Approximations to Density Functional Theory,” *Phys. Rev. Lett.* **104**, 075502 (2010)
- [219] Stephan Lany and Alex Zunger, “Many-body GW calculation of the oxygen vacancy in ZnO,” *Phys. Rev. B* **81**, 113201 (2010)
- [220] Yuchen Ma and Michael Rohlfing, “Optical excitation of deep defect levels in insulators within many-body perturbation theory: The F center in calcium fluoride,” *Phys. Rev. B* **77**, 115118 (2008)

- [221] Yuchen Ma, Michael Rohlfing, and Adam Gali, “Excited states of the negatively charged nitrogen-vacancy color center in diamond,” *Phys. Rev. B* **81**, 041204 (2010)

Acknowledgment

I am indebted to Prof. Dr. Herbert Pfnür for providing me with the chance to pursue my PhD project in his group. During the time I spent in Uni. Hannover, I was constantly inspired by his open-mindedness and broad knowledge. He is always so kind, and the open and relaxing atmosphere stimulated a great deal of ideas in this work.

I would like to thank Dr. Christoph Tegenkamp for his valuable discussion and kindness. By the way, thanks for inviting us to the Bundesliga match in the AWD Arena. That was an impressive experience. My thanks also go to all the co-workers in the group and those who have left the group, as well as the department secretary Mrs. Heike Kahrs. In particular, I appreciate Dirk Müller-Sajak, my office mate, who helped us make quite a lot phone calls when we just arrived in Hannover and knew little German. The credit of the Zusammenfassung of this thesis also goes to him. I also thank Prof. Thomas Bredow and Dr. Florian Janetzko for the one-week one-on-one workshop on CRYSTAL in Uni. Bonn. The introductions given by Dr. Volodymyr Maslyuk and Jörg Meyer are appreciated.

I owe my gratitude to Mrs. Elke Trolp and her husband, who picked us up at the airport on the first rainy night we arrived here and waited for over two hours due to the flight delay. We really appreciate for all the things they have prepared and arranged for us for our stay in the student dorm in the first few weeks.

This work is financially supported by K+S Group. The computing allocation time is generously provided by the HLRN supercomputing center and the RRZN of Uni. Hannover. I thank Bernd Kallies for debugging the installation of VASP 5.2 on HICE-II clusters at HLRN.

I am grateful to my family in Shanghai for their encouragement and support. This work would have never been possible without the understanding and tolerance from my wife Jiaying. I am indebted to her for always backing me up and for preparing all the lekker dinners over the last couple of years.

Publications

Parts of the thesis have been peer-reviewed and published as:

- [1] W. Chen, C. Tegenkamp, H. Pfnür, and T. Bredow, “Tailoring band gaps of insulators by adsorption at surface defects: Benzoic acids on NaCl surfaces,” *Phys. Rev. B* **79**, 235419 (2009)
- [2] Wei Chen, Christoph Tegenkamp, Herbert Pfnür, and Thomas Bredow, “The interplay of van der Waals and weak chemical forces in the adsorption of salicylic acid on NaCl(001),” *Phys. Chem. Chem. Phys.* **11**, 9337–9340 (2009)
- [3] Wei Chen, Christoph Tegenkamp, Herbert Pfnür, and Thomas Bredow, “Insight from first-principles calculations into the interactions between hydroxybenzoic acids and alkali chloride surfaces,” *J. Phys. Chem. C* **114**, 460–467 (2010)
- [4] Wei Chen, Christoph Tegenkamp, Herbert Pfnür, and Thomas Bredow, “Anomalous molecular orbital variation upon adsorption on a wide band gap insulator,” *J. Chem. Phys.* **132**, 214706 (2010)
- [5] Wei Chen, Christoph Tegenkamp, Herbert Pfnür, and Thomas Bredow, “Color centers in NaCl by hybrid functionals,” *Phys. Rev. B* **82**, 104106 (2010)

Index

- adiabatic connection, 14
- basis set superposition error, 21
- benzoic acid, 39
- Bethe-Salpeter equation, 36
- Born-Oppenheimer approximation, 6
- charge transfer model, 3
- counterpoise method, 21
- dielectric function, 34
- Dyson equation, 29
- electron energy loss spectra, 34
- exchange hole, 9
- exchange-correlation energy, 14
- exchange-correlation hole, 14
- excitonic effect, 45
- Fock exchange, 9
- Fock operator, 9
- functional derivative discontinuity, 16
- fundamental gap, 16
- Gaussian primitives, 20
- generalized gradient approximation, 15
- Green's function, 29
- GW* approximation, 32
- Hartree equations, 8
- Hartree-Fock equations, 9
- Hohenberg-Kohn theorem, 12
- HSE, 18
- hybrid functional, 17
- image charge model, 77
- inverse dielectric function, 34
- inverse photoemission, 29
- KB separable pseudopotential, 24
- Kohn-Sham DFT, 13
- Koopmans' theorem, 9
- KS gap, 16
- Lehmann representation, 30
- local density approximation, 14
- local field effect, 34
- macroscopic dielectric function, 34
- MP2, 10
- Newns-Anderson model, 58
- norm-conservation, 23
- para*-salicylic acid, 39
- photoemission, 29
- plasmon-pole approximation, 35
- polar step models, 92
- projected density of states, 47
- PW1PW, 18
- quasiparticle, 30
- random phase approximation, 32
- salicylic acid, 39
- self-consistent field, 8
- self-interaction, 16
- Slater determinants, 7
- Slater exchange, 12
- split-valence scheme, 21
- surface color center, 85
- Tamm-Dancoff approximation, 37
- Thomas-Fermi approximation, 11
- van der Waals force, 18
- vertex correction, 35

Curriculum Vitae

Personal Information

Name: Wei Chen
Genre: Male
Date of Birth: August 11, 1980
Place of Birth: Shanghai, P.R. China
Marital Status: Married
Address: Leibniz Universität Hannover
Institut für Festkörperphysik
Atomare und Molekulare Strukturen (ATMOS)
Appelstr. 2, 30167 Hannover, Germany
Tel: +49 511 762 4876
E-Mail: chen@fkp.uni-hannover.de

Education

09.1998 – 07.2002 B.Sc, Fudan University, Shanghai, China
Department of Illuminating and Light Engineering
09.2002 – 07.2005 M.Sc, Fudan University, Shanghai, China
Department of Microelectronics (Prof. David W. Zhang)
Thesis: "DFT of ALD for High- k Gate Dielectrics"
08.2007 – 03.2011 PhD, Leibniz Universität Hannover, Germany
Institut für Festkörperphysik
Atomare und Molekulare Strukturen (Prof. Herbert Pfnür)
Thesis: "Organic Molecules on Wide-gap Insulator"